

Akira Kunashiro

Proposal and Improvement of a Novel Magnetic-gearred Motor with Bearingless High-speed Rotor

〈〈博士論文〉〉

Doctoral Thesis

ベアリングレス高速ロータを持つ磁気ギアードモータの
提案と特性改善に関する研究

Proposal and Improvement of a Novel Magnetic-gear Motor with
Bearingless High-speed Rotor

令和 6 年 2 月

指導教員 千葉 明 教授

東京工業大学 工学院 電気電子系

熊代 明

Author: Akira Kunashiro

Supervisor: Akira Chiba

Chiba Kiyota laboratory, Department of Electrical and Electronic Engineering,

School of Engineering, Tokyo Institute of Technology

February, 2024

The author's grandfather, the late Mr. Futoshi Ikenaga, spent many years as a firefighter engaged in lifesaving work, and also inspired the author's curiosity about science. I dedicate this thesis to the late Mr. Futoshi Ikenaga,

Akira Kumashiro

本研究を遂行するにあたって、以下の支援を賜りました。ここに御礼申し上げます。

This work has been supported by the “LCM – K2 Center for Symbiotic Mechatronics” within the framework of the Austrian COMET-K2 program.

JMAG ソフトウェアのライセンスを許諾いただいた株式会社 JSOL に謝意を表します。

本研究は、JST 次世代研究者挑戦的研究プログラム JPMJSP2106 の支援を受けたものです。

本研究の一部はパワーアカデミー研究助成により実施されたものである。

In conducting this research, we received the following support. We would like to express our sincere gratitude here.

This work has been supported by the “LCM – K2 Center for Symbiotic Mechatronics” within the framework of the Austrian COMET-K2 program.

The author is grateful for the academic JMAG software license from JSOL Corporation.

This work was also partly supported by JST SPRING, Grant Number JPMJSP2106.

This study was also partly supported by research grant from the Japan Power Academy.

誤字等修正版は以下のページにアップロードしております。

English version is available in follows;

https://github.com/akira-kumashiro/doctoral_thesis

この論文は 2024 年 2 月に作成された論文の誤字修正版です。

This paper is the revised version of the doctoral thesis written in February 2024.

Contents

Contents	i
List of Figures	v
List of Tables	xii
Chapter 1. Introduction	1
1. 1. Basics of Magnetic-Geared Motors	4
1. 1. 1 Types of Winding Components.....	5
1. 1. 2 Types of Topologies.....	8
1. 2. Basics of Bearingless Motors.....	11
1. 2. 1 Types of Actively Controlled Axis Number.....	12
1. 2. 2 Types of Magnetic Suspension Current.....	14
1. 3. Thesis Abstract.....	15
1. 4. Thesis Outline.....	17
Chapter 2. Research Trends on High-Speed Magnetic-Geared Motors/Magnetic Gear and High-Torque Bearingless Motors	19
2. 1. Research Trends in High-Speed Magnetic-Geared Motors and High-Speed Magnetic Gears	19
2. 2. Research Trends in Low-Speed High-Torque Bearingless Motors.....	21
2. 3. Solutions to Current Issues and Objectives of This Research.....	23
2. 4. Summary of Chapter 2.....	25
Chapter 3. Structure and Principle of Magnetic-Geared Motor with Magnetic-Suspended High-Speed Rotor	26
3. 1. Structure of Proposed Motor	26
3. 1. 1 Structure of Reluctance-Type Magnetic-Geared Motor with Magnetic Suspended High-Speed Rotor	28
3. 1. 2 Structure of Surface Permanent Magnet Type Magnetic-Geared Motor with Magnetic Suspended High-Speed Rotor	30
3. 1. 3 Structure of Consequent-Pole Type Magnetic-Geared Motor with Magnetic Suspended High-Speed Rotor.....	32

3. 2. Operating Principle of Proposed Magnetic-Geared Motors	34
3. 2. 1 Operating Principle of Reluctance Magnetic-Geared Motors	34
3. 2. 2 Operating Principle of Surface Permanent Magnet Type and Consequent-Pole Type Magnetic-Geared Motors	41
3. 3. Principle of Magnetic Suspension Force Generation of the Proposed Motors.....	44
3. 3. 1 Principle of Active Magnetic Suspension Force Generation in Surface Permanent Type Two-Degree-Of-Freedom Actively Position Regulated Bearingless Motor.....	44
3. 3. 2 Principle of Active Magnetic Suspension Force Generation in Consequent-Pole Type Two-Degree-Of-Freedom Actively Position Regulated Bearingless Motor.....	48
3. 3. 3 Principle of Force Generation by Passive Magnetic Suspension in Two-Degree-of-Freedom Actively Position Regulated Bearingless Motor.....	51
3. 4. Summary of Chapter 3.....	52
Chapter 4. Proposal and Analysis of High-Speed Rotor Magnetic Suspension for Reluctance-Type Magnetic-Geared Motors.....	55
4. 1. Analysis of the Relationship between the Pole / Slot Combinations and Motor / Suspension Characteristics	55
4. 1. 1 Analysis Settings.....	55
4. 1. 2 Analysis Result.....	56
4. 2. Analysis of Stator Back Yoke Thickness and Various Characteristics	63
4. 2. 1 Analysis Settings.....	63
4. 2. 2 Air-gap Flux-density Distribution	68
4. 2. 3 Torque Characteristics.....	70
4. 2. 4 Stator Back Yoke and Suspension Force	73
4. 3. Analysis of mutual interference between motor current and suspension current..	76
4. 4. Consideration of Hall element placement for angle position detection	78
4. 5. Consideration of Maximum Transmission Torque Improvement by Flux Strengthening.....	80
4. 6. Analysis of Stack Length and Motor Characteristics	82
4. 6. 1 Relationship between Stack Length and Torque	82
4. 6. 2 Relationship between Stack Length and Tilting Stiffness.....	85
4. 6. 3 Relationship between Stack Length and Radial Force	87
4. 7. Summary of Chapter 4.....	92

Chapter 5. Experimental Verification of High-Speed Rotor Magnetic Suspension for Reluctance-Type Magnetic-Geared Motors	93
5. 1. Experimental Setup	93
5. 1. 1 Specifications.....	93
5. 1. 2 Control Method	97
5. 1. 3 Windings	99
5. 1. 4 Angle Detection.....	115
5. 1. 5 Displacement Sensor	120
5. 2. Magnetic Suspension Start-up Test in Non-Rotating State	123
5. 2. 1 Magnetic Suspension Start-up without Low-speed Rotor	123
5. 2. 2 Magnetic Suspension Start-up with Low-speed Rotor	126
5. 3. Magnetic Suspension During Rotation.....	129
5. 4. Speed Test	132
5. 5. Radial Force Measurement	139
5. 6. Measurement of Magnetic-Geared Motor Performance	145
5. 7. Breakage of Prototype	149
5. 8. Summary of Chapter 5.....	151
Chapter 6. Investigation of High-Speed Rotor Magnetic Suspension for Consequent-Pole Type Magnetic-Geared Motors	153
6. 1. Problems with the Motor Proposed in Chapter 4	153
6. 1. 1 Low Torque Density	153
6. 1. 2 Difficulty in Accurately Detecting the Angle Position of High-Speed Rotor....	154
6. 2. Investigation of Pole Number and Magnetic Suspension Characteristics by Two-Dimensional Finite Element Method	155
6. 2. 1 Analysis Settings.....	155
6. 2. 2 Radial Force of Single-Sided Consequent Pole Type Magnetic-Geared Motors	157
6. 2. 3 Radial Force of Single-Sided Consequent Pole Type Magnetic-Geared Motors	161
6. 3. Summary of Chapter 6.....	166
Chapter 7. Optimization and Verification of High-Speed Rotor Magnetic Suspension for Consequent-Pole Type Magnetic-Geared Motors.....	167

7.1.	Optimization Using Two-Dimensional Finite Element Method	167
7.1.1	Optimization Settings	167
7.1.2	Optimization Results	171
7.2.	Verification of Optimal Model Using Three-Dimensional Finite Element Method	
	175	
7.3.	Summary of Chapter 7.....	182
Chapter 8.	Conclusion.....	183
8.1.	Summary.....	183
8.2.	Future Work.....	186
8.2.1	Change in Tilt Stiffness by d -Axis Current.....	186
8.2.2	Investigation of the Optimal Stack Length for Reluctance-Type Magnetic-Geared Motors	186
8.2.3	Reduction of Power Consumption During Magnetic Suspension	186
8.2.4	Detailed Measurement of Efficiency and Losses	187
8.2.5	Evaluation for Prototype Manufacturing of a Consequent-Pole Type Magnetic-Geared Motor	187
8.2.6	Investigation of Torque Density Improvement by Changing the Magnetic Suspension Method.....	187
Annex A.	Programs for the Experiment	188
Annex B.	Model Analyzed in Section 4.1	189
Annex C.	Reluctance-Type Magnetic-Geared Motor Model After Section 4.2.....	192
Dedication	195	
Reference.....	198	
List of publications.....	210	
Peer-Reviewed Papers	210	
International Conferences.....	210	
Domestic Conference	211	
List of Awards	214	

List of Figures

Fig. 1. 1. Spur gears commonly used in mechanical reducers.....	1
Fig. 1. 2. Magnetic gear without magnetic modulation.....	2
Fig. 1. 3. Magnetic gear with magnetic modulation.....	2
Fig. 1. 4. Example of magnetic-gearred motor structure.	4
Fig. 1. 5. Internal stator type magnetic-gearred motor.....	7
Fig. 1. 6. Outer stator type magnetic-gearred motor.....	7
Fig. 1. 7. Magnetic-gearred motor with winding on modulator.	7
Fig. 1. 8. Interior permanent magnet type magnetic-gearred motor.....	9
Fig. 1. 9. Reluctance-type magnetic-gearred motor.	10
Fig. 1. 10. Consequent-pole type magnetic-gearred motor.	10
Fig. 3. 1. Cross-sectional view of reluctance-type magnetic-gearred motor with magnetic-suspended high-speed rotor.....	29
Fig. 3. 2. Cross-sectional view of surface permanent magnet type magnetic-gearred motor with magnetic-suspended high-speed rotor.	31
Fig. 3. 3. Cross-sectional view of a consequent-pole type magnetic-gearred motor with magnetic suspended high-speed rotor.....	33
Fig. 3. 4. Vector diagram of a reluctance-type magnetic-gearred motor.	35
Fig. 3. 5. Principle of radial-force generation as surface permanent magnet type bearingless motor.	46
Fig. 3. 6. Principle of radial-force generation as consequent-pole type bearingless motor.	49
Fig. 3. 7. Principle of passive magnetic suspension force generation in the axial direction.	51
Fig. 3. 8. Principle of passive magnetic suspension force generation in the tilting direction.	51
Fig. 4. 1. Relationship between the number of stator slots and the average maximum transmitted torque $Tlmax$	57
Fig. 4. 2. Relationship between the number of stator slots and the torque ripple.	57
Fig. 4. 3. Relationship between the symmetry factor xs and the average value of the	

radial force magnitude for a single mechanical angle cycle for two-pole high-speed rotors	58
Fig. 4. 4. Relationship between the symmetry factor \mathbf{xs} and the torque ripple for two-pole high-speed rotors.....	58
Fig. 4. 5. Relationship between the symmetry factor \mathbf{xs} and the average value of the radial force magnitude for a single mechanical angle cycle for four-pole high-speed rotors	60
Fig. 4. 6. Relationship between the symmetry factor \mathbf{xs} and the torque ripple for four-pole high-speed rotors.....	60
Fig. 4. 7. Flux-density distribution of the 140 mm outer diameter model.....	65
Fig. 4. 8. Winding arrangement of the analyzed model.....	67
Fig. 4. 9. Air-gap flux-density distributions in the radial direction.....	69
Fig. 4. 10. Magnitudes of flux density in spatial harmonic components between the low-speed rotor and stator.....	69
Fig. 4. 11. Torque waveform in different conditions with and without q -axis current \mathbf{imq}	70
Fig. 4. 12. Output and losses at each low-speed rotor rotational speed at maximum torque.	
.....	71
Fig. 4. 13. Efficiency at each low-speed rotor rotational speed at maximum torque.....	72
Fig. 4. 14. Flux-density distribution of the 130 mm outer diameter model. (a) Suspension current $\mathbf{isy} = \mathbf{0}$ A. (b) Suspension current $\mathbf{isy} = \mathbf{20}$ A.....	74
Fig. 4. 15. Flux-density distribution of the 140 mm outer diameter model. (a) Suspension current $\mathbf{isy} = \mathbf{0}$ A. (b) Suspension current $\mathbf{isy} = \mathbf{20}$ A.....	74
Fig. 4. 16. Suspension characteristics of the different stator diameter models with respect to the rotational angular position of the high-speed rotor (HSR) θ_h	75
Fig. 4. 17. Analysis results of the mutual interference between the motor current and suspension current.	77
Fig. 4. 18. Analysis results for magnetic flux density variations in each direction.	79
Fig. 4. 19. Amplitude of the magnetic flux density in the z-direction along the \mathbf{x} -axis on the outer side of the high-speed rotor.....	79
Fig. 4. 20. Magnetic flux density between the high-speed rotor and low-speed rotor with q -axis current applied.....	81
Fig. 4. 21. torque of the high-speed rotor with and without a low-speed rotor at a q -axis	

current of 1 A.....	81
Fig. 4. 22. Relationship between stack length and maximum transmission torque.....	83
Fig. 4. 23. Relationship between stack length and torque density.	83
Fig. 4. 24. Relationship between axial position and magnetic flux density with varying stack length L in relative axial position z/L	84
Fig. 4. 25. Relationship between axial position and magnetic flux density with varying stack length L in absolute axial position z	84
Fig. 4. 26. Relationship between tilt angle and tilting restoring torque with varying stack length L	86
Fig. 4. 27. Relationship between the force-displacement factor k_x and the stack length.	88
Fig. 4. 28. relationship between the force-current factor k_i and the stack length.	88
Fig. 4. 29. Radial force-displacement factor k_x per stack length for different stack lengths.....	90
Fig. 4. 30. Radial force-current density factor k_i per stack length for different stack lengths.....	90
Fig. 4. 31. Current density required for magnetic suspension start-up with different stack lengths.....	91
Fig. 5. 1. CAD model of the prototype.	95
Fig. 5. 2. Prototype of the proposed machine.....	96
Fig. 5. 3. Control system for rotor radial position and motor current.....	98
Fig. 5. 4. Relationship between the high-speed rotor rotation speed and phase voltage with different numbers of two-pole motor winding strands.	100
Fig. 5. 5. Relationship between the high-speed rotor rotation speed and apparent power and true power for the two-pole motor winding.	100
Fig. 5. 6. Relationship between the high-speed rotor rotation speed and phase voltage with different numbers of four-pole suspension winding strands.....	100
Fig. 5. 7. Relationship between the high-speed rotor rotation speed and apparent power and true power for the four-pole suspension winding.....	101
Fig. 5. 8. Bobbin used for winding.	102
Fig. 5. 9. Stator after completing the two-pole motor winding.....	102
Fig. 5. 10. stator after completing the winding for one slot.....	103

Fig. 5. 11. Winding after the winding design was changed.	104
Fig. 5. 12. Sample of the measurement results approximated by the program.	105
Fig. 5. 13. Error in the magnitude of the impedance of each slot in a two-pole motor winding.....	107
Fig. 5. 14. Error in the impedance phase of each slot in a two-pole motor winding....	107
Fig. 5. 15. Resistance error for each slot in the two-pole motor winding.....	108
Fig. 5. 16. Self-inductance error for each slot in the two-pole motor winding.	108
Fig. 5. 17. Mutual inductance error for each slot in the two-pole motor winding.	109
Fig. 5. 18. DC resistance errors of each slot in the two-pole motor winding.....	110
Fig. 5. 19. DC resistance errors of each slot in the four-pole magnetic suspension winding.	110
Fig. 5. 20. Stator after being pressed into the frame.	112
Fig. 5. 21. Windings where the short-circuits occurred.	112
Fig. 5. 22. Short circuit countermeasures implemented.	113
Fig. 5. 23. Short circuit at the stator corners caused by insufficient length of the insulating paper.....	113
Fig. 5. 24. Comparison of the induced voltage analysis results and the experimental results.	114
Fig. 5. 25. Experimental setup for the calibration bearing support mode.	115
Fig. 5. 26. Angle detection error of the Hall element obtained by analysis.	116
Fig. 5. 27. Comparison between the angle detection values of the Hall element and the rotary encoder in the experiment.....	117
Fig. 5. 28. Error between the angle detection values of the Hall element and the rotary encoder in the experiment.	118
Fig. 5. 29. Fourier transform results of Fig. 5. 28(b).	119
Fig. 5. 30. Displacement of the displacement sensor target and the output voltage....	120
Fig. 5. 31. Results of displacement sensor output compensation.....	121
Fig. 5. 32. Displacement during rotation by the motor current without magnetic suspension.	122
Fig. 5. 33. Displacement trace with rotation by the motor winding without magnetic suspension.	122
Fig. 5. 34. Amplitude response to time obtained in MATLAB using the transfer function	

without a low-speed rotor.....	125
Fig. 5. 35. Amplitude response to time obtained in MATLAB using the transfer function with a low-speed rotor.....	126
Fig. 5. 36. Experimental result of the magnetic suspension start-up.	128
Fig. 5. 37. Experimental results at the rotational speed reference of the high-speed rotor Nh *= 1300 r/min while the rotor is magnetically suspended.	130
Fig. 5. 38. High-speed rotor displacement (disp.) orbit at the rotational speed reference of the high-speed rotor Nh *= 7020 r/min while the rotor is magnetically suspended.	131
Fig 5. 39. Amplitude of displacement with changing rotational speed.....	133
Fig. 5. 40. Displacement traces with changing rotational speed.....	134
Fig 5. 41. Experimental results of the speed test while the rotor is magnetically suspended.	137
Fig 5. 42. Variation of natural frequencies of forward precession movement with respect to the rotational speed of the prototype machine.	138
Fig. 5. 43. Experimental setup for measuring radial force Fx	140
Fig. 5. 44. Experimental results of suspension currents isx under different radial forces Fx with respect to the rotational angular position of the high-speed rotor (HSR) θh	141
Fig. 5. 45. Experimental results of suspension current and direction under the gravity applied in the x -axis with respect to the rotational angular position of the high- speed rotor (HSR) θh	142
Fig. 5. 46. Modified experimental setup for applying radial force Fx	143
Fig. 5. 47. Magnetic suspension current isx at the rotation angle position of the high- speed rotor (HSR) with different radial force Fx were applied using the modified experimental device.	144
Fig. 5. 48. Torque measurement bench.....	145
Fig. 5. 49. Comparison of efficiency with and without bearings.....	146
Fig. 5. 50. Comparison of losses with and without bearings.....	147
Fig. 5. 51. Maximum transmission torque verification test.	148
Fig. 5. 52. Broken parts of the prototype.....	150
Fig. 6. 1. Magnetic suspension characteristics of single-sided consequent-pole type	

magnetic-geared motors with $isx = 20$ A suspension current.....	158
Fig. 6. 2. Unbalanced magnetic pull generated in single-sided consequent-pole magnetic-geared motors with a high-speed rotor radially displaced by 0.5 mm in the x -axis direction.....	159
Fig. 6. 3. Magnetic flux density distribution of each model of single-sided consequent-pole type magnetic-geared motors without current.....	160
Fig. 6. 4. Magnetic suspension characteristics of double-sided consequent-pole type magnetic-geared motors with $isx = 20$ A suspension current.....	163
Fig. 6. 5. Unbalanced magnetic pull generated in double-sided consequent-pole magnetic-geared motors with a high-speed rotor radially displaced by 0.5 mm in the x -axis direction.....	164
Fig. 6. 6. Magnetic flux density distribution of each model of single-sided consequent-pole type magnetic-geared motors without current.....	165
Fig. 7. 1. Design parameters of optimization.....	169
Fig. 7. 2. Pareto optimal solutions of each model.....	173
Fig. 7. 3. Suspension characteristics waveform with respect to the high-speed rotor (HSR) angular position θh	176
Fig. 7. 4. Unbalanced magnetic pull force Fux waveforms with a high-speed rotor radially displaced by 0.5 mm in the x -axis direction without current.....	177
Fig. 7. 5. Low-speed rotor output torque waveforms Tl without current.....	177
Fig. 7. 6. Comparisons between two-dimensional and three-dimensional finite element method analysis results.....	178
Fig. 7. 7. Flux-density distribution of full model and enlarged view with x -axis direction suspension current $isus = 10$ A.....	180
Fig. 7. 8. Iron loss in the optimal models for each topology.....	181
Fig. B. 1. Schematic diagram of all components of a reluctance-type magnetic-geared motor.....	189
Fig. B. 2. Dimensional drawing of high-speed rotor (HSR).....	189
Fig. B. 3. Dimensional drawing of low-speed rotor (LSR).....	189
Fig. B. 4. Dimensional drawing of low-speed rotor (LSR) (partial enlargement).....	190
Fig. B. 5. Dimensional drawing of stator.....	190
Fig. B. 6. Stator dimension diagram (partial enlargement).....	190

Fig. B. 7. Tooth width of the low-speed rotor (LSR).....	191
Fig. C. 1. Stator.....	192
Fig. C. 2. Low-speed rotor.....	193
Fig. C. 3. High-speed rotor.....	194

List of Tables

Table 2. 1. Torque density comparison of the two-axis actively controlled bearingless motors.....	22
Table 3. 1. Combination of magnetic gear topology and magnetic suspension methods.	52
Table 3. 2. Advantages and disadvantages of each magnetic-gearred motor topology....	53
Table 4. 1. Relationship between the symmetry factor \mathbf{xs} and the radial force and torque for two-pole high-speed rotor.....	59
Table 4. 2. Relationship between the symmetry factor \mathbf{xs} and the radial force and torque for four-pole high-speed rotor.	61
Table 4. 3. Specifications of the analyzed model.	64
Table 5. 1. Parameters of the prototype machine	94
Table 5. 2. Comparison of the winding designs before and after the change.	103
Table 6. 1. Dimensions of the analyzed motor.	155
Table 6. 2. Pole combination in the analysis of single-sided consequent-pole magnetic-gearred motors.	157
Table 6. 3. Pole combination in the analysis	161
Table 6. 4. Analysis results in Chapter 6.	166
Table 7. 1. Fixed parameters of the optimization models.....	167
Table 7. 2. Pole combinations of each topology.....	168
Table 7. 3. Objectives of the optimization.....	170
Table 7. 4. Value of the design parameters for the selected optimum points.....	174
Table 7. 5. Comparisons between two-dimensional and three-dimensional finite element method analysis results for the optimization objectives.	178

Chapter 1. Introduction

In recent years, the development of electric vehicles and robots, as well as the electrification of various industrial components, has led to an increase in demand for small, high-torque motors [1]. Generally, torque can be increased by increasing the stack length or radius of a motor. However, increasing the size of a motor has undesirable effects such as increased volume and weight. For this reason, a configuration known as a geared motor is widely used, which improves output by increasing the rotational speed while maintaining the volume of the motor, and then reduces the speed to the desired rotational speed range using a mechanical reducer to achieve a compact, high-torque motor. Fig. 1. 1 shows the spur gears commonly used in mechanical reducers. For example, in [2], a geared motor is used to drive an exoskeleton that requires compactness, light weight, and high torque. In this system, power is transmitted through gear friction, which causes problems such as wear and friction loss. In addition, mechanical reducers require lubrication, which is not suitable for applications that require the prevention of lubricant splashing or contamination. Furthermore, gear wear is unavoidable, requiring regular replacement, and there is a risk of damage during excessive input, which can lead to increased costs [3]. To prevent these issues, when using mechanical reducers, it is necessary to add lubrication to the gear surfaces, install protective devices to prevent overloading, and perform regular maintenance.

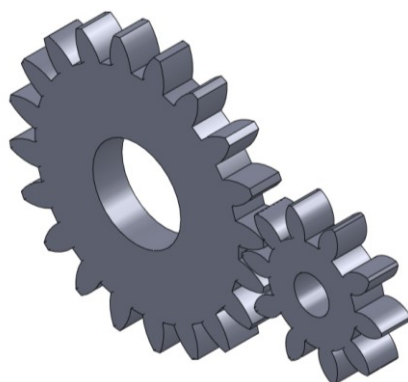


Fig. 1. 1. Spur gears commonly used in mechanical reducers.

To solve these problems, magnetic gear has been proposed, which uses magnetic force instead of friction between tooth surfaces to transmit power. Magnetic gear can be classified into two types [17]: those that use magnetic modulation [12][13][14][15] [16] and those that do not [4] [5][6][7][8][9][10] [11]. Fig. 1. 2 shows an example of magnetic gear that does not use magnetic modulation, and Fig. 1. 3 shows an example of magnetic gear that uses magnetic modulation.

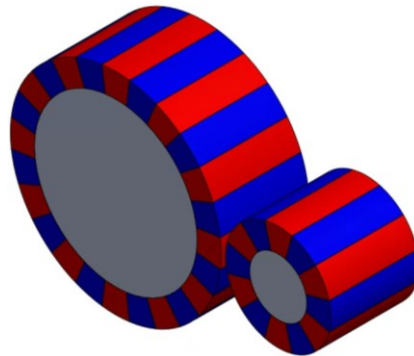


Fig. 1. 2. Magnetic gear without magnetic modulation.

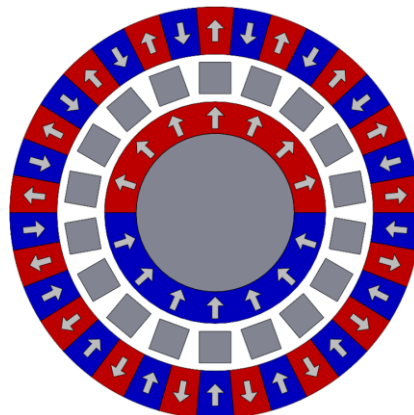


Fig. 1. 3. Magnetic gear with magnetic modulation.

Early magnetic gearboxes did not use magnetic modulation and were simply mechanical gearboxes with the mechanical parts replaced by magnetic parts. As a result, only some of the magnets contributed to torque transmission, and the gearboxes were large in size relative to their maximum transmission torque. In addition, the permanent magnets used at the time were not very high performance, so they could not replace mechanical gears.

To solve this problem, magnetic gearboxes using magnetic flux modulation were proposed in the 1960s. This system consists of three parts: a rotor connected to a low-speed shaft, a rotor connected to a high-speed shaft, and a stator. Generally, one of these parts is made of a ferromagnetic material with a salient pole structure, and the other two parts each have permanent magnets with different numbers of poles. In this configuration, all magnets contribute to torque transmission, enabling the transmission of larger torques. Furthermore, a research [18] published in 2001 demonstrated that by using powerful neodymium magnets in the permanent magnets, torque transmission comparable to that of mechanical reducers could be achieved.

1. 1. Basics of Magnetic-Geared Motors

A magnetic-gear motor [19] [20] (also known as magnetically-geared machine [21]: MGM) is a motor that integrates the magnetic gear described above with a motor [22]. This system was proposed by Venturini *et al.* [23], and subsequently, Razzell *et al.* [24], Chau *et al.* [25], and Jian *et al.* [26] proposed a structure in which a magnetic gear and a synchronous motor are combined on the same plane. In addition, Atallah *et al.* [27] and Jian *et al.* [28] have demonstrated the principle through experiments. Fig. 1. 4 shows an example of the structure of a magnetic-gear motor. Note that synchronous motors are generally used for the combined motor, but there are also examples of combining induction motors [29] and switch reluctance motors [30]. This motor uses magnetic force instead of friction force for power transmission, enabling non-contact power transmission. This solves problems such as wear and lubrication associated with mechanical reducers. Additionally, even when excessive torque is applied, physical damage does not occur due to the non-contact power transmission [31]. Furthermore, since the magnets of the motor and gearbox are shared, smaller sizes have been reported compared to motors with equivalent torque [27] [32].

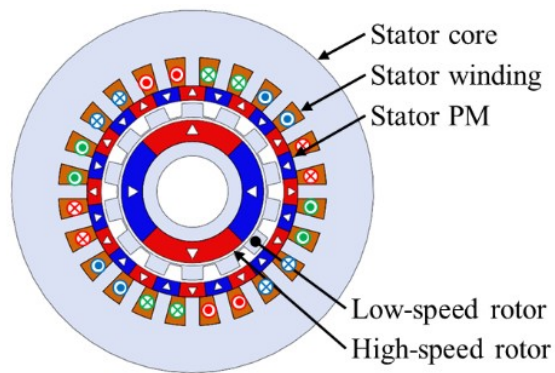


Fig. 1. 4. Example of magnetic-gear motor structure.

1. 1. 1 Types of Winding Components

A magnetic gear using magnetic modulation consists of three parts: two sets of parts with permanent magnets and a part with a salient pole structure made of ferromagnetic material that modulates the magnetic flux (referred to as a modulator). Meanwhile, the components of a magnetic gear motor are classified by rotational speed into three types: a rotor connected to the low-speed shaft (low-speed rotor, LSR), a rotor connected to the high-speed shaft (high-speed rotor, HSR), and a stator. Magnetic-gearred motors generate torque by winding the stator, but in principle, any of the components containing the modulator and two permanent magnets can be the stator. Therefore, they can be classified according to the components that are wound and their positions.

However, considering the machine configuration and rotor peripheral speed, the combination of magnetic-gearred motor configurations is limited. According to reference [22], there are generally three types of magnetic-gearred motor configurations.

- (1) The configuration where the fixed modulations and the stator with windings are located inside the high-speed rotor [24] [25] [32][33] [34].

Fig. 1.5 shows a diagram of an internal stator type magnetic-gearred motor. This configuration is also called a mechanically coupled machine because the rotor of the magnetic-gearred motor and the rotor of the permanent magnet synchronous motor are mechanically coupled [35]. In this configuration, the stator spans two parts: the modulator and the winding components. That means that a total of four parts, two stators and two rotors, must be arranged coaxially, which is extremely complicated. However, the high-speed rotor driven by the windings and the stator with windings are located close to each other. This reduces the number of gaps through which the magnetic flux generated by the windings passes, resulting in low magnetic resistance. Therefore, the torque coefficient of the windings is expected to be large.

In addition, in a decoupled type with permanent magnets magnetized in different directions on the inside and outside of the high-speed rotor, the magnetic circuits of the motor and magnetic gear are separated. This makes flux weakening control effective [36]. In contrast, in a coupled type, where the permanent magnets on the inside and outside of the high-speed rotor are magnetized in the same direction, the back yoke of

the high-speed rotor can be made thin, which is effective for achieving high torque density.

- (2) The configuration where the stator is located on the outermost and the permanent magnets are mounted to the gap surface [27].

Fig. 1.6 shows a diagram of an external stator type magnetic-gear motor. This configuration is similar to a conventional direct drive motor with an additional rotor, hence it is also referred to as a pseudo direct drive machine (PDD) [27] [35]. Compared to (1), the number of air gaps has been reduced from three to two, thereby simplifying the mechanical structure. Additionally, if sufficiently compact, this configuration can achieve performance equivalent to that of (1) [37].

- (3) The configuration where winding is located on the modulator [26].

Fig. 1.7 shows a diagram of a modulator winding type magnetic-gear motor. This structure has the advantages of a simple mechanical structure and low manufacturing costs. In addition, since the rotor is located on the outside, the load can be attached directly. As with (2), this system is also called a pseudo direct drive motor because it has a configuration similar to a general direct drive motor with one additional rotor [35].

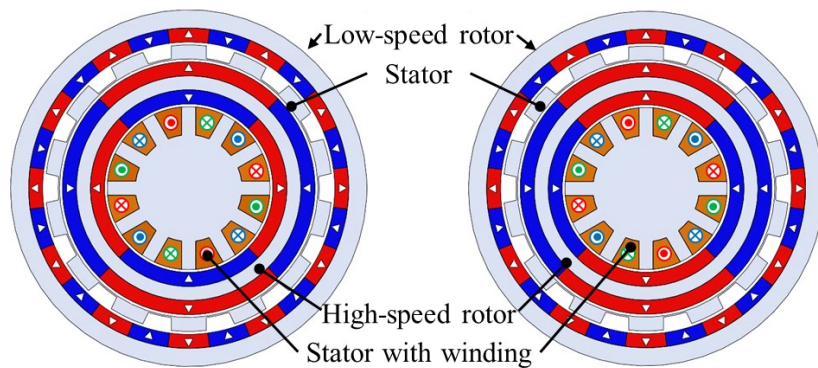


Fig. 1. 5. Internal stator type magnetic-gear motor.

(Left): Non-coupled type (Right): Coupled type

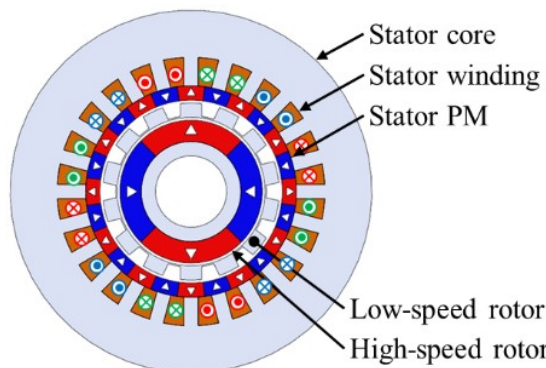


Fig. 1. 6. Outer stator type magnetic-gear motor.

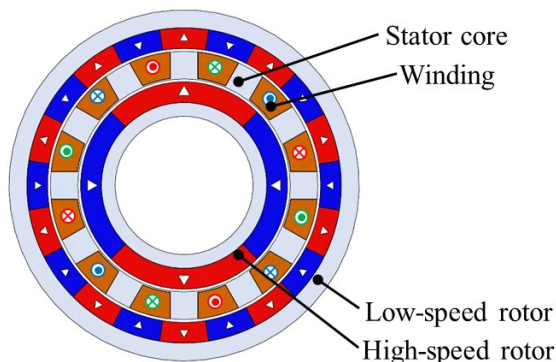


Fig. 1. 7. Magnetic-gear motor with winding on modulator.

1. 1. 2 Types of Topologies

Most magnetic-gear motors have a configuration in which two rotors are equipped with surface permanent magnets (SPMs). However, there are also reported configurations that do not match this description, despite being combinations of synchronous machines and magnetic modulation-type magnetic gears. Some of the topologies that have been reported are listed below.

- (1) Surface permanent magnet (SPM) type magnetic-gear motor [27]

Fig. 1. 4 shows a diagram of a surface magnet type magnetic-gear motor. In this structure, permanent magnets are provided in two parts in an SPM structure. This structure eliminates permeance fluctuations caused by the magnet structure, thereby suppressing the generation of magnetic flux harmonics. In magnetic-gear motors, harmonic magnetic flux is intentionally generated, and unintended harmonic components of the magnetic flux increase torque ripple. Therefore, low harmonic characteristics are desirable in magnetic-gear motors. However, because permanent magnets are located in the winding magnetic circuit, the equivalent magnetic resistance increases. This reduces the motor torque generated per current. Meanwhile, in [27], the current density of the motor winding is kept low, so this is not a major problem in a typical configuration. In magnetic gear motors, eddy current losses in permanent magnets are a common problem due to the large amount of asynchronous magnetic flux components. In this structure, eddy current losses are particularly problematic because high-order magnetic flux passes through the permanent magnets due to their proximity to the air gap.

- (2) Interior permanent magnet (IPM) type magnetic-gear motor [38]

Fig. 1. 8 shows a simplified diagram of an interior permanent magnet type magnetic-gear motor. In this structure, permanent magnets are buried inside the iron core, which suppresses eddy current losses in the permanent magnets that cause efficiency degradation in magnetic-gear motors. However, because the back yoke of the high-speed rotor is thin, the magnetic flux of the windings affects the maximum transmission torque.

- (3) Reluctance-type magnetic-gear motor [39] [19]

Fig. 1. 9 shows a diagram of a reluctance-type magnetic-gear motor. In this structure, the SPM structure on one side of the structure shown in (1) is replaced with a salient

pole structure. This replacement reduces the maximum transmission torque. However, it suppresses the generation of eddy current losses in the permanent magnets, which are a factor in the poor efficiency of magnetic-gear motors. Meanwhile, it has been reported that the efficiency of magnetic gear with the same structure remains the same because the maximum transmission torque decreases and the output also decreases [40]. In addition, since the permanent magnet is replaced with a salient pole, the magnetic resistance in the magnetic path of the winding flux decreases, improving the torque coefficient of the winding current.

(4) Consequent-pole permanent magnet (CPM) type magnetic-gear motor [41]

Fig. 1.10 shows a diagram of a consequent-pole magnetic-gear motor. This structure is a magnetic-gear motor in which the permanent magnets in (1) have been replaced with consequent poles. Instead of the SPM structure, permanent magnets magnetized in the same direction are inserted between the iron core poles, reducing the amount of permanent magnets used compared to (1). Therefore, while the maximum transmitted torque is reduced compared to (1), it is improved compared to (3) [41]. Additionally, the magnetic resistance of the magnetic path of the winding flux is reduced, and the torque coefficient of the winding current is improved to the same level as in (3).

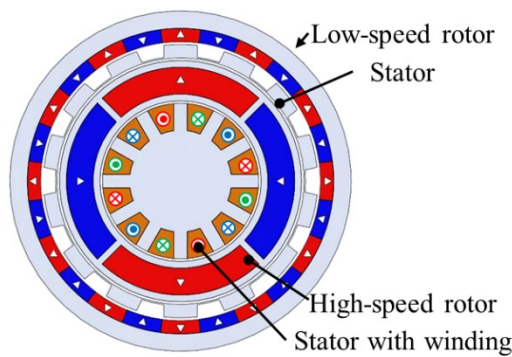


Fig. 1.8. Interior permanent magnet type magnetic-gear motor.

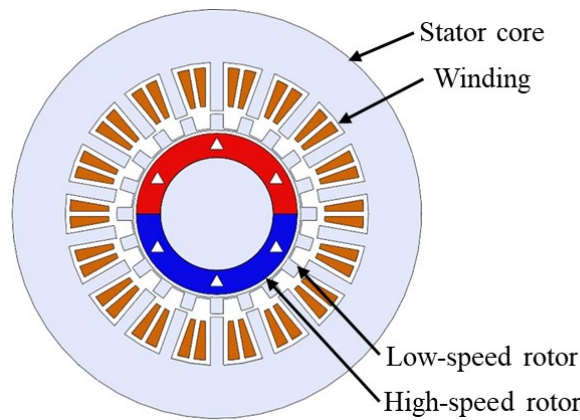


Fig. 1. 9. Reluctance-type magnetic-gear motor.

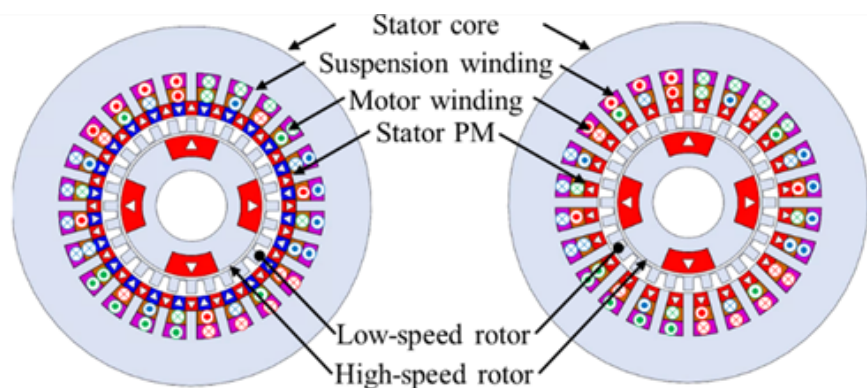


Fig. 1. 10. Consequent-pole type magnetic-gear motor.

Left: single-sided consequent-pole Right: double-sided consequent-pole

1. 2. Basics of Bearingless Motors

Mechanical bearings are the components most likely to fail first in machinery equipped with motors [42]. In recent years, advancements in semiconductor switch device performance have enabled motors to operate at high speeds. While this is an effective method for miniaturizing motors while maintaining output, it increases the load on bearings, making long-life bearings essential for improving product longevity.

To solve this problem, non-contact bearings that do not use mechanical bearings have been proposed. Three types of non-contact bearings are mainly used in practical applications [42]: fluid bearings, air bearings, and magnetically suspended bearings. Fluid bearings, which suspend rotating shafts in fluids such as oil, are not suitable for high-speed rotation, and air bearings have limitations in terms of size. Magnetic bearings, which suspend rotating shafts using magnetic attractions, have no restrictions on rotational speed or equipment size, but adding magnetic bearings to motors makes the equipment larger.

Bearingless motors were developed to miniaturize magnetically suspended motors. Bearingless motors are motors that magnetically integrate motor functions and magnetic bearings [43], and can generate torque and magnetic suspension force with an integrated magnetic circuit. This results in a large ratio of effective volume for generating suspension force and torque compared to the total volume of the motor, which is advantageous in terms of suspension force density per unit volume [43]. Additionally, since the magnetic bearing and motor components are integrated, the number of parts is reduced, making manufacturing easier. To date, bearingless motors have been proposed for applications such as centrifugal pumps [44] [45], centrifugal pumps for artificial hearts [46] [47], mixers for bioreactors [48] [49], rotating tables for process chambers [50], flywheels [51], compressors [52] [53], and cooling fans [54].

1. 2. 1 Types of Actively Controlled Axis Number

Bearingless motors can be classified according to the number of axes that actively control magnetic suspension. The rotor has six degrees of freedom: the x -axis, y -axis, and z -axis, as well as the θ_x -axis, θ_y -axis, and θ_z -axis of rotational motion around each axis. Assuming that the motor rotation axis is the z -axis, the rotor rotation direction is the θ_z -axis, so the five degrees of freedom other than the θ_z -axis must be magnetically suspended. However, for the θ_x -axis and θ_y -axis, the motor can be divided into upper and lower motor units, and the radial motion of the upper and lower motor units, i.e., the x_1 , y_1 , x_2 , and y_2 -axes, can be used for notation. In this case, the five degrees of freedom to be magnetically suspended are the x_1 , y_1 , x_2 , y_2 and z axes. In general, a large number of actively controlled axes requires a large number of sensors and inverters, which increases the cost. However, a small number of actively controlled axes imposes many restrictions on the shape, making it difficult to achieve stable magnetic suspension.

(1) Five-axis actively controlled bearingless motor

The five-axis actively controlled bearingless motor is a system that actively controls a total of five degrees of freedom, including the z -axis, which is the rotor axis, and the x_1 , y_1 , x_2 , and y_2 axes, which are the radial axes [55] [56]. The five-axis actively controlled type has fewer design constraints than other topologies and is expected to be particularly useful in large-scale applications.

(2) Four-axis actively controlled bearingless motor

The four-axis actively controlled bearingless motor is a system that actively controls four degrees of freedom in the x_1 , y_1 , x_2 , and y_2 by connecting two two-axis actively controlled bearingless motor units in tandem, as described below [57][58][59][60][61][62] [63]. In the axial direction, the system passively stabilizes due to the attractive force of permanent magnets. In this configuration, since the rotors are connected in tandem, combinations with homopolar motors that generate a bias flux in the axial direction have been reported [51] [64][65][66] [67].

(3) Two-axis actively controlled bearingless motor

The two-axis actively controlled bearingless motor is a system that actively controls only the two radial axes [44][45][46] [47] [49] [53]

[68][69][70][71][72][73][74][75][76][77][78] [79]. The axial and tilt directions are passively stabilized by the attractive force of the rotor permanent magnets. Compared to five-axis and four-axis actively controlled bearingless motors, this control method reduces the number of inverters and displacement sensors, thereby significantly reducing costs and the drive system. In this method, the rotor must be thin and flat in order to improve the stiffness of the tilt direction, which is passively stabilized. However, there is an upper limit to the rotational speed due to strength constraints in order to increase the motor speed, so there is a trade-off between high speed and high output. The maximum output of a two-axis actively controlled bearingless motor is about 1.2 kW [44] [76], but the maximum rotational speed is $100,000 \text{ min}^{-1}$ [77] [78].

(4) One-axis actively controlled bearingless motor

A single-axis actively controlled bearingless motor is a system that actively controls only the z-axis, which is the rotor axis [80][81] [82]. In this system, a single inverter controls both rotational torque and axial position, while the remaining degrees of freedom are stabilized by passive magnetic attraction. This system is cost-effective due to its use of fewer inverters and sensors; however, its size is limited, typically to 30W or less.

(5) Passively controlled bearingless motor

Passively controlled bearingless motors are systems that do not actively control any degrees of freedom. According to Earnshaw's theorem, stable levitation cannot be achieved by magnetic force only. Therefore, systems that automatically stabilize the motor using the Lorentz force generated by induced current [83][84] [85] and bearingless motors using diamagnetic materials [86] have been proposed.

1. 2. 2 Types of Magnetic Suspension Current

In bearingless motors, in order to generate magnetic suspension force, it is necessary to supply alternating current or direct current synchronized with the rotation of the rotor [43] [87]. These differ depending on the motor topology and are classified as follows. Note that the number of rotor pole pairs is denoted by p , and the number of magnetic suspension flux pole pairs is denoted by p_s .

- (1) The method utilizing $p_s = p \pm 1$ pole-pair magnetic suspension flux generated by alternating current suspension current.

(a)Surface permanent magnet synchronous motor (SPMSM) [44] [48] [59][60] [61] [68][69][70][71] [72] [79] [88][89] [90]

(b)Interior permanent magnet synchronous motor (IPMSM) [53] [58] [70]

(c)Induction Motor (IM) [57] [69]

(d)Synchronous reluctance motor (SynRM) [91] [92]

- (2) The method utilizing $p_s = 1$ pole-pair magnetic suspension flux generated by direct current suspension current.

(a)Consequent-pole Permanent Magnet Synchronous Motor (CPMSM) [65] [66] [74]

(b)Homopolar permanent magnet synchronous motor (HPMSM) [51] [62][63] [64] [67]

According to reference [93], (1) and (2) can both be explained by the same magnetic suspension principle. However, because the supply current and number of poles differ greatly, they are treated as separate methods in this research.

1. 3. Thesis Abstract

As mentioned above, magnetic-gear motors have mainly been used for low-speed, high-torque applications. This is because magnetic-gear motors use magnetic flux harmonics, which cause excessive iron loss at high speeds. However, as shown in Section 2. 1, research is also being conducted on high-speed magnetic-gear motors. In this research, bearing loss in the high-speed rotor of magnetic-gear motors has been an issue. Furthermore, magnetic-gear motors require two rotors to be assembled on the same axis. However, it is extremely difficult to assemble these with high precision, which raises concerns about increased costs for industrial applications.

To solve these problems, this research presents the first magnetic-gear motor with magnetically suspended high-speed rotor in the world. In this motor, a three-phase winding that generates a radial force on the high-speed rotor is added, enabling non-contact magnetic suspension without mechanical bearings on the high-speed rotor. This structure solves the problems of heat generation and lifetime of mechanical bearings on the high-speed rotor, which are issues in conventional magnetic-gear motors. In addition, conventional magnetic-gear motors require two rotors to be assembled with high precision on the same axis, which increases manufacturing costs. However, the proposed motor has advantages such as reduced manufacturing costs due to the ability to actively control the radial position.

However, the functions of a bearingless motor and a magnetic-gear motor are contradictory. Furthermore, it is unclear what pole combination is suitable for the proposed motor. To solve this problem, the selection of pole combinations was verified in principle in Section 3. 3. In addition, unlike general bearingless motors, the proposed motor requires a large magnetic suspension magnetomotive force due to its two air gaps, large and thick permanent magnets, and low permeability resulting from the shape of the low-speed rotor and high magnetic flux density. This problem was solved by adopting a configuration that does not interfere with the magnetic flux path of the magnetic suspension, as shown in Chapter 4, Chapter 6, and Chapter 7.

In addition, this research performs electromagnetic field analysis of a magnetic-gear motor with a high-speed rotor in magnetic suspension, derives a suitable structure, and analyzes the magnetic suspension performance and torque performance. Furthermore, a pro-

totype of the proposed motor was fabricated, and magnetic suspension and rotation experiments were conducted. This prototype is the first of its kind in the world, and the error between the analysis and the actual machine is unknown. For this reason, a suspension winding was added to a reluctance-type magnetic-gearied motor in this prototype. Although this structure has the disadvantage of reducing torque density, it has the effect of increasing the torque and magnetic suspension force per current because the magnetic resistance in the magnetic circuit of the winding magnetic field is reduced. The adoption of this structure made testing easier by allowing for a margin in the winding performance. This prototype was the first in the world to demonstrate magnetic suspension of a high-speed rotor in a magnetic-gearied motor.

Meanwhile, the prototype had the disadvantage of low torque density. To overcome this disadvantage, the magnetic-gearied motor with magnetically suspended high-speed rotor with improved torque density was also proposed. In the proposed motor, the magnetic-gearied motor was changed from the reluctance type to the consequent-pole type. This structure has the advantage of improving torque density while maintaining low magnetic resistance in the magnetic circuit of the winding magnetic field, thereby achieving both torque density and magnetic suspension performance. In addition, since it is not necessary to detect the rotational angular position for magnetic suspension, deterioration of magnetic suspension performance due to errors in the sensor that detects the rotational angle can be prevented. In this research, the dimensions of the magnetic-gearied motor with a magnetically suspended high-speed rotor adopting the consequent-pole structure were optimized, and the advantages and disadvantages of each topology were compared.

1. 4. Thesis Outline

This paper consists of eight chapters, which verify a new motor combining a magnetic-gearred motor and a high-speed bearingless motor through analysis and experiments. The outline of each chapter is as follows.

Chapter 1: Introduction

Chapter 1 presents the background and types of magnetic-gearred motors and bearingless motors, and clarifies the purpose and significance of this research. It also provides an overview of this thesis.

Chapter 2: Research Trends on High-Speed Magnetic-Geared Motors/Magnetic Gear and High-Torque Bearingless Motors

Chapter 2 describes research trends and issues related to high-speed magnetic-gearred motors and magnetic gears. In addition, research trends and issues related to bearingless motor topologies using magnetic modulation are described. The current issues with these motors are presented, and the objectives of this research and solutions to the research issues are described.

Chapter 3: Structure and Principle of Magnetic-Geared Motor with Magnetic-Suspended High-Speed Rotor

Chapter 3 shows the structure and principle of the magnetic-gearred motor with a high-speed rotor on magnetic suspension proposed in this research.

Chapter 4: Proposal and Analysis of High-Speed Rotor Magnetic Suspension for Reluctance-Type Magnetic-Geared Motors

Chapter 4 proposes the novel reluctance-type magnetic-gearred motor integrated with high-speed bearingless motor. Analysis is used to derive the torque generation principle and magnetic suspension force of the proposed motor, and to clarify the structure that enables magnetic suspension.

Chapter 5: Experimental Verification of High-Speed Rotor Magnetic Suspension for Reluctance-Type Magnetic-Geared Motors

Chapter 5 verifies the magnetic suspension performance through experiments conducted using a prototype machine manufactured based on the model proposed in Chapter 4. Thus, the principle of the proposed reluctance-type magnetic-geared motor integrated with a high-speed bearingless motor has been confirmed by experiments.

Chapter 6: Investigation of High-Speed Rotor Magnetic Suspension for Consequent-Pole Type Magnetic-Geared Motors

Chapter 6 proposes a bearingless high-speed rotor for magnetic-geared motors using consequent poles to improve the torque density of the model proposed in Chapter 4. The characteristics of each motor topology are evaluated by analysis.

Chapter 7: Optimization and Verification of High-Speed Rotor Magnetic Suspension for Consequent-Pole Type Magnetic-Geared Motors

Chapter 7 optimizes the dimensions of the motor proposed in Chapter 6, evaluates the torque and magnetic suspension force characteristics of each motor topology, and clarifies a structure capable of magnetic suspension while improving torque density.

Chapter 8: Conclusion

Chapter 8 consists of a short chapter summary, the main contributions of the thesis, a conclusion, and suggestions for future work.

Chapter 2. Research Trends on High-Speed Magnetic-Geared Motors/Magnetic Gear and High-Torque Bearingless Motors

2. 1. Research Trends in High-Speed Magnetic-Geared Motors and High-Speed Magnetic Gears

High-speed magnetic-geared motors and high-speed magnetic gears are generally more challenging than low-speed, high-torque magnetic-geared motors. This is due to the principle of magnetic gears. In magnetic gears with magnetic modulation, harmonics are used to transmit torque. As a result, harmonic flux passing through permanent magnets in the magnetic gear causes eddy current losses to occur in ferromagnetic materials and permanent magnets. These eddy current losses are proportional to the square of the frequency, so they increase significantly as the rotational speed increases. For this reason, research on magnetic gear applications has generally focused on low-speed applications, which have relatively low eddy current losses.

Meanwhile, several research proposals have been made on applying magnetic gearboxes to high-speed applications.

For example, [94] proposes a motor in which a magnetic gearbox and a high-speed motor are connected in series. In this literature, a motor with a stack length of 30.5 mm and an outer diameter of 44 mm is connected to a magnetic gear with the same outer diameter and stack length. The motor has two poles, a toroidal-wound stator, a high-speed rotor with two permanent magnets, 22 salient poles, a low-speed rotor with 34 permanent magnets, and a gear ratio of 18:1. In this literature, the rated value of the low-speed rotor is 2.5 Nm of output torque and $1,258 \text{ min}^{-1}$ of rotational speed, and the efficiency of the entire system, including bearing losses, is calculated to be 87.5% at this operating point. At the rated point, the high-speed rotor rotates at $22,644 \text{ min}^{-1}$, and the bearing loss is calculated to be 9.7 W. This value is approximately 20.6% of the total loss and cannot be ignored.

In reference [95], a magnetic gear for high-speed rotation is proposed in which the innermost permanent magnet rotor of the magnetic gear shown in Fig. 1.3 is replaced by a salient

pole structure made of ferromagnetic material. In this reference, the efficiency of a reluctance type magnetic gear with a salient pole structure is compared with that of a conventional magnetic gear shown in Fig. 1.3 for a magnetic gear with an outer diameter of 200 mm and a rated low-speed rotor output torque of 80 Nm. According to this, at a low-speed rotor rotational speed of $5,000 \text{ min}^{-1}$ and a high-speed rotor rotational speed of $30,000 \text{ min}^{-1}$, the efficiency of the conventional magnetic gear was 90%, while that of the reluctance magnetic gear was 92%, demonstrating the effect of replacing the permanent magnets in reducing magnetic eddy losses. Furthermore, replacing the high-speed rotor with a salient pole structure has also demonstrated an improvement in mechanical strength during high-speed rotation. Meanwhile, reference [40] shows that replacing permanent magnets with a salient pole structure reduces torque density. Furthermore, it shows that conventional magnetic gear structures are superior in terms of efficiency with optimized design. In particular, in terms of torque density, even in [95], the stack length of a conventional magnetic gear is 22.5 mm, while that of a reluctance magnetic gear is 74 mm, indicating that a decrease in torque density is unavoidable.

Reference [32] proposes a large magnetic-geared motor for automotive applications. This reference describes a magnetic-geared motor with an outer diameter of 268.5 mm and a stack length of 100 mm, which achieves a maximum transmission torque of 642 Nm, a maximum rotational speed of $14,000 \text{ min}^{-1}$ for the high-speed rotor, and a gear ratio of 8.83 [96]. This motor has an extremely high torque density of approximately 100 kNm/m^3 , demonstrating performance equivalent to that of a mechanical geared motor. Meanwhile, despite being such a high-speed motor, the machine is extremely large, resulting in very low bearing losses, with most losses occurring in the magnetic eddy losses, titanium sleeves for protecting the permanent magnets, and laminated silicon steel.

2. 2. Research Trends in Low-Speed High-Torque Bearingless Motors

Bearingless motors are generally applied to high-speed motors. This is because eliminating bearings improves efficiency in high-speed ranges where bearing losses are significant. Meanwhile, research is also progressing on low-speed, high-torque motors to take advantage of the benefits of eliminating bearings, such as reduced maintenance frequency and no contamination from lubricant leakage.

Table 2. 1 shows the dimensions and performance of low-speed application motors with two-axis active control bearingless motors. Reference [90] proposes a bearingless motor with a rated rotational speed of $1,500 \text{ min}^{-1}$. This motor is a 26-pole, 24-slot bearingless motor, and the rotor uses an inner rotor SPM. Additionally, in [97], an SPM-type bearingless motor with a rated speed of $1,000 \text{ min}^{-1}$, 8 poles, and 12 slots is proposed. In [98], a flux-switching type bearingless motor with a rated speed of $1,000 \text{ min}^{-1}$ is proposed. In [99], a 32-pole, 48-slot inner rotor CPM-type bearing-less motor with a rated speed of 500 min^{-1} is proposed. In [100], a 20-pole, 24-slot outer rotor CPM-type bearing-less motor with a rated speed of $1,000 \text{ min}^{-1}$ is proposed. In [89], a 26-pole, 6-segmented stator inner rotor SPM-type bearing-less motor with a rated speed of $2,000 \text{ min}^{-1}$ is proposed. [89] and [90] are very large motors with an outer diameter of 500 mm and a stack length of 20 mm. Table 2. 1 summarizes the dimensions and rated torque specified in these references. According to Table 2. 1, the torque density of general two-axis active control bearingless motors is generally 4 kNm/m^3 or less. This is closely related to the design of two-axis active control-type bearingless motors. Compared to four-axis or five-axis active control-type bearingless motors, two-axis active control-type bearingless motors offer the advantage of reduced costs by eliminating inverters and sensors. However, in this configuration, the rotor must be designed as a thin, flat shape to enhance the passive stability of the tilt direction. In this case, the stiffness of the degrees of freedom that passively stabilize the system is achieved using leakage flux from the fringed magnetic flux of the permanent magnets and end effects. Therefore, a certain amount of leakage flux is necessary to improve stiffness, but this flux does not contribute to torque generation, resulting in a lower torque density compared to conventional motors.

Table 2. 1. Torque density comparison of the two-axis actively controlled bearingless mo-
tors.

Reference number	[101]	[98]	[90]	[89]
Volume (cm ³)	31	556	3927	3927
Outer diameter (mm)	63	266	500	500
Axial Length(mm)	10	10	20	20
Torque (Nm)	0.022	1.00	13.1	15.0
Torque density(kNm/m ³)	0.71	1.8	3.3	3.8
Rated speed (min ⁻¹)	-	1000	1500	2000

Therefore, literature has been reported on combining a vernier motor, a type of motor that uses magnetic modulation to generate high torque, with a bearingless motor [102]. However, this literature only performs analysis using two-dimensional finite element methods, and the actual torque is unknown. Meanwhile, attempts to make motors that use magnetic modulation bearingless are related to this study.

In addition, attempts have been reported to combine a rotating machine based on the principle of a bearingless motor with magnetic modulation to magnetically suspend a high-speed rotor of a magnetic gear [103]. Although this literature also only performs analysis using a two-dimensional finite element method, it is closely related to this study. In this literature, the principle of generating a radial force for the inner high-speed rotor by applying a three-phase winding to the modulation part of the magnetic gear with magnetic modulation shown in Fig. 1. 3 is proposed. This magnetic gear has a high-speed rotor PM with four poles, twenty-one modulations, and a low-speed rotor PM with thirty-eight poles, and a two-pole suspension winding is wound between the twenty-one modulations. Additionally, the magnetic gear sections are arranged in series, and axial magnetic bearings are installed, so the number of active control axes is estimated to be five.

2. 3. Solutions to Current Issues and Objectives of This Research

Based on the research trends in high-speed magnetic-geared motors and high-speed magnetic gear discussed in Section 2. 1, and the research trends in low-speed high-torque bearingless motors discussed in Section 2. 2, this section presents solutions to these issues and the objectives of this study.

- (1) Solving problems related to mechanical bearings in high-speed magnetic-geared motors (Chapter 4 and Chapter 5)

In the high-speed magnetic-geared motors described in Section 2. 1, bearing losses are particularly significant in small high-speed magnetic-geared motors such as those shown in reference [94]. Therefore, these sections propose a structure for magnetically suspending the high-speed rotor of a magnetic-geared motor, and shows a structure that enables the reduction of bearing losses. Furthermore, a prototype of the proposed motor is fabricated, and magnetic suspension and rotation tests are performed. This prototype is the first of its kind in the world, and the errors between the analysis and the prototype are unknown. For this reason, the prototype is a reluctance-type magnetic-geared motor with a suspension winding. Although this structure has the disadvantage of reducing torque density, it has the effect of increasing the torque and magnetic suspension force per unit current because the magnetic resistance in the magnetic path of the winding magnetic field is reduced. The adoption of this structure has made testing easier by allowing for a margin in the winding performance. This prototype will be the first in the world to demonstrate the magnetically suspended high-speed rotor of a magnetic-geared motor.

- (2) Increasing the torque of low-speed, high-torque bearingless motors (Chapter 6 and Chapter 7)

The low-speed, high-torque bearingless motor described in Section 2.2 was designed mainly for rotational speeds of 500 to 2,000 min⁻¹. However, two-axis actively controlled bearingless motors operating at such rotational speeds suffer from lower torque density than motors with conventional structures. Therefore, these sections propose a magnetic-geared motor with magnetically suspended high-speed rotor with improved torque density. In the motor proposed in these chapters, the magnetic-geared motor system was changed from a reluctance type to a consequent-pole type. This structure has the advantage of improving torque density while maintaining low magnetic resistance in the magnetic circuit of the winding magnetic field, thereby achieving both torque density and magnetic suspension performance. In addition, since it is not necessary to detect the rotational angular position for magnetic suspension, deterioration of magnetic suspension performance due to errors in the sensor that detects the rotational angle can be prevented. In this research, the dimensions of a magnetic-geared motor with a consequent-pole structure and magnetically suspended high-speed rotor are optimized, and the advantages and disadvantages of each system are compared.

2. 4. Summary of Chapter 2

This chapter summarizes research trends on high-speed magnetic-geared motors/magnetic gear and high-torque bearingless motors. Furthermore, based on these research trends, this research presents the problems to be solved and the solutions, as well as the objectives of this research.

Section 2.1 shows research trends in high-speed magnetic-geared motors and high-speed magnetic gear. In general, magnetic-geared motors are mainly used in low-speed, high-torque applications. However, as shown in Section 2.1, there are also high-speed applications. These references report that bearing losses are significant in small magnetic-geared motors, and methods to reduce these losses are required.

In Section 2.2, the research trends in low-speed high-torque bearingless motors were investigated. Bearingless motors are generally used in small, high-speed applications. However, low-speed high-torque motors also exist for applications that require mechanical bearings. The performance of these low-speed high-torque bearingless motors was investigated.

In Section 2.3, solutions to current issues and objectives of this research are presented based on the content of Sections 2.1 and 2.2. In this research, a design that eliminates bearings in high-speed rotors by using magnetic suspension for high-speed rotors in magnetic-geared motors is proposed. This proposal solves the problem of bearing loss in high-speed magnetic-geared motors and also solves the problem of low torque density in bearingless motors that has been proposed previously.

Chapter 3. Structure and Principle of Magnetic-Geared Motor with Magnetic-Suspended High-Speed Rotor

3. 1. Structure of Proposed Motor

This research proposes a magnetic-geared motor with a high-speed rotor using magnetic suspension. In a bearingless motor, some of the five degrees of freedom of the rotor, *i.e.*, the x -axis, y -axis, z -axis, and rotational movements θ_x and θ_y in the x -axis and y -axis directions, are actively controlled. The proposed motor employs a two-axis active control system that controls only the two degrees of freedom in the x -axis and y -axis directions. Accordingly, the motor is thin to stabilize the tilt and axial degrees of freedom, which are passively stable. In this structure, the number of inverters and sensors is small because there are few degrees of freedom to control. In contrast, the torque density is lower than that of a general motor with the same diameter and stack length because the effect of magnetic flux leakage at the ends is significant. However, since this research is only preliminary research on magnetic-geared motors with magnetic suspension of high-speed rotors, only methods for improving torque density in the two-axis active control type shown in Chapter 6 and Chapter 7 are presented, and other topologies are not discussed. Meanwhile, to improve torque density, methods such as using a four-axis active control type that can extend the shaft length or applying single-axis active control to an axial gap magnetic-geared motor can be used.

The magnetic-geared motor with a high-speed rotor and magnetic suspension proposed in this research provides greater flexibility in connecting loads compared to conventional bearingless motors. For example, [44] shows an example of a bearingless motor applied to a pump. In this motor, the rotor and impeller are integrated, and the impeller is thinner than the axial length of the rotor. In [49], an example of a bearingless motor applied to an agitator motor is shown. In this motor, the axial length of the rotor is also similar to the axial length of the agitator blades. This is because when controlling the magnetic suspension of the rotor, it is difficult to control the rotor when its center of gravity is far from the center of the stator. In addition, bearingless motors are known to be more efficient than mechanical bearings at high rotational speeds. However, when a reduction gear is attached to the rotor, physical

contact occurs within the reduction gear, making it difficult to take advantage of the benefits of non-contact rotation. Taking these factors into consideration, conventional bearingless motors have been limited to applications where the load is close to the rotor and does not require a reduction gear. Meanwhile, in the proposed motor, the high-speed rotor achieves non-contact support while outputting power through a reduction gear without physical contact. Therefore, it can be expected to have various applications like general motors.

3. 1. 1 Structure of Reluctance-Type Magnetic-Geared Motor with Magnetic Suspended High-Speed Rotor

Fig. 3. 1 shows the cross-sectional view of reluctance-type magnetic-geared motor with magnetic-suspended high-speed rotor. The proposed motor consists of three parts: a magnetic-suspended high-speed rotor located at the inside, a stator with windings located at the outside, and a low-speed rotor located between them. The magnetically suspended high-speed rotor has p_h pole pair of surface permanent magnet structure. In this structure, as shown in 1. 2. 2(1), the radial force is generated by the interaction of the magnetic flux of the p pole pair and the $p \pm 1$ pole pair. Therefore, the three-phase magnetic suspension windings are connected as $p_h \pm 1$ pole pair.

In reluctance-type magnetic-geared motors, the torque density is significantly lower than that of magnetic-geared motors with permanent magnets placed on the stator [40] [41]. However, the magnetic resistance in the magnetic circuit is reduced because there are fewer permanent magnets in the magnetic circuit of the winding flux. In magnetic-geared motors, the current density in the motor windings is relatively low compared to other PM motors. For example, in reference [27], the current density in the motor windings is reported to be $2 \text{ A}_{\text{rms}}/\text{mm}^2$. This is because, unlike general permanent magnet motors, magnetic-geared motors have a maximum transmission torque, which is the upper limit of torque, and currents exceeding this limit cannot be effectively utilized. Meanwhile, analysis shows that the magnetic suspension current must be larger than the motor current (see Section 4. 2. 4). Therefore, in order to ensure sufficient magnetic suspension performance, a reluctance-type magnetic-geared motor was selected for the motor in Chapter 4.

In addition, the characteristics of magnetic-geared motors integrated with bearingless motors have not been experimentally verified. For example, in [103], a structure in which a high-speed rotor of a magnetic gear is magnetically suspended is proposed, but it has not been verified by experiments. In magnetic suspension for rotating machines using such magnetic modulation, it is necessary to consider the occurrence of disturbances caused by mechanical and magnetic manufacturing errors of permanent magnets. In particular, in SPM-type magnetic-geared motors, the large pole pair number of the permanent magnets makes disturbances caused by manufacturing errors to be a problem. For example, [104]

shows the generation of magnetic attraction due to mechanical errors. In contrast, in reluctance-type magnetic-gear motors, the permanent magnets are located only on the high-speed rotor, which has a small pole pair number, thus making the structure less susceptible to errors in the permanent magnets. These characteristics make reluctance-type magnetic-gear motors suitable for verifying the characteristics of the proposed motor.

Compared to a vernier motor, the proposed motor has two air gaps, resulting in a lower magnetic flux per current. However, since the number of poles in the motor winding is the same as the number of poles in the rotor PM, it offers the advantage of improved power factor [105].

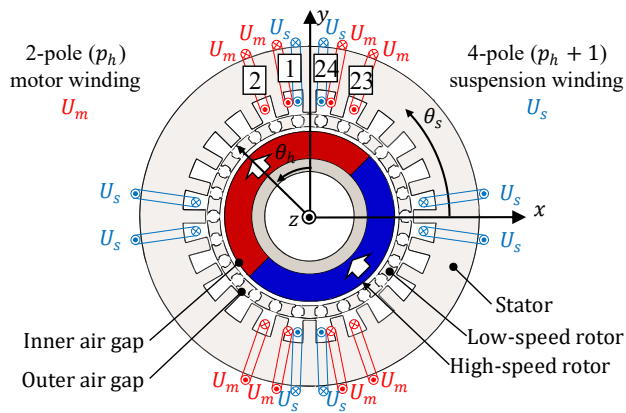


Fig. 3. 1. Cross-sectional view of reluctance-type magnetic-gear motor with magnetic-suspended high-speed rotor.

3. 1. 2 Structure of Surface Permanent Magnet Type Magnetic-Geared Motor with Magnetic Suspended High-Speed Rotor

Fig. 3. 2 shows the cross-sectional view of surface permanent magnet type magnetic-geared motor with magnetic-suspended high-speed rotor. The proposed motor consists of three parts: a magnetic-suspended high-speed rotor located at the inside, a stator with windings located at the outside, and a low-speed rotor located between them. The stator consists of a permanent magnet with p_s pole-pairs magnetized in the radial direction and windings. In a high-speed rotor, permanent magnets with p_h pole-pairs magnetized in the radial direction are attached to the core surface of the high-speed rotor. The low-speed rotor is located between the stator and the high-speed rotor and has n_l salient poles made of ferromagnetic material. These salient poles modulate the magnetic flux generated by the permanent magnets.

This structure has a high torque density, as shown in [41]. However, there are two issues to consider in combination with a bearingless motor.

- (1) Detection of rotor angular position is necessary.

As in the motor combining a reluctance-type magnetic-geared motor and a bearingless motor shown in 3. 1. 1, the three-phase magnetic suspension windings are connected with $p_h \pm 1$ pole-pair. Therefore, as shown in 1. 2. 2(1), detection of the rotor angular position is necessary to achieve accurate magnetic suspension.

- (2) Increase of magnetic resistance in the magnetic path of the magnetic suspension flux.

As shown in Fig. 3. 2, compared to the reluctance-type magnetic geared motor shown in Fig. 3. 1, permanent magnets are added to the gap surface of the stator. Although this structure increases the torque density as mentioned above. However, the permanent magnets increase the magnetic resistance in the magnetic path of the magnetic suspension flux. This reduces the magnetic flux generated, even with the same winding magnetomotive force, and reduces the magnetic suspension force.

However, in a design such as that shown in Fig. 1. 8, where the winding and the magnetic suspension rotor are close to each other, the increase in magnetic resistance may not be a problem. However, it is necessary to consider the interference between the winding magnetic flux and the magnetic gear magnetic flux as shown in 3. 2. 2.

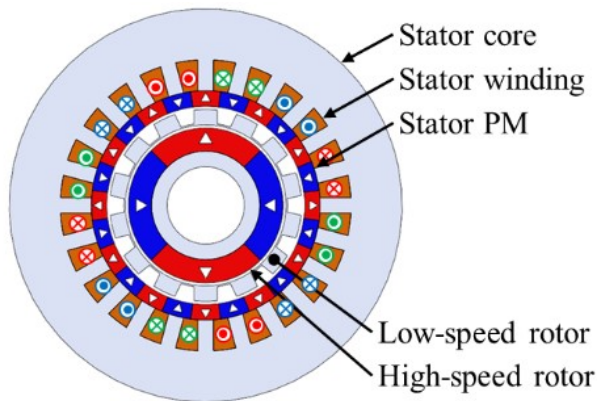


Fig. 3. 2. Cross-sectional view of surface permanent magnet type magnetic-gear motor with magnetic-suspended high-speed rotor.

3. 1. 3 Structure of Consequent-Pole Type Magnetic-Geared Motor with Magnetic Suspended High-Speed Rotor

Fig. 3. 3 shows the cross-sectional view of a consequent-pole type magnetic-geared motor with magnetic suspended high-speed rotor. These machines added the magnetic suspension capability to the model proposed in [41].

Fig. 3. 3 (a) shows the proposed single-sided consequent-type permanent magnet (SCPM) MGM. The high-speed rotor has a consequent-pole permanent magnet (CPM) structure. In an eight-pole CPM high-speed rotor, p_h set of permanent magnets are installed inside the rotor iron yoke, and p_h set of iron poles are arranged between the permanent magnet poles. The permanent magnet poles are all magnetized radially outwards, while the iron poles are magnetized radially inwards, consequently. In this structure, the magnetic suspension rotor has a consequent-pole structure. Therefore, as shown in 1. 2. 2(2), a connection that results in one pole per phase can be selected for the three-phase magnetic suspension windings. This structure solves the problem of detecting the angular position of the rotor shown in 3. 1. 2(1).

Fig. 3. 3 (b) shows the proposed double-sided consequent-pole type permanent magnet (DCPM) MGM. In this topology, the stator permanent magnets are changed to a consequent-pole structure as well. Compared to the structure shown in Fig. 3. 3 (a), the iron core poles are extended to the stator gap surface. As a result, the magnetic resistance in the magnetic path of the magnetic suspension flux is reduced to the same level as that of the motor combining a reluctance-type magnetic-geared motor and a bearingless motor shown in 3. 1. 1. This solves the problem of increased magnetic resistance shown in 3. 1. 2(2).

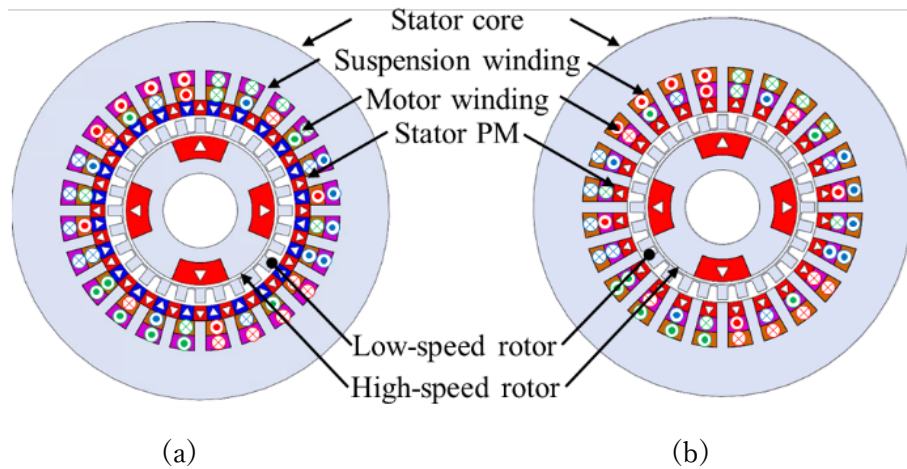


Fig. 3. 3. Cross-sectional view of a consequent-pole type magnetic-geared motor with magnetic suspended high-speed rotor.

(a) Single-sided Consequent-Pole type Permanent Magnet: SCPM (b) Double-sided Consequent-Pole type Permanent Magnet: DCPM

3. 2. Operating Principle of Proposed Magnetic-Geared Motors

3. 2. 1 Operating Principle of Reluctance Magnetic-Geared Motors

In a reluctance-type magnetic-geared motor [19] [39], the permanent magnet flux and the winding flux of the high-speed rotor are modulated by the low-speed rotor and the stator teeth. Fig. 3. 4 shows the vector diagram of a reluctance-type magnetic-geared motor. In magnetic-geared motors, the number of poles of the motor windings and the high-speed rotor are generally the same. Thus, in the magnetic modulation of a magnetic-geared motor, the magnetic flux generated by the motor windings must also be considered, unlike in magnetic gears. Consequently, the combined magnetic flux of the permanent magnets of the high-speed rotor and the motor winding magnetic flux is magnetically modulated.

However, in reluctance-type magnetic-geared motors, thicker permanent magnets are arranged radially to compensate for the low torque density. Additionally, there are two air gaps, and the magnetic flux density of the low-speed rotor is close to the saturation region, resulting in high magnetic resistance in the magnetic path of the motor winding magnetic flux. Thus, the magnetic flux in this motor is dominated by the permanent magnets, and the operating principle described in this research ignores the influence of the winding magnetic flux, treating it as equivalent to the principle of magnetic gears.

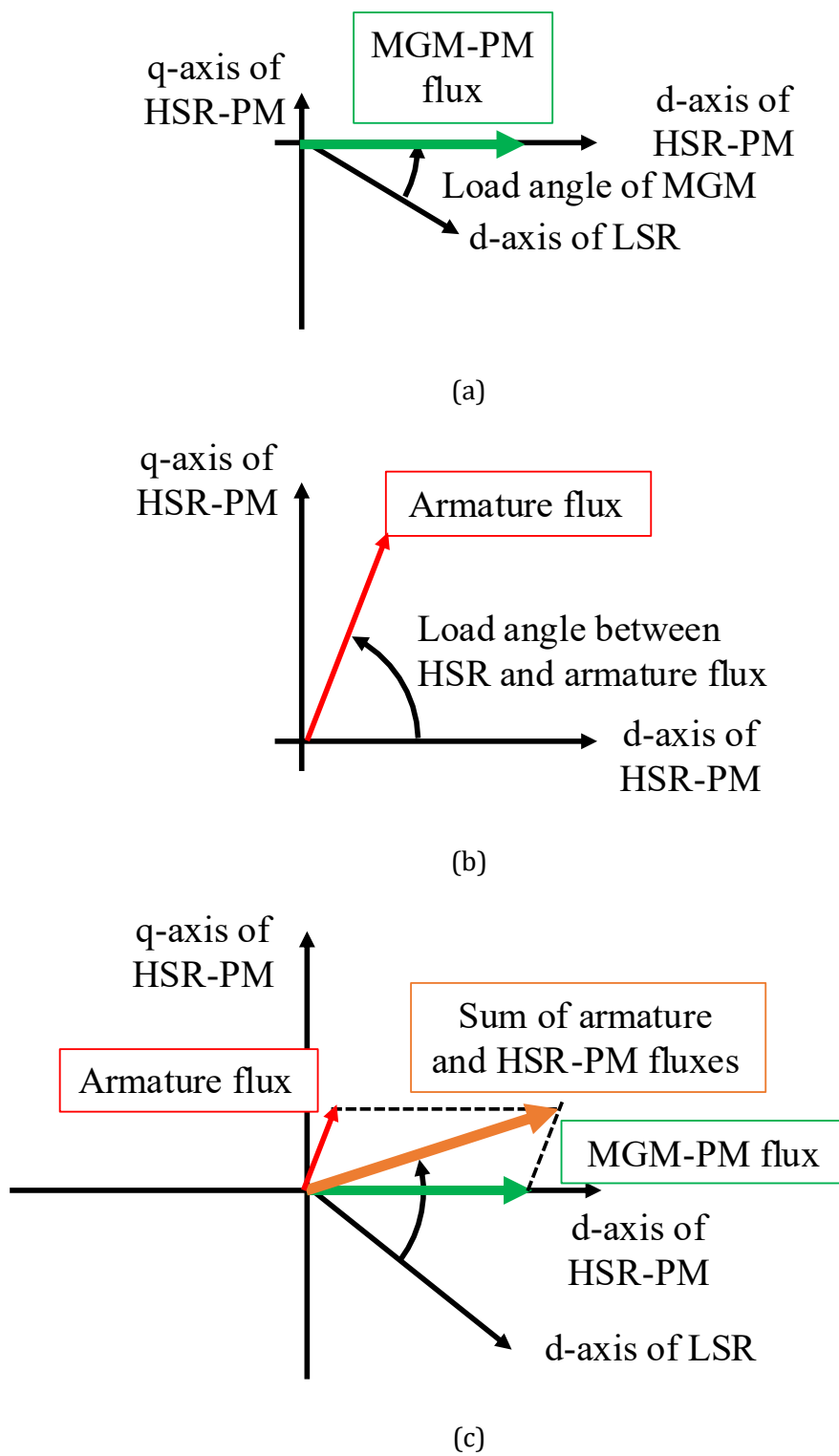


Fig. 3.4. Vector diagram of a reluctance-type magnetic-gear motor.

(a) Vector diagram of magnetic gear part (b) Vector diagram as a synchronous motor (c)
Vector diagram considering interference between magnetic gear and motor current

Let us define the stator angular coordinate θ_s . The mean and amplitude of the stator permeance are given by P_{s0} and P_{s1} , respectively. Then, the permeance distribution $P_s(\theta_s)$ is expressed as

$$P_s(\theta_s) = P_{s0} + P_{s1} \cos(n_s \theta_s) \quad (3.1)$$

Let us assume the mean and amplitude of the low-speed rotor permeance distribution are given by P_{l0} and P_{l1} , respectively. The angular velocity of the low-speed rotor is assumed as ω_l , and the deviation angle between the x -axis and the center of the low-speed rotor iron piece is δ_l at $t = 0$. Consequently, the permeance $P_l(\theta_s, t)$ of the low-speed rotor is expressed as

$$P_l(\theta_s, t) = P_{l0} + P_{l1} \cos[n_l(\theta_s - \omega_l t - \delta_l)] \quad (3.2)$$

Let us assume that the magnetomotive force amplitude of the PMs of the high-speed rotor is F_{h1} . Additionally, the angular velocity of the high-speed rotor is ω_h , and the deviation angle between the x -axis and the magnetization direction of the high-speed rotor PM is δ_h at $t = 0$. Consequently, the magnetomotive force $F_h(\theta_s, t)$ of the high-speed rotor is expressed as

$$F_h(\theta_s, t) = F_{h1} \cos[p_h(\theta_s - \omega_h t - \delta_h)] \quad (3.3)$$

From (3.1) and (3.3), the flux-density distribution $B_{sh}(\theta_s, t)$ in the air gap between the low-speed rotor and the stator, where the stator teeth modulates the magnetomotive force of the permanent magnet on the high-speed rotor, can be obtained as

$$\begin{aligned} B_{sh}(\theta_s, t) &= P_s(\theta_s) F_h(\theta_s, t) \\ &= \{P_{s0} + P_{s1} \cos(n_s \theta_s)\} F_{h1} \cos[p_h(\theta_s - \omega_h t - \delta_h)]. \\ &= F_{h1} P_{s0} \cos[p_h(\theta_s - \omega_h t - \delta_h)] \\ &\quad + \frac{F_{h1} P_{s1}}{2} \cos[(n_s + p_h) \theta_s - p_h \omega_h t - p_h \delta_h] \\ &\quad + \frac{F_{h1} P_{s1}}{2} \cos[(n_s - p_h) \theta_s + p_h \omega_h t + p_h \delta_h] \end{aligned} \quad (3.4)$$

From (3.2) and (3.3), the flux-density distribution $B_{lh}(\theta_s, t)$ in the air gap between the low-speed rotor and the stator, where the salient pole of the low-speed rotor modulates the magnetomotive force of the permanent magnet on the high-speed rotor, can be obtained as

$$\begin{aligned}
 B_{lh}(\theta_s, t) &= P_l(\theta_s, t)F_h(\theta_s, t) \\
 &= \{P_{l0} + P_{l1}\cos[n_l(\theta_s - \omega_l t - \delta_l)]\}F_{h1}\cos[p_h(\theta_s - \omega_h t - \delta_h)] \\
 &= F_{h1}P_{l0}\cos[p_h(\theta_s - \omega_h t - \delta_h)] \\
 &\quad + \frac{F_{h1}P_{l1}}{2}\cos[(n_l + p_h)\theta_s - (p_h\omega_h + n_l\omega_l)t - (p_h\delta_h + n_l\delta_l)] \\
 &\quad + \frac{F_{h1}P_{l1}}{2}\cos[(n_l - p_h)\theta_s + (p_h\omega_h - n_l\omega_l)t + (p_h\delta_h - n_l\delta_l)]
 \end{aligned} \tag{3.5}$$

Note that both (3.4) and (3.5) are flux-density distributions at the same air gap. Hence, the coefficients of θ_s at the second or third term in (3.4) must be identical to the second or third term in (3.5). Thus, the following relation must be satisfied

$$|n_s \pm p_h| = |n_l \pm p_h| \tag{3.6}$$

(3.6) contains eight states as follows

$$\left\{
 \begin{array}{l}
 n_s + p_h = n_l + p_h \dots (a) \\
 n_s + p_h = n_l - p_h \dots (b) \\
 n_s - p_h = n_l + p_h \dots (c) \\
 n_s - p_h = n_l - p_h \dots (d) \\
 -n_s + p_h = n_l + p_h \dots (e) \\
 -n_s + p_h = n_l - p_h \dots (f) \\
 -n_s - p_h = n_l + p_h \dots (g) \\
 -n_s - p_h = n_l - p_h \dots (h)
 \end{array}
 \right. \tag{3.7}$$

However, (a), (d), (e), and (h) are not suitable because these equations can be simplified as $n_s = n_l$, or $n_s = -n_l$. Thus, these equations are negligible, and (3.7) can be expressed as

$$\left\{
 \begin{array}{l}
 n_s + p_h = n_l - p_h \dots (b) \\
 n_s - p_h = n_l + p_h \dots (c) \\
 -n_s + p_h = n_l - p_h \dots (f) \\
 -n_s - p_h = n_l + p_h \dots (g)
 \end{array}
 \right. \tag{3.8}$$

By transposing p_h and n_l , (3.8) can be simplified as

$$\left\{
 \begin{array}{l}
 n_s - n_l = -2p_h \dots (b) \\
 n_s - n_l = 2p_h \dots (c) \\
 -n_s - n_l = -2p_h \dots (f) \\
 -n_s - n_l = 2p_h \dots (g)
 \end{array}
 \right. \tag{3.9}$$

(b) and (c) have the same left-hand side and different signs on the right-hand side. Similarly, (f) and (g) also satisfy the same condition. Thus, these equations can be simplified by using absolute value symbols on the right-hand side.

$$\begin{cases} n_s - n_l = |2p_h| \dots (b) \text{ and } (c) \\ -n_s - n_l = |2p_h| \dots (f) \text{ and } (g) \end{cases} \quad (3.10)$$

By transpose (3.10),

$$\begin{cases} n_l + n_s = |2p_h| \dots (f) \text{ and } (g) \\ n_l - n_s = |2p_h| \dots (b) \text{ and } (c) \end{cases} \quad (3.11)$$

Using plus-minus sign, (3.11) can be simplified as

$$n_l \pm n_s = |2p_h| \quad (3.12)$$

By using the absolute value symbol on the left side instead of the right side, the equation becomes as

$$|n_l \pm n_s| = 2p_h \quad (3.13)$$

Moreover, to transmit torque between high-speed and low-speed rotors continuously, the coefficients of t at the second or third term in (3.4) must be identical to the second or third term in (3.5). Thus, the following relation must be satisfied

$$2p_h \omega_h = \pm n_l \omega_l \quad (3.14)$$

From (3.14), the gear ratio G_r is given as

$$G_r = \frac{\omega_h}{\omega_l} = \pm \frac{n_l}{2p_h} \quad (3.15)$$

According to (3.15), the gear ratio is proportional to n_l and inversely proportional to p_h . Thus, the small p_h and large n_l model is suitable to achieve a high gear ratio. Therefore, the condition of (3.13) in the proposed machine is chosen as

$$n_l - n_s = 2p_h \quad (3.16)$$

In addition, the constraints on reluctance-type magnetic-geared motors and the combinations of pole numbers adopted in Chapter 4 are shown below.

(1) High reduction ratio requirement.

In general, high-speed motors are effective for miniaturizing motors. Accordingly, high-speed rotors must achieve high rotational speeds. Assuming that the target rotational speed of the low-speed rotor is fixed, the rotational speed of the high-speed rotor can be increased by adopting a high reduction ratio. To achieve a high reduction ratio, the high-speed rotor must have a low number of poles. The reduction ratio G_r is given by the ratio of the number of segments n_l of the low-speed rotor to the number of pole pairs p_h of the high-speed rotor, $G_r = n_l/2p_h$. Therefore, in order to maximize the reduction ratio for a given number of segments n_l of the low-speed rotor, the number of pole pairs of the high-speed rotor is selected to be 1.

(2) Avoidance of fractional slots.

Fractional slots have the advantage of reducing torque ripple. However, the magnetic flux distribution becomes asymmetric. In general motors, asymmetric magnetic flux is not a major issue. In contrast, in bearingless motors, asymmetric magnetic flux distribution causes the generation of radial forces, which are a source of disturbance. Therefore, the number of stator slots n_s is set to $6n$ (where n is an integer). From (1), since a larger n is preferable, n is set to 4, resulting in $n_s = 24$.

(3) Limitations on minimizing the number of stator slots and teeth.

Several combinations satisfy (1) and (2). In (3.16), selecting a larger number of slots increases the gear ratio. However, a larger number of slots reduces the slot cross-sectional area, making winding difficult. Furthermore, the magnetic gear transmission torque is related to the permittance variation of the stator slots and the low-speed rotor salient poles. Therefore, selecting a large number of slots reduces the permittance variation, which may reduce the transmission torque. Therefore, 24 slots and 26 low-speed rotor salient poles are selected. These constraints are verified in Section 4.1.

Therefore, these conditions lead to a gear ratio G_r of 13 in this prototype.

Let us assume that the torque of the high-speed rotor and low-speed rotor are T_h and T_l , respectively. The maximum transmission torque of the high-speed rotor is T_{hmax} . When the rotational speed relationship $\omega_h = G_r \omega_l$ defined in (3.15) is satisfied, i.e., under conditions where each rotor is rotated synchronously, each rotor torque is expressed as,

$$\begin{cases} T_h = T_{hmax} \sin(-n_l \delta_l + 2p_h \delta_h) \\ T_l = T_{hmax} G_r \sin(n_l \delta_l - 2p_h \delta_h) \end{cases} \quad (3.17)$$

The torques depend on $n_l \delta_l - 2p_h \delta_h$. This parameter behaves as the load angle in a synchronous motor. Hence, let $n_l \delta_l - 2p_h \delta_h$ be defined as the magnetic gear load angle δ_g . Thus, (3.17) can be expressed as,

$$\begin{cases} T_h = -T_{hmax} \sin(2\delta_g) \\ T_l = T_{hmax} G_r \sin(2\delta_g) \end{cases} \quad (3.18)$$

Consequently, the output torque of the low-speed rotor is 13 times of the high-speed rotor torque.

3. 2. 2 Operating Principle of Surface Permanent Magnet Type and Consequent-Pole Type Magnetic-Geared Motors

The magnetic gear principle of the SPM-type magnetic-gear motor shown in Fig. 3. 2 and the consequent-pole type magnetic-gear motor shown in Fig. 3. 3 is reported to be the same [41]. However, as shown in [38], depending on the shape and arrangement of the rotor and stator, the winding magnetic flux affects the operation of the magnetic-gear motor. In particular, in the interior permanent magnet type magnetic-gear motor shown in Fig. 1. 8, the magnetic resistance in the winding magnetic flux path is relatively low, and it is necessary to consider the composite vector shown in Fig. 3. 4. However, in the magnetic-gear motors discussed in this research, there are two air gaps between the stator with windings and the high-speed rotor, and the magnetic resistance in the magnetic flux path of the motor windings is high because the magnetic flux density of the low-speed rotor is close to the saturation region. Therefore, in this section, the effect of the winding magnetic flux is ignored, and the same principle as that of magnetic gears is assumed.

Let us define the stator angular coordinate θ_s , the magnetomotive force amplitude F_{s1} of the PMs of the stator. Then, the magnetomotive force $F_s(\theta_s)$ of the stator PMs is expressed as

$$F_s(\theta_s) = F_{s1}\cos(p_s\theta_s). \quad (3.19)$$

Let us assume the mean and amplitude of the low-speed rotor permeance distribution as P_{l0} and P_{l1} , respectively. The angular velocity of the low-speed rotor is ω_l . The deviation angle between the x -axis and the center of the low-speed rotor is δ_l . Hence, the permeance $P_l(\theta_s, t)$ of the low-speed rotor is expressed as

$$P_l(\theta_s, t) = P_{l0} + P_{l1}\cos\{n_l(\theta_s - \omega_l t - \delta_l)\}. \quad (3.20)$$

Let us assume the magnetomotive force amplitude F_{h1} of the PMs of the high-speed rotor, the angular velocity ω_h of the high-speed rotor, and the deviation angle δ_h between the x -axis and the center of the high-speed rotor. Then, the magnetomotive force $F_h(\theta_s, t)$ of the high-speed rotor is expressed as

$$F_h(\theta_s, t) = F_{h1}\cos\{p_h(\theta_s - \omega_h t - \delta_h)\}. \quad (3.21)$$

From (3.19) and (3.20), the flux distribution $B_{sl}(\theta_s, t)$ of the inner air-gap located between the high-speed and low-speed rotors is obtained as

$$\begin{aligned} B_{sl}(\theta_s, t) &= F_s(\theta_s) \cdot P_l(\theta_s, t) \\ &= F_{s1}P_{l0} \cos(p_s\theta_s) \\ &\quad + \frac{1}{2}F_{s1}P_{l1}\cos\left[(n_l+p_s)\left(\theta_s - \frac{n_l}{p_s+n_l}\omega_lt - \frac{n_l}{p_s+n_l}\delta_l\right)\right] \\ &\quad + \frac{1}{2}F_{s1}P_{l1}\cos\left[(n_l-p_s)\left(\theta_s + \frac{n_l}{p_s-n_l}\omega_lt + \frac{n_l}{p_s-n_l}\delta_l\right)\right] \end{aligned} \quad (3.22)$$

The first term in (3.22) is the stationary magnetic flux component while the second and third terms are the magnetic fluxes that rotate at different speeds compared to the low-speed rotor. Thus, the phase of the high-speed rotor magnetomotive force $F_h(\theta_s, t)$ must be identical to the second or third term in (3.22). Hence, the relations

$$|p_h(\theta_s - \omega_h t - \delta_h)| = |(n_l \pm p_s)\theta_s \mp n_l\omega_lt \mp n_l\delta_l| \quad (3.23)$$

must be satisfied. The coefficient of t must be identical in (3.23). Thus, the following relations must be satisfied

$$|p_h\omega_h| = |n_l\omega_l| \quad (3.24)$$

From (3.24), the gear ratio G_r is given as

$$G_r = \frac{\omega_h}{\omega_l} = \left| \frac{n_l}{p_h} \right| \quad (3.25)$$

According to (3.25), the gear ratio is proportional to n_l and inversely proportional to p_h . Thus, small p_h and large n_l are suitable to achieve a high gear ratio.

Moreover, the coefficient of the stator angular coordinate θ_s must be identical in (3.23). Thus, the following relations must be satisfied

$$|p_h| = |n_l \pm p_s| \quad (3.26)$$

(3.26) contains four states as follows

$$\begin{cases} p_h = n_l + p_s \dots (a) \\ p_h = n_l - p_s \dots (b) \\ -p_h = n_l + p_s \dots (c) \\ -p_h = n_l - p_s \dots (d) \end{cases} \quad (3.27)$$

However, (c) in (3.27) is not suitable because $p_h < 0$. Furthermore, (d) satisfies $n_l < p_s$, but does not satisfy the condition of maximizing the gear ratio, which is n_l maximization. Thus, it is not suitable. In addition, (a) does not satisfy the condition of maximizing the gear ratio, which is p_h minimization, and is also not suitable. Therefore, only (b) is appropriate.

$$p_h = n_l - p_s \quad (3.28)$$

From (3.23) and (3.28), the gear ratio G_r of the proposed magnetic-geared motor is given as

$$G_r = \frac{n_l}{p_h} \quad (3.29)$$

3. 3. Principle of Magnetic Suspension Force Generation of the Proposed Motors

In this research, the motor proposed has a suspension winding added to a general magnetic-geared motor as shown in Fig. 1. 4, which enables magnetic suspension of the high-speed rotor. However, as shown in Section 1. 2. 2, the principle of magnetic suspension varies depending on the topology of the magnetic suspension rotor.

In this research, the motors are proposed with both bearingless motor principles. The method utilizing $p_s = p \pm 1$ pole-pair magnetic suspension flux generated by alternating current suspension and the method utilizing $p_s = 1$ pole-pair magnetic suspension flux generated by direct current suspension as shown in 1. 2. 2(1) and 1. 2. 2(2), respectively. Thus, this section shows both magnetic suspension principles.

To achieve non-contact magnetic suspension of the rotor, it is necessary to magnetically stabilize all movements of the rotor (three degrees of translational freedom x, y, z and two degrees of rotational freedom θ_x, θ_y). In this method, the movement of the rotor in the radial direction x, y is positioned by applying a suspension current to the suspension windings. Meanwhile, the movements in the axial z and tilt directions θ_x, θ_y are passively stabilised by the magnetic attraction of permanent magnets. The proposed motor has two rotating parts, a low-speed rotor and a high-speed rotor, but only the high-speed rotor, which has a high rotational speed and is expected to greatly reduce losses due to the elimination of bearings, is magnetically suspended. To avoid mutual interference between the magnetic suspension force and torque, the magnetic flux component used to generate torque in the proposed motor must be different from the magnetic flux component used for magnetic suspension.

3. 3. 1 Principle of Active Magnetic Suspension Force Generation in Surface Permanent Type Two-Degree-Of-Freedom Actively Position Regulated Bearingless Motor

In the motor proposed in Chapter 4, the high-speed rotor is magnetically suspended by the principle of the two-axis actively position regulated surface-mounted permanent magnet bearingless motor [44], [68], [69], [70], [71], [72].

In this kind of magnetic suspension, only the x - and y -axis positions of the rotor are regulated by the $p_h \pm 1$ pole-pair suspension winding. Meanwhile, the other degrees of freedom,

which are the z -axis, the tilting θ_x , and θ_y , are passively stabilized using the reluctance forces generated by the PMs.

Fig. 3.5 shows the principle of suspension-force generation in the proposed motor. Let us suppose that the rotor is centered with zero suspension current and that the flux-density distribution of the air gap is symmetrical. Thus, the amplitude of the air-gap flux density is identical at points 1 and 2. In this case, the attraction forces cancel each other, and the overall radial force on the rotor is zero. When a three-phase suspension current is applied in the suspension winding as shown in Fig. 3.5 (a), the radial force is generated in positive y -axis direction, because the air-gap flux density is increased and decreased at points 1 and 2, respectively. For suspension current in the opposite direction as shown in Fig. 3.5(a), a negative y -axis force is generated. The x -axis force is generated by providing current in the four-pole winding perpendicular to the one shown in Fig. 3.5(a), as shown in Fig. 3.5(b). In this case, the radial force is basically proportional to the suspension current. With the feedback of the rotor radial position, the radial force is controlled for stable non-contact magnetic suspension.

As shown in (a) and (b) of Fig. 3.5, when the angular position of the rotor changes, the current phase of the magnetic suspension winding must also be changed in order to generate magnetic suspension force in the same direction. Thus, the magnetic suspension current of an SPM bearingless motor depends on the angular position of the rotor.

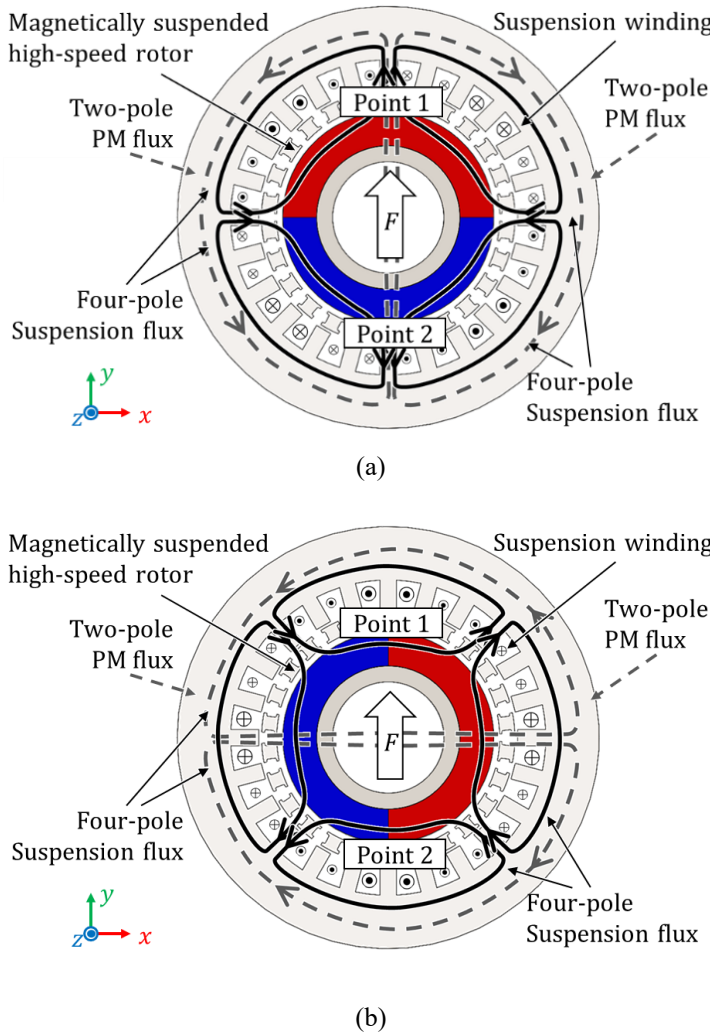


Fig. 3. 5. Principle of radial-force generation as surface permanent magnet type bearingless motor.

(a) N pole of PM towards $y+$ (b) N pole of PM towards $x+$

As previously mentioned, the interaction between p and $p \pm 1$ pole-pair magnetic flux generates radial forces. From (3.4) and (3.5), the proposed motor topology generates magnetic flux harmonics, specifically $n_s \pm p_h$ and $n_l \pm p_h$. Thus, these harmonics must avoid the $p_h \pm 1$ order to prevent interaction. Furthermore, to prevent radial force generation with no suspension current in the centered position, a symmetry factor x_s is important for selecting the pole combination previously presented by a part of the authors [106]

$$x_s = \gcd(2p_h, n_s) = \gcd(2p_h, n_l) = 2 \quad (3.30)$$

If $x_s > 1$, the magnetic gear does not produce radial force in the centered position. Hence, the proposed motor can achieve magnetic suspension without suspension current when the

rotor is centered theoretically. In this research, the pole combination is chosen based on (3.30).

To achieve stable magnetic suspension, the error angle of the radial active force must be as small as possible. Let us assume that the reference suspension force is $\mathbf{F}^* = [F_x^* \ F_y^*]^T$ and the actual suspension force generated by applying the suspension current is $\mathbf{F} = [F_x \ F_y]^T$. The error angle θ_{err} can be expressed as

$$\theta_{err} = \tan^{-1}\left(\frac{F_y}{F_x}\right) - \tan^{-1}\left(\frac{F_y^*}{F_x^*}\right) \quad (3.31)$$

3. 3. 2 Principle of Active Magnetic Suspension Force Generation in Consequent-Pole Type Two-Degree-Of-Freedom Actively Position Regulated Bearingless Motor

The motors proposed in Chapter 6 and Chapter 7 adapt the principle of magnetic suspension to general consequent-pole motors [50] [65] [66] [73] [74] [75] [107] [108] [109]. This means that a magnetic suspension flux equal to one pole pair is generated for a permanent magnet rotor with p_h pole pairs. Fig. 3. 6 shows the principle of radial-force generation as consequent-pole type bearingless motor.

Let us suppose the rotor is centered with zero suspension current and symmetrical air-gap flux density distribution. Thus, the amplitude of the air-gap flux density is identical at points 1 and 2. In this case, the attraction forces cancel each other, and the radial force on the rotor is zero. When a three-phase suspension current is applied to the suspension windings, the radial force is generated in a positive y -axis direction, because the air-gap flux density is increased and decreased at points 1 and 2, respectively. With a suspension current in opposite direction as shown in Fig. 3, a negative y -axis force is generated. The x -axis force is generated by providing current in the two-pole winding perpendicular to the fluxes shown in Fig. 3. 6. With the feedback of the rotor radial position, the radial force is controlled for stable non-contact magnetic suspension.

Unlike the SPM-type bearingless motor shown in 3. 3. 1, the magnetic suspension current of the consequent-pole motor can be a direct current determined by the magnetic suspension force reference. This is because, as shown in Fig. 3. 6(a) and (b), the magnetic suspension flux passes only through the iron core poles and not through the permanent magnets. Therefore, even if the rotational position changes, the position where the magnetic flux density changes does not change. Consequently, when using a direct current, it is not necessary to control the magnetic suspension current according to the angular position of the rotor [107].

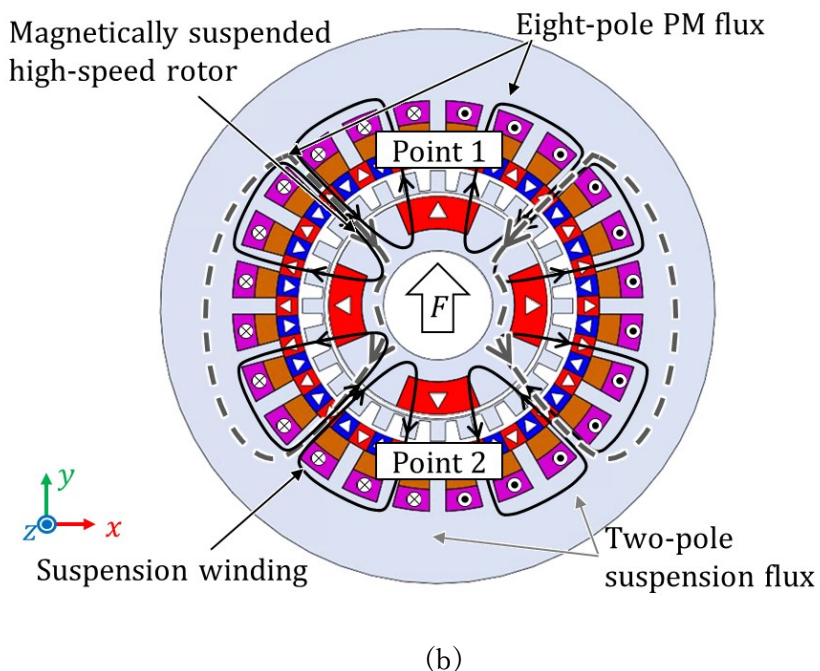
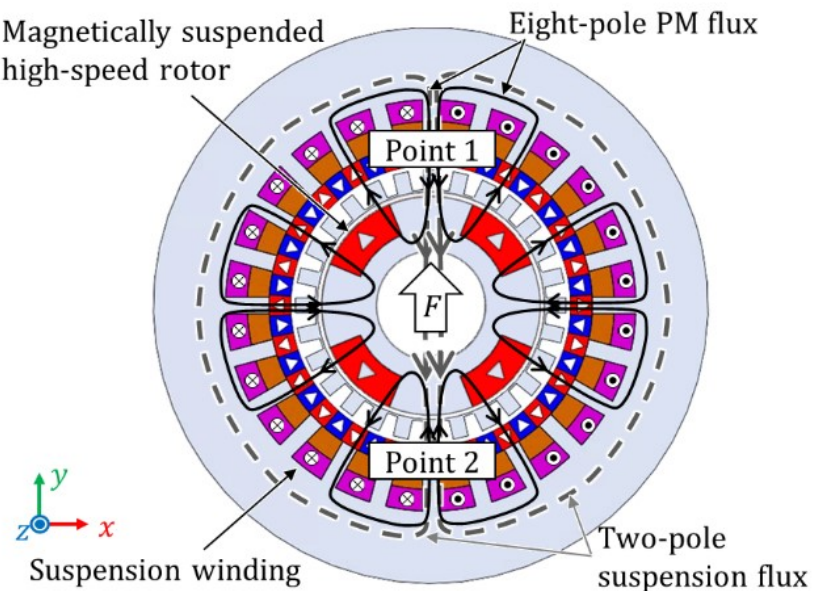


Fig. 3. 6. Principle of radial-force generation as consequent-pole type bearingless motor.

(a) N pole of PM towards $y +$ (b) N pole of PM towards $x +$

To achieve stable magnetic suspension, the error angle, defined in (3.31), of the radial active force must be as small as possible. Let us assume that the reference suspension force toward angle $\theta^* = \tan^{-1}(F_y^*/F_x^*)$ from the x -axis is $\mathbf{F}^* = [F_x^* \ F_y^*]^T$. Moreover, let us define the radial force the parallel component F_{\parallel} and perpendicular component F_{\perp} . Hence, the relationship between these forces is expressed as

$$\begin{pmatrix} F_{\parallel} \\ F_{\perp} \end{pmatrix} = \frac{1}{F^*} \begin{pmatrix} F_x^* & F_y^* \\ -F_y^* & F_x^* \end{pmatrix} \begin{pmatrix} F_x \\ F_y \end{pmatrix} \quad (3.32)$$

3.3.3 Principle of Force Generation by Passive Magnetic Suspension in Two-Degree-of-Freedom Actively Position Regulated Bearingless Motor

Fig. 3.7 and Fig. 3.8 show the principle of passive magnetic suspension force generation in axial and tilting directions, respectively. When the rotor is displaced in the axial direction, a restoring force f_z is generated due to the fringing magnetic flux on the edge of the rotor PM. Similarly, when the rotor is displaced in tilting direction, a restoring torque $\tau_{\theta y}$ is generated. To improve the stiffness in the tilting direction, the rotor axial length should be thin, and the rotor diameter should be large. By adopting this method, the ratio of variation in the area facing the rotor and air gap surface increases even for the same displacement. Therefore, in the two-axis actively controlled bearingless motor, the stack length is typically disc-type to stabilize the rotor passively.

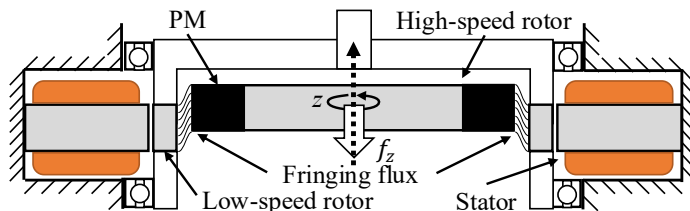


Fig. 3.7. Principle of passive magnetic suspension force generation in the axial direction.

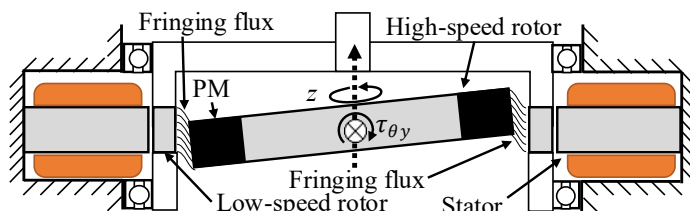


Fig. 3.8. Principle of passive magnetic suspension force generation in the tilting direction.

3. 4. Summary of Chapter 3

This chapter describes the structure and principle of magnetic-geared motor with magnetic-suspended high-speed rotor. Table 3.1 shows the combination of magnetic gear topology and magnetic suspension methods that mentioned in this chapter. Bearingless motors are abbreviated as BelM, and magnetic-geared motors are abbreviated as MGM.

Table 3. 1. Combination of magnetic gear topology and magnetic suspension methods.

	SPM-type BelM	Consequent-pole type BelM
SPM-type MGM	Applicable	Inapplicable
Reluctance-type MGM	Applicable	Inapplicable
Consequent-pole type MGM	Applicable	Applicable w/o rotor angular position feedback

Table 3.1 shows that magnetic suspension must be used in SPM-type and reluctance-type magnetic-geared motors using the magnetic suspension method described in Section 3.3.1, and that consequent-pole magnetic suspension cannot be used. Meanwhile, for consequent-pole magnetic geared motors, either the SPM-type magnetic suspension method shown in Section 3.3.1 or the consequent-pole magnetic suspension method shown in Section 3.3.2 can be used. In this case, the consequent-pole type magnetic suspension method described in Section 3.3.2 does not require angular position of the high-speed rotor for magnetic suspension control. Thus, it is possible to omit the angle sensor and simplify the control by using open-loop control for motor control, since it is not necessary to obtain the angular position of the high-speed rotor.

Table 3.2 shows the advantages and disadvantages of each magnetic-geared motor topology.

Table 3. 2. Advantages and disadvantages of each magnetic-geared motor topology.

	Rel-type MGM (Chapter 4)	DCPM-MGM (Chapter 5/6)	SCPM-MGM (Chapter 5/6)	SPM-type MGM
Torque density (Aimed for MGM torque)	Smallest	Small	Medium	Highest
Minimum pole-number of HSR	2	8	8	2
Magnetic Resistance	Small	Smallest	Medium	Highest
Consequent-pole type BelM	Inapplicable	Applicable	Applicable	Inapplicable
Rotor angular position requirement for magnetic suspension control	Necessary	Unnecessary	Unnecessary	Necessary
Possibility of disturbance generation caused by PM magnetization error	Low	High	High	High
Flux leakage in z-axis direction		High	High	

As shown in Section 1.1.2 and [41], the magnetic gear torque density is lowest for reluctance-type magnetic-geared motors, followed by double-sided consequent-pole magnetic-geared motors, single-sided consequent-pole magnetic-geared motors, and SPM-type magnetic-geared motors.

The number of poles of the high-speed rotor is the denominator in the gear ratio calculation equation, as shown in (3.15) and (3.25). For this reason, the minimum number of poles of the high-speed rotor is an essential indicator for designing magnetic-geared motors with high gear ratios. The minimum number of high-speed rotor poles is basically 2. Meanwhile, the minimum number of poles for a high-speed rotor with a consequent-pole type is 8 to avoid interference with the magnetic suspension flux.

Magnetic resistance is lowest in magnetic-geared motors with a double-sided consequent-pole type. In this structure, the magnetic suspension is not required to pass through permanent magnets, and the magnetic circuit to the high-speed rotor can be formed. As a result, the magnetic resistance is extremely low. Therefore, the largest magnetic suspension is expected to occur with the same magnetic suspension winding magnetomotive force.

Consequent-pole magnetic suspension and angular position detection of high-speed rotors are described in Table 3.1.

Disturbances caused by magnetization errors are considered to be significant in magnetic-geared motors with multiple permanent magnets. In reluctance-type magnetic-geared motors, permanent magnets are only located in the high-speed rotor, so disturbances caused by magnetization errors are considered to be unlikely.

As shown in Section 3.3.2, axial leakage flux is significant in motors with high-speed rotors of the consequent-pole type.

Based on these characteristics, this research evaluates a reluctance-type magnetic geared motor with a high gear ratio, a high-speed rotor with low magnetic excitation error and low magnetoresistance, and magnetic suspension. Chapter 4 investigates the feasibility of combining a magnetic geared motor and a bearingless motor. Based on this investigation and evaluation of prototypes, it was difficult to detect the angular position of high-speed rotors used for magnetic suspension control. Therefore, in Chapter 6 and Chapter 7, a consequent-pole magnetic-geared motor that does not require angular position detection of high-speed rotors used for magnetic suspension control was evaluated.

Chapter 4. Proposal and Analysis of High-Speed Rotor Magnetic Suspension for Reluctance-Type Magnetic-Geared Motors

In this chapter, the structure of a magnetic-geared motor with a magnetic-suspended high-speed rotor is proposed, and a structure that enables reduction of bearing loss is shown. In addition, the radial force and torque of the proposed structure are analyzed by a three-dimensional finite element method. The analysis shows the magnetic suspension characteristics and torque characteristics of the reluctance-type magnetic-geared motor proposed in this chapter.

4. 1. Analysis of the Relationship between the Pole / Slot Combinations and Motor / Suspension Characteristics

4. 1. 1 Analysis Settings

Magnetic-geared motors can combine various numbers of poles, as shown in equations (3.15) and (3.25). However, depending on the combination of poles, some combinations are not suitable for magnetic-geared motors with magnetic suspension of high-speed rotors [106]. Therefore, this section investigates which combinations are suitable for magnetic-geared motors with magnetic suspension of high-speed rotors.

The analysis model and analysis method are described in this section. The analysis was performed on reluctance-type magnetic-geared motors with two-pole or four-pole high-speed rotors. Fig. B. 1 to Fig. B. 7 show the dimensions of reluctance-type magnetic-geared motors. The width of the salient poles of the low-speed rotor is expressed as a ratio l_{LSR} , as shown in Fig. B. 7. The equation for calculating the ratio is shown in (4.1). The tooth width of the reluctance-type magnetic-geared motor is the same as the width of the salient pole of the low-speed rotor.

$$l_{LSR} = \frac{L_{LSR}}{L_{LSRmax}} \quad (4.1)$$

where, L_{LSR} is the width of the low-speed rotor salient pole, L_{LSRmax} is the maximum width at the number of the low-speed rotor salient pole.

In addition, all analyses in this section were performed using a two-dimensional finite element method, with both motor current and suspension current set to 0 A and no radial displacement of the high-speed rotor. The maximum transmission torque indicates the maximum torque T_{lmax} that can be transmitted by the low-speed rotor. The torque is output at the maximum load angle of the magnetic gear. The torque of the low-speed rotor is $-T_{hmax} = -T_{lmax}/G_r$, as shown in (3.18).

The analysis was performed using 10JNEX900 laminated silicon steel for the low-speed rotor core and stator core and N55 for the magnets. Note that all magnets were magnetized in parallel. Since the analysis in this section is comprehensive, losses are not included. Therefore, the actual torque is lower than the values analyzed in this section due to loss compensation.

4. 1. 2 Analysis Result

An analysis was conducted on the maximum transmitted torque T_{lmax} and torque ripple under varying stator slot numbers of 12, 13, ..., and 27. Note that the gear ratio, as determined from (3.15), is 7, 7.5, ..., and 14.5 for a high-speed rotor with 2 poles, and 4, 4.25, ..., and 7.75 for a high-speed rotor with 4 poles.

Fig. 4. 1 shows the **relationship** between the number of stator slots and the average maximum transmitted torque T_{lmax} . Fig. 4. 2 shows the relationship between the number of stator slots and the torque ripple. As the number of stator slots increases and the gear ratio increases, the maximum transmitted torque decreases. This is because the increase in the number of slots reduces the fluctuation in the permittivity. Additionally, the torque ripple was generally lower for high-speed rotors with 2 poles compared to those with 4 poles.

Fig. 4. 3 shows the relationship between the symmetry factor x_s and the average value of the radial force magnitude for a single mechanical angle cycle for two-pole high-speed rotors. Fig. 4. 4 shows the relationship between the symmetry factor x_s and the torque ripple for two-pole high-speed rotors. Note that the symmetry factor x_s is as shown in (3.30). Table 4. 1 shows the relationship between the symmetry factor x_s and the radial force and torque for two-pole high-speed rotor. From Fig. 4. 3, it was confirmed that the radial force

occurs when $x_s = 1$, as shown in (3.30). According to [106], the torque ripple increases at $x_s = 2$. Meanwhile, Fig. 4. 4 shows that torque ripple is not significantly large for large gear ratios.

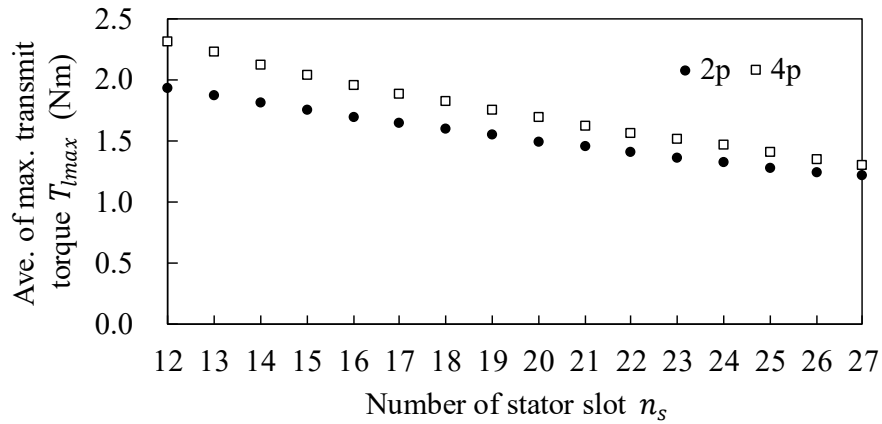


Fig. 4. 1. Relationship between the number of stator slots and the average maximum transmitted torque T_{lmax} .

Ave. of max. transmit torque: average of maximum transmission torque.

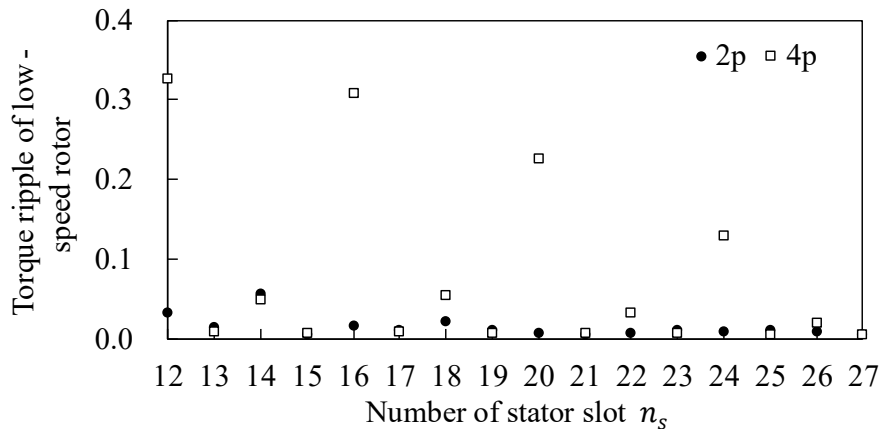


Fig. 4. 2. Relationship between the number of stator slots and the torque ripple.

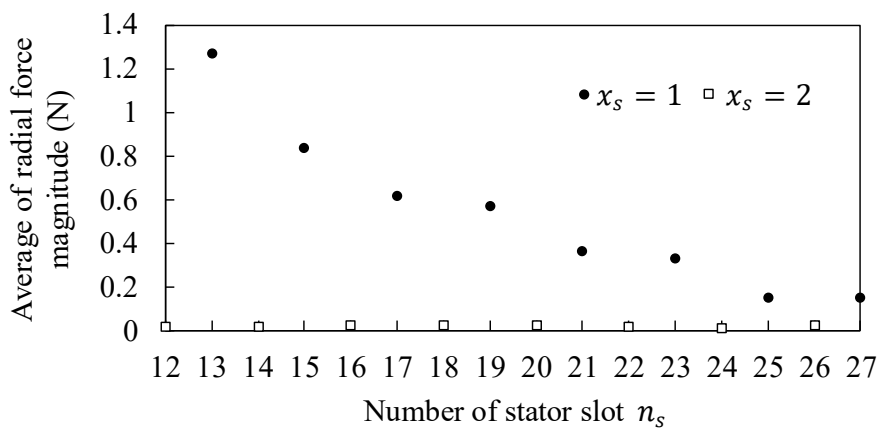


Fig. 4. 3. Relationship between the symmetry factor x_s and the average value of the radial force magnitude for a single mechanical angle cycle for two-pole high-speed rotors.

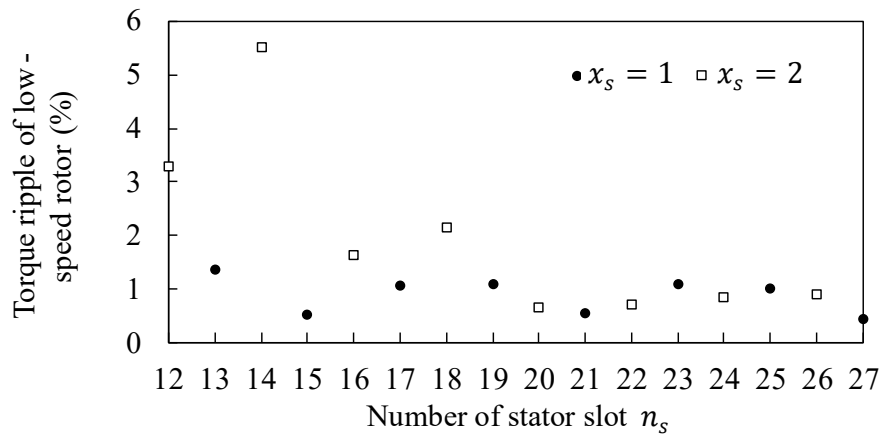


Fig. 4. 4. Relationship between the symmetry factor x_s and the torque ripple for two-pole high-speed rotors.

Table 4. 1. Relationship between the symmetry factor x_s and the radial force and torque for two-pole high-speed rotor.

$2p_h$	n_l	n_s	G_r	x_s	Ave. of radial force magn. (N)	Ave. of max. torque T_{lmax} (Nm)	Torque ripple of LSR (%)
2	14	12	7.0	2	0.02	1.94	3.29
	15	13	7.5	1	1.27	1.88	1.35
	16	14	8.0	2	0.02	1.83	5.52
	17	15	8.5	1	0.84	1.77	0.50
	18	16	9.0	2	0.03	1.71	1.62
	19	17	9.5	1	0.62	1.66	1.05
	20	18	10.0	2	0.02	1.61	2.15
	21	19	10.5	1	0.57	1.56	1.07
	22	20	11.0	2	0.02	1.50	0.63
	23	21	11.5	1	0.37	1.47	0.54
	24	22	12.0	2	0.02	1.42	0.70
	25	23	12.5	1	0.34	1.38	1.07
	26	24	13.0	2	0.02	1.33	0.82
	27	25	13.5	1	0.15	1.29	0.99
	28	26	14.0	2	0.02	1.26	0.90
	29	27	14.5	1	0.15	1.23	0.41

where $2p_h$ is the pole number of the high-speed rotor, n_l is the number of the low-speed rotor segments, G_r is the gear ratio, x_s is the symmetry factor calculated by (3.30), “Ave. of radial force magn.” stands for “average of radial force magnitude”, “Ave. of max. torque T_{lmax} ” stands for “average of maximum torque”.

Fig. 4. 5 shows the relationship between the symmetry factor x_s and the average value of the radial force magnitude for a single mechanical angle cycle for four-pole high-speed rotors. Fig. 4. 6 shows the relationship between the symmetry factor x_s and the torque ripple for four-pole high-speed rotors. Table 4. 2 shows the relationship between the symmetry factor x_s and the radial force and torque for four-pole high-speed rotor. In the four-pole high-speed rotor, the radial force at $x_s = 1$ is increased compared to the two-pole rotor. Furthermore, the torque ripple is significantly increased in $x_s = 4$. Thus, the pole slot combination must be selected more carefully for the four-pole high-speed rotor than for the two-pole rotor.

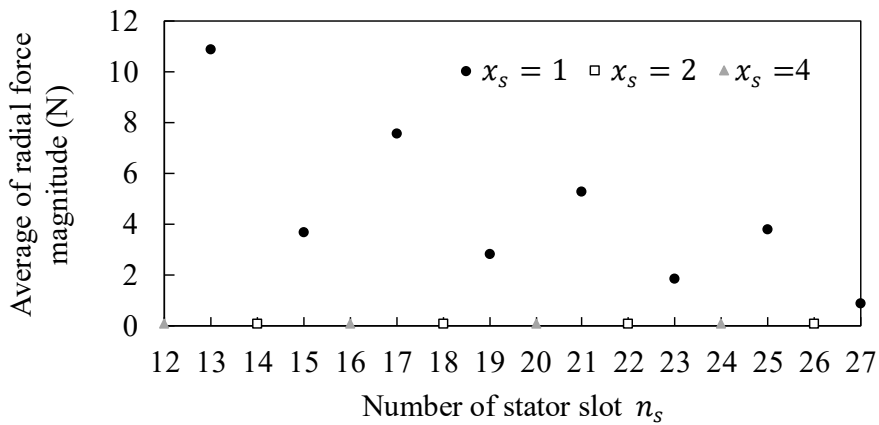


Fig. 4. 5. Relationship between the symmetry factor x_s and the average value of the radial force magnitude for a single mechanical angle cycle for four-pole high-speed rotors.

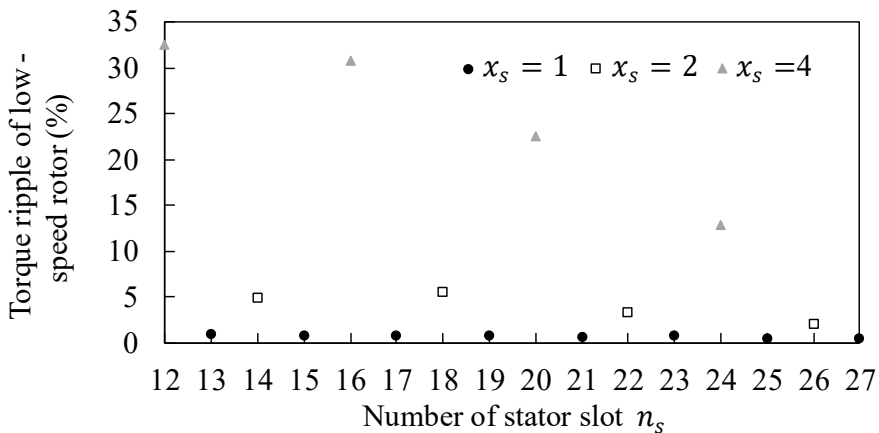


Fig. 4. 6. Relationship between the symmetry factor x_s and the torque ripple for four-pole high-speed rotors.

Table 4. 2. Relationship between the symmetry factor x_s and the radial force and torque for four-pole high-speed rotor.

$2p_h$	n_l	n_s	G_r	x_s	Ave. of radial force magn. (N)	Ave. of max. torque T_{lmax} (Nm)	Torque ripple of LSR (%)
4	16	12	4.00	4	0.10	2.33	32.57
	17	13	4.25	1	10.93	2.24	0.90
	18	14	4.50	2	0.11	2.13	4.84
	19	15	4.75	1	3.74	2.05	0.70
	20	16	5.00	4	0.11	1.97	30.81
	21	17	5.25	1	7.63	1.90	0.81
	22	18	5.50	2	0.10	1.83	5.44
	23	19	5.75	1	2.89	1.76	0.73
	24	20	6.00	4	0.10	1.70	22.58
	25	21	6.25	1	5.34	1.63	0.59
	26	22	6.50	2	0.09	1.58	3.30
	27	23	6.75	1	1.89	1.53	0.68
	28	24	7.00	4	0.09	1.48	12.84
	29	25	7.25	1	3.81	1.42	0.42
	30	26	7.50	2	0.09	1.36	1.99
	31	27	7.75	1	0.93	1.32	0.41

where $2p_h$ is the pole number of the high-speed rotor, n_l is the number of the low-speed rotor segments, G_r is the gear ratio, x_s is the symmetry factor calculated by (3.30), “Ave. of radial force magn.” stands for “average of radial force magnitude”, “Ave. of max. torque T_{lmax} ” stands for “average of maximum torque”.

According to these results, the pole slot combination of the proposed motor is suitable for a symmetry factor x_s of 2, which is less likely to generate radial force without radial displacement. In addition, two poles are favorable for high-speed rotors because the gear ratio increases. Therefore, four pole magnetic suspension windings are selected as shown in 3.3. 1.

Note that with a symmetry factor $x_s = 2$, torque ripple is known to increase compared to $x_s = 1$. However, as shown in Fig. 4.4, when the number of stator slots is large, torque ripple is low, so the drawbacks of selecting a symmetry factor $x_s = 2$ are minimal.

4. 2. Analysis of Stator Back Yoke Thickness and Various Characteristics

4. 2. 1 Analysis Settings

To investigate the influence of stator yoke thickness on the magnetic suspension performance, a 3D-FEM transient magnetic field analysis (using JMAG-Designer 20.2, JSOL corp.) was conducted. Table 4.3 shows the specifications of the analyzed model. Fig. 4.7 shows the flux and the mesh condition.

In this analysis, two motor models were employed: a 130 mm stator outer diameter model with a magnetic circuit volume comparable to that of the motor proposed in [94], and a 140 mm stator outer diameter model with a more spacious magnetic design. Based on the authors' experience, stable magnetic suspension control can be achieved within an angle error of ± 5 degrees. For this reason, a model with the smallest angle error within ± 5 degrees can be selected for a model with a larger torque density and the same topology.

In this model, the stack length is thin to enhance the passive suspension characteristics. As a result, the edge effect and fringing flux effect are not negligible as shown in Fig. 4.7 (b). Thus, a 3D-FEM is necessary for this model. The analyses are conducted by dividing one revolution into 90 segments, because the torque and radial force ripple are small. Most of the analyses except for the unbalanced magnetic pull force analysis are conducted at the centered position. When switched off, the rotor is generally touched-down to the radial position determined by the touchdown clearance. In order to start the magnetic suspension, the FEM analysis was carried out to check if the magnetic suspension can be possible at the limited starting current. The FEM mesh is automatically generated considering the rotor radial displacement.

Table 4. 3. Specifications of the analyzed model.

Parameter	Unit	Value
Stator outer diameter	mm	130/140
Stator inner diameter	mm	86
Slot depth	mm	9.3
High-speed rotor outer diameter D	mm	70
Low-speed rotor radial thickness	mm	5
Stack length L	mm	10
Inner air-gap length	mm	2
Touchdown length of the high-speed rotor	mm	0.5
Outer air-gap length	mm	1
Turn number of motor winding	-	12
Turn number of suspension winding	-	21
Winding diameter	mm	0.4
Stator core material	-	20HX1300
Low-speed rotor material	-	20HX1300
High-speed rotor PM material	-	N48
High-speed rotor core material	-	S45C

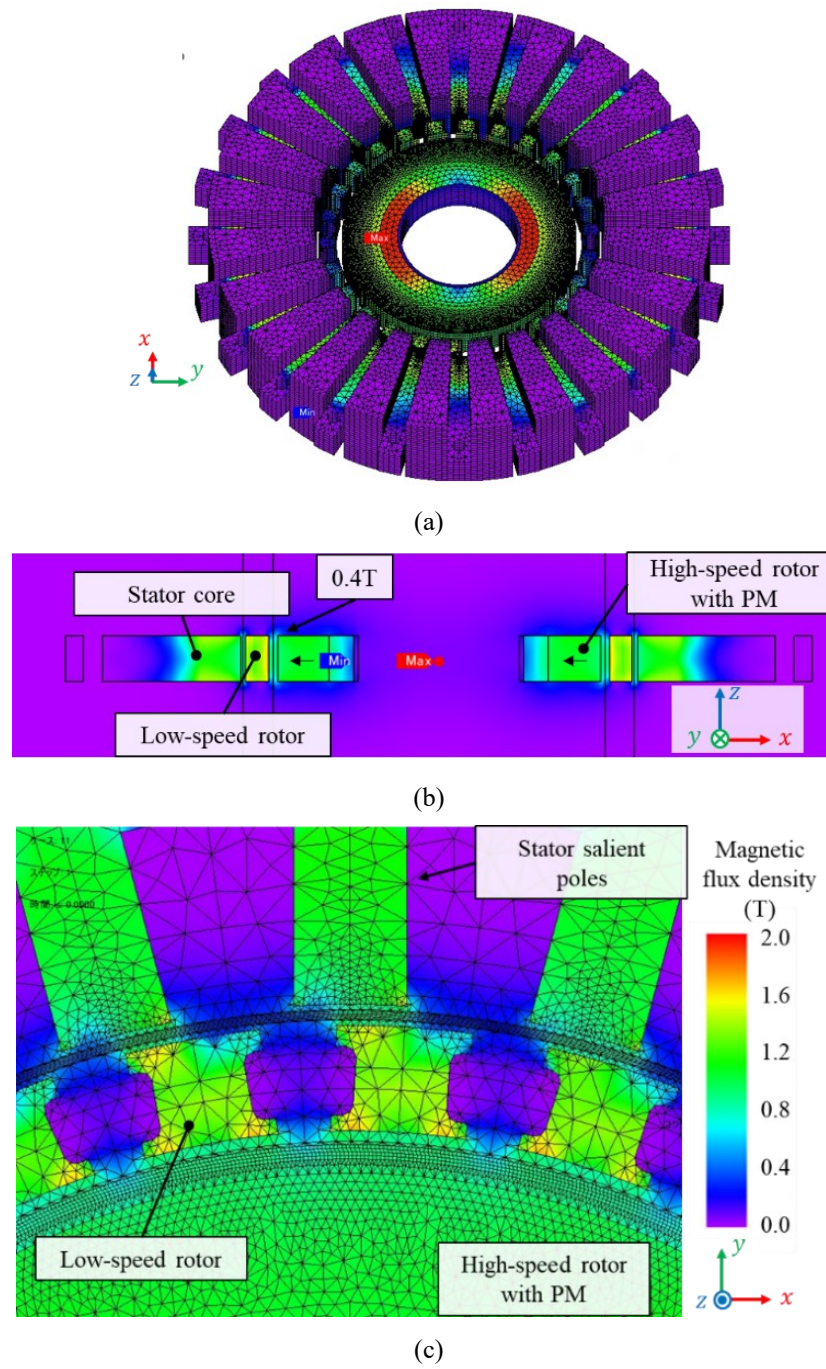


Fig. 4.7. Flux-density distribution of the 140 mm outer diameter model.

- (a) 3D view of the analyzed model. (b) Flux leakage distribution in x-z cross-section.
- (c) Mesh view around the air gaps.

In the proposed motor shown in this chapter, the number of pole pairs of the high-speed rotor permanent magnets is set to $p_h = 1$, the number of salient poles of the low-speed rotor is set to $n_l = 26$, the number of stator teeth is set to $n_s = 24$, and the number of pole pairs of the suspension windings for generating magnetic suspension force is set to 2. The reasons for setting these pole combinations are shown in Sections 3.2.1 and 3.3.1.

However, as described below, the high-speed rotor of the proposed motor is lightweight, so the suspension winding is not expected to carry a large current in constant operation. In addition, since the maximum current density in the motor winding is relatively low at approximately 2 A/mm^2 , the problem of reduced winding utilization due to the use of toroidal winding does not have a significant effect. For this reason, the proposed motor offers the significant advantage of achieving a high winding factor with short coil end lengths through toroidal winding. While concentrated winding is also effective for shortening coil end lengths, it cannot simultaneously achieve a high winding factor and low imbalance in air gap flux density caused by the motor windings, hence it is not adopted in the proposed motor.

The windings of the model employed the toroidal winding to reduce the end winding. In two-axis actively controlled bearingless motor, the end winding length must be short since a flat disc-type rotor is required for passive stabilization [110] [78] [111]. The conductors located at the inside of the stator yoke are effective in generating magnetomotive force. Meanwhile, the conductors located outside of the stator yoke are not effective in generating magnetomotive force.

The numbers of strands in the suspension and motor windings are both five. Fig. 4.8 shows the winding arrangement of the proposed motor. Every slot has a motor conductor and a suspension conductor. The number of the conductors in the slots is evenly distributed.

In this machine, the two-axis position is actively regulated. Thus, the diameter of the suspended high-speed rotor D is set as 70 mm and the stack length L is set as 10 mm to stabilize the rotor passively. Hence, the aspect ratio $D/L = 7$.

The 0-degree rotational angle of the high-speed rotor θ_h in this paper is defined as the position where the y -axis aligns with the magnetization direction of the PM.

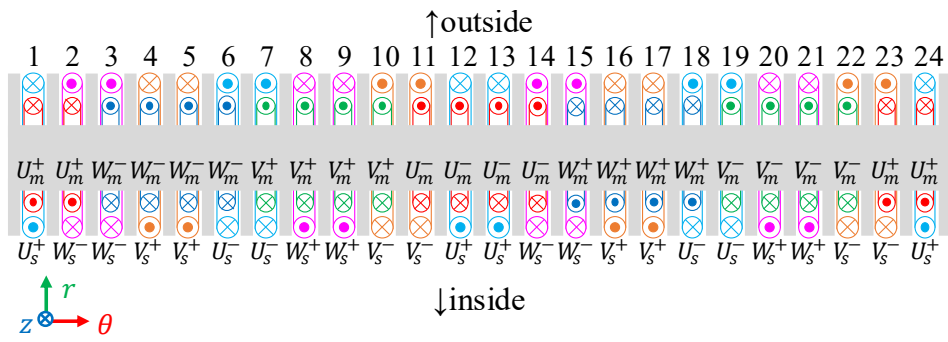


Fig. 4. 8. Winding arrangement of the analyzed model.

Note that the model in this section differs from the model in Section 4.1 in that the following improvements have been made to enhance the manufacturability of prototypes.

(a) Straightening of the stator teeth

In many motors, the pole shoes are located at the tips of the stator teeth. This design prevents the windings from extending beyond the slots and also reduces permeability variations in the stator, which minimizes slot harmonics. However, the proposed motor utilizes magnetic modulation, so larger slot harmonics are desirable. Additionally, the toroidal winding structure prevents the extension of the winding from the slots. Furthermore, pole shoes are structurally weak and reduce the slot fill factor. For these reasons, straight teeth were selected.

(b) Modification of the shape of the low-speed rotor pole pieces

In many magnetic-geared motors, the teeth are connected through a thin bridge section, as shown in the model in Section 4.1. However, this structure makes it difficult to manufacture and assemble due to the low strength of the bridge section. For this reason, in the structure introduced in this section, the low-speed rotor pole pieces are made as independent parts to improve manufacturability. Additionally, to securely hold the pole pieces, a dumbbell-shaped design with a narrowed central section was adopted to ensure positional stability in both the radial and rotational directions.

The precise dimensions are listed in Appendix C.

4. 2. 2 Air-gap Flux-density Distribution

The flux-density distribution in the two air gaps was analyzed. As described in Section 3.2.1, the proposed motor utilizes the magnetic flux harmonics generated by magnetic modulation. Thus, the spatial harmonics of the flux density verify flux modulation of the magnetic gear. Also, as described in Section 3.3.1, the flux density must be asymmetrical when suspension current is applied. Hence, the air gap flux densities with the magnetic suspension current were also analyzed.

Fig. 4. 9 shows the radial flux-density distributions in the two air gaps. The black solid line and the red dashed line show the flux densities at the suspension currents i_{sy} of 0 A and 20 A, respectively. Fig. 4. 9 (a) shows the inner air-gap flux density B_{ri} between the high-speed and low-speed rotors. When i_{sy} is 20 A, the flux density B_{ri} is increased around $\theta_s = 90^\circ$ although it is reduced around $\theta_s = 270^\circ$. This unbalanced air-gap flux density generates radial suspension force in the $\theta_s = 90^\circ$ direction. Fig. 4. 9 (b) shows the outer air-gap flux density B_{ro} between the low-speed rotor and stator. There is an increase and decrease in the flux density at $\theta_s = 90^\circ$ and $\theta_s = 270^\circ$ as in case of Fig. 4. 9 (a). This result shows that the radial force is generated in the low-speed rotor when the suspension force is generated in the high-speed rotor. The radial force in the low-speed rotor is supported by the ball bearings.

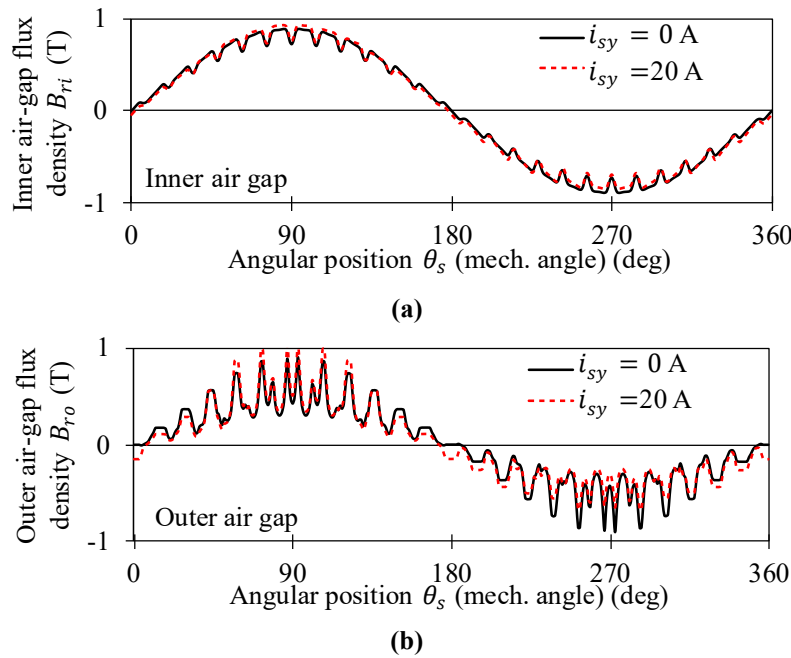


Fig. 4. 9. Air-gap flux-density distributions in the radial direction.

(a) Inner air gap: between high-speed rotor and low-speed rotor. (b) Outer air gap: between low-speed rotor and stator.

Fig. 4. 10 shows the magnitudes of the spatial harmonic components of the flux density B_{ro} in the outer air gap. The 2nd component, corresponding to $p_h + 1$ in Section 3. 3. 1, is created by the suspension current. Also, harmonic fluxes are generated such as 23rd, 25th, and 27th. These components are generated by the modulation due to the stator teeth and the low-speed rotor as shown in (3.4) and (3.5).

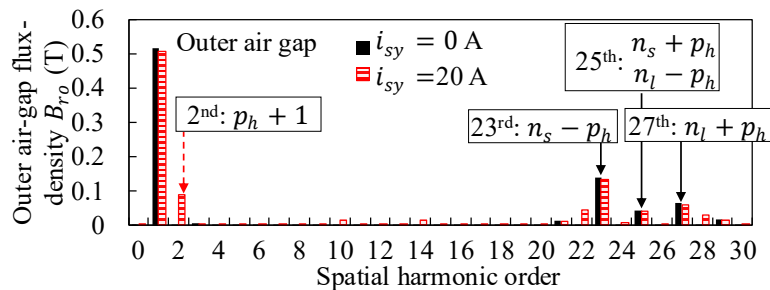


Fig. 4. 10. Magnitudes of flux density in spatial harmonic components between the low-speed rotor and stator.

4. 2. 3 Torque Characteristics

Fig. 4. 11 shows the torque waveform with and without q -axis current i_{mq} . According to Fig. 4. 11, the q -axis current i_{mq} affects only the high-speed rotor torque. Fig. 4. 11 (a) shows the torque under $\delta_g = \pi/2$ and synchronous $\omega_h = G_r\omega_l$ conditions, which produces the maximum torque of the low-speed rotor continuously. From this figure, the torque ripple is small, less than 1% for all waveforms, and condition (3.18) is verified. Additionally, when i_{mq} is applied, counter-torque is compensated and this model acts as a geared motor. Fig. 4. 11 (b) shows the torque under $\delta_l = 0$ and δ_h is changed from 0 to 2π , which means that the low-speed rotor is locked and only the high-speed rotor is rotated. This waveform validates (3.17). Note that the low-speed rotor salient poles number n_l is an even number, thus that waveform is the second-order sinusoidal wave.

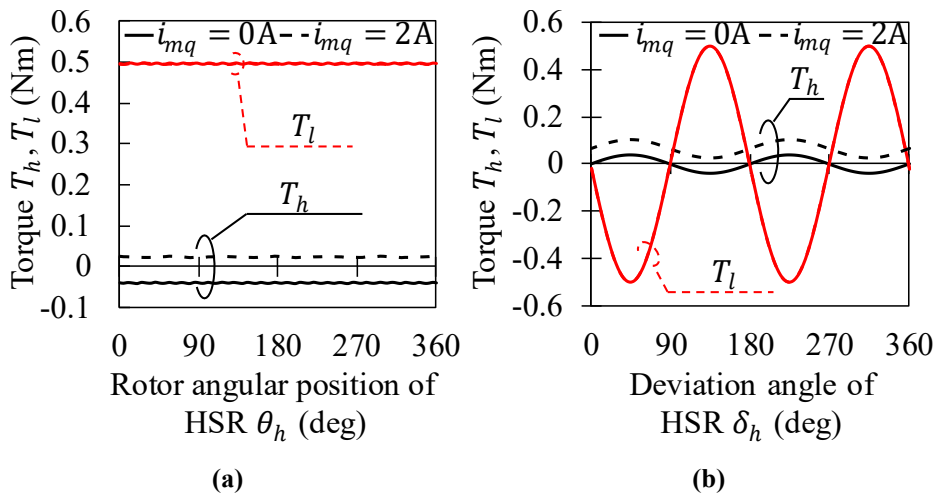
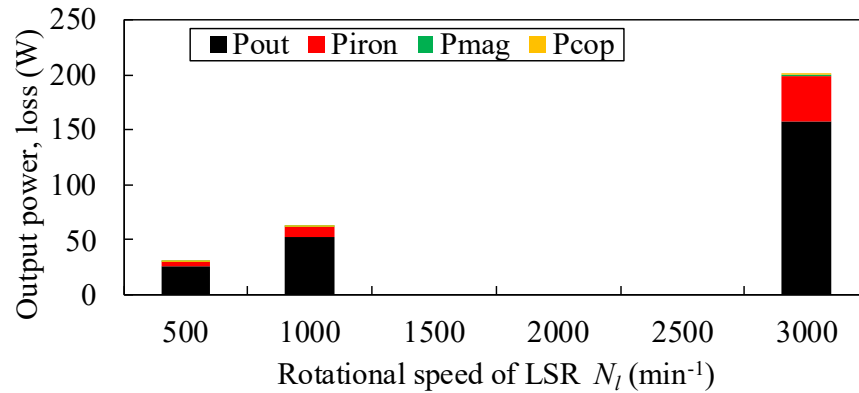


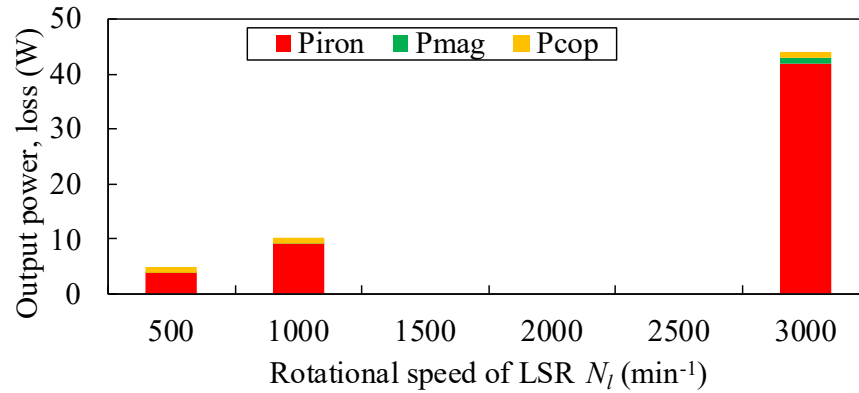
Fig. 4. 11. Torque waveform in different conditions with and without q -axis current i_{mq} .

- (a) Synchronous rotation with respect to the rotational angular position of the high-speed rotor (HSR) θ_h .
- (b) Low-speed rotor is fixed and the deviation angle of the high-speed rotor (HSR) δ_h is changed.

Fig. 4.12 shows the output and losses at each low-speed rotor rotational speed at maximum , as shown in Fig. 4.11. In Fig. 4.12, the output, iron loss in the silicon steel, permanent magnet eddy current loss, and copper loss are denoted by P_{out} , P_{iron} , P_{mag} , and P_{cop} , respectively. Fig. 4.13 shows the efficiency at each low-speed rotor rotational speed at maximum torque.



(a)



(b)

Fig. 4.12. Output and losses at each low-speed rotor rotational speed at maximum torque.

(a)Losses and output (b)Losses

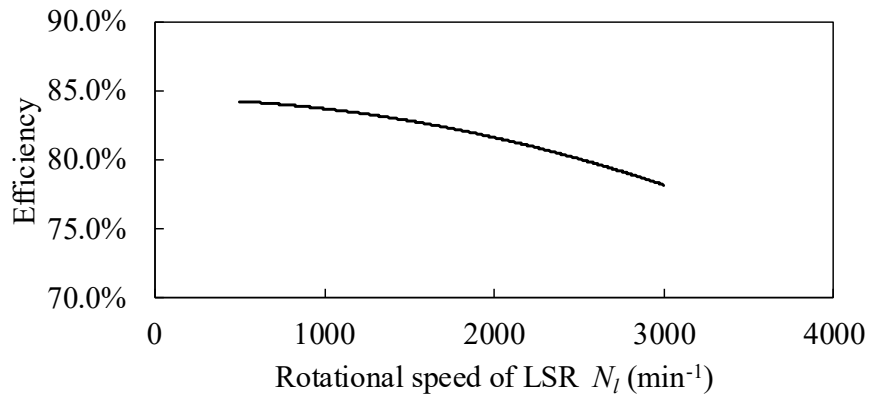


Fig. 4. 13. Efficiency at each low-speed rotor rotational speed at maximum torque

According to Fig. 4.12, iron loss dominates in the high-rotational-speed region. Meanwhile, due to the long air gap length of the proposed motor, eddy current loss in the permanent magnet is quite small. Furthermore, Fig. 4.13 shows that the peak efficiency is approximately 500 min^{-1} at low rotor rotational speed. However, even at speeds exceeding 2000 min^{-1} , the efficiency is approximately 80%. Therefore, despite the use of magnetic modulation, the efficiency does not decrease significantly at high rotational speed.

4. 2. 4 Stator Back Yoke and Suspension Force

To compare the suspension characteristics, analyses with different yoke thicknesses are conducted. In this model, four pole of the magnetic suspension flux is significantly lower than twenty-six of the low-speed rotor pole pieces. Thus, the suspension characteristics are not dependent on the δ_l and δ_h . Hence, these analyses are conducted in $\delta_g = 0$ condition.

In the proposed motor, a MWINV-5R022 (Myway Plus Corp. Japan) was required for the magnetic suspension inverter at the maximum capacity due to budgetary constraints. The instantaneous maximum current specified in the data sheet for this inverter is 31.25 A_{uvw}. Accordingly, the inverter must be capable of compensating for the unbalanced magnetic pull at the maximum eccentricity of 0.5 mm within the instantaneous maximum current. Nevertheless, considering errors in analysis, a design capable of canceling unbalanced magnetic pull at approximately half the maximum current is required. Furthermore, based on the authors' experience, angle error must be within ± 5 degrees to achieve stable control.

Fig. 4. 14 and Fig. 4. 15 show the flux-density distribution when the suspension force is generated towards positive y -axis. To reduce the error angle θ_{err} , the stator must avoid flux density saturation to increase suspension flux. Thus, the flux density of the stator yoke must be small when no suspension current is applied. In the 130 mm outer diameter model, the maximum value of the flux density in the stator yoke is 1.67 T. In the 140 mm outer diameter model, it is decreased to 1.50 T since the thickness of the stator yoke is enlarged and higher suspension fluxes can be applied.

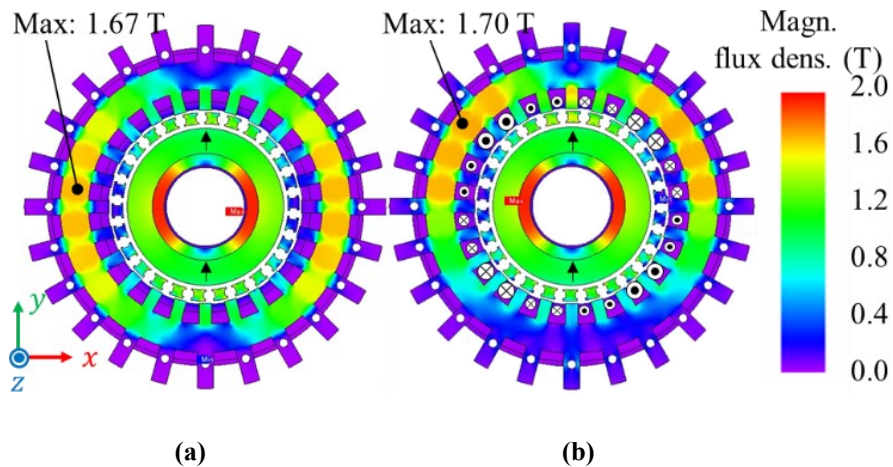


Fig. 4. 14. Flux-density distribution of the 130 mm outer diameter model. (a) Suspension current $i_{sy} = 0$ A. (b) Suspension current $i_{sy} = 20$ A.

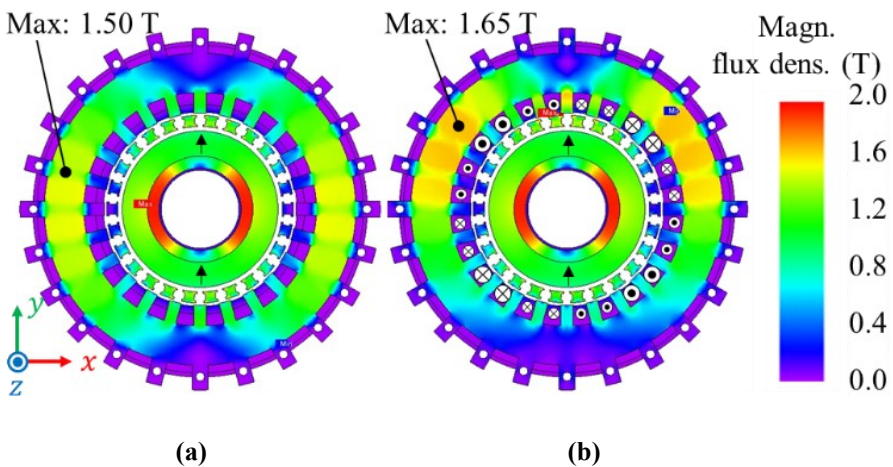


Fig. 4. 15. Flux-density distribution of the 140 mm outer diameter model. (a) Suspension current $i_{sy} = 0$ A. (b) Suspension current $i_{sy} = 20$ A.

Fig. 4. 16 shows the suspension characteristics of the proposed motor for each model. In Fig. 4. 16 (a) and (b), the generated suspension forces are shown at the suspension current $i_{sx} = 10$ A and 20 A. Fig. 4. 16 (a) and (b) show the radial force F_x and F_y in x - and y -axis directions, respectively. In Fig. 4. 16 (a), the averages \bar{F}_x of the radial force in the x -axis direction at $i_{sy} = 20$ A are 25.9 N and 32.2 N for the 130 mm and 140 mm outer diameter models, respectively. Fig. 4. 16 (c) shows the error angle θ_{err} , as defined in (3.31). In Fig. 4. 16 (c), the error angle θ_{err} does not depend on the suspension current, whereas the error angle of the 140 mm model is smaller than that of the 130 mm outer diameter model. Thus,

in terms of suspension performance, a thick stator back yoke is favorable. Fig. 4.16 (d) shows the unbalanced magnetic pull force F_{ux} , that is the x -axis radial force and the rotor radial displacement x in the high-speed rotor. In Fig. 4.16 (d), the averages of the unbalanced pull force $\overline{F_{ux}}$ at the radial displacement 0.50 mm are 14.4 N and 17.3 N for the 130 mm and 140 mm outer diameter models, respectively.

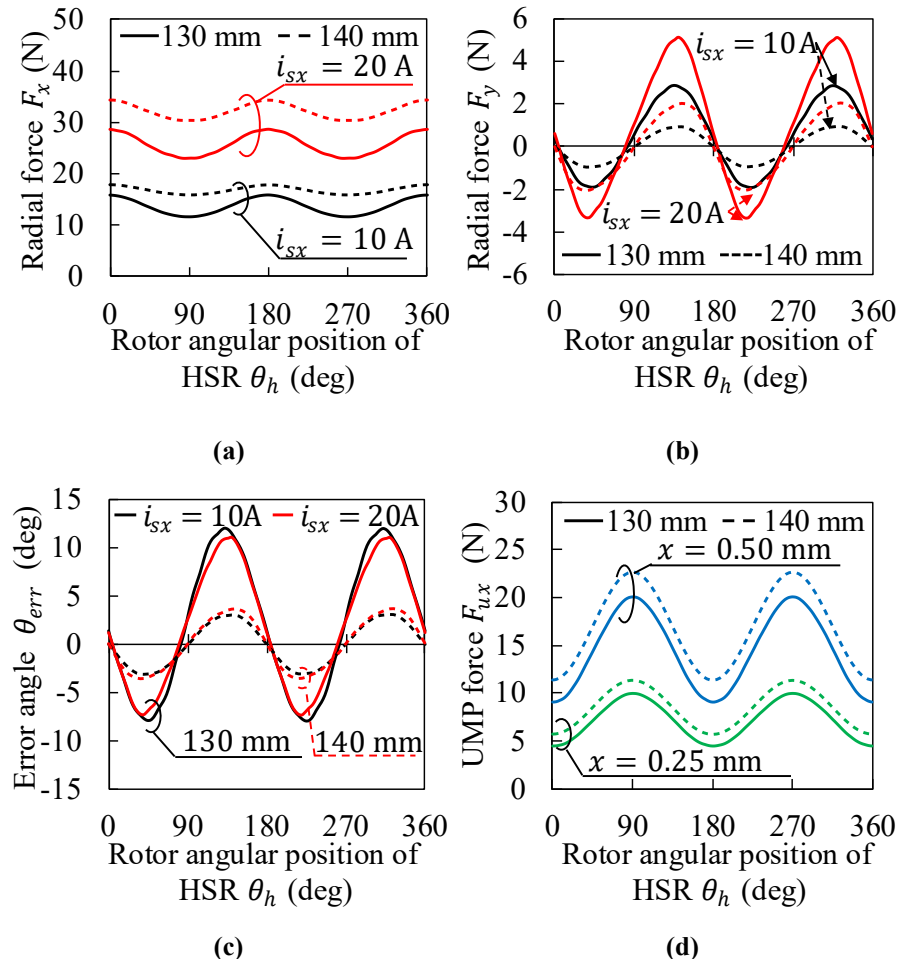


Fig. 4.16. Suspension characteristics of the different stator diameter models with respect to the rotational angular position of the high-speed rotor (HSR) θ_h .

(a) Suspension force F_x . (b) Suspension force F_y . (c) Error angle θ_{err} . (d) Unbalanced magnetic pull (UMP) force F_{ux} .

4. 3. Analysis of mutual interference between motor current and suspension current

According to the analysis results in Section 4.2.4, the 140 mm outer diameter model was superior. Then, the mutual interference between the motor current and suspension current was verified using the 140 mm outer diameter model. From the analysis results, the maximum current density of the motor and suspension current of the proposed motor are approximately 2 A/mm^2 and 25 A/mm^2 , respectively. Thus, the low-speed rotor torque and magnetic suspension force were analyzed with each and both currents applied.

Fig. 4.17 shows the analysis results of the mutual interference between the motor current and suspension current. In (a) magnetic suspension force, the motor current has almost no effect. In (b) low-speed rotor torque, although the average is about 3.5% larger when the magnetic suspension current is applied compared to without application, the effect is extremely small.

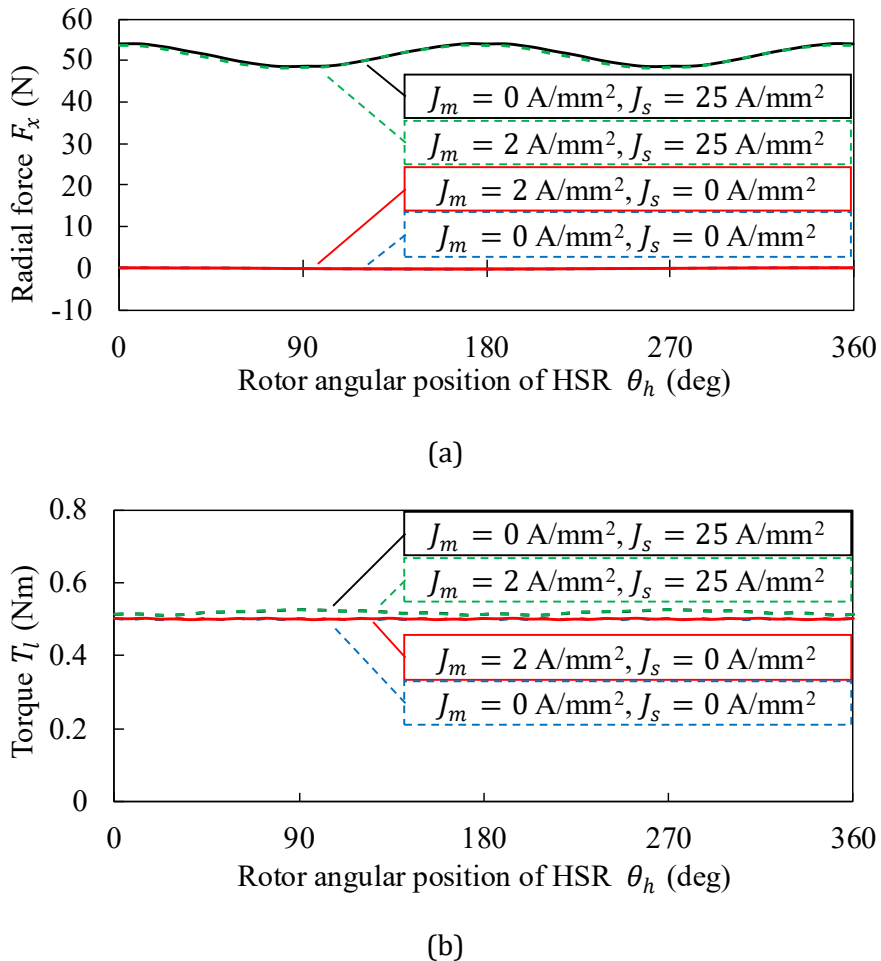


Fig. 4. 17. Analysis results of the mutual interference between the motor current and suspension current.

(a)Magnetic suspension force F_x (b)Low-speed rotor (LSR) torque T_l

4. 4. Consideration of Hall element placement for angle position detection

To achieve accurate detection using a Hall element, it is desirable for the magnetic flux density to vary sinusoidally with respect to the angular position of the high-speed rotor. Thus, the variation of magnetic flux density was analyzed using a three-dimensional finite element method at positions 7 mm in the z direction and 10 mm in the r direction from the surface of the high-speed rotor. Fig. 4. 18 shows the analysis results for magnetic flux density variations in each direction. The analysis results show that the fundamental components of the magnetic flux density are 21.6 mT, 27.9 mT, and 36.1 mT in the r , θ , and z directions, respectively. According to Fig. 4. 18, the z -axis direction is the largest. Therefore, the Hall elements were positioned to detect the magnetic flux in the z -axis direction.

Then, the position of the Hall element was evaluated. Fig. 4. 19 shows the amplitude of the magnetic flux density in the z -direction along the x -axis on the outer side of the high-speed rotor. Note that the origin of the z -axis is the center of the high-speed rotor. Additionally, the inner diameter of the high-speed rotor is 35 mm, and it is difficult to place the Hall element outward from the inner diameter of the high-speed rotor. Accordingly, an analysis was conducted within a range of 8 mm to 12 mm in the radial direction, considering the size of the Hall element. As shown in Fig. 4. 19, a maximum value exists near $z = 10$ mm and $r = 12$ mm. Therefore, in the prototype, $z = 12$ mm and $r = 11.15$ mm was selected.

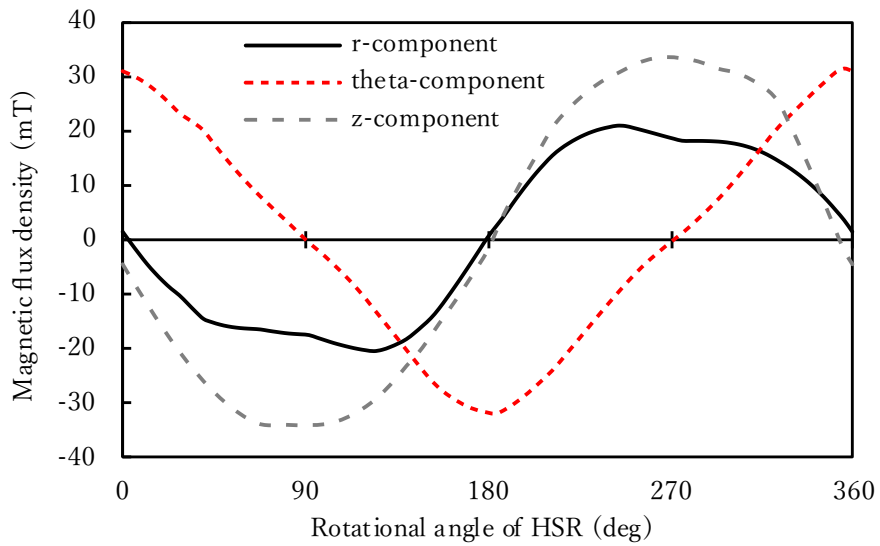


Fig. 4. 18. Analysis results for magnetic flux density variations in each direction.

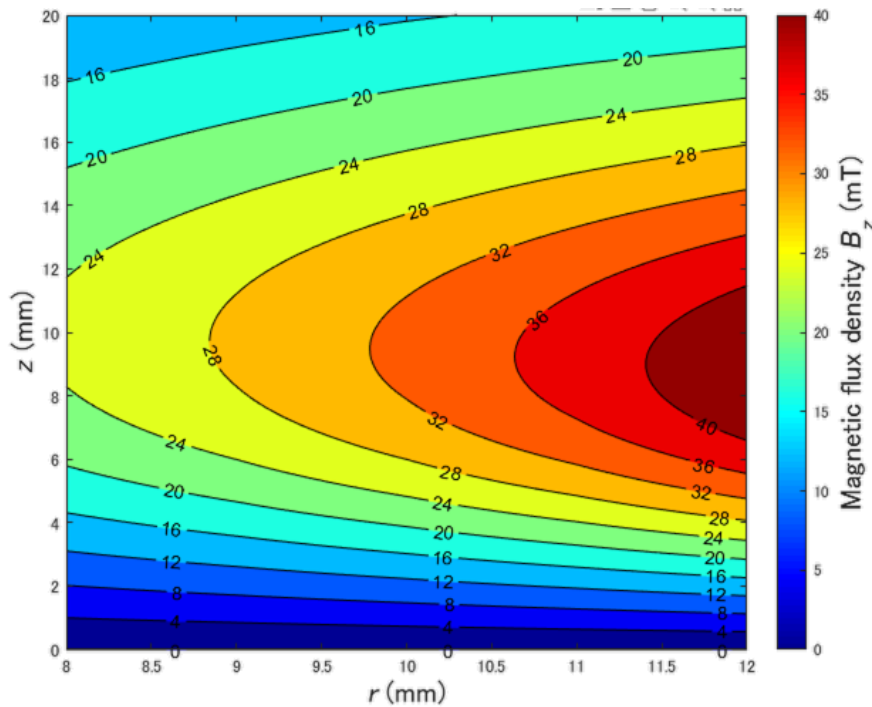


Fig. 4. 19. Amplitude of the magnetic flux density in the z -direction along the x -axis on the outer side of the high-speed rotor.

4. 5. Consideration of Maximum Transmission Torque Improvement by Flux Strengthening

Generally, in PMSMs, torque is increased by increasing the q -axis current. However, in magnetic-geared motors, the maximum transmitted torque is constant, so there is a limit to the effective q -axis current. In the proposed motor, as shown in Section 4. 2. 3, the maximum value of the q -axis current is approximately 2 A, which corresponds to a current density of approximately $2 \text{ A}_{\text{rms}}/\text{mm}^2$. Thus, the motor winding usage is very low. Therefore, to enhance the maximum transmitted torque, a flux strengthening was utilized. The principle is illustrated in Fig. 3. 4.

In the proposed motor, a large amount of magnetic flux is generated by the high-speed rotor permanent magnets. This means that the flux path in the flux strengthening is the same as the magnetic path of the permanent magnets. Accordingly, even when a positive current is applied to the d -axis, it is difficult to observe the effect of changes in magnetic flux density due to the increase in magnetoresistance caused by magnetic saturation. Therefore, in this study, the change in magnetic flux density with q -axis current was analyzed at first. Fig. 4. 20 shows the magnetic flux density between the high-speed rotor and low-speed rotor with q -axis current applied. Even though 1 A was applied to the axis current, the magnetic flux amplitude was only approximately 2 mT, which is very small compared to the permanent magnet magnetic flux. Therefore, maximum transmission torque improvement due to flux strengthening is not expected.

Fig. 4. 21 shows the torque of the high-speed rotor with and without a low-speed rotor at a q -axis current of 1 A. The radial thickness of the low-speed rotor, the inner magnetic air gap, and the outer magnetic air gap are 5 mm, 2 mm, and 1 mm, respectively. Thus, the motor is an SPM motor with an air gap length of 8 mm without the low-speed rotor. The analysis results show that the motor torque of the high-speed rotor is maintained at approximately 70% even without the low-speed rotor. Therefore, the permeability of the low-speed rotor is very low, and the motor can be regarded as a wide-gap bearingless motor. Meanwhile, the magnetic flux of the motor windings is very small compared to that of the permanent magnets, and it is not expected that the motor performance will change significantly due to the motor current.

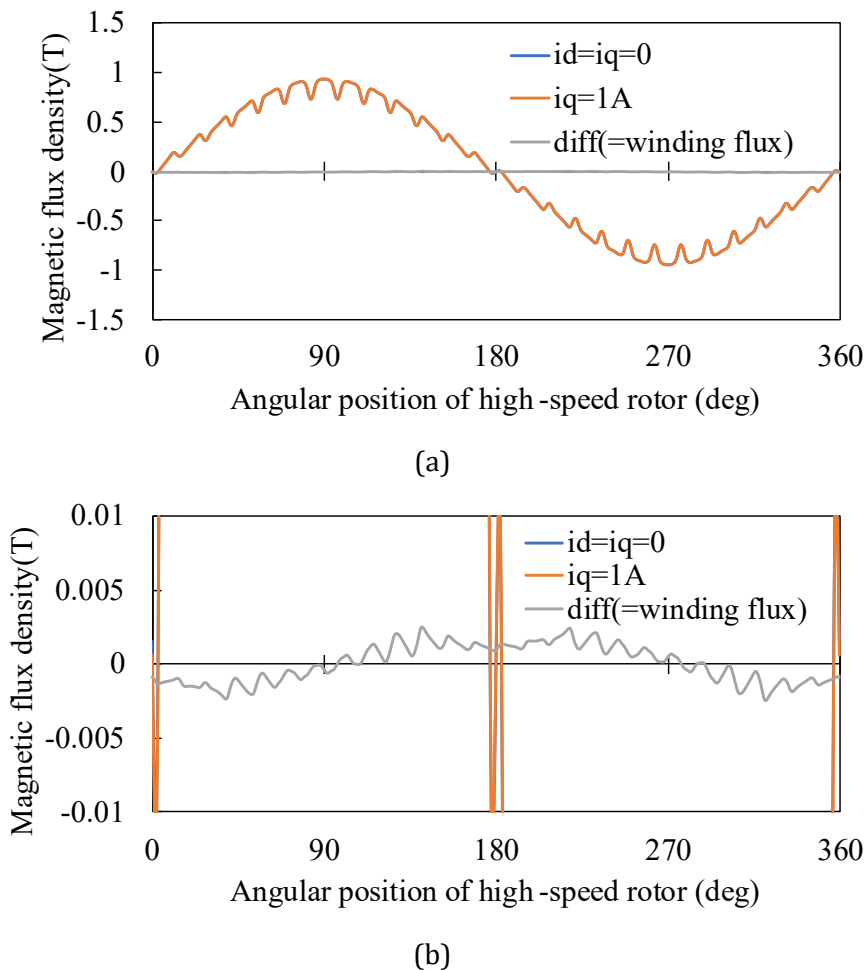


Fig. 4. 20. Magnetic flux density between the high-speed rotor and low-speed rotor with q -axis current applied.

(a) Overall view (b) Enlarged view

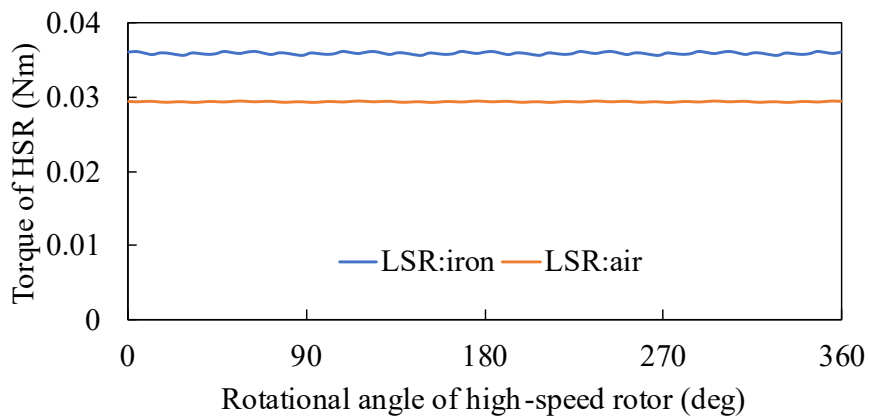


Fig. 4. 21. torque of the high-speed rotor with and without a low-speed rotor at a q -axis current of 1 A.

4. 6. Analysis of Stack Length and Motor Characteristics

In this section, the characteristics of the model shown in the analysis results in Section 4.2. 4 were analyzed using a three-dimensional finite element method by changing the stack length of the motor. Generally, two-axis active control bearingless motors are designed to be flat and thin to improve the passive stability in the tilt direction as shown in Section 3. 3. 3. In these bearingless motors, the rotor diameter is typically six times the stack length. However, to facilitate control, the air gap length is typically longer than that of motors of the same size. These factors increase the effect of magnetic flux leakage at the edges. Therefore, in this section, the stack length was varied from 10 mm to 30 mm, and the changes in torque, tilt rigidity, and radial force performance were investigated.

4. 6. 1 Relationship between Stack Length and Torque

Fig. 4. 22 and Fig. 4. 23 show the relationship between the stack length L and the maximum transmission torque T_b , and the relationship between the stack length and the torque density, respectively. In this section, motor volume is calculated based on the outer diameter of the stator and the stack length, and does not include the coil ends, etc. Fig. 4. 23 reveals that the torque density also increases as the thickness increases. The reason for the decrease in the torque density at thin stack length is that the magnetic flux density leaks at the edges due to the edge effect. In magnetic gears, the magnetic flux density amplitude at the air gap is proportional to the maximum transmission torque [95]. Therefore, the reduction in magnetic flux density due to the end effect results in the decreased maximum transmission torque.

Fig. 4. 24 shows the maximum value of the magnetic flux density in the air gap between the high-speed and low-speed rotors with respect to the relative axial position z/L for $L=10, 15, 20, 25$, and 30 mm, where z is the axial position and the origin is the top of the motor in the axial direction. Fig. 4. 25 shows the maximum value of the magnetic flux density in the air gap between the high-speed and low-speed rotors with respect to the absolute axial position with same analysis model as shown in Fig. 4. 24. It is seen that the flux density is decreased near the edge when the stack length is thin. Meanwhile, according to Fig. 4. 25, there is no significant dependency on L . This indicates that the edge effect is significant when the stack length L is thin, thus the torque density is decreased.

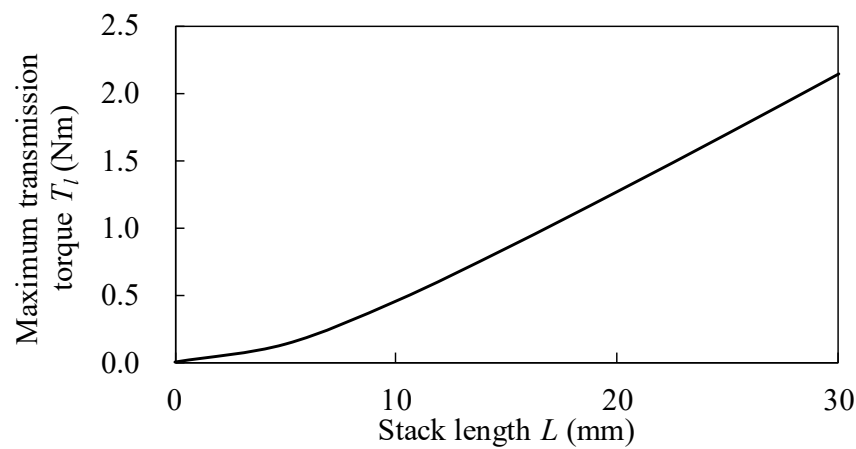


Fig. 4. 22. Relationship between stack length and maximum transmission torque.

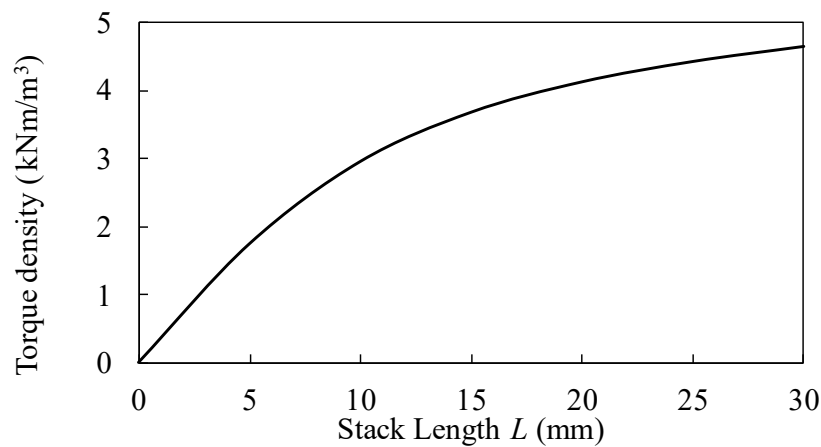


Fig. 4. 23. Relationship between stack length and torque density.

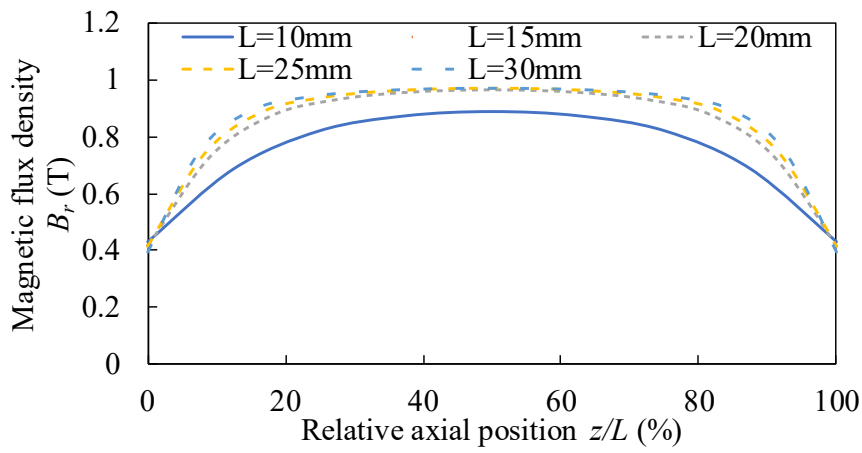


Fig. 4. 24. Relationship between axial position and magnetic flux density with varying stack length L in relative axial position z/L .

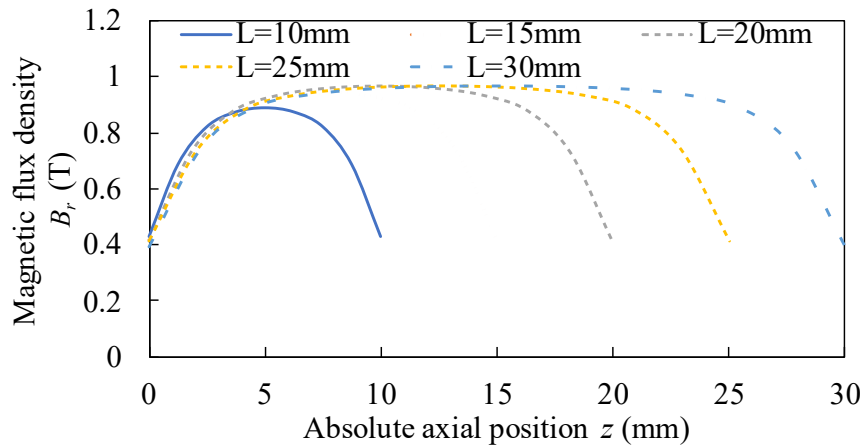
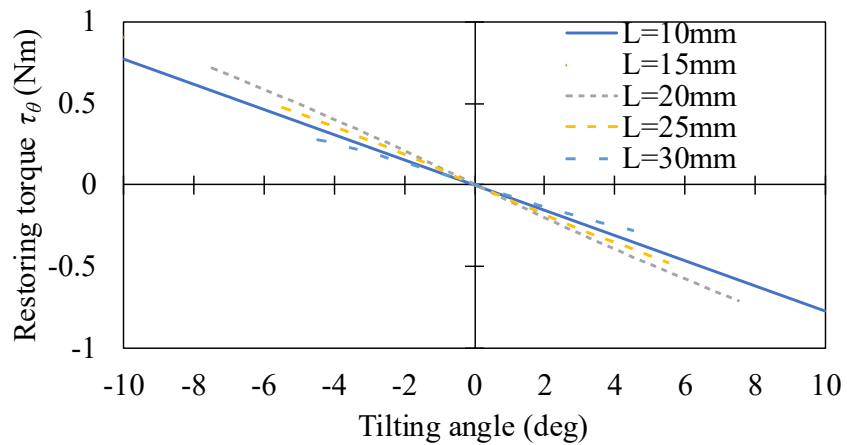


Fig. 4. 25. Relationship between axial position and magnetic flux density with varying stack length L in absolute axial position z .

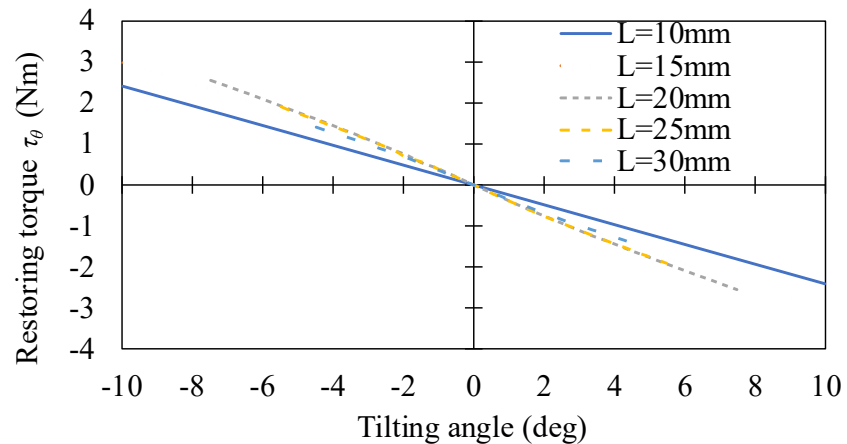
4. 6. 2 Relationship between Stack Length and Tilting Stiffness

The tilting stiffness of the proposed motor was also analyzed. Generally, in two-axis active control bearingless motors, the tilting rigidity increases as the flat disc-type rotor. This is because the ratio of variation in the area facing the rotor and air gap surface increases even for the same displacement, as mentioned in Section 3. 3. 3. Fig. 4. 26 shows the restoring torque τ_θ by tilting the high-speed rotor until it touches the low-speed rotor. Since the high-speed rotor in this analysis consists of two poles, the stiffness significantly changes depending on the angle between the direction of magnetization and the tilting axis. Therefore, the angle between the direction of magnetization and the tilt axis of 0 degree is shown in Fig. 4. 26(a), and the angle of 90 degree is shown in Fig. 4. 26(b). Since the rotational angle of both rotors does not affect the axial stiffness, the analysis with a different rotational angle of the rotor was not implemented.

The analysis results show that the highest tilt stiffness is observed around the stack length $L = 20$ mm. The tilt stiffness is adversely reduced because the magnetic flux density in the air gap decreases when the stack length becomes too thin.



(a)



(b)

Fig. 4. 26. Relationship between tilt angle and tilting restoring torque with varying stack length L .

(a) Tilt axis and magnetization direction are parallel (b) Tilt axis and magnetization direction are perpendicular

4. 6. 3 Relationship between Stack Length and Radial Force

To evaluate the performance of the bearingless motor, the force-displacement factor k_x , which is the relationship between radial displacement and unbalanced magnetic pull force, and the force-current factor k_i , which is the relationship between magnetic suspension current density and magnetic suspension force, were analyzed using a three-dimensional FEA.

Fig. 4. 27 shows the relationship between the force-displacement factor k_x and the stack length. Fig. 4. 28 shows the relationship between the force-current factor k_i and the stack length. As shown in Fig. 4. 22 and Fig. 4. 23, the force-displacement factor k_x increases with stack length due to the increase in the magnetic flux density between the air gaps as the stack length increases. Similarly, the force-current factor k_i shown in Fig. 4. 28 also increases with stack length. Additionally, the ripple of the force-displacement factor k_x is decreased with the thick stack length model, whereas the ripple of the force-current factor k_i is increased. However, the changing ratio of the force-current factor k_i is smaller than the force-displacement factor k_x . Therefore, the thick stack length is suitable in the radial magnetic suspension.

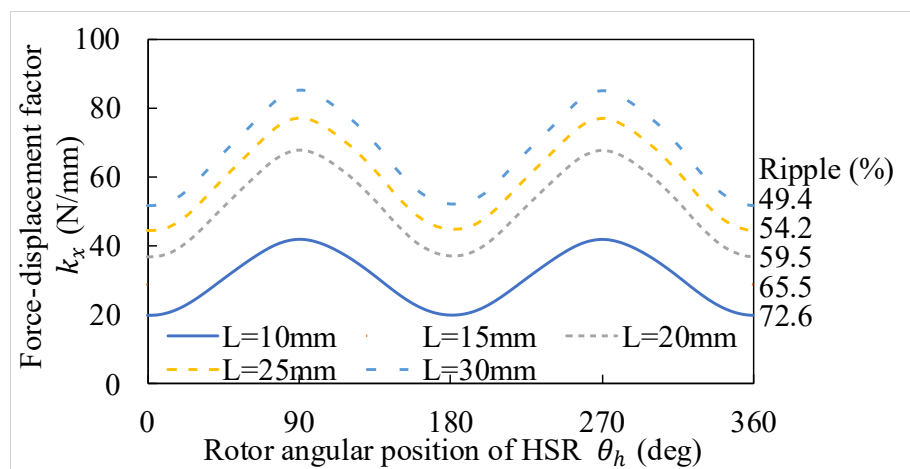


Fig. 4. 27. Relationship between the force-displacement factor k_x and the stack length.

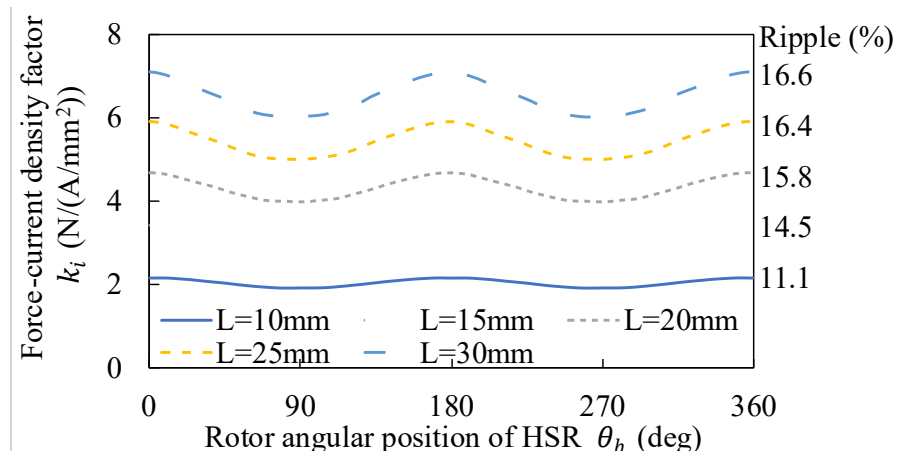


Fig. 4. 28. relationship between the force-current factor k_i and the stack length.

Now, if the effect of leakage flux is ignored, the radial force factor per stack length should be constant. This means that the radial force-displacement factor k_x and radial force-current density factor k_i per stack length are effective for visualizing the effect of leakage flux. Fig. 4.29 shows the radial force-displacement factor k_x per stack length for different stack lengths, and Fig. 4.30 shows the radial force-current density factor k_i per stack length for different stack lengths. The radial force-current density factor k_i per stack length shows that the radial force-current density factor k_i increases as the ratio of leakage flux decreases. Meanwhile, the radial force-displacement factor k_x per stack length shows that the radial force-displacement factor k_x decreases as the stack length increases. Therefore, the radial force-displacement factor k_x also increases as the leakage flux increases. This is because in models with large leakage flux, the amount of leakage flux decreases significantly when the high-speed rotor is radially displaced and the air gap decreases.

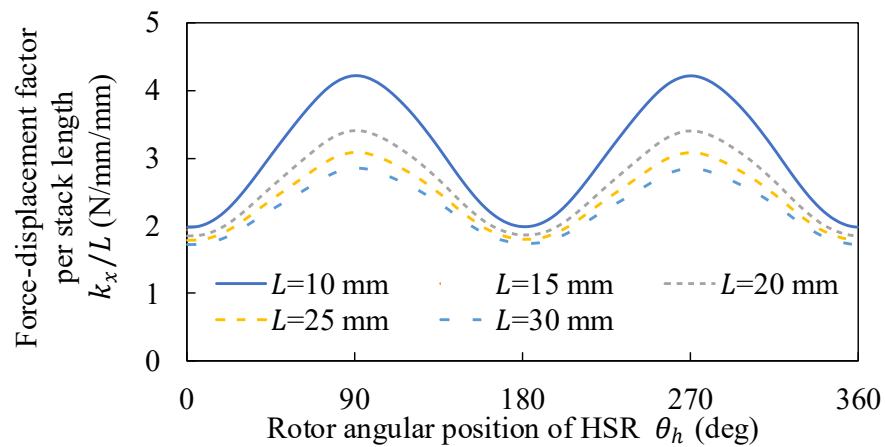


Fig. 4. 29. Radial force-displacement factor k_x per stack length for different stack lengths.

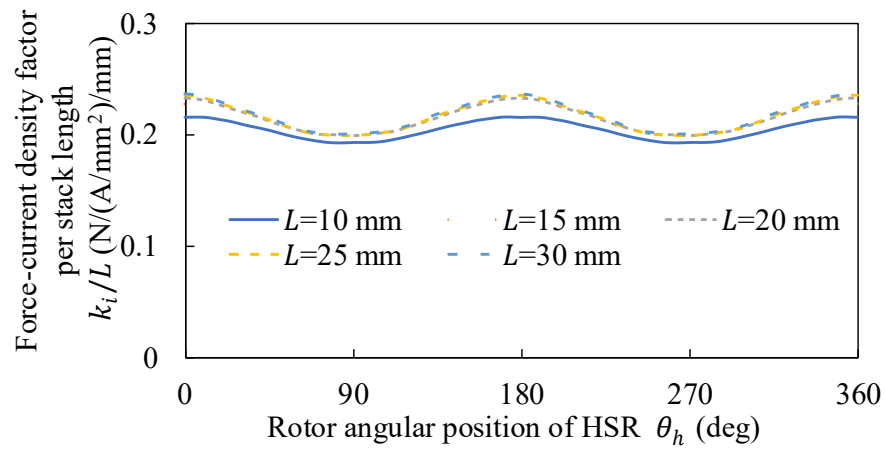


Fig. 4. 30. Radial force-current density factor k_i per stack length for different stack lengths.

Fig. 4.31 shows the current density required for magnetic suspension start-up with different stack lengths. As in the prototype in Chapter 5, the maximum displacement x_{max} of the high-speed rotor was assumed to be 0.5 mm, and the current density J_{start} required for magnetic suspension start-up from the unbalanced magnetic pull was calculated using $J_{start} = k_x x_{max} / k_i$. According to this, the required current density at stack length $L = 30$ mm is about 30% lower than that at $L = 10$ mm. Therefore, the required performance of the windings and inverter is reduced, and a cost reduction effect can be expected for the inverter.

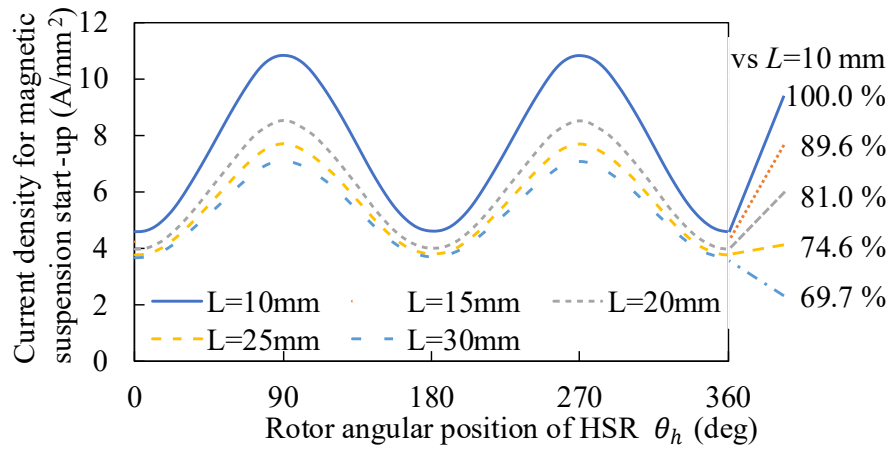


Fig. 4.31. Current density required for magnetic suspension start-up with different stack lengths.

4.7. Summary of Chapter 4

In this chapter, the structure of a magnetic-geared motor with a magnetic-suspended high-speed rotor is proposed, and a structure that enables reduction of bearing loss is shown. In addition, the radial force and torque of the proposed structure are analyzed by a three-dimensional finite element method. The analysis shows the magnetic suspension characteristics and torque characteristics of the reluctance-type magnetic-geared motor proposed in this chapter.

The analysis results in this chapter were applied to the prototype in Chapter 5, except for Section 4.6, which could not be applied due to time constraints during the research period. However, the results in Section 4.6 are different from the characteristics of bearingless motors that have been generally described. This is because the magnetic-geared motor topology adopted in this study has more air gaps between the winding and the magnetic suspension rotor than conventional bearingless motors, and the magnetic resistance of the low-speed rotor is also large, resulting in significant leakage flux. Accordingly, in the future, experimental results are expected for a model with improved torque density by extending the stack length relative to the rotor outer diameter based on the results in Section 4.6. However, in the prototype in Chapter 5, it is difficult to further increase the stack length due to machining problems with the low-speed rotor holder. Conversely, shortening the outer diameter of the high-speed rotor would make the pole pieces per pole of the low-speed rotor too small, making machining difficult. Furthermore, it is difficult to shorten the air gap length any further due to machining limitations. For these reasons, increasing the stack length relative to the rotor outer diameter may result in a decrease in performance due to a decrease in the gear ratio and permeability. Therefore, in order to reflect the results of Section 4.6, a fundamental design change is necessary, taking machining into consideration. This is expected to be very difficult.

Additionally, Section 4.5 demonstrated that the influence of motor current on performance other than torque generation is significantly small. However, since the d -axis current is expected to slightly change the tilt stiffness, there is a possibility of slightly improving the maximum speed shown in Section 5.4.

Chapter 5. Experimental Verification of High-Speed Rotor Magnetic Suspension for Reluctance-Type Magnetic-Geared Motors

In this chapter, the prototype motor proposed in Chapter 4 is manufactured, and magnetic suspension and rotation tests are conducted. This prototype is the world's first demonstration of magnetic suspension for a magnetic-gear motor with a high-speed rotor.

5. 1. Experimental Setup

5. 1. 1 Specifications

A prototype motor was fabricated to evaluate the analysis results. The prototype machine consists of a stator with an outer diameter of 140 mm. Table 5. 1 shows parameters of the prototype machine. The all values shown in Table 5. 1 are calculated from analysis results and CAD model. Fig. 5. 1 shows the CAD model of the prototype. Fig. 5. 2 shows the manufactured experimental setup. The motor and suspension windings are separated and are each supplied from two different three-phase inverters. The high-speed rotor PMs are made of N48 material, and the outside is covered with 1 mm thick carbon fiber reinforced plastic. The stator and the low-speed rotor core are made of laminated silicon steel 20HTH1200^a. Meanwhile, the high-speed rotor core is made of S45C material because the iron loss is negligible due to the magnetic flux at the high-speed rotor core generated by the permanent magnet is dominant. The frame and low-speed rotor holder, which are not part of the magnetic circuit, are made of non-magnetic SUS304 stainless steel and MC901 nylon plastic, respectively. In

^a Since magnetic modulation is used in this prototype, laminated silicon steel with high permeability and low iron loss is desirable.

Thinner 10 materials or amorphous materials would be preferable, but 20HTH1200 was selected due to research budget constraints.

addition, the touchdown target uses self-lubricating UNILATE^b (UNITIKA Ltd., Japan) plastic. To prevent rust on the iron core and frame, aluminum^c is contacted with the stator.

Table 5. 1. Parameters of the prototype machine

Parameter	Symbol	Unit	Value
Rotor mass	m	kg	0.23
Maximum torque of low-speed rotor	T_l	Nm	0.499
Maximum tilting stiffness	$k_{\theta max}$	N/rad	17.0
Minimum tilting stiffness	$k_{\theta min}$	N/rad	5.0
Motor power factor (at $N_l = 2,000 \text{ min}^{-1}$)	$\cos\theta_m$		96.2%
Coil resistance in ma- and mb- axis	R_{ma}	Ω	0.443
Coil inductance in ma- and mb- axis	L_{ma}	mH	0.980
Coil resistance in sa- and sb- axis	R_{sa}	Ω	0.622
Coil inductance in sa- and sb- axis	L_{sa}	mH	1.059

^b <https://www.unitika.co.jp/plastics/e/products/unilate/>

^c Contact between dissimilar metals causes corrosion in metals with a high ionization tendency. In this prototype, the frame that contacts the stator core is made of stainless steel. As a result, the laminated silicon steel of the stator core, which has a higher ionization tendency, is prone to corrosion. To prevent corrosion, aluminum, which has an even higher ionization tendency, was contacted with the stator core.

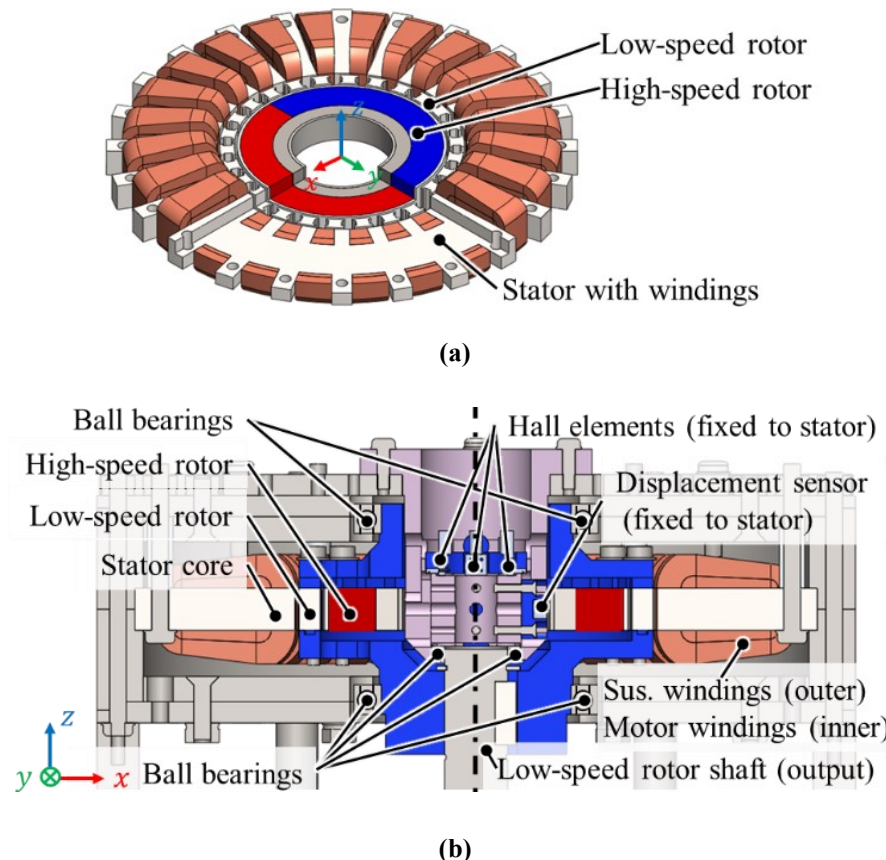


Fig. 5. 1. CAD model of the prototype.

(a) Isometric projection drawing. (b) Cross-sectional view.

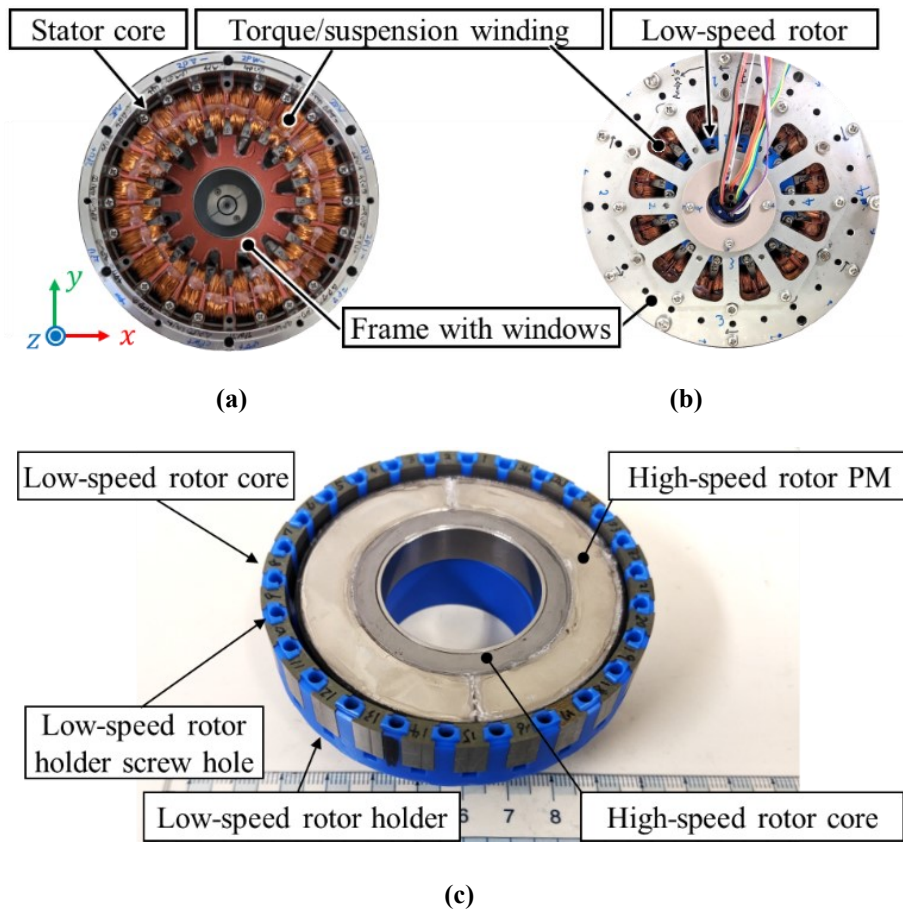


Fig. 5.2. Prototype of the proposed machine.

(a) Stator with winding and frame. (b) Assembled machine. (c) High-speed rotor and low-speed rotor.

5. 1. 2 Control Method

Fig. 5. 3 shows the radial position and current control system. The superscript (*) and the subscripts (m), and (s) denote the reference, motor, and suspension, respectively. The motor and suspension current references are generated from the feedback signals. In the magnetic suspension, eddy current displacement sensors (PU-03A, Applied Electronics Corp., Japan) are used to measure the rotor displacement. The errors of the radial rotor positions are calculated from the measured radial positions x and y and the position references x^* and y^* . The x - and y -axis current references i_{sx}^* and i_{sy}^* are generated from the errors of the radial positions by PID controller with a first-order low-pass filter in the derivative path. The voltage commands v_{sx}^* and v_{sy}^* are generated by nested PI controller. These voltage commands are transformed to the three-phase voltage references v_{su}^* , v_{sv}^* , and v_{sw}^* , and then impressed into the windings by the inverters to regulate the suspension currents. The motor speed regulation is also closed-loop-controlled by detecting the rotor rotational position. The reference rotational position θ^* is generated from the time integral of the reference rotational speed of the high-speed rotor ω^* .

This prototype uses MWINV-1R022 (Myway Plus Corp., Japan) for the motor inverter, MWINV-5R022 (Myway Plus Corp., Japan) for the magnetic suspension inverter, and PE-PRO/F28335A (Myway Plus Corp., Japan) for the controller.

The measured rotor angular position $\hat{\theta}$ is obtained by the four Hall elements (EQ-733L, Asahi Kasei Microdevices Corp., Japan). The rotor angular position is calculated by the inverse tangent of Hall elements signals in the x - and y -axis. Each signal is calculated by the summation of two Hall elements located on opposite sides of the same axis to compensate for the error caused by the rotor radial displacements. As shown in Section 4. 4, the change in magnetic flux density is generally linear. So, even if the high-speed rotor is tilted or radially displaced, the increase or decrease is generally the same for the two Hall elements on the same axis. Then, the total is not greatly affected. Also, if the high-speed rotor moves in the axial direction, the absolute values of all Hall element outputs increase or decrease, so the inverse tangent value does not change.

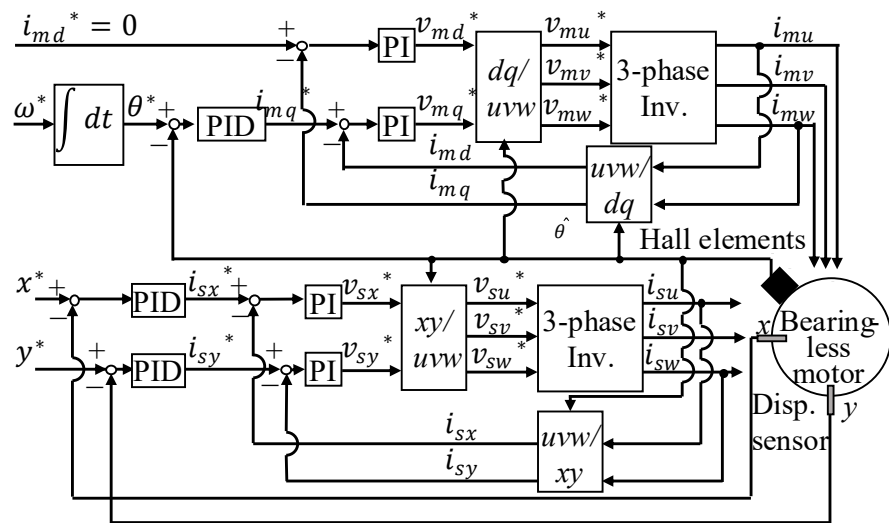


Fig. 5. 3. Control system for rotor radial position and motor current.

5. 1. 3 Windings

The analysis in Chapter 4 showed the suspension force required for magnetic suspension and the suspension force with respect to the current density^d. Meanwhile, the upper voltage limit for the experiment is equal to the lower of the inverter withstand voltage and half of the DC voltage input to the inverter^e. For this reason, a winding design that does not exceed the maximum voltage in the assumed operating range is required. In addition, since the feasible wire fill factor depends on the winding technique, adjustments are necessary in the actual machine. The relationship between the number of winding strands ^f and voltage in was calculated based on the resistance and inductance values calculated from the analysis results in Chapter 4.

Fig. 5. 4 shows the relationship between the high-speed rotor rotation speed and phase voltage with different numbers of two-pole motor winding strands. Fig. 5. 5 shows the relationship between the high-speed rotor rotation speed and apparent power and true power for the two-pole motor winding. In this case, the motor current density is the maximum current density of 2 A/mm^2 used in the analysis.

Fig. 5. 6 shows the relationship between the high-speed rotor rotation speed and phase voltage with different numbers of four-pole suspension winding strands. Fig. 5. 7 shows the relationship between the high-speed rotor rotation speed and apparent power and true power for the four-pole suspension winding. In this case, the magnetic suspension current density is also the maximum current density of 25 A/mm^2 used in the analysis.

^d Chapter 4 shows the relationship between the magnetic suspension current and the magnetic suspension force in the xy axis. Meanwhile, a current source was used in the analysis. For this reason, if the upper limit of the voltage is not considered, the magnetic suspension force is determined by the current density when the slot cross-sectional area is constant. Therefore, the magnetic suspension force does not depend on the number of turns if the current density is the same.

^e In the case of three-phase AC input, this is the voltage after rectification by the full-wave rectification circuit inside the inverter.

^f Here, “strand” means a method of winding multiple wires together. Assuming that the slot cross-sectional area is constant, in n strands, the number of turns is $1/n$ times that of a single wire, the cross-sectional area per turn is n times that of a single wire, the resistance is $1/n^2$ times that of a single wire, and the inductance is $1/n$ times that of a single wire.

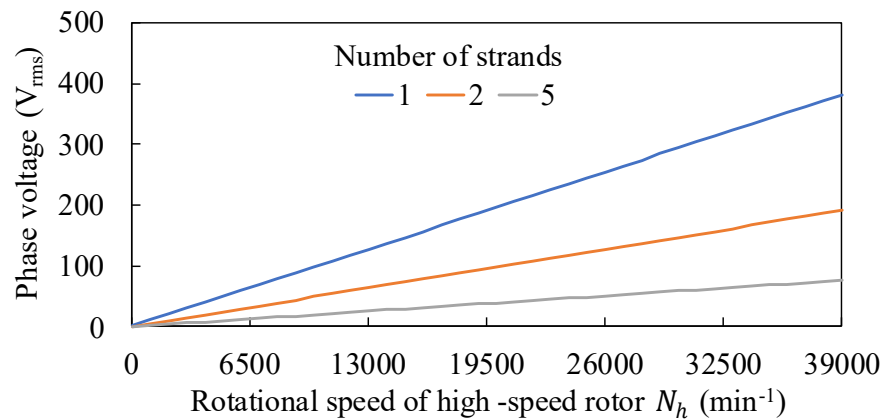


Fig. 5. 4. Relationship between the high-speed rotor rotation speed and phase voltage with different numbers of two-pole motor winding strands.

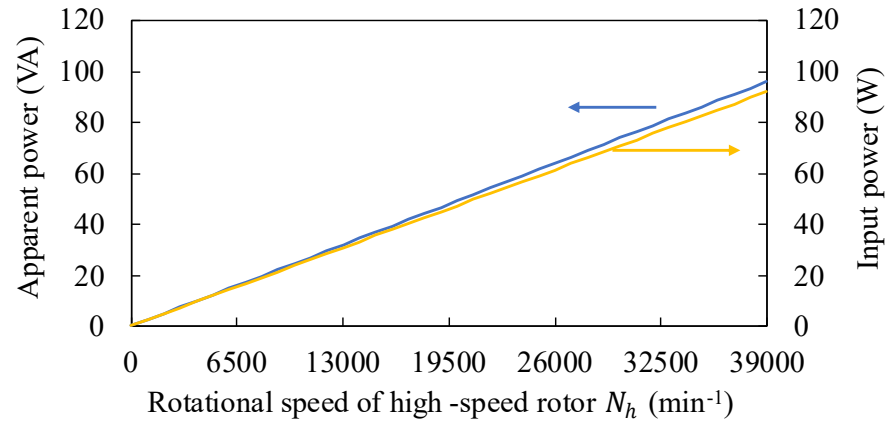


Fig. 5. 5. Relationship between the high-speed rotor rotation speed and apparent power and true power for the two-pole motor winding.

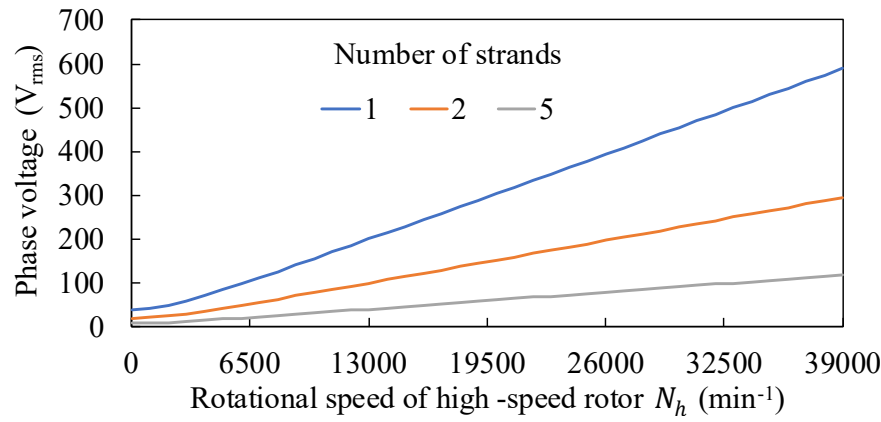


Fig. 5. 6. Relationship between the high-speed rotor rotation speed and phase voltage with different numbers of four-pole suspension winding strands.

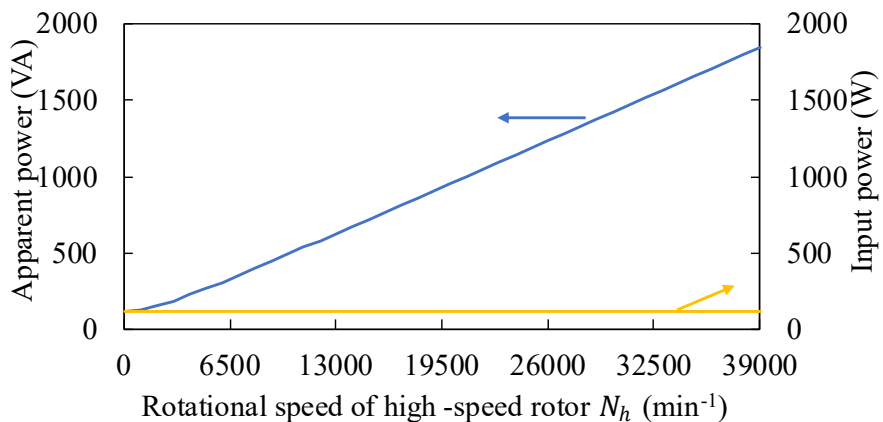


Fig. 5. 7. Relationship between the high-speed rotor rotation speed and apparent power and true power for the four-pole suspension winding.

Due to experimental environment and inverter constraints, the maximum supply voltage to the inverter is 200 V_{rms} three-phase AC from the commercial power supply. Since the DC

voltage V_{dc} from the line-to-line voltage V_l to the full-wave rectifier circuit is $V_{dc} = \frac{3\sqrt{2}}{\pi} V_l$,

the maximum output voltage from the inverter is 135 V instantaneous, 95.5 V_{rms}. Additionally, at the start of the experiment, the maximum rotational speed was initially assumed to be 39,000 min⁻¹ based on the high-speed rotor. Thus, as shown in Fig. 5. 4 and Fig. 5. 6, both windings can be set to five strands, within the maximum output voltage of the inverter. Therefore, five strands were selected for the windings.

Based on the analysis results, five strands of twelve windings were used for the two-pole motor windings, and five strands of twenty-seven windings were used for the four-pole magnetic suspension windings. Fig. 5. 8 shows a bobbin used for winding. The windings were wound onto these bobbins in advance. Pulling the bobbin after each winding makes the winding more dense and improves the fill factor. Fig. 5. 9 shows the stator after completing the two-pole motor winding, and Fig. 5. 10 shows the stator after completing the winding for one slot. However, the winding fill factor was lower than expected. As a result, the winding protruded beyond the stator gap surface, as shown in Fig. 5. 10. This indicates that the winding design is not feasible. Therefore, the winding design was changed to five bundles of twenty-one windings for the four-pole magnetic suspension winding. Table 5. 2 shows a comparison of the winding designs before and after the change. Since the design had some

margin, the necessary magnetic suspension performance can be satisfied even with a reduction in the number of windings.

Fig. 5. 11 shows the winding after the winding design was changed. Due to the winding design change, the winding is contained within the stator slot. Additionally, the prototype windings are toroidal windings. To facilitate connection changes after winding, each slot is isolated. The windings in each slot are connected to the external terminal block in the same configuration as shown in Fig. 4. 8. Furthermore, the winding lengths were adjusted to be the same for all slots.



Fig. 5. 8. Bobbin used for winding.

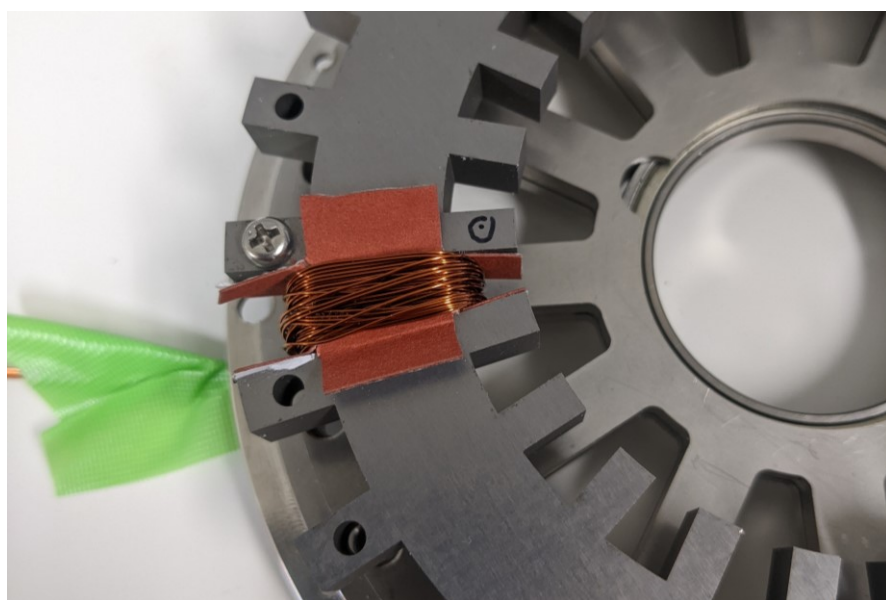


Fig. 5. 9. Stator after completing the two-pole motor winding.



Fig. 5. 10. stator after completing the winding for one slot.

Table 5. 2. Comparison of the winding designs before and after the change.

Parameter	Symbol	Unit	Old:	New:
			2p12turn/4p27turn	2p12turn/4p21turn
Slot cross-sectional area	S_{slot}	mm^2	65.95	65.95
Conductor cross-sectional area		mm^2	24.5	20.7
Slot fill factor		%	37.1	31.4
Wire (w/ wire insulator) cross-sectional area	①	mm^2	31.8	26.9
Insulator paper cross-sectional area	②	mm^2	12.56	12.56
Sum of ① and ②	$S_{winding}$	mm^2	44.4	39.5
$S_{winding}/S_{slot}$		%	67.3	60.0
Winding length per slot 2p/4p		m	1.5/3.0	1.5/2.4



Fig. 5. 11. Winding after the winding design was changed.

After completing the winding of the two-pole motor, a sinusoidal current was applied to each slot to measure the resistance and inductance of the slots. The sinusoidal current was generated by applying a 50 Hz sinusoidal voltage from a function generator to the input of a current-driven linear amplifier, producing a 50 Hz, 0.6 A sinusoidal current. The current and voltage of the winding were measured using an oscilloscope (DLM2024, Yokogawa Test & Measurement Corp., Japan). The amplitude and phase were calculated using the program shown in Appendix A a. Fig. 5. 12 shows the sample of the measurement results approximated by the program.

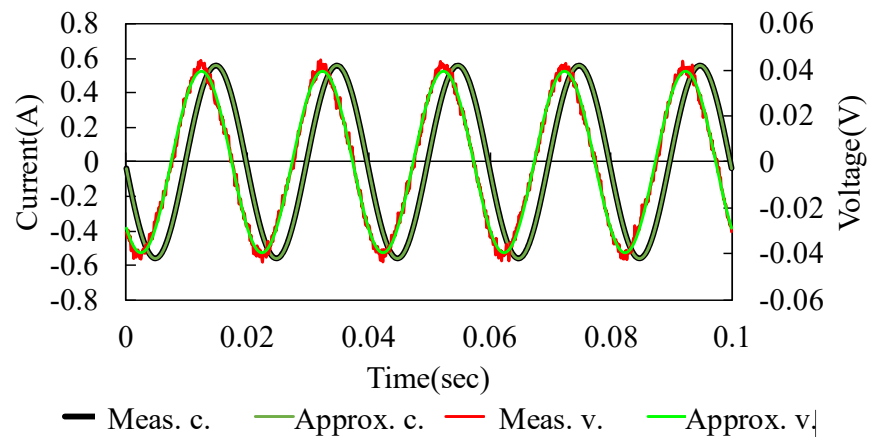


Fig. 5.12. Sample of the measurement results approximated by the program.

“Meas. c.”: measured current, “Approx. c.”: approximated current,

“Meas. v.”: measured voltage, “Approx. v.”: approximated voltage.

Fig. 5.13 shows the error in the magnitude of the impedance of each slot in a two-pole motor winding, and Fig. 5.14 shows the error in the impedance phase of each slot in a two-pole motor winding. In this case, the magnitude and the phase of the impedance are calculated from the phasor of the current and the voltage of the n th slot, $I_n \angle I_n$ and $V_n \angle V_n$, respectively. The impedance magnitude $|Z_n|$ is calculated as $|Z_n| = |V_n|/|I_n|$, the impedance magnitude error of the n th slot $Z_{n,err}$ is calculated as $Z_{n,err} = (|Z_n| - \sum|Z_n|)/\sum|Z_n|$, the impedance phase of the n th slot $\angle Z_n$ is calculated as $\angle Z_n = \angle V_n - \angle I_n$, and the impedance angle phase of the n th slot of the n th slot $\angle Z_{n,err}$ is calculated as $\angle Z_{n,err} = \angle Z_n - (\sum \angle Z_n)/24$.

Fig. 5.15 shows the resistance error for each slot in the two-pole motor winding, and Fig. 5.16 shows the self-inductance error for each slot in the two-pole motor winding. In this case, the resistance R_n for the n th slot is $R_n = \text{Re}\{Z_n\} = |Z_n|\cos(\angle Z_n)$, the inductance L_n for the n th slot is $L_n = \text{Im}\{Z_n\}/\omega = |Z_n|/\omega|\sin(\angle Z_n)|$, and the error is calculated in the same method as for the impedance magnitude error. According to Fig. 5.15, only slot No. 18 had an error of 20%. This was due to a conduction fault in the winding of slot No. 18, which was resolved by crimping new terminals. The average resistance value is 51.8 mΩ, and the average impedance value is 0.1518 mH.

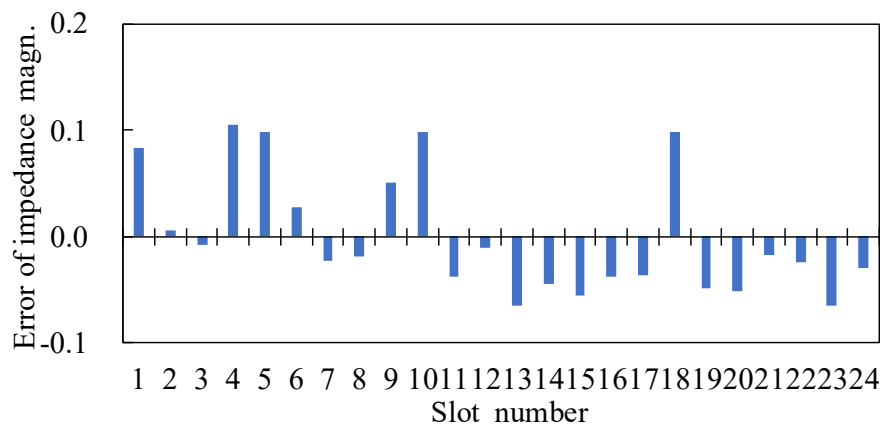


Fig. 5. 13. Error in the magnitude of the impedance of each slot in a two-pole motor winding.

“Error of impedance magn.”: “Error of impedance magnitude”

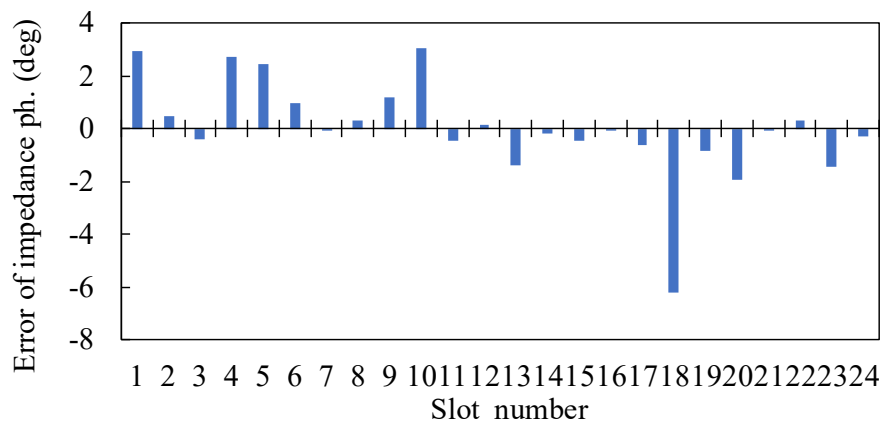


Fig. 5. 14. Error in the impedance phase of each slot in a two-pole motor winding.

“Error of impedance ph.”: “Error of impedance phase”

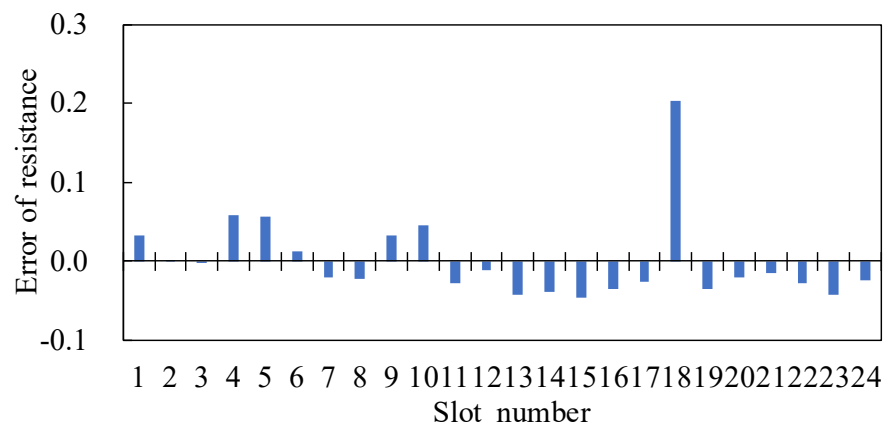


Fig. 5. 15. Resistance error for each slot in the two-pole motor winding.

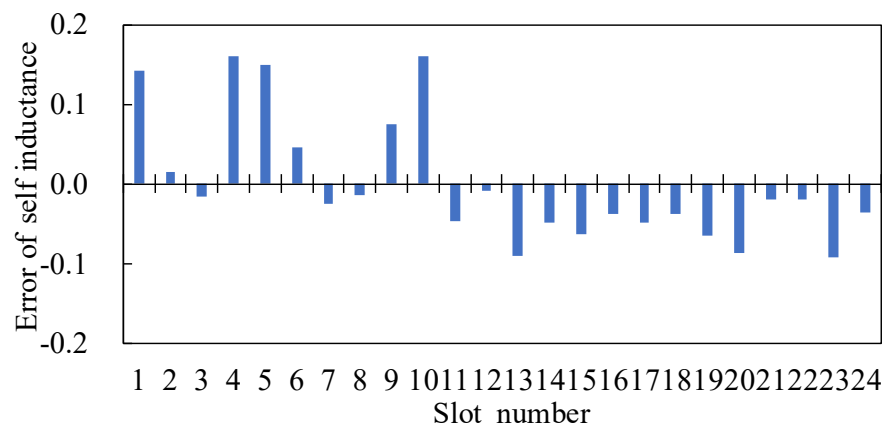


Fig. 5. 16. Self-inductance error for each slot in the two-pole motor winding.

According to Fig. 5.16, the error in self-inductance ranged from -9% to 16%. Since the self-inductance of a toroidal solenoid is proportional to the square of the number of turns, the self-inductance for ± 1 turn relative to the standard 12 turns is -15% to 19%. Thus, the experimental results shown in Fig. 5.16 may indicate an error in the number of turns. To resolve the issue, inductance was remeasured using induced voltage. Typically, the rotor is rotated externally, and the induced voltage in the windings is measured. However, since assembly was incomplete at this stage, this method could not be used. Instead, voltage was applied to one slot, and the induced voltage in the other slots was measured to calculate mutual inductance and evaluate the error. Fig. 5.17 shows the mutual inductance error for each slot in the two-pole motor winding. In Fig. 5.17 (a), a 1 kHz voltage was applied to slot 1. In Fig. 5.17 (b), a 1 kHz voltage was applied to slot 13. As a result, the error was found to be -2% to 4%, indicating that the number of turns is correct.

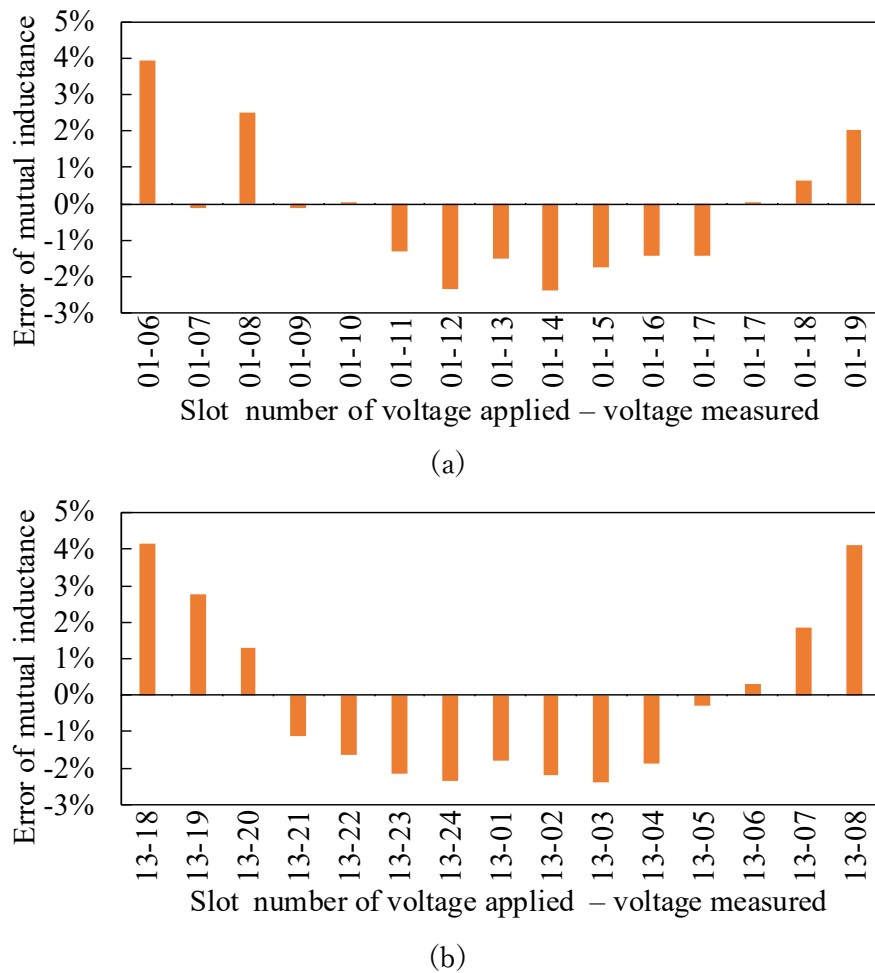


Fig. 5.17. Mutual inductance error for each slot in the two-pole motor winding.

(a) voltage was applied to slot 1 (b) voltage was applied to slot 13

In addition, to investigate the winding continuity failure observed in Fig. 5.15, the resistance values of each slot were remeasured using a DC stabilized power supply. Fig. 5.18 shows the DC resistance errors of each slot in the two-pole motor winding, and Fig. 5.19 shows the DC resistance errors of each slot in the four-pole magnetic suspension winding. The errors were found to be very small compared to Fig. 5.15, indicating that there were no winding continuity issues. However, the winding resistance was approximately $10 \text{ m}\Omega$ higher than the calculated value, which is attributed to the terminal resistance of the crimp terminals or the terminal resistance itself.

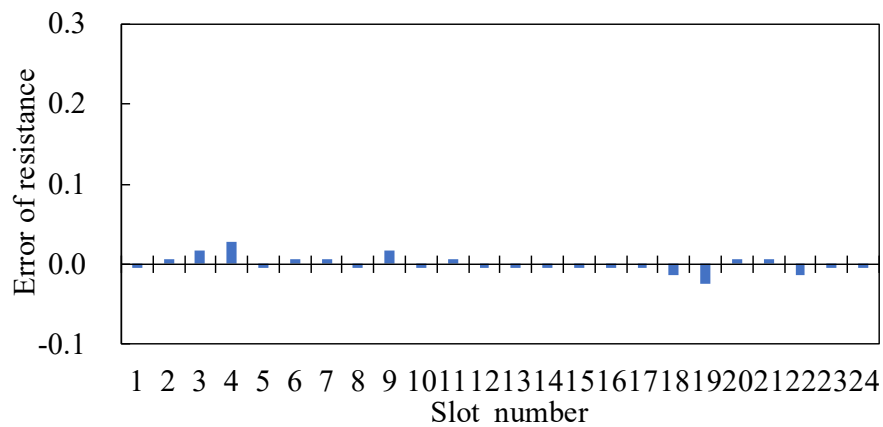


Fig. 5.18. DC resistance errors of each slot in the two-pole motor winding.

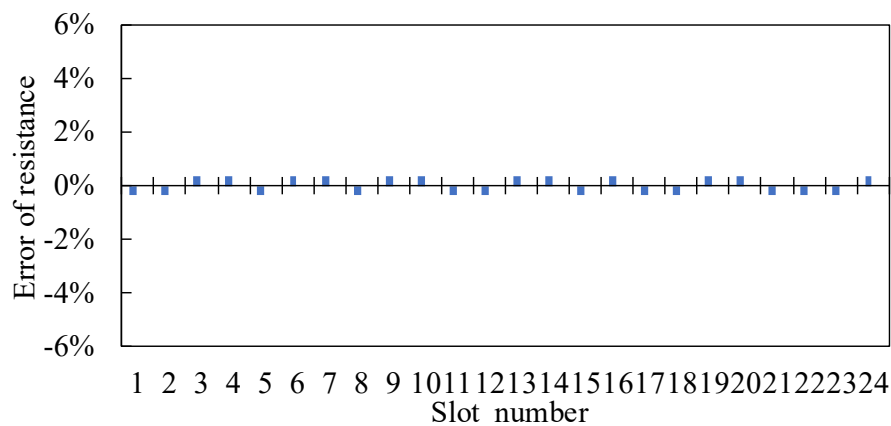


Fig. 5.19. DC resistance errors of each slot in the four-pole magnetic suspension winding.

After confirming these points, the stator was pressed into the frame, and the prototype was assembled. Fig. 5.20 shows the stator after being pressed into the frame. After assembly, the windings were short-circuited with the frame. This short-circuit was caused by two types of short-circuits. Fig. 5.21 shows the windings where the short-circuits occurred. For the short circuit between the winding lead-out section and the frame shown in Fig. 5.21 (a), the following countermeasures were implemented: insulating paper was applied to the frame sections that could come into contact with the winding lead-out section, and the corners were protected with hot-melt adhesive. Fig. 5.22 shows the short circuit countermeasures implemented. Additionally, the short circuit between the internal winding and the stator shown in Fig. 5.21 (b) occurred due to insufficient length of the insulating paper, resulting in a short circuit at the stator corners. This was addressed by extending the insulating paper. Fig. 5.23 shows the short circuit at the stator corners caused by insufficient length of the insulating paper.

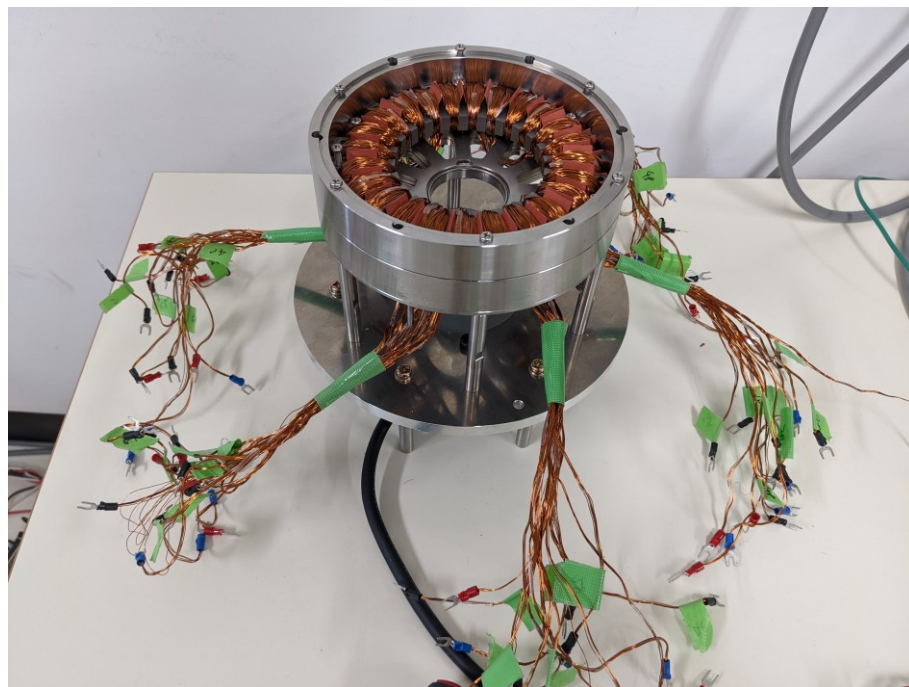


Fig. 5. 20. Stator after being pressed into the frame.

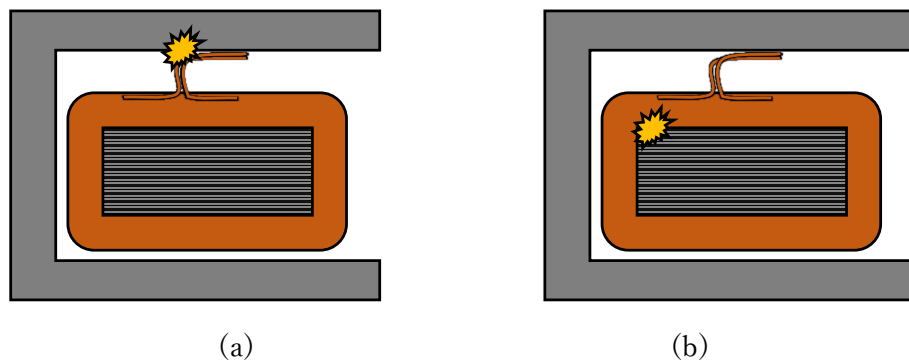


Fig. 5. 21. Windings where the short-circuits occurred.

(a) short circuit between the winding lead-out section and the frame

(b) short circuit at the stator corners

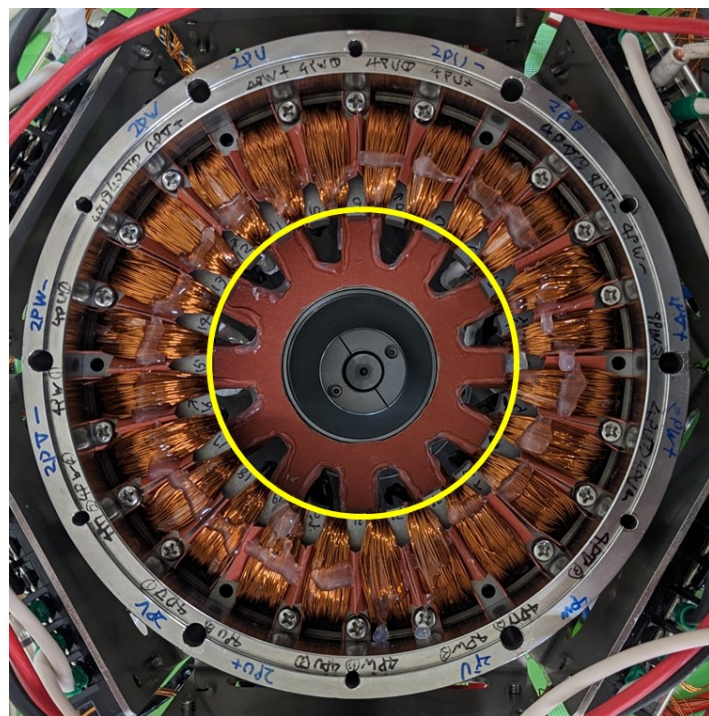


Fig. 5. 22. Short circuit countermeasures implemented.

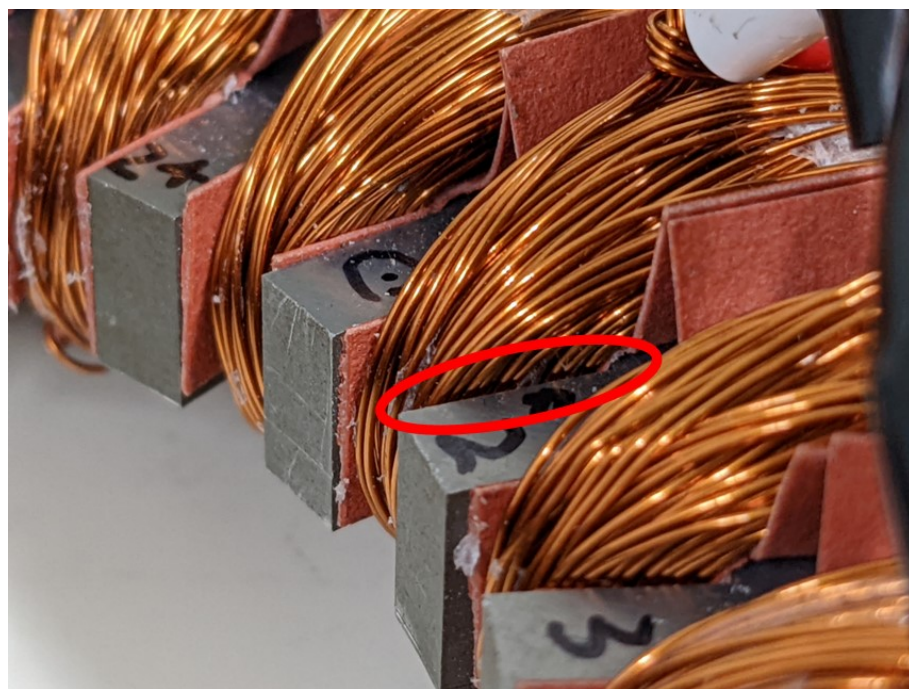


Fig. 5. 23. Short circuit at the stator corners caused by insufficient length of the insulating paper.

After implementing these countermeasures, assembly, including winding, was completed. Then, the low-speed rotor was rotated using an external motor, and the induced voltage was measured. Fig. 5. 24 shows the comparison of the induced voltage analysis results and the experimental results. Compared to the analysis results, the experiment generated an induced voltage of 90% or more, confirming that the winding was as designed.

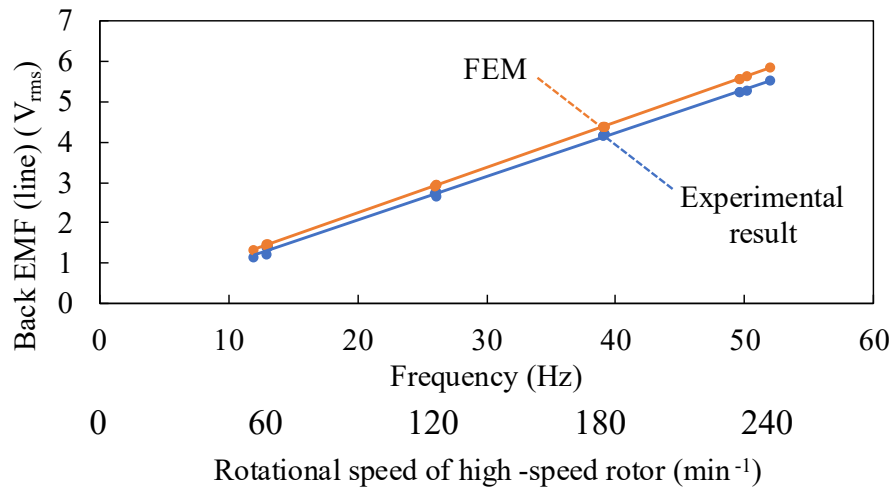


Fig. 5. 24. Comparison of the induced voltage analysis results and the experimental results.

EMF: electromotive force.

5. 1. 4 Angle Detection

As described in Section 3. 3. 1, accurate angle detection is essential for SPM-type bearingless motors. In conventional bearingless motors, the angle calculated from the Hall element is compared with the angle calculated from the rotary encoder connected to the magnetic suspension rotor through the shaft, and the angle calculated from the Hall element is calibrated. Meanwhile, in the prototype in this research, the magnetic suspended high-speed rotor cannot directly transmit power to the outside. Thus, the prototype in this research was designed to enable two modes, magnetic suspension mode and calibration bearing support mode, to be performed on the same prototype by reassembling the high-speed rotor. In the calibration bearing support mode, the high-speed rotor shaft and high-speed rotor support bearing can be assembled at the location where the distance sensor is normally located. Additionally, the Hall element is installed at the same location in both modes. This enables the calculation of calibration values from the calculated values in both modes. Fig. 5. 25 shows the experimental setup for the calibration bearing support mode.

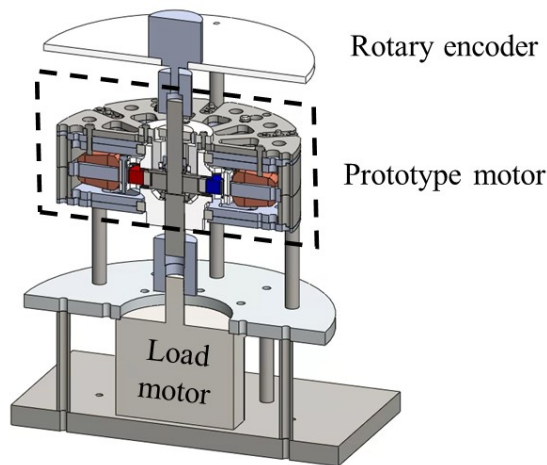


Fig. 5. 25. Experimental setup for the calibration bearing support mode.

Fig. 5. 26 shows the angle detection error of the hall element obtained by analysis. As shown in Fig. 5.1, the Hall element position shown in Section 4. 4 is located far from the high-speed rotor. Consequently, the angle detection value of the Hall element calculated from the magnetic flux value obtained by analysis also has a slight error.

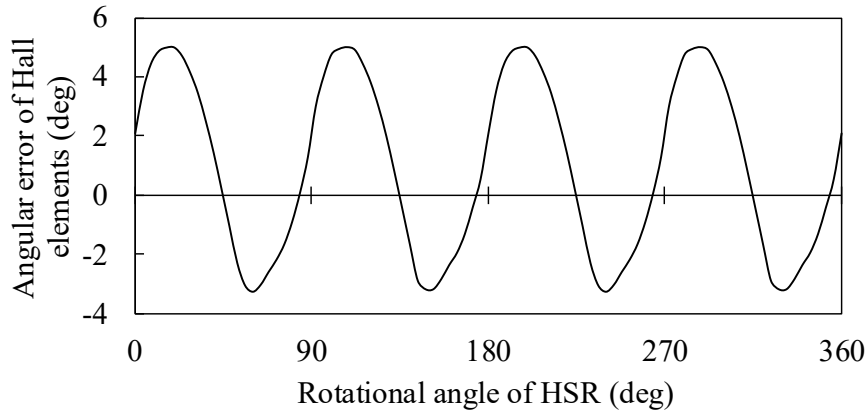


Fig. 5. 26. Angle detection error of the Hall element obtained by analysis.

Fig. 5. 27 shows a comparison between the angle detection values of the hall element and the rotary encoder in the experiment. Compared to the angle detection values from the rotary encoder, the angle detection values from the Hall element show slight fluctuations. Fig. 5. 28 shows the error between the angle detection values of the hall element and the rotary encoder in the experiment. According to these error values, the error has increased compared to Fig. 5. 26, and higher-order harmonics that were not observed in Fig. 5. 26 are detected. Fig. 5. 29 shows the Fourier transform results of Fig. 5. 28(b). From the Fourier transform results, the amplitude and phase for each order were obtained. In the experiment, a function was generated to cancel out the errors generated by the Hall element detection, and the values were compensated. However, to reduce the calculation cost, only the even components up to the first and eighth orders, which have a significant influence, were compensated. Furthermore, this method can only be used to make accurate compensations in the calibration bearing support mode. Therefore, the compensation values include assembly errors in the calibration bearing support mode, and errors caused by radial displacement in the magnetic suspension mode cannot be compensated.

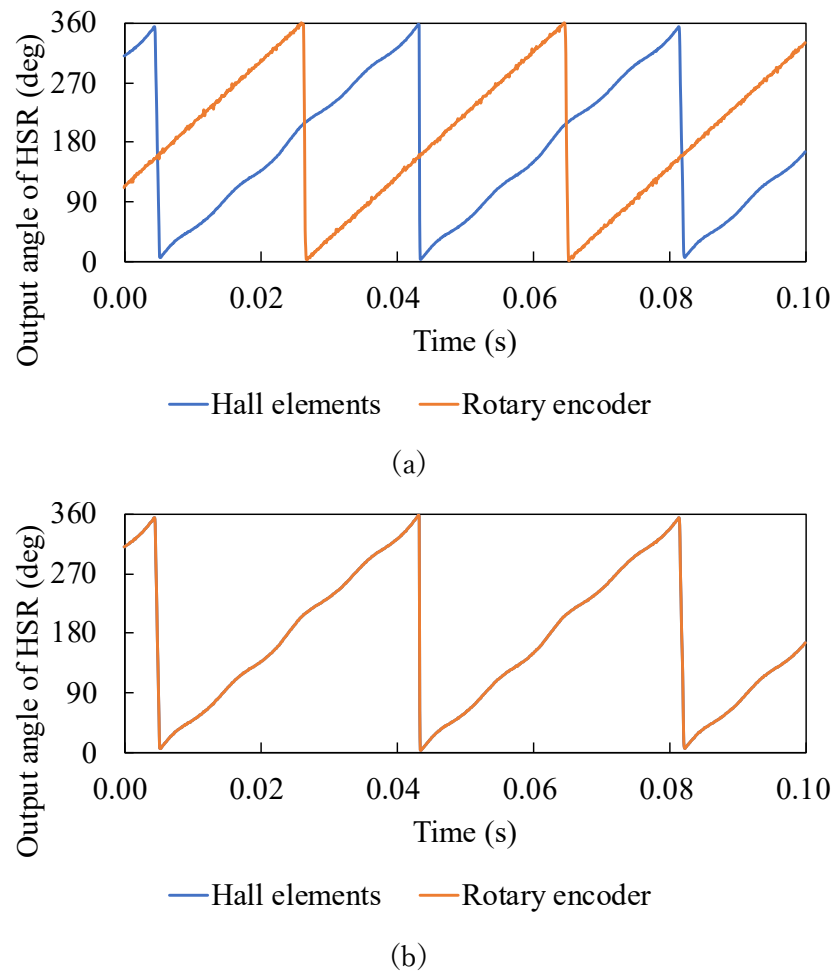


Fig. 5.27. Comparison between the angle detection values of the Hall element and the rotary encoder in the experiment.

- (a) Before initial phase adjustment of rotary encoder
- (b) After initial phase adjustment of rotary encoder

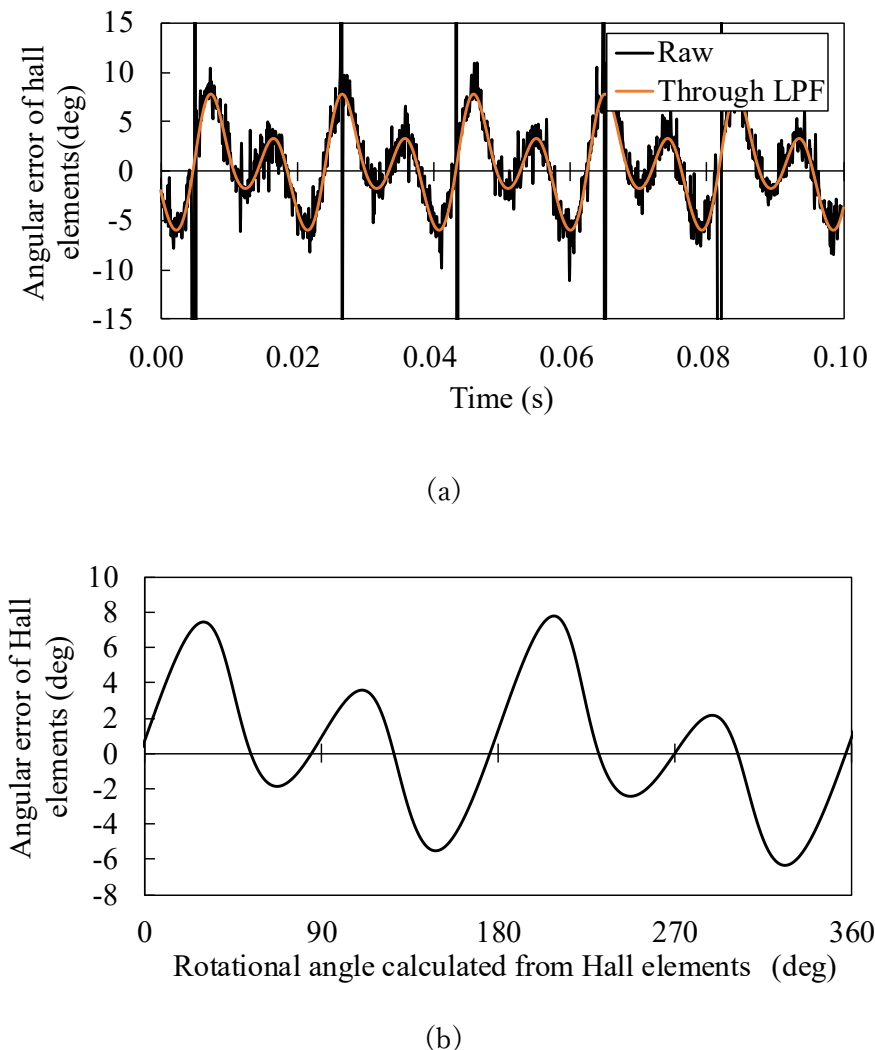


Fig. 5. 28. Error between the angle detection values of the Hall element and the rotary encoder in the experiment.

- (a) Comparison between with and without of low-pass filter
- (b) Rotational angle calculated from the Hall elements and the angular error calculated from the Hall elements

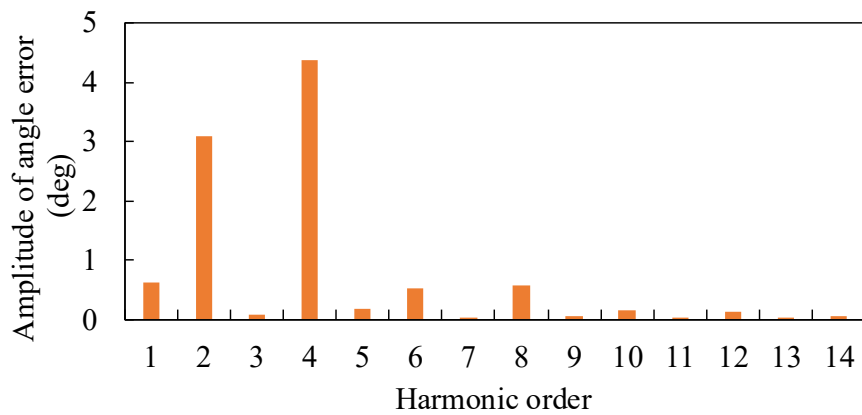


Fig. 5. 29. Fourier transform results of Fig. 5. 28(b).

5. 1. 5 Displacement Sensor

As shown in Section 5.1.2, the accuracy of the displacement sensor measurements is important for controlling the displacement of the high-speed rotor. However, the SUS304 material used as the sensor target in this experiment causes errors in the displacement sensor measurements. Fig. 5.30 shows the displacement of the displacement sensor target and the output voltage. For this reason, it is necessary to correct the output values of the displacement sensor, especially in the region where the displacement is greater than 0.7 mm, to reduce the error. The compensation function is shown as follows

$$d_{fix} = \alpha V_{out} + \beta \{\exp(\gamma V_{out} - 1)\} \quad (5.2)$$

where, d_{fix} is the compensated displacement, V_{out} is the output voltage of the displacement sensor, and α , β , and γ are any real numbers. Since the slope in the linear range is 0.2 for α , α was accepted and β and γ were adjusted.

Fig. 5.31 shows the results of displacement sensor output compensation. The values without compensation are when $\beta = \gamma = 0$. With compensation, it can be seen that the linearity is significantly improved. Note that $\beta = 3.293 \times 10^{-5}$ and $\gamma = 1.8234$ were used for the displacement sensor for the x -axis, and $\beta = 1.211 \times 10^{-5}$ and $\gamma = 1.959$ were used for the displacement sensor for the y -axis.

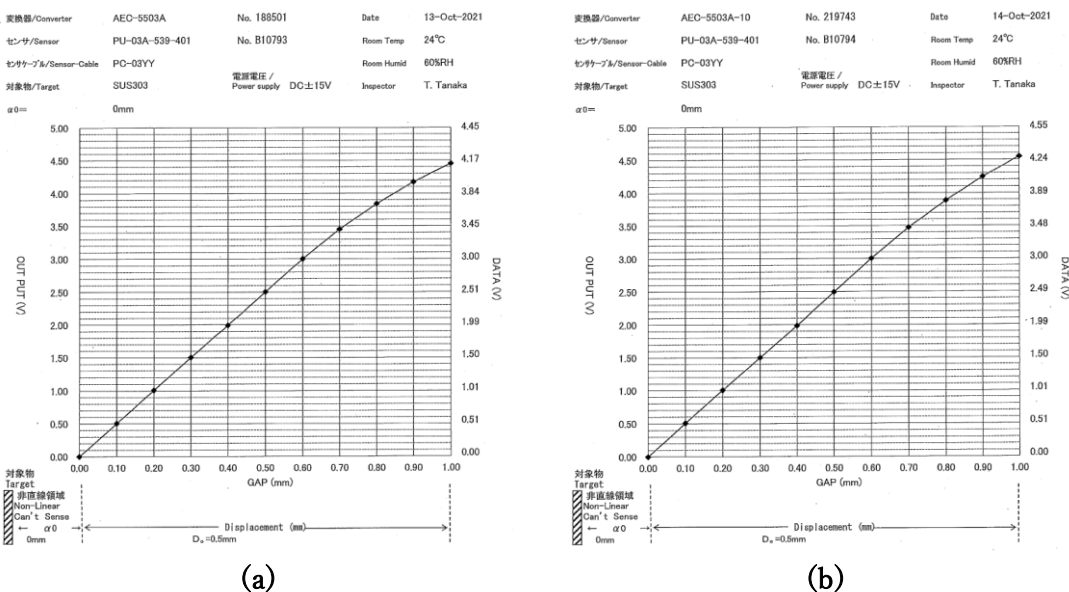


Fig. 5.30. Displacement of the displacement sensor target and the output voltage.

(a) x -axis sensor (b) y -axis sensor

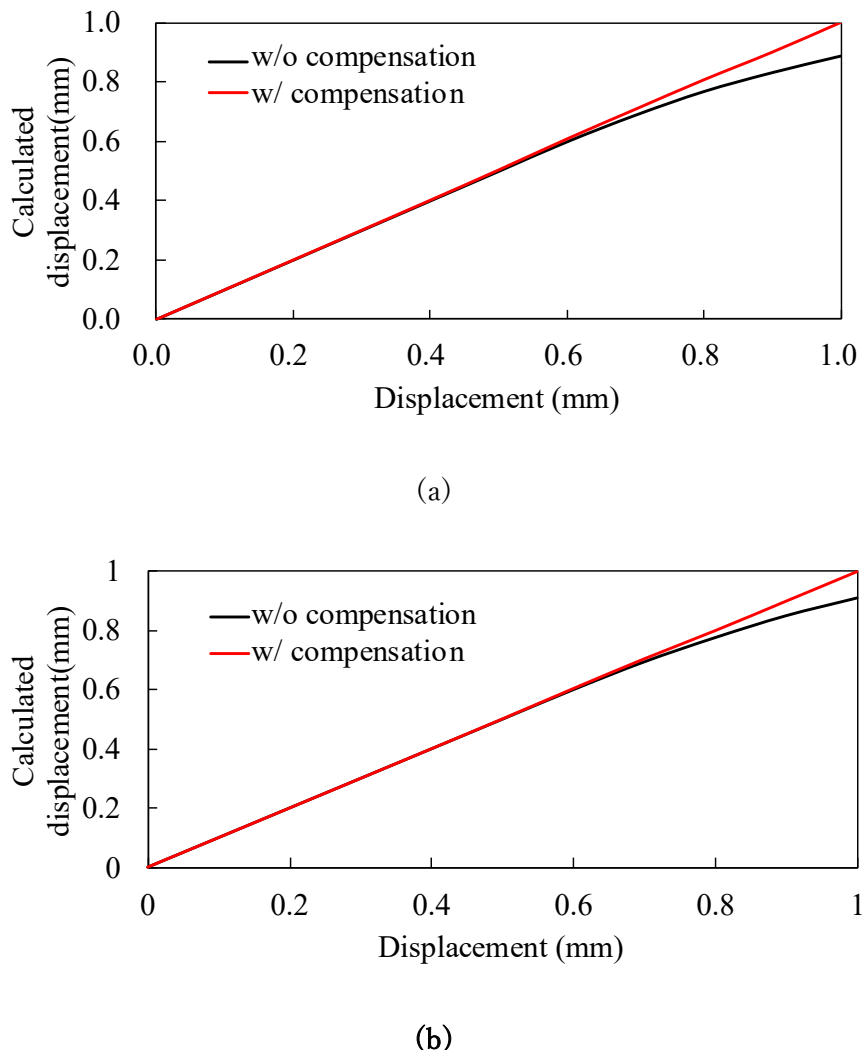


Fig. 5.31. Results of displacement sensor output compensation.

(a) x-axis sensor (b) y-axis sensor

Due to budgetary constraints, only two displacement sensors were installed in this prototype. If four sensors were installed, as with Hall elements, the center position could be easily calculated using a differential method. However, with only two sensors, as in this prototype, manual setting is required. Therefore, the center position of the displacement was measured by rotating the high-speed rotor using the motor current without magnetic suspension. From this result, the approximate center position was calculated.

Fig. 5.32 shows the displacement during rotation by the motor current without magnetic suspension. This experiment showed that the center position was approximately 0.62 mm. Therefore, this value was adopted as the command displacement in the initial experiment.

Fig. 5. 33 shows the displacement trace with rotation by the motor winding without magnetic suspension. Using the center position calculated in Fig. 5. 32, the displacement trace is symmetrical around the center. Therefore, it is shown that this setting is acceptable.

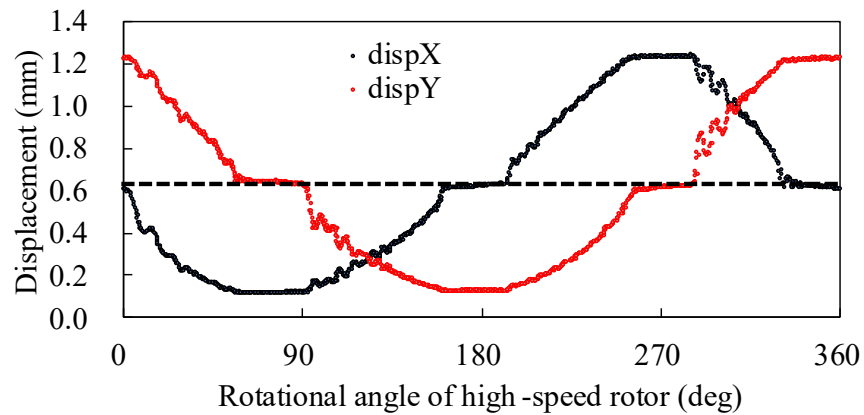


Fig. 5. 32. Displacement during rotation by the motor current without magnetic suspension.

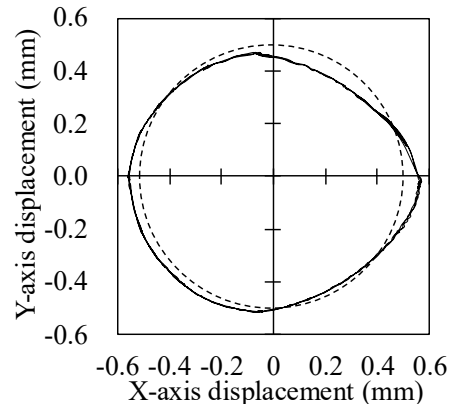


Fig. 5. 33. Displacement trace with rotation by the motor winding without magnetic suspension.

5. 2. Magnetic Suspension Start-up Test in Non-Rotating State

Unlike typical bearingless motors, this prototype has an additional low-speed rotor. In the analysis in Chapter 4, it was assumed that the low-speed rotor does not affect magnetic suspension, but this is uncertain in the prototype. Therefore, magnetic suspension start-up tests were conducted without the low-speed rotor, and then with the low-speed rotor. Before this experiment, it was confirmed that the suspension force was generated in the reference direction. In the experiments described in the following sections, the DC bus voltage of the inverter was adjusted to approximately 70 V.

5. 2. 1 Magnetic Suspension Start-up without Low-speed Rotor

In this prototype, the relationship between the magnetic suspension force and the magnetic suspension current is proportional. Let us assume the suspension current is assumed as i_{sx} . The magnetic suspension force F_{sx} is expressed as

$$F_{sx} = k_i i_{sx} \quad (5.3)$$

where k_i is defined as the suspension current-radial force factor.

Similarly, the relationship between the unbalanced magnetic pull force and the radial displacement is proportional. The unbalanced magnetic pull force in x -axis direction F_{ux} is expressed as

$$F_{ux} = k_x x \quad (5.4)$$

where k_x is defined as the radial displacement-unbalanced magnetic pull force factor.

Let us define the mass of the high-speed rotor m . Hence, from (5.3) and (5.4), the equations of motion in x -axis direction is expressed as

$$m \frac{d^2}{dt^2} x(t) = (F_{sx} + F_{ux}) = (k_i i_{sx}(t) + k_x x(t)). \quad (5.5)$$

Let us Laplace transform $x(t)$ and $i_{sx}(t)$ as $X(s)$ and $I_{sx}(s)$, respectively. Then, (5.5) is expressed as

$$ms^2 X(s) = (k_i I_{sx}(s) + k_x X(s)). \quad (5.6)$$

(5.6) can be expressed as

$$X(s) = \frac{k_i}{m} \frac{1}{(s-\sqrt{k_x/m})(s+\sqrt{k_x/m})} I_{sx}(s). \quad (5.7)$$

Therefore, the transfer function $G(s)$ can be expressed as

$$G(s) = \frac{k_i}{m} \frac{1}{(s-\sqrt{k_x/m})(s+\sqrt{k_x/m})}. \quad (5.8)$$

MATLAB includes a PID Tuner app^g, which can be used to easily determine PID gains when the transfer function is known. From previous analyses, the values $k_i = 1.27 \text{ N/A}_{xy}^*$, $m = 0.23 \text{ kg}$, and $k_x = 6.35 \times 10^3 \text{ N/m}$ were obtained for the condition without a low-speed rotor, so the transfer function is expressed as

$$G(s) = \frac{5.52}{(s-166)(s+166)}. \quad (5.9)$$

Inputting this transfer function into MATLAB's PID Tuner app yields a proportional (P) gain of 31647.5133, an integral (I) gain of 971377.4713, and a derivative (D) gain of 257.7693. Fig. 5.34 shows the amplitude response to time obtained in matlab using the transfer function without a low-speed . As a result of inputting this PID gain, magnetic suspension was achieved without a low-speed rotor.

^g <https://jp.mathworks.com/help/control/ref/pidtuner-app.html>

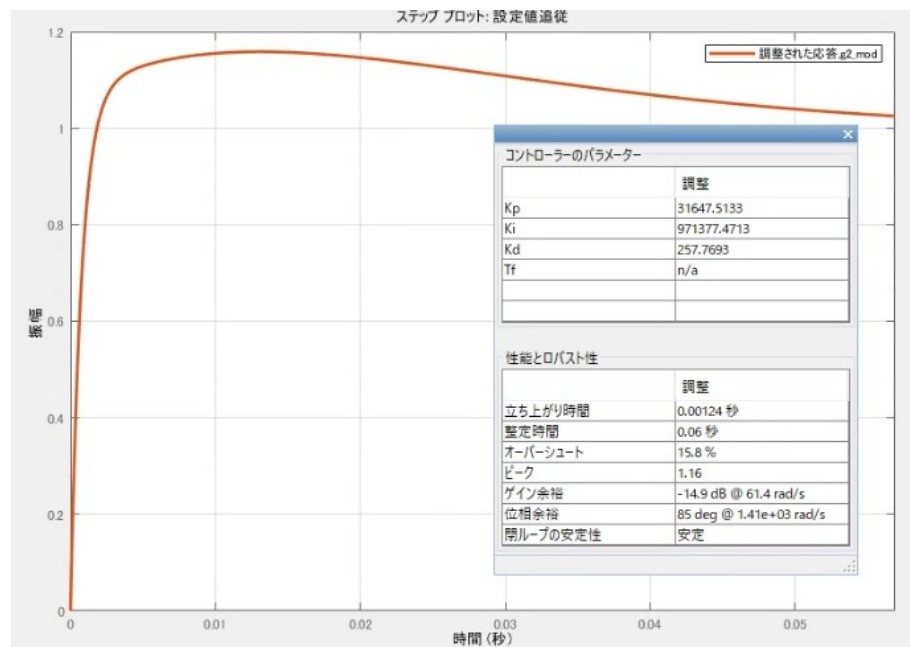


Fig. 5. 34. Amplitude response to time obtained in MATLAB using the transfer function without a low-speed rotor.

5. 2. 2 Magnetic Suspension Start-up with Low-speed Rotor

Determine the PID gains using the same method as in Section 5. 2. 1. Using $k_i = 1.70$ N/A_{xy*}, $m = 0.23$ kg, and $k_x = 34.6 \times 10^3$ N/m, the transfer function is expressed as follows

$$G(s) = \frac{7.39}{(s-387.6)(s+387.6)}. \quad (5.10)$$

Fig. 5. 35 shows the amplitude response to time obtained in matlab using the transfer function with a low-speed rotor. Proportional (P) gain = 139145, Integral (I) gain = 10770510, Derivative (D) gain = 449. The cutoff frequency of the derivative controller is 1000 Hz, the x -axis displacement reference value is 0.6746 mm, the y -axis displacement reference value is 0.617 mm, The maximum value for the integral controller was set to 30000.0 mm sec.

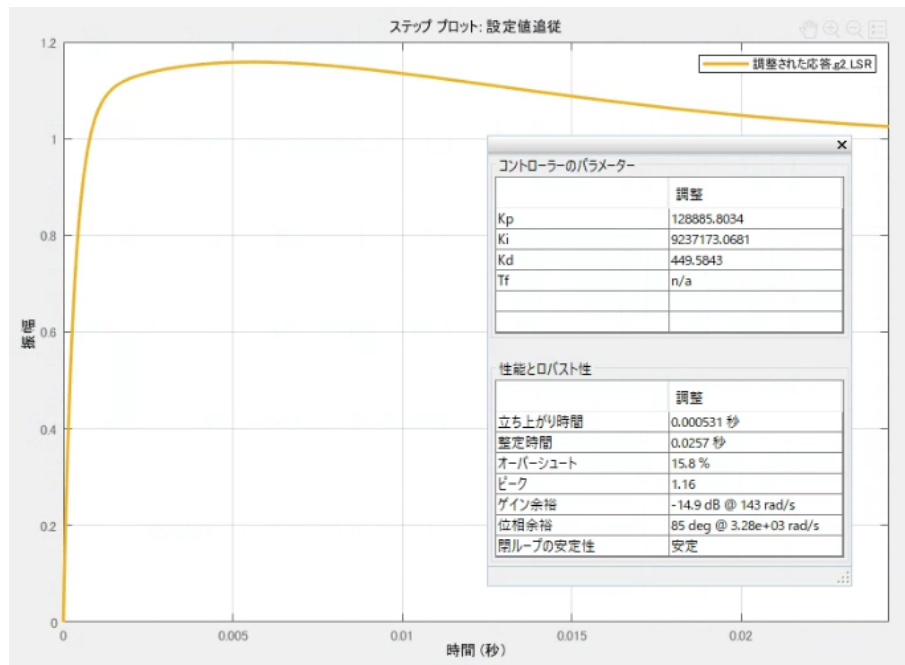


Fig. 5. 35. Amplitude response to time obtained in MATLAB using the transfer function with a low-speed rotor.

Fig. 5.36 shows radial rotor displacements and suspension currents i_{su} , i_{sv} , and i_{sw} during the magnetic suspension start-up. Radial displacement sensor outputs are measured by an oscilloscope (DLM2024, Yokogawa Test & Measurement Corp., Japan), as well as the suspension currents. The rotor radial position references x and y are set to the centered position. At the touchdown condition, the rotor position of x and y are -0.04 and -0.52 mm, respectively. These two positions are randomly chosen in the experiment, whereas the rotational angle of the high-speed rotor is set to 0° , where the rotor is aligned to the y -axis. At $t = 0$, magnetic suspension control is activated, and suspension currents are provided. The limit of suspension currents i_{sx} and i_{sy} are set to 14.9 A, that corresponds the current density of $14.9\text{A} = 20.5 \text{ A/mm}^2$. This current limit is applied for the short time only for the start-up current for 100 ms at the maximum based on the experimental result presented [100] [111]. As a result, the magnetic suspension start-up is successfully achieved with a maximum current of $i_{sv} = 18.8$ A. In Section 4.2.4, the start-up current was calculated by FEM as $i_{sx} = 15.0$ A in xy coordinates, which is $i_{sv} = 12.2$ A in uvw coordinates. Thus, the current measured in this experiment is 53.5% higher than the FEM result because of the transient condition.

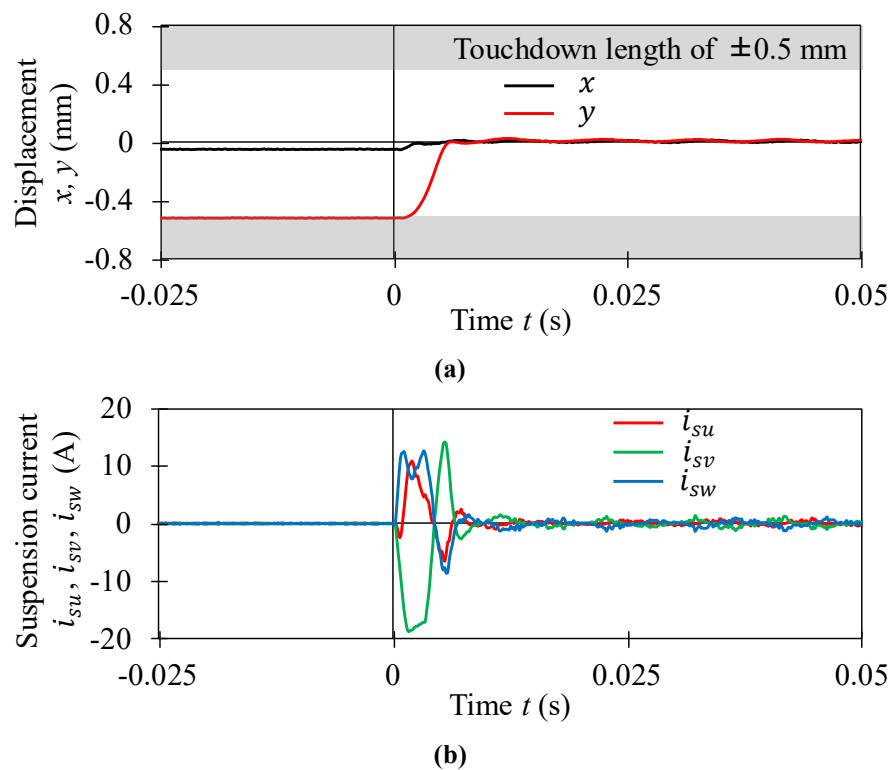


Fig. 5.36. Experimental result of the magnetic suspension start-up.
 (a) Radial displacements x and y . (b) Three-phase suspension currents.

5.3. Magnetic Suspension During Rotation

Fig. 5.37 shows the waveforms of radial displacements, suspension currents, and rotational speeds of each rotor while the high-speed rotor is magnetically suspended. The radial displacements and suspension currents are measured. The rotational speed of the high-speed rotor is calculated from the derivative of the measured rotor angular position $\hat{\theta}$. The rotational speed of the low-speed rotor is detected by a digital tachometer (HT-5500, Ono Sokki Co., Ltd., Japan). The rotational speeds of both rotors are monitored by an oscilloscope (DLM2024, Yokogawa Test & Measurement Corp., Japan). In this experiment, the reference speed of the high-speed rotor N_h^* is 1300 r/min, and the low-speed rotor stably rotates at the synchronized speed of 100 r/min.

As a result, the magnetic suspension and rotation are successfully achieved. The vibrations of suspension currents are small enough compared to the start-up currents. The radial vibration is also small enough compared to the touchdown length of ± 0.5 mm. Therefore, it is experimentally demonstrated that the suspension current is small when the rotor is centered.

However, in Fig. 5.37(b), a current amplitude of approximately 4 A was observed during magnetic suspension. This value is very large compared to [100] and [112]. Meanwhile, the high-speed rotor of the proposed motor is magnetically suspended and does not have a shaft for output to the outside. Thus, ideally, the only force applied to this rotor is gravity. Therefore, if magnetic suspension control is improved in the future, it may be possible to achieve magnetic suspension with even less power than that shown in Fig. 5.37(b).

In addition, Fig. 5.37(c) shows that the average speed of the high-speed rotor is 1296 r/min, while the low-speed rotor rotates at 104 r/min. Thus, the high-speed rotor in prototype machine rotates mostly 13 times faster than the low-speed rotor. The difference between theoretical and experimental values is caused by the error introduced by the measurement equipment^h. Accordingly, the gear ratio G_r is 13, as designed.

^h The HT-5500, which measured the rotation speed of a low-speed rotor, has a specification of 1 mV per 1 min^{-1} . Since this signal was measured with an oscilloscope, an error of several min^{-1} may occur.

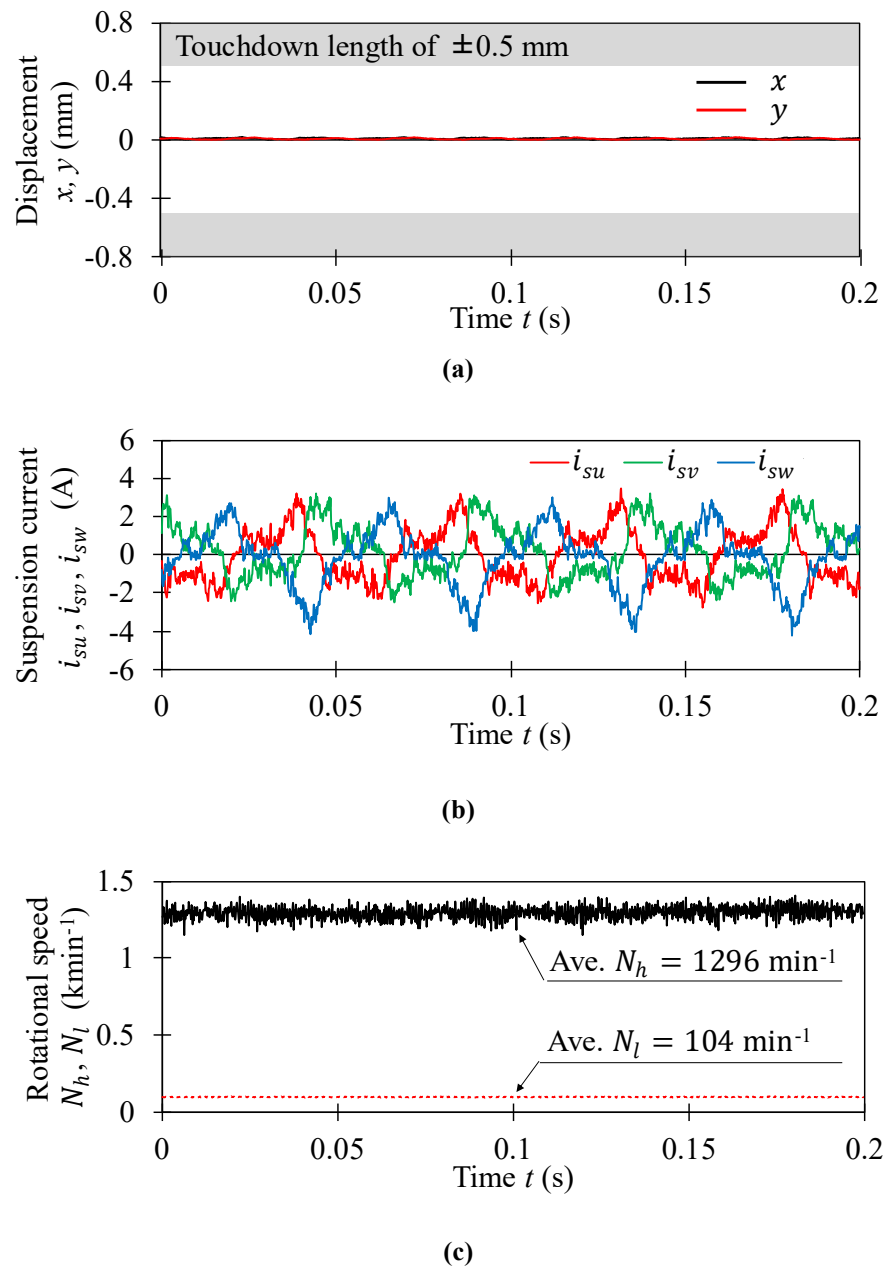


Fig. 5.37. Experimental results at the rotational speed reference of the high-speed rotor

$N_h^* = 1300$ r/min while the rotor is magnetically suspended.

(a) Radial displacements x and y . (b) Three-phase suspension currents. (c) Roational speed of each rotor.

Fig. 5.38 shows the high-speed rotor displacement orbit at $N_h^* = 7020$ r/min while the rotor is magnetically suspended. The high-speed rotor rotates within the mechanical air gap of 0.5 mm radius. Subsequently, the prototype achieves continuous rotation at $N_h^* = 7020$ r/min and 540 r/min at the low-speed rotor.

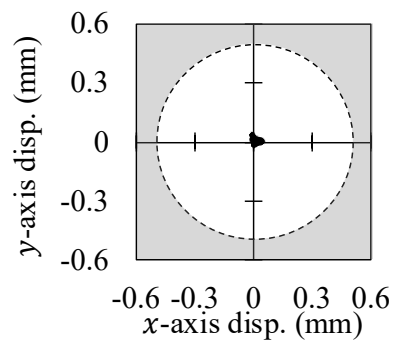


Fig. 5. 38. High-speed rotor displacement (disp.) orbit at the rotational speed reference of the high-speed rotor $N_h^* = 7020$ r/min while the rotor is magnetically suspended.

5. 4. Speed Test

To measure the behavior with changing rotational speed, the displacement changes at each rotational speed were measured. Note that in this experiment, the purpose was to measure steady-state values at each speed, so the speed command value of the high-speed rotor was increased from 780 min^{-1} by increments of 780 min^{-1} . Fig 5.39 shows the amplitude of displacement with changing rotational speed, and Fig. 5.40 shows the displacement traces with changing rotational speed. Note that the rotational speeds of Fig 5.39 were not measured values; the rotational speed of the high-speed rotor is the reference value, and the rotational speed of the low-speed rotor was estimated by (3.15) with the reference rotational speed of the high-speed rotor. Since the displacement in this experiment was measured using an oscilloscope, Fig. 5.40 includes measurement errors. As a result, there is a slight deviation from the center position, but in fact, the rotor is magnetically suspended at the center position. In this section, the vibration range was calculated using the 3σ value, which is six times the standard deviation, as the vibration rangeⁱ.

The results of this experiment showed that steady rotation was possible up to 7020 min^{-1} , but touchdown occurred at 7800 min^{-1} .

ⁱ When calculating the range using the maximum and minimum values, outliers caused by noise are included.

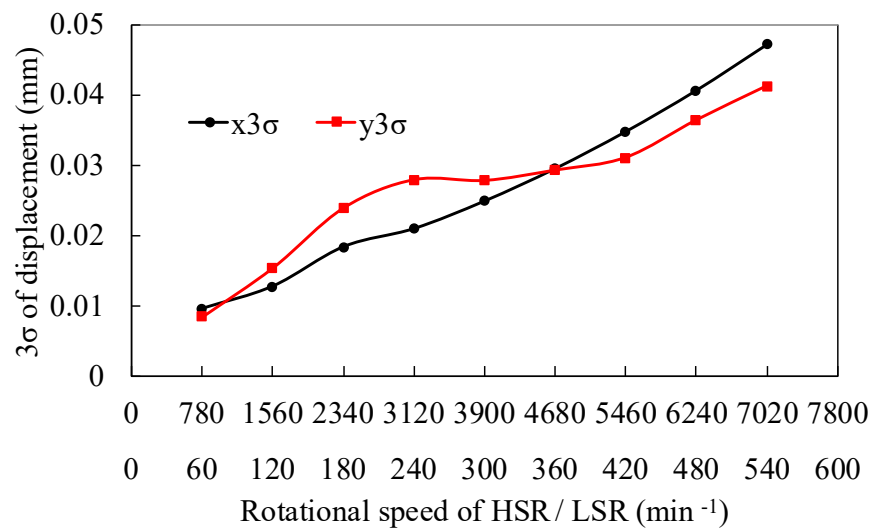
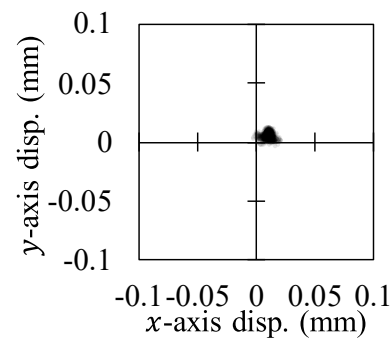
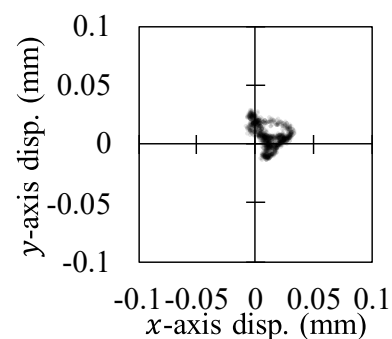


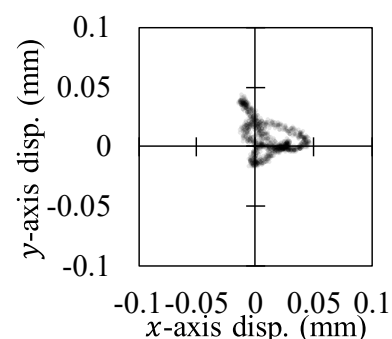
Fig 5. 39. Amplitude of displacement with changing rotational speed.



(a)



(b)



(c)

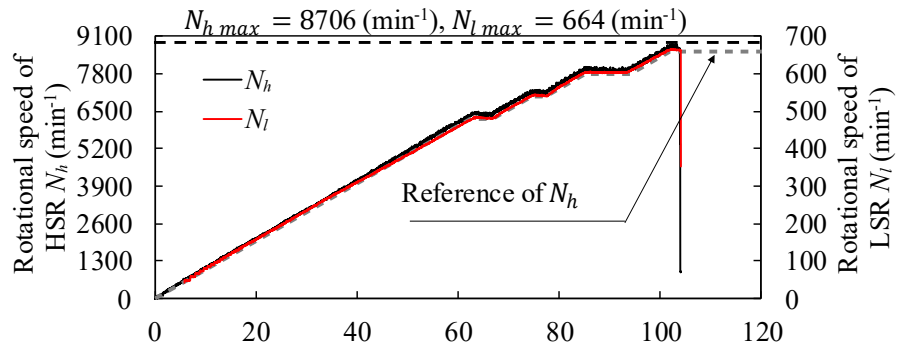
Fig. 5. 40. Displacement traces with changing rotational speed.

(a) 780 min^{-1} (b) 4680 min^{-1} (c) 7020 min^{-1}

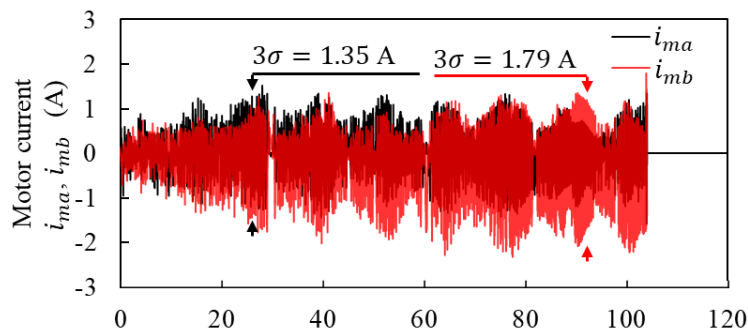
Fig 5. 39 and Fig. 5. 40 show that displacement increases as speed increases, but stable rotation is possible within the touchdown gap range up to 7020 min^{-1} .

Fig 5. 41 shows the experimental results of the speed test while the rotor is magnetically suspended. The rotational speed of the high-speed rotor is calculated from the derivation of the measured angle $\hat{\theta}$. The rotational speed of the low-speed rotor is measured using a tachometer (HT-5500, Ono Sokki Co., Ltd., Japan). The rotational speed of both rotors is measured using an oscilloscope (DLM2024, Yokogawa Test & Measurement Corp., Japan) and passive voltage probes. Motor currents i_{mu} and i_{mv} are detected using two current probes and waveforms are captured by the oscilloscope (DLM2024, Yokogawa Test & Measurement Corp., Japan). Radial displacement sensor outputs are measured using an oscilloscope (DLM2024, Yokogawa Test & Measurement Corp., Japan) and passive voltage probes. i_{ma} and i_{mb} can be calculated by the measured i_{mu} and i_{mv} using $\alpha - \beta$ transformation. Suspension currents i_{sx} and i_{sy} are measured using two passive voltage probe outputs by the digital-analog converter of the controller using current sensors of the inverter and waveforms are captured by the oscilloscope. The reference rotational speed of the high-speed rotor increased to 100 r/min per second to prevent a spike in the current. In addition, the rotational speed reference value was initially set at $N_h^* = 6240$ r/min, and after it stabilized, the speed was increased repeatedly by 780 r/min.

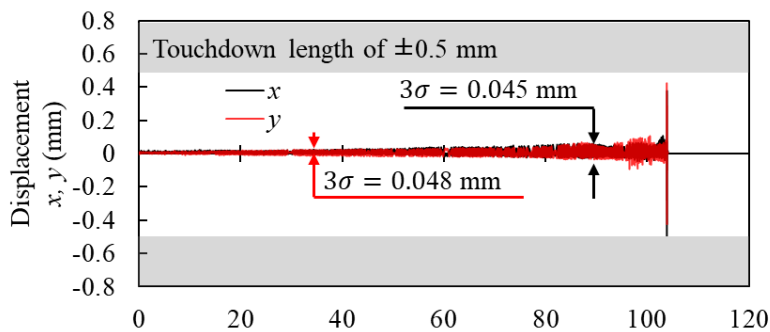
As a result of the experiment, continuous rotation could not be maintained at rotational speeds of $N_h = 8706$ min⁻¹ of the high-speed rotor. This is due to radial position vibration and the occurrence of touchdown. In steady state, the vibration of motor current i_{sa} is 1.35 A, and the vibration of i_{sb} is 1.79 A. Additionally, the vibrations of the rotor radial positions x and y are 0.045 mm and 0.048 mm, respectively.



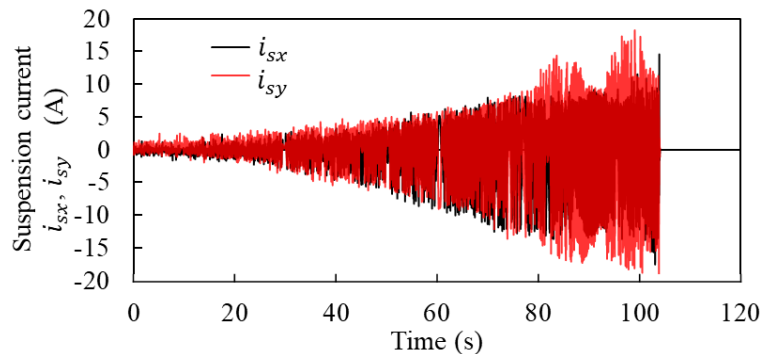
(a)



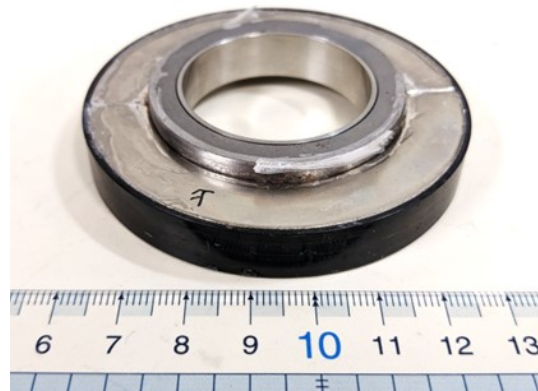
(b)



(c)



(d)



(e)

Fig 5.41. Experimental results of the speed test while the rotor is magnetically suspended.

(a) Rotational speed of each rotor and reference speed of HSR. (b) Motor currents i_{mu} , i_{mv} and i_{mw} . (c) Radial displacements x and y . (d) suspension currents i_{sx} and i_{sy} . (e) Mechanical failure of high-speed rotor due to forward precession movement resonance at natural frequency

After this experiment, the permanent magnet detached from the core of the high-speed rotor, as shown in Fig 5. 41(e). Based on this, it can be seen that this touchdown is caused by the tilt direction rather than the radial direction. According to [113], resonance caused by forward precession in the tilt direction can be expressed as follows when focusing only on disturbances caused by rotor rotation.

$$P_f(\theta_t) = \frac{J_r \omega_h + \sqrt{(J_r \omega_h)^2 + 4k_\theta(\theta_t) J_t}}{2J_t} \quad (5.11)$$

where $k_\theta(\theta_t)$ is the tilt stiffness at angle θ_t between the magnetization direction of the permanent magnet and the tilt axis. J_r and J_t are the inertia moment of rotation about the rotation axis and the radial axis, respectively. The prototype machine uses a two-pole high-speed rotor permanent magnet, as shown in Table 5. 1, the tilt direction stiffness varies significantly with θ_t . Therefore, the tilt direction resonance frequency P_f also becomes a function of θ_t .

Fig 5. 42 shows the calculation results of (5.11). Resonance with the 2f component begins at $N_h = 7789 \text{ min}^{-1}$, which is close to the resonance of 8706 min^{-1} observed in the experiment.

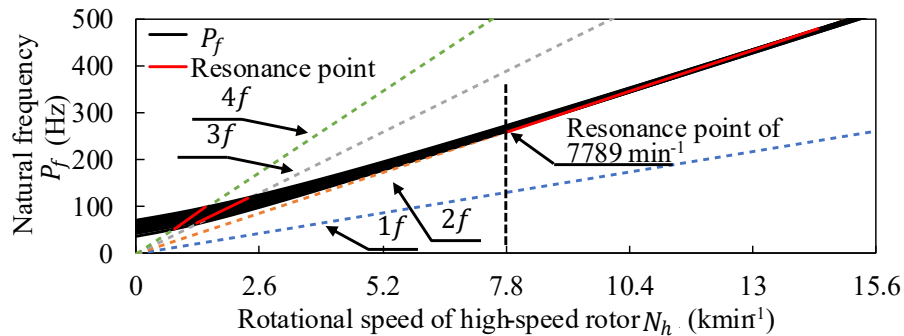


Fig 5. 42. Variation of natural frequencies of forward precession movement with respect to the rotational speed of the prototype machine.

5.5. Radial Force Measurement

To compare the analysis and experiment of the prototype machine, a radial force is applied. The suspension current is measured and compared with the FEM analysis.

Fig. 5.43 shows the experimental setup for radial force measurement. The high-speed rotor is surrounded by the low-speed rotor, which makes it difficult to input force directly from the outside. Thus, the prototype motor was mounted vertically, and an additional device was installed that can apply gravity force as a radial force to the high-speed rotor. This device consists of a push rod mounted on a linear rail that can move in the x -direction. Hence, the gravity on the high-speed rotor and the push rod is applied in the radial direction of the high-speed rotor. The weight of the push rod assembly is 0.25 kg. Furthermore, the external radial force can be applied by attaching weights. In this experiment, the suspension current is defined as the difference in the zero-suspension current since the radial forces inevitably occur due to mechanical errors, non-uniformity of magnetization, and other factors. The zero-suspension current is defined under the conditions that the prototype is installed horizontally, and the high-speed rotor is suspended at center position.

Additionally, as defined in (3.31) and shown in Fig. 4.16(c), when a magnetic suspension current i_{sx} is applied, a force F_y in the y -axis direction is also generated. However, when the weights are applied, the high-speed rotor and the stator are connected through the push rod. Thus, the force in the y -axis direction F_y generated by the suspension current i_{sx} is compensated by the friction force with the push rod. Consequently, this experimental setup is not suitable for the measurement of the error angle θ_{err} or the torque during the radial force is applied.

As shown in Section 4.2.4, this motor generates an unbalanced magnetic pull of approximately 23 N at maximum radial displacement. For this reason, it is desirable to apply a radial force equal to the unbalanced magnetic pull at maximum radial displacement in this experiment. However, during the experiment, it was confirmed that the current density increased to about 10 A/mm² at a radial force of 18.9 N. Therefore, since applying a greater radial force could damage the winding, the experiment was conducted with a radial force between 4.2 N and 18.9 N.

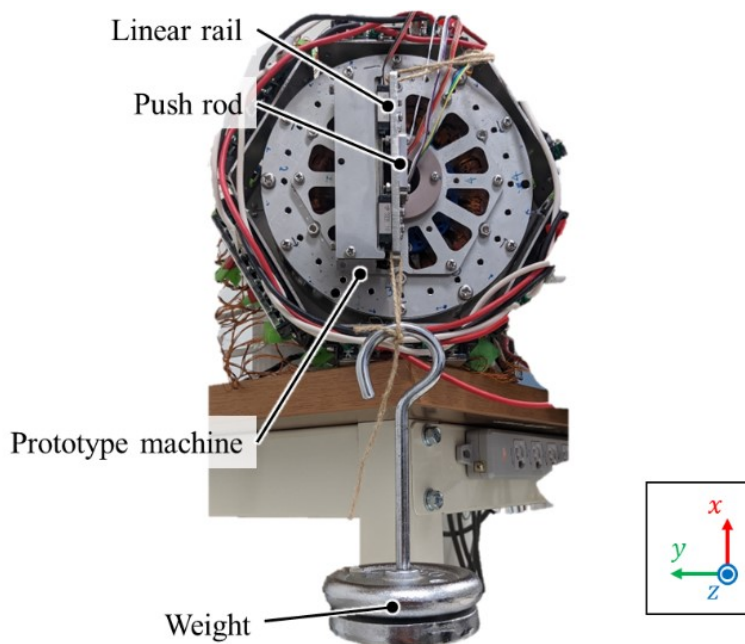


Fig. 5.43. Experimental setup for measuring radial force F_x .

Fig. 5.44 shows the suspension current i_{sx} at a steady state. Suspension currents i_{su} and i_{sv} are detected using two current probes and waveforms are captured by the oscilloscope. i_{sx} and i_{sy} can be calculated by the measured i_{su} and i_{sv} using dq transformation. The rotor radial position references x and y are set to 0 mm. The doted currents show the experimental result, and the solid currents show the FEM analysis results. As a result, analytical and experimental suspension currents are quite comparable, with only minor differences. The difference was caused by three factors: the hysteresis effect, the reduction of the PM flux in the test machine, and the fluctuation of the magnetic-center-position. According to Fig. 4.14 and Fig. 4.15, the fluctuation of the suspension characteristics is caused by the flux saturation at the stator back yoke. In the prototype, the flux at the stator back yoke is decreased by the reduction of the PM flux. In the experiment result, the back EMF in the experiment is 10 % less, as shown in Fig. 5.24. In addition, the fluctuation of the magnetic-center-position has significant influence on small radial force, because the unbalanced magnetic pull force is identical.

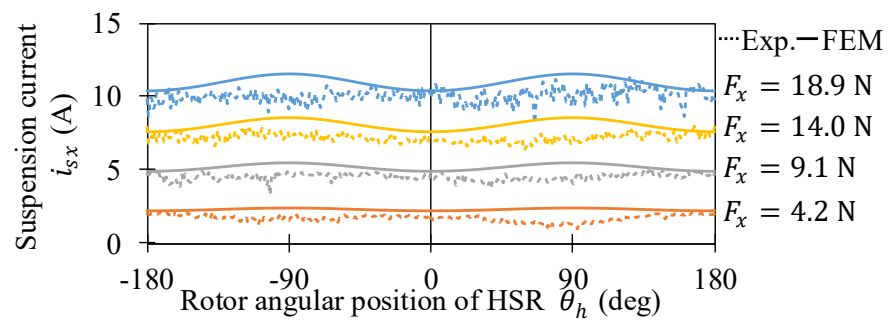


Fig. 5. 44. Experimental results of suspension currents i_{sx} under different radial forces F_x with respect to the rotational angular position of the high-speed rotor (HSR) θ_h .

Fig. 5.45 shows the suspension current and its direction under the gravity applied in the x -axis at a steady state. In **Fig. 5.45(a)**, the currents are similar to those of the FEM analysis results. Meanwhile, the result in **Fig. 5.45(b)** indicates that the current direction $\angle i_s = \tan^{-1}(i_{sx}/i_{sy})$ is enlarged compared to the FEM analysis result. This is caused by the mechanical and magnetic errors. In ideal conditions, the magnetic-centered position is constant with respect to the rotational angular position of the high-speed rotor θ_h . However, the error of the magnetic-centered position occurred in the experiment. Generally in bearingless motors, the additional weight is applied to increase the suspension current and reduce the influence of the magnetic-centered position error. In contrast, it is quite difficult to add weights directly in this experimental setup. Therefore, the precise measurement of θ_{err} requires further investigation.

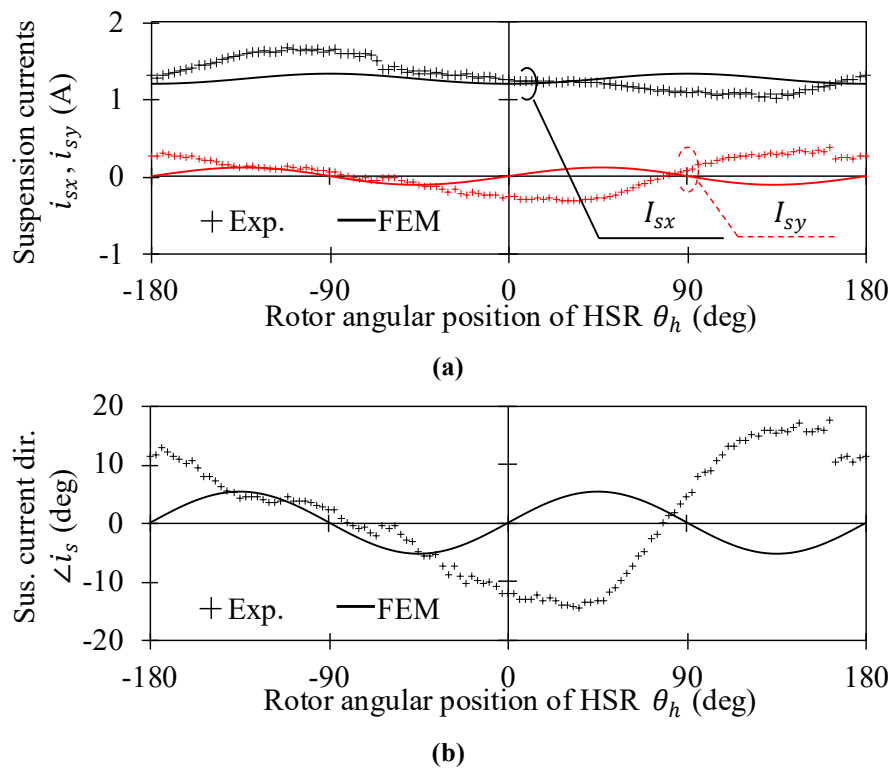


Fig. 5.45. Experimental results of suspension current and direction under the gravity applied in the x -axis with respect to the rotational angular position of the high-speed rotor (HSR) θ_h .

(a) Suspension currents i_{sx} and i_{sy} (b) Suspension current direction $\angle i_s = \tan^{-1}(i_{sx}/i_{sy})$.

Fig. 5.44 shows the experimental results obtained with the motor in a horizontal position. This prototype was not originally designed to be placed in a horizontal position. For this reason, the terminal block connected to the motor frame by a thin stainless-steel plate supports the weight of the motor instead of the motor frame. Under these conditions, fluctuations in the experimental results may occur due to vibrations of the motor body or the weight, which makes the horizontal orientation unsuitable as an experimental setup. Therefore, the experimental setup was modified, and additional experiments were conducted. Fig. 5.46 shows the modified experimental setup for applying radial force F_x . In this setup, pulleys were used to install the prototype horizontally. Fig. 5.47 shows the magnetic suspension current i_{sx} at the rotation angle position of the high-speed rotor (hsr) with different radial force F_x were applied using the modified experimental device. Compared with the experimental results shown in **Fig. 5.44**, the experimental results are closer to the analyzed values. However, it should be noted that the resolution in the rotational angle direction is 3 degrees in Fig. 5.47, whereas it was 1 degree in **Fig. 5.44**.

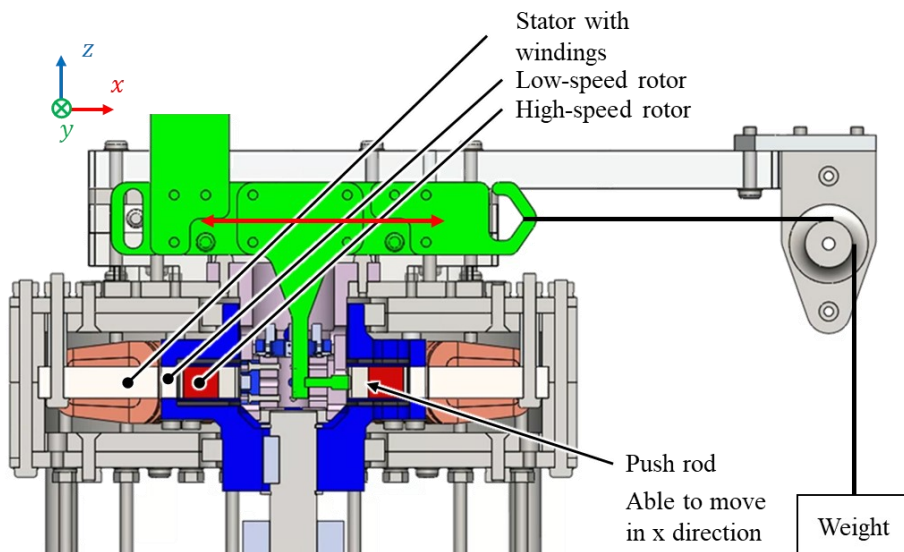


Fig. 5.46. Modified experimental setup for applying radial force F_x .

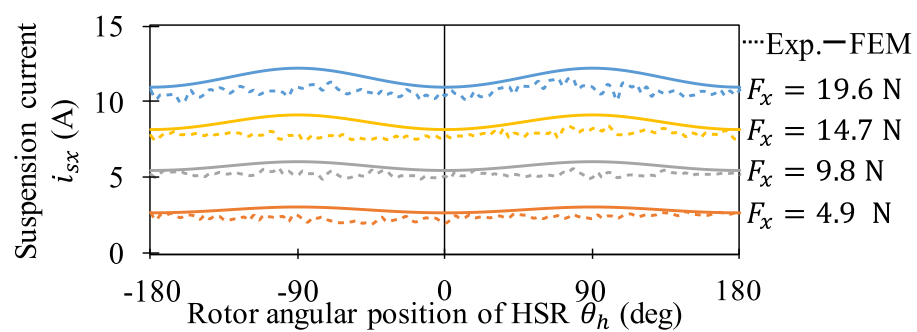


Fig. 5. 47. Magnetic suspension current i_{sx} at the rotation angle position of the high-speed rotor (HSR) with different radial force F_x were applied using the modified experimental device.

5. 6. Measurement of Magnetic-Geared Motor Performance

To compare the analysis results of the magnetic-gear motor performance in the prototype with experimental data, an external motor BLM5400-A (Oriental Motor Co., Ltd., Japan) and a torque meter UTM II-5Nm (Unipulse Corp., Japan) were used to measure the torque and efficiency of the magnetic-gear motor.

Fig. 5. 48 shows the torque measurement bench. The low-speed rotor of the prototype machine is connected to the external motor via the torque meter. Since the external motor can only provide speed control, the experiments in this section were conducted with the external motor providing speed control.

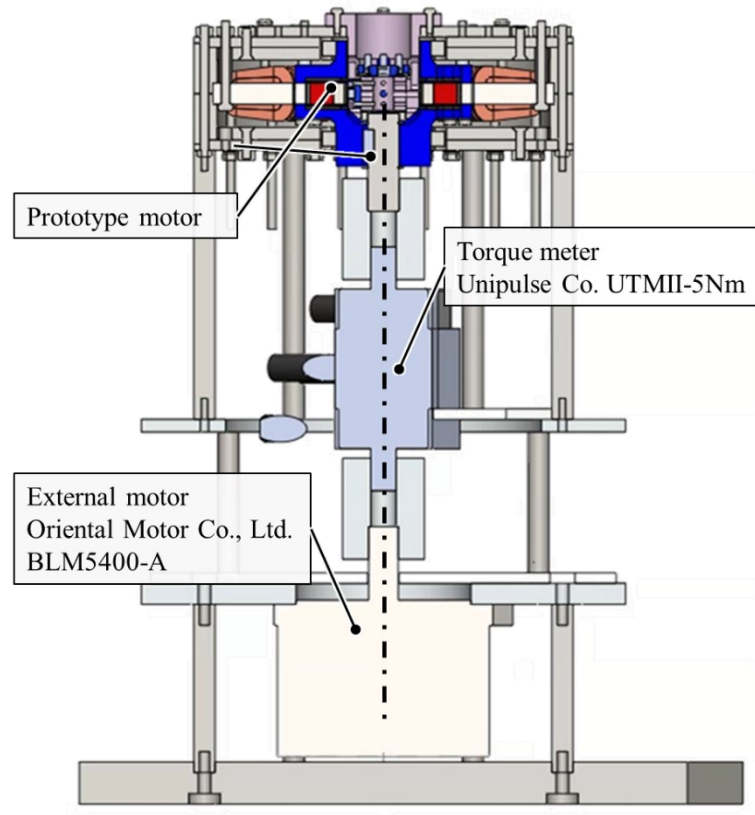


Fig. 5. 48. Torque measurement bench.

Fig. 5.49 shows a comparison of efficiency with and without bearings. In this experiment, the external motor rotation speed reference was varied, and the efficiency with and without mechanical bearings was calculated at a motor q -axis current reference value of $i_{mq}^* = 1.1$ A. Note that the efficiency η (analy) in the analysis was approximately derived from the results in Fig. 4.13. From Fig. 5.49, it can be estimated that the efficiency reverses at a low rotor speed $N_l = 400$ min⁻¹, and that the magnetic suspension of the high-speed rotor improves efficiency at higher speeds.

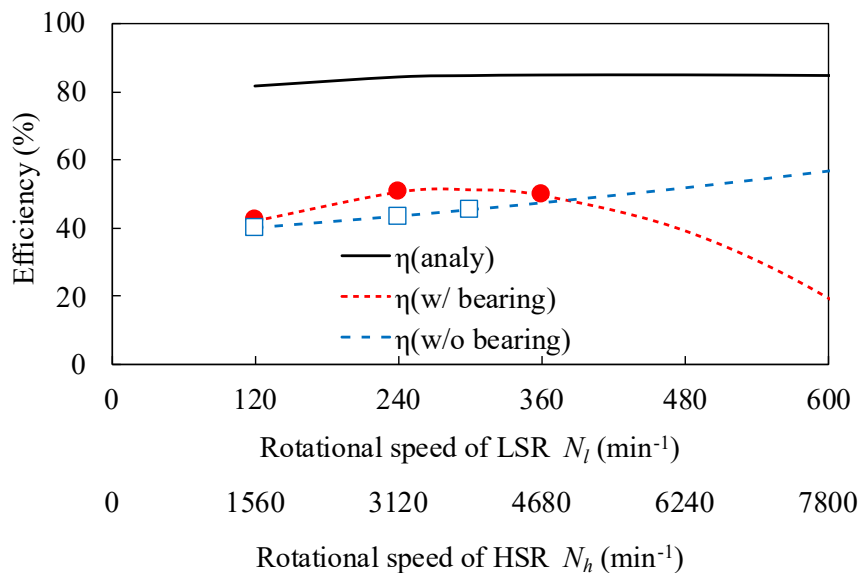


Fig. 5.49. Comparison of efficiency with and without bearings.

Fig. 5.50 shows a comparison of losses with and without bearings. Note that in the experimental results shown in Fig. 5.50 (b) and (c), copper losses could not be directly measured. Accordingly, the no-load loss (Piron + Pmech in Fig. 5.50) was obtained as the output of the external motor when the motor d -axis current command value $i_{md}^* = 0$ A and the motor q -axis current command value $i_{mq}^* = 0$ A. The load loss (Pcu in Fig. 5.50) was calculated by subtracting the output value obtained with a torque meter and the no-load loss from the input power when the motor d -axis current reference value was $i_{md}^* = 0$ A and the motor q -axis current reference value was $i_{mq}^* = 1.1$ A. Meanwhile, since the suspension power is not sinusoidal in either current or voltage, it was measured using a power analyzer (WT1803E, Yokogawa Test & Measurement Corp., Japan).

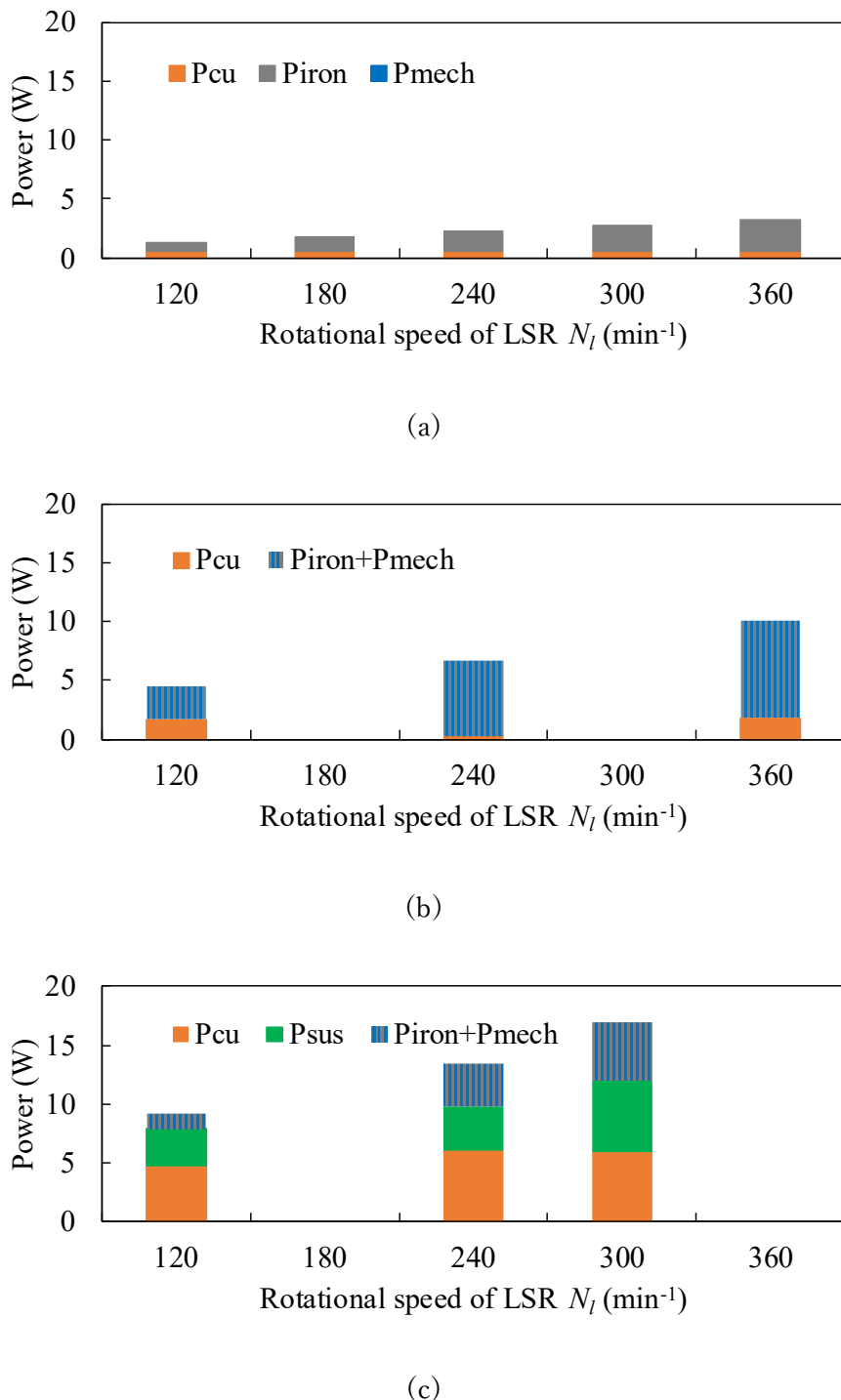


Fig. 5. 50. Comparison of losses with and without bearings.

(a) Analysis result

(b) Losses with bearings (c) Losses without bearings (with magnetic suspension)

According to Fig. 5.50, losses have significantly increased compared to the analysis. However, the analysis does not include mechanical losses, while the experimental results include mechanical losses in no-load losses, so it is considered that mechanical losses have increased the losses. Additionally, load losses have also significantly increased compared to the analysis. In the analysis, iron losses did not change depending on the current. Meanwhile, the applied current in the experiment contained harmonic components, so it is considered that iron losses increased under load conditions. Furthermore, comparing Fig. 5.50 (b) and (c), the no-load loss is smaller in (c) with magnetic suspension, but the load loss is smaller in (b) with mechanical suspension. It is considered that the mechanical loss was reduced by magnetic suspension for the no-load loss. The reason for the increase in load loss with magnetic suspension is considered to be that the magnetic suspension power also increased when the motor current was applied, resulting in an increase in iron loss.

In addition, the maximum transmission torque shown in Fig. 4.11 (b) was verified by experiment. Fig. 5.51 shows the experimental results. In this experiment, the high-speed rotor rotation speed of the prototype machine was controlled to 1560 min^{-1} , which is the expected low-speed rotor rotation speed of 120 min^{-1} , and the speed reference value of the external motor was delayed by approximately 1 min^{-1} from 120 min^{-1} to generate a phase difference between the high-speed rotor and the low-speed rotor. When this occurs, the torque that causes the system to de-synchronize is equal to the maximum transmission torque of the magnetic-gear motor. According to Fig. 5.51, the maximum transmission torque was 0.489 Nm , which is close to the value shown in Table 5.1.

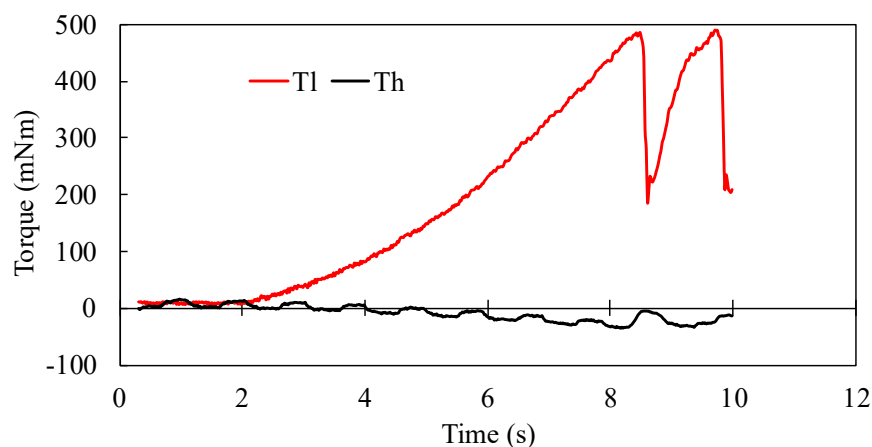


Fig. 5.51. Maximum transmission torque verification test.

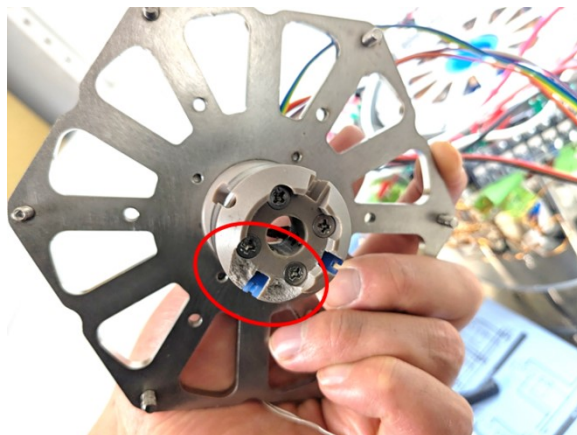
5. 7. Breakage of Prototype

During experiments related to Section 5. 6, the prototype was destroyed. Fig. 5. 52 shows the Broken parts of the prototype. This breakdown made it impossible to magnetically suspend the high-speed rotor.

This part has three functions: it acts as a touchdown target that comes into contact with the high-speed rotor when magnetic suspension becomes impossible, it holds the Hall element and displacement sensor, and it holds the bearing that mechanically restrains this part and the low-speed rotor.

To fulfill its role as a touchdown target, this component was purposely made from a unilate plastic, which is lower in strength compared to metal. This was intended to protect the expensive high-speed rotor by designing the component to break first, as it is less durable than the high-speed rotor. Additionally, it was chosen because it reduces the cost of the component due to the risk of damage, has self-lubricating properties to reduce friction during contact, and requires a non-conductive component to prevent errors in the displacement sensor.

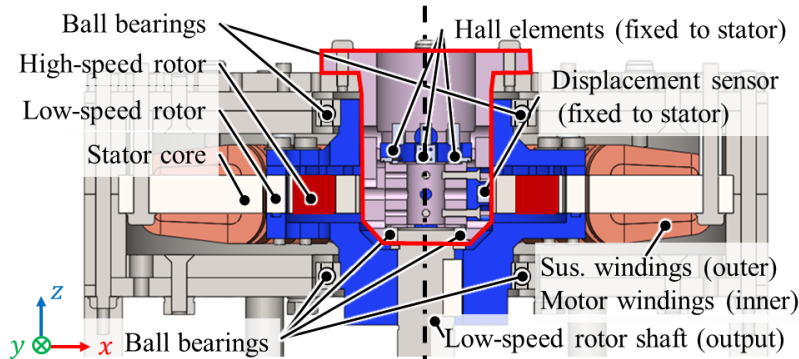
Meanwhile, sharp corners existed in the broken parts, leading to failure due to stress concentration. Therefore, a design eliminating corners through features like fillets was necessary.



(a)



(b)



(c)

Fig. 5. 52. Broken parts of the prototype.

(a) Damaged part (b) Main assembly (c) CAD drawing

5.8. Summary of Chapter 5

In this chapter, the prototype motor proposed in Chapter 4 was manufactured, and magnetic suspension and rotation tests were conducted. This prototype was the world's first demonstration of magnetic suspension of a magnetic-gear motor with a high-speed rotor.

In this prototype, the angular position detection and displacement sensor detection values, which are essential for accurate control, were corrected using original methods as shown in Sections 5.1.4 and 5.1.5. However, angular position detection could not be corrected in magnetic suspension mode because the compensation function was generated in the calibration bearing support mode. For this reason, as shown in Sections 5.3 and 5.6, even after the start of magnetic suspension, which ideally does not require a suspension current, a relatively large current was applied, causing the magnetic suspension current to increase. To prevent these problems, methods for reducing the magnetic suspension power, such as zero-power control [114], have been proposed. However, this research does not specifically address the reduction of magnetic suspension power, which remains a future research topic.

In addition, in the speed test shown in Section 5.4, magnetic suspension failed at a high-speed rotor rotational speed of $8,700 \text{ min}^{-1}$. The proposed motor is novel because it is the first of its kind in the world. However, with a maximum output speed of 664 min^{-1} , it is difficult to apply it to industrial applications that take advantage of the benefits of magnetic suspension. Therefore, a motor design with a structure that can rotate at higher speeds is desired. In particular, the change in tilt rigidity due to the d -axis current shown in Section 4.5 is expected to improve speed without changing the mechanical design. However, since a large magnetomotive force is required, the change in tilt rigidity due to the d -axis current may not be effective enough in this topology. Therefore, it is necessary to devise a method such as integrated windings that integrate the magnetic suspension windings and motor windings.

Moreover, the motor efficiency shown in Section 5.6 does not accurately observe the change in power consumption with or without magnetic suspension. However, the inverter used in this experiment has a very large rating of 5 kVA to allow for output margin. In addition, the winding design emphasizes low resistance rather than the number of windings,

which is not optimal. However, the experiment showed that the power required after magnetic suspension started was only a few tens of watts, so in the future, it would be desirable to measure the magnetic suspension power including the inverter using a smaller capacity inverter. In addition, losses could only be classified as load losses and no-load losses, and the proportions of iron losses, mechanical losses, and copper losses are unknown. Furthermore, further consideration is necessary because the main causes of losses are unknown.

Chapter 6. Investigation of High-Speed Rotor Magnetic Suspension for Consequent-Pole Type Magnetic-Geared Motors

In this chapter, the magnetic-geared motor proposed in Chapter 4 is modified to a consequent-pole structure, and the magnetic suspension force and unbalanced magnetic pull are analyzed by two-dimensional finite element analysis.

6. 1. Problems with the Motor Proposed in Chapter 4

6. 1. 1 Low Torque Density

In the motor proposed in Chapter 4, the maximum transmitted torque was 0.499 Nm in analysis. This corresponds to a torque density of 3.25 kNm/m^3 , which is significantly lower than that of typical magnetic-geared motors. However, the main purpose of the motor proposed in Chapter 4 was to demonstrate the principle. For this reason, the focus was on improving the magnetic suspension performance by reducing the magnetic resistance in the suspension flux path. On the other hand, the performance as a magnetic-geared motor was compromised. Reference [41] compares the torque density of the magnetic-geared motor topology proposed in Chapter 4 with that of a consequent-pole type magnetic-geared motor and an SPM type magnetic-geared motor. Among them, the consequent-pole type magnetic-geared motor had an excellent torque factor. These results potentially indicate that even with a high-speed rotor using magnetic suspension, the magnetic resistance in the suspension flux path is sufficiently low. However, the actual magnetic suspension characteristics are unknown.

6. 1. 2 Difficulty in Accurately Detecting the Angle Position of High-Speed Rotor

As shown in Section 3. 3. 1, the SPM type bearingless motor requires accurate angular position of the rotor for magnetic suspension control. In the prototype, Hall elements capable of non-contact detection of magnetic flux density were used to measure the angular position of the rotor. However, as shown in Section 5. 1. 4, the angular position of the rotor calculated from the Hall elements exhibited errors compared to the actual angular position of the rotor. Nevertheless, in the proposed motor, there are additional degrees of freedom beyond the rotation direction of the rotor, making it extremely difficult to correct these errors by considering such displacements. Therefore, a consequent-pole type magnetic-gear motor, in which the rotor angle position is not essential for magnetic suspension control, was considered.

6. 2. Investigation of Pole Number and Magnetic Suspension Characteristics by Two-Dimensional Finite Element Method

6. 2. 1 Analysis Settings

In this chapter, two-dimensional finite element analysis of radial forces and unbalanced magnetic pull was conducted for models with different numbers of poles in single-sided and double-sided consequent-pole type magnetic-gear motors.

Table 6. 1 shows the dimensions of the analyzed motor. To avoid asymmetric distribution of magnetic flux density, the number of slots was set to three times of the least common multiple of the number of p_h pole pairs of the motor windings and the number of one pole pair of the suspension windings. The windings were distributed winding to suppress harmonic magnetic flux. The number of turns of the suspension windings and motor windings were set to twelve and twenty-one, respectively. The winding layout is shown in Fig. 3. 3.

As in Section 4. 2. 4, this analysis also focuses on minimizing the current required to start magnetic suspension while keeping the angle error within ± 5 degrees.

Table 6. 1. Dimensions of the analyzed motor.

Parameter	Unit	Value
Stator outer diameter	mm	140
HSR outer diameter	mm	70
LSR radial thickness	mm	5
Stator PM radial thickness	mm	4.5
Stack length	mm	10
Inner air gap length	mm	2
Outer air gap length	mm	1

Furthermore, in order to eliminate the unbalanced magnetic pull that occurs at the center position of the high-speed rotor, the pole combination is limited by the symmetry factor x_s (3.30) introduced in Section 3.3.1, which evaluates the symmetry of the magnetic flux density. From (3.28), p_h must be even to satisfy (3.30). In addition, in consequent-pole type bearingless motors, when the number of pole pairs of the magnetic suspension rotor is 2, large fluctuations occur in the suspension force [66]. To satisfy these conditions and maximize the gear ratio, $p_h = 4$ was selected.

In this chapter, the electrical angle of 0° of the high-speed rotor is when the magnetization direction of the y -axis in Fig. 3.6 and one of the poles of the high-speed rotor permanent magnet are parallel.

6. 2. 2 Radial Force of Single-Sided Consequent Pole Type Magnetic-Geared Motors

Three models with different numbers of poles were analyzed for single-sided consequent-pole type magnetic-geared motors. Table 6. 2 shows the combinations of pole numbers for the models analyzed.

**Table 6. 2. Pole combination in the analysis
of single-sided consequent-pole magnetic-geared motors.**

Model	Pole combination
A	$p_h = 4, n_l = 16, p_s = 12, n_s = 48$
B	$p_h = 4, n_l = 22, p_s = 18, n_s = 48$
C	$p_h = 4, n_l = 28, p_s = 24, n_s = 48$

Fig. 6. 1 shows the magnetic suspension characteristics of each model with a suspension current I_{sx} of 20 A to generate a magnetic suspension force in the positive x -axis direction. (a) and (b) show the x -axis and y -axis components of the radial force, respectively. (c) shows the angular error calculated from the values in (a) and (b) using equation (3.31). From (c), the difference between the maximum and minimum angle errors is 19.5 degrees for model B and 16.8 degrees for model C, while it is particularly large at 41.1 degrees for model A. This is because the number of salient poles n_l of the low-speed rotor and the number of pole pairs p_s of the stator permanent magnets are close to the number of pole pairs p_h of the high-speed rotor, and the effects of permittivity and magnetic flux fluctuations are large. Meanwhile, compared to previous research [74], the maximum angular error is still relatively large, even in Model C, which has the smallest maximum angular error at approximately 9 degrees. However, by increasing the thickness of the stator back yoke, the maximum angular error was reduced from approximately 9.4 degrees to approximately 4.8 degrees in the design optimization conducted in Chapter 4. Therefore, it is necessary to optimize the design to reduce the angular error.

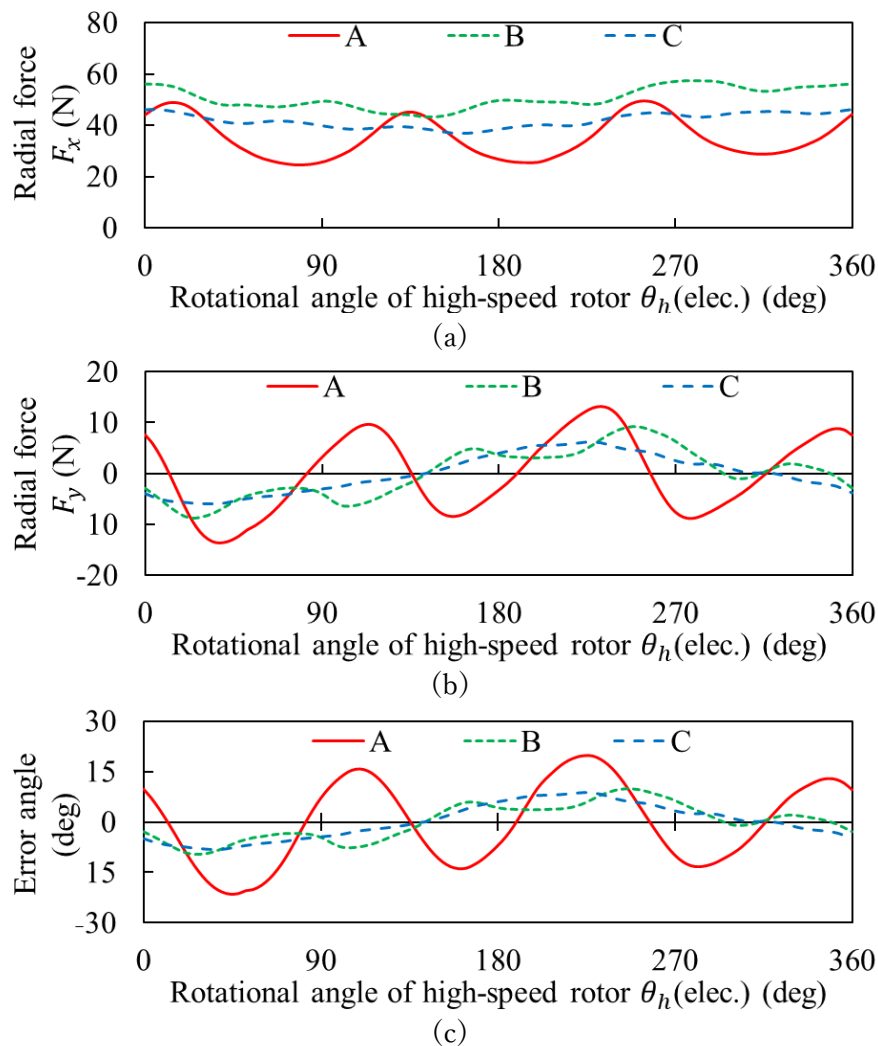


Fig. 6.1. Magnetic suspension characteristics of single-sided consequent-pole type magnetic-gear motors with $i_{sx} = 20$ A suspension current.

- (a) x -axis component of radial force F_x
- (b) y -axis component of radial force F_y
- (c) Angular error

Fig. 6.2 shows the unbalanced magnetic pull at a radial displacement of 0.5 mm in the x direction of the high-speed rotor without current. As in Fig. 6.1, the fluctuation of Model A is particularly large. This is because the number of salient poles n_l of the low-speed rotor and the number of pole pairs p_s of the stator permanent magnets are close to the number of pole pairs p_h of the high-speed rotor, and the effects of permittivity and magnetic flux fluctuations are large. However, since the average values are the same for all models, it can be assumed that the same startup current is required regardless of the pole combination.

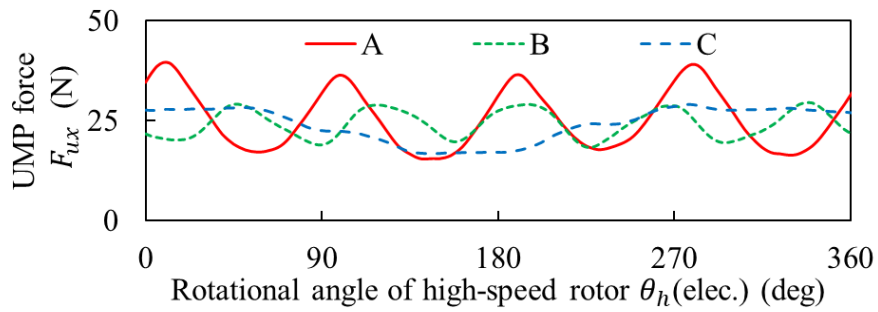


Fig. 6.2. Unbalanced magnetic pull generated in single-sided consequent-pole magnetic-gear motors with a high-speed rotor radially displaced by 0.5 mm in the x -axis direction.
(Unbalanced magnetic pull: UMP)

Fig. 6.3 shows the magnetic flux density distribution of each model without current. The motor dimensions used in this investigation are generally based on the models in Chapter 4. As a result, the magnetic flux density of the stator back yoke has decreased due to the increase in the number of poles of the high-speed rotor. Based on this magnetic flux density, the thickness of the stator back yoke is excessive, and the dimensions need to be optimized. However, since there are two magnetic suspension poles, if the magnetic suspension current increases, the magnetic flux density may increase beyond that shown in Fig. 6.3 and reach saturation. Therefore, optimization is necessary with the magnetic suspension current applied.

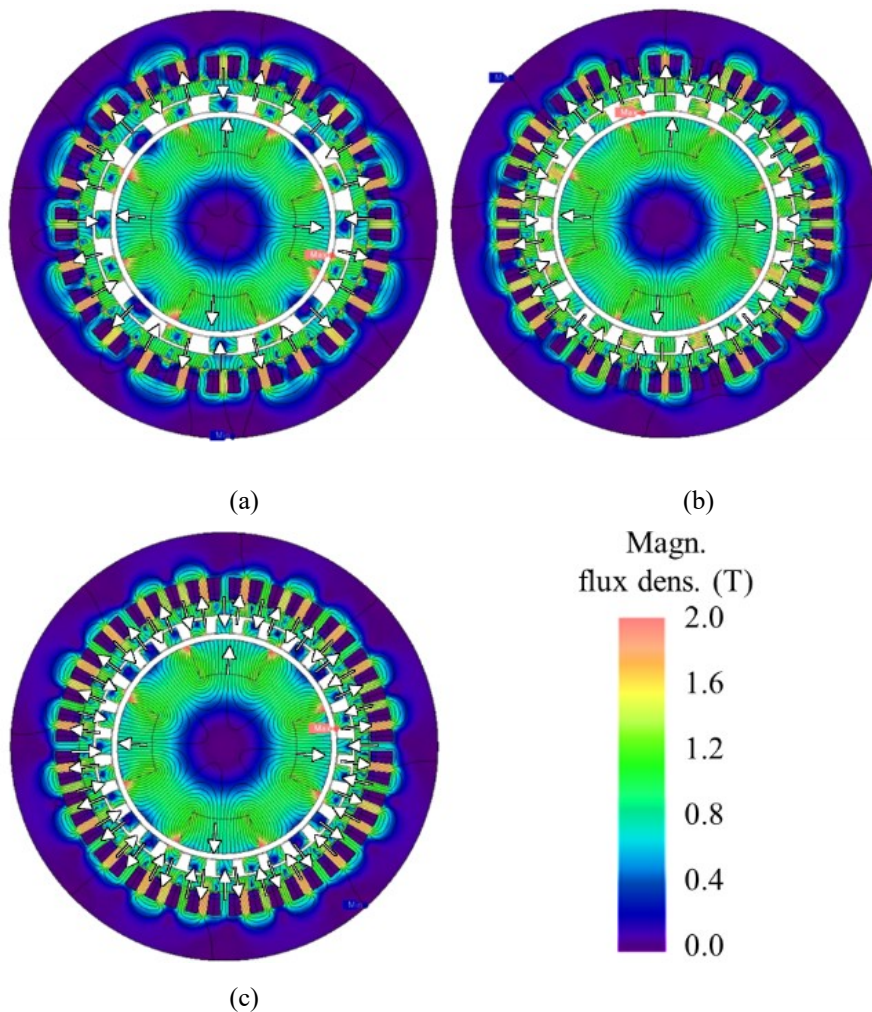


Fig. 6.3. Magnetic flux density distribution of each model of single-sided consequent-pole type magnetic-gear motors without current.

(a) Model A (b) Model B (c) Model C

6. 2. 3 Radial Force of Single-Sided Consequent Pole Type Magnetic-Geared Motors

In this topology, three models with different numbers of poles were analyzed, as in the previous section. Table 6. 3 shows the combinations of pole numbers for the models investigated. Since this topology is of the double-sided consequent-pole type, there are several possible combinations of magnetization directions for the permanent magnets of the stator and high-speed rotor. In this section, the magnetization of the high-speed rotor was fixed on the outside, and two magnetization directions of the permanent magnets of the stator, inward and outward, were analyzed. For the distinction, the inward magnetization model, in which the magnetization directions of the stator and high-speed rotor are different, was given the suffix ('') in the model name.

Table 6. 3. Pole combination in the analysis of double-sided consequent-pole magnetic-geared motors.

Model	Pole combination
a, a'	$p_h = 4, n_l = 16, p_s = 12, n_s = 12$
b, b'	$p_h = 4, n_l = 22, p_s = 18, n_s = 18$
c, c'	$p_h = 4, n_l = 28, p_s = 24, n_s = 24$

Fig. 6. 4 shows the magnetic suspension characteristics of each model with a suspension current I_{sx} of 20 A to generate a magnetic suspension force in the positive x -axis direction. (a) and (b) show the x -axis and y -axis components of the radial force, respectively. (c) shows the angular error calculated from the values in (a) and (b) using equation (3.31). In this model, the number of turns per slot is fixed, thus the magnetomotive force increases as the number of slots increases. Accordingly, it should be noted that the radial force in (a) increases in models with a large number of slots. Meanwhile, even with the same combination of pole pairs, it was shown that models with a stator marked with (') and a high-speed rotor with permanent magnets magnetized on the opposite side generate a larger radial force. Furthermore, models b' and c' greatly exceeded the radial force of a single-sided consequent-pole magnetic-geared motor, resulting in a large radial force even with the same suspension current. However, except for model a, which had a very large angle error, the maximum angle error for all models was around degrees. As shown in Section 6. 2. 2, this

angle error is insufficient. Therefore, it is necessary to reduce the angular error through shape optimization in the same method.

Fig. 6.5 shows the unbalanced magnetic pull at a radial displacement of 0.5 mm in the x -direction of the high-speed rotor. There is no significant difference between the models in terms of the average unbalanced magnetic pull. Thus, in terms of magnetic suspension performance, the model with the permanent magnets of the stator and high-speed rotor are magnetized in opposite directions, which marked with ('), is superior. In addition, as in Fig. 6.4, the pulsation of the unbalanced magnetic pull in Fig. 6.5 tends to increase as the gear ratio decreases.

Fig. 6.6 shows the magnetic flux density distribution of each model without current. In models with permanent magnets of the stator and high-speed rotor are magnetized in the same direction, the magnetic flux density is high in the teeth not facing the permanent magnets of the high-speed rotor, while in models with permanent magnets magnetized in opposite directions, the magnetic flux density is high in the teeth facing the permanent magnets of the high-speed rotor. Therefore, the latter model generates a larger radial force because the magnetic resistance of the magnetic circuit passing through the iron core poles of the high-speed rotor is low.

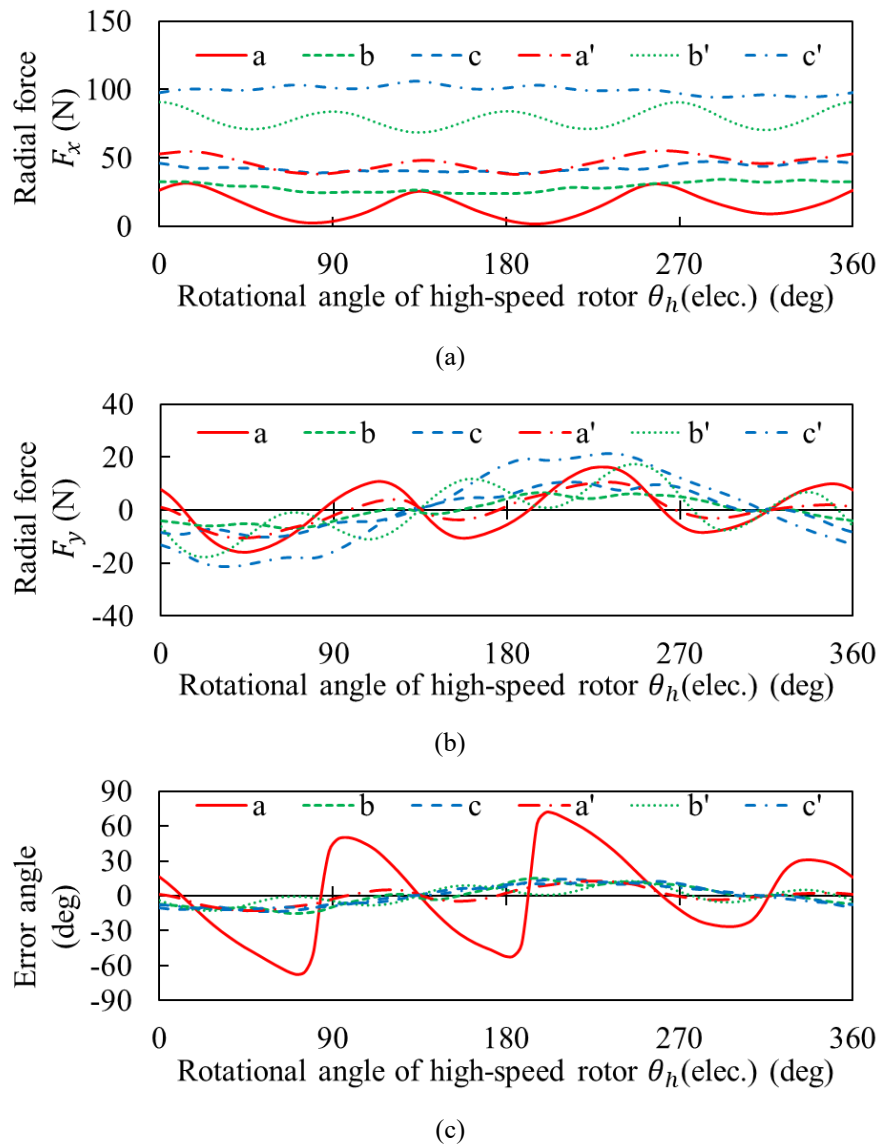


Fig. 6.4. Magnetic suspension characteristics of double-sided consequent-pole type magnetic-gear motors with $i_{sx} = 20$ A suspension current.

(a) x -axis component of radial force F_x (b) y -axis component of radial force F_y

(c) Angular error

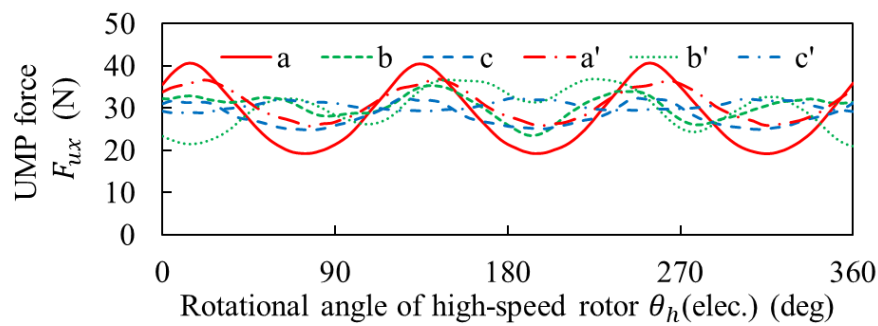


Fig. 6. 5. Unbalanced magnetic pull generated in double-sided consequent-pole magnetic-gear motors with a high-speed rotor radially displaced by 0.5 mm in the x -axis direction.
(Unbalanced magnetic pull: UMP)

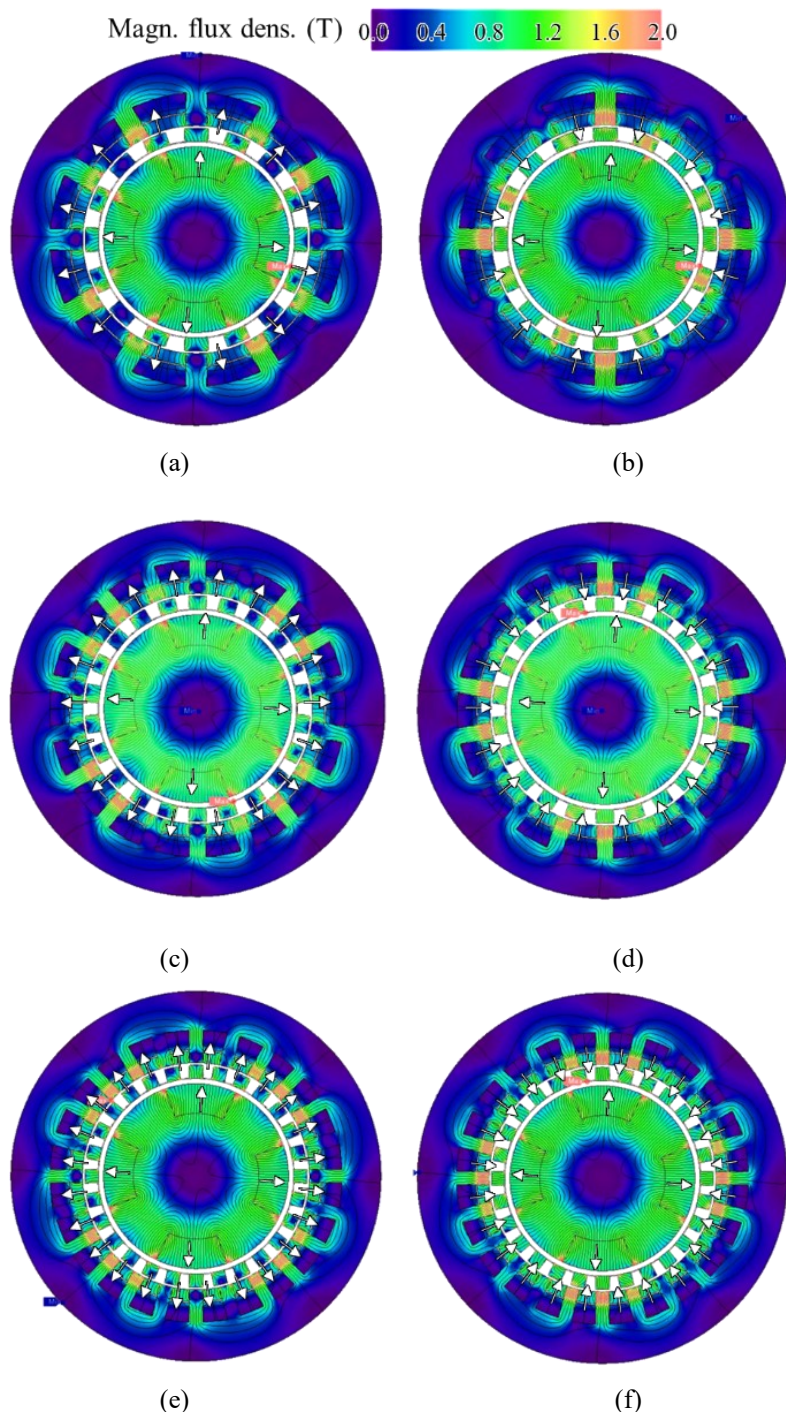


Fig. 6. 6. Magnetic flux density distribution of each model of single-sided consequent-pole type magnetic-geared motors without current.

(a) Model a (b) Model a' (c) Model b (d) Model b' (e) Model c (f) Model c'

6. 3. Summary of Chapter 6

In this chapter, the magnetic-geared motor proposed in Chapter 4 is modified to a consequent-pole structure, and the magnetic suspension force and unbalanced magnetic pull are analyzed by two-dimensional finite element analysis.

Table 6. 4 shows the analysis results in Chapter 6. SCPM stands for single-sided consequent-pole magnetic-geared motor, and DCPM stands for double-sided consequent-pole magnetic-geared motor. -F and -O indicate models in which the magnetization directions of the permanent magnets of the high-speed rotor and stator are the same and opposite, respectively. $F_{sx\ min}$ is the minimum magnetic suspension force in one electrical angle cycle, $F_{ux\ max}$ is the maximum unbalanced magnetic pull in one electrical angle cycle, $I_{sx\ max}$ is the maximum startup current calculated as $F_{ux\ max}/F_{sx\ min}$, and $\theta_{err\ max}$ is the maximum angle error in one electrical angle cycle. According to the analysis in this chapter, the configuration in which the magnetization direction of the permanent magnets is opposite between the high-speed rotor and the stator in a double-sided consequent-pole type magnetic-geared motor has the largest magnetic suspension force at the same magnetic suspension current. However, since the angle error did not meet the target of ± 5 degrees in any model, further shape optimization is necessary.

Table 6. 4. Analysis results in Chapter 6.

	SCPM			DCPM-F			DCPM-O		
	A	B	C	a	b	c	a'	b'	c'
$F_{sx\ min}$	24.6	43.1	36.9	1.5	23.8	39.0	38.3	69.0	94.5
$F_{ux\ max}$	39.6	29.8	29.6	40.7	35.5	32.4	36.9	37.6	32.5
$I_{sx\ max}$	32.2	13.8	16.1	543.8	29.7	16.6	19.2	10.9	6.9
$\theta_{err\ max}$	19.7	9.8	8.8	71.0	15.2	14.3	12.4	12.4	12.2

Chapter 7. Optimization and Verification of High-Speed Rotor Magnetic Suspension for Consequent-Pole Type Magnetic-Geared Motors

In this chapter, the dimensions of the motor proposed in Chapter 6 are optimized, and its performance is compared with that of an SPM-type magnetic-gear motor. In addition, the characteristics of the optimized model are analyzed using a three-dimensional finite element method.

7.1. Optimization Using Two-Dimensional Finite Element Method

7.1.1 Optimization Settings

To investigate the influence of motor topology on the magnetic suspension characteristics and output torque, an optimization by two-dimensional FEM analysis was conducted for the three topologies shown in Fig. 3.2 and Fig. 3.3. Table 7.1 shows the fixed parameters of the optimization models.

Table 7.1. Fixed parameters of the optimization models.

Parameter	Unit	Value
Stator outer diameter	mm	140
HSR outer diameter	mm	70
HSR inner diameter	mm	35
Stack length	mm	10
Inner / outer air-gap length	mm	2 / 1

The winding is a full-pitch distributed winding and the fill factor of the windings is 40 %. The turn number of the winding is obtained from the winding area and the fill factor. The number of strands in the suspension and motor windings is five for both, as shown in Section 5.1.3. In addition, the winding conductor diameter is 0.4 mm with a thick 0.05 mm insulator. The high-speed rotor PMs and the stator PMs are made of N48 material. The stator and the low-speed rotor core are made of laminated silicon steel 20HX1300. Meanwhile, the high-speed rotor core is made of S45C material because the iron loss is negligible. Table 7.2 shows the selected pole combinations. In the analysis of the double-sided consequent pole type magnetic-geared motor (DCPM) model in this section, two magnetization directions of the permanent magnets of the stator, inward and outward, were analyzed as in Section 6.2.3. To distinguish between them, models with the same magnetization direction of the stator and high-speed rotor have “-F” added to their model names, and models with different magnetization directions have “-O” added to their model names.

Table 7.2. Pole combinations of each topology.

Topology	Pole combination
SPM	$p_h = 2, n_l = 14, p_s = 12, n_s = 24, p_{sus} = 1$
SCPM	$p_h = 4, n_l = 28, p_s = 24, n_s = 24, p_{sus} = 1$
DCPM-F / DCPM-O	$p_h = 4, n_l = 28, p_s = 24, n_s = 24, p_{sus} = 1$

Fig. 7.1 shows the design parameters that were varied during the optimization. In this optimization, the main objectives are the maximization of the mean output torque T_l of the low-speed rotor and maximization of the mean suspension force F_{sus} . In addition, the error angle factor k_{err} is provided for a constraint function to improve the magnetic suspension characteristics. For simplification of analysis, the suspension force in this optimization is calculated as the average of the suspension forces at $i_{sus} = 10$ A during one electric cycle.

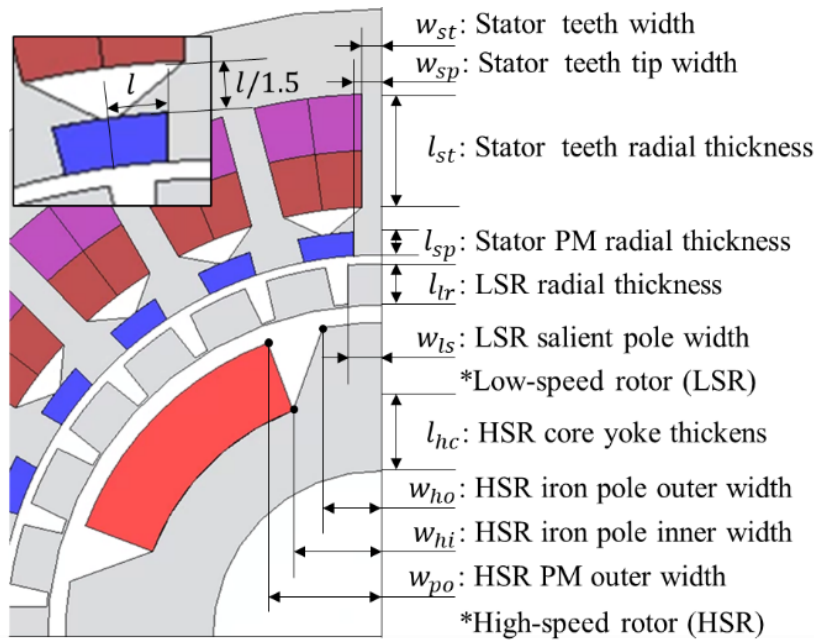


Fig. 7. 1. Design parameters of optimization.

Furthermore, to improve the suspension controllability, the error angle must be small enough. Meanwhile, the error angle is changed with the rotational angle of the high-speed rotor. According to the analysis result in Section 4. 2. 4, the highest error angle is observed at the rotational angle when the highest F_{\perp} and average F_{\parallel} are generated. Thus, the error angle factor k_{err} is defined as

$$k_{err} = \tan^{-1}\left(\frac{\max(F_{\perp})}{\text{average}(F_{\parallel})}\right) \quad (6.1)$$

Table 7. 3 shows the objectives of the optimization. The target value was calculated from the prototype model in Chapter 4 while the same analysis condition. As a result, each factor was obtained as $T_l = 0.987$ Nm, $F_{sus} = 15.8$ N, and $k_{err} = 3.30^\circ$. Therefore, the optimal value is chosen as the model within the error angle factor k_{err} is less than 3.30° . Furthermore, the minimal torque of the optimal value is configured as 4.62 Nm = 30 Nm/L, so that the torque density is close to the optimization result that was previously presented in [106].

Table 7. 3. Objectives of the optimization.

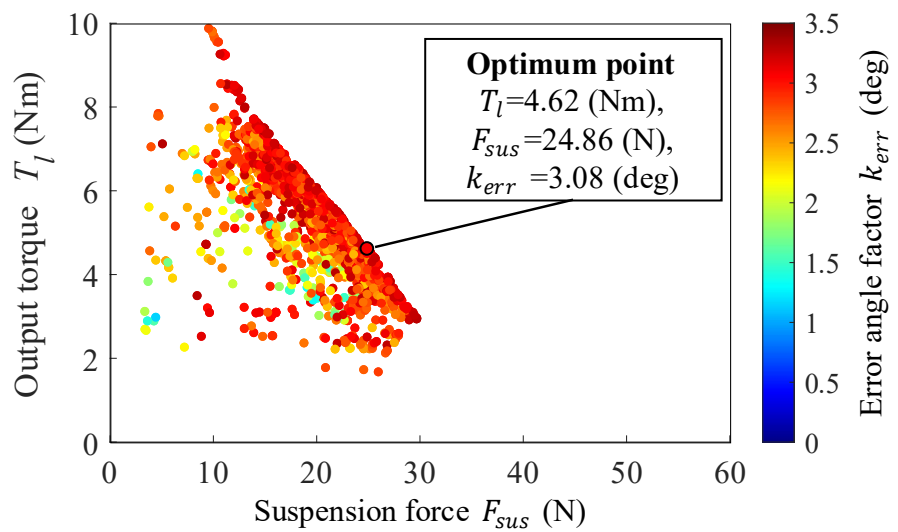
Statement	Description
$\max(T_l)$	Maximize the mean torque of the low-speed rotor
$\max(F_{sus})$	Maximize the mean radial force
$k_{err} < 3.30$ (deg)	The error angle factor is small enough compared to the prototype model in Chapter 5

7. 1. 2 Optimization Results

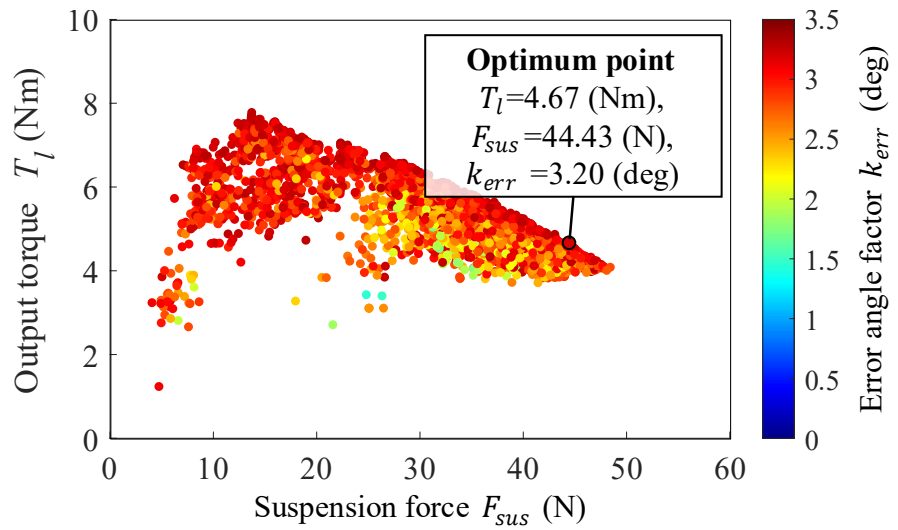
To compare the topologies, optimizations were conducted. In these optimizations for comparison, the SPM model also was analyzed, besides the magnetic-geared motor with consequent-pole structure as shown in Fig. 3. 3.

Fig. 7. 2 shows the optimization results on each topology. From Fig. 7. 2 (c) and (d), the Pareto front values show better characteristics than the DCPM-F MGM model although it has an identical structure except for the polarity of the PMs. Additionally, from Fig. 7. 2, the SPM MGM model has the potential to achieve high output torque T_l compared to the CPM model. This result is similar to the previous research in [41]. Meanwhile, the models with CPM structures can generate higher suspension force F_{sus} , especially, the DCPM-O MGM model can generate the highest suspension force F_{sus} . This is due to the high permeance caused by the CPM structure. Hence, the DCPM MGM has an advantage in suspension force F_{sus} .

In this optimization, the optimal points are focused on maximizing the suspension force at the similar output torque T_l and error angle factor k_{err} . According to the analysis results, the DCPM-O MGM model has the potential to achieve the highest suspension force F_{sus} compared to the other topologies. Therefore, the DCPM-O MGM model has a high potential for achieving a balance between suspension characteristics and output torque.



(a)



(b)

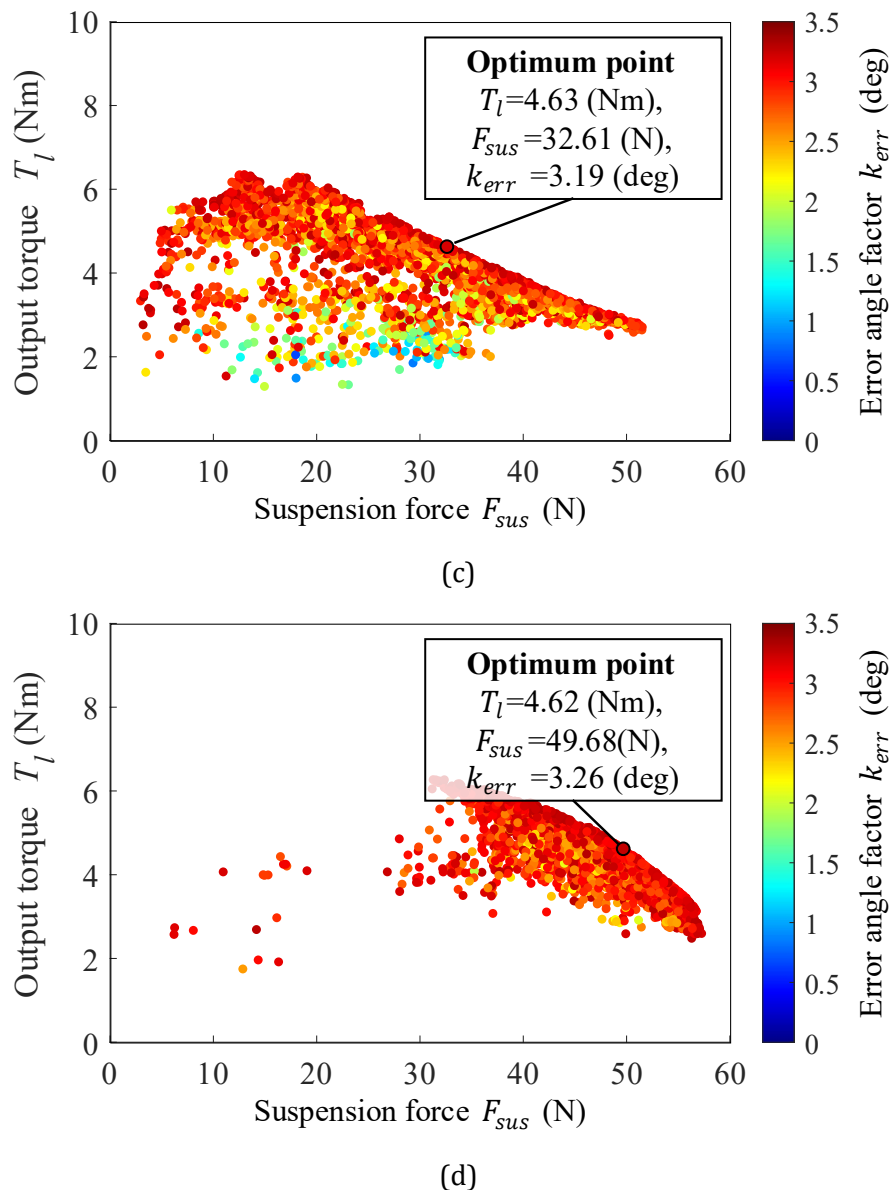


Fig. 7.2. Pareto optimal solutions of each model.

- (a) SPM-MGM model. (b) SCPM-MGM model.
- (c) DCPM-F-MGM model. (d) DCPM-O-MGM model.

Table 7. 4 shows the value of the design parameters for the selected optimum points. In this table, the width of the iron poles of the high-speed rotor is wider on the inside and narrower on the outside for CPM models. This design prevents the concentration of magnetic flux at the corners of the iron poles. Thus, flux saturation in the magnetic paths of the suspension flux is avoided.

Table 7. 4. Value of the design parameters for the selected optimum points.

Parameters	SPM (mm)	SCPM (mm)	DCPM-F (mm)	DCPM-O (mm)
w_{st}	1.14	1.61	1.44	2.03
w_{sp}	N/A	N/A	2.13	2.25
l_{st}	14.89	13.56	11.28	13.22
l_{sp}	2.38	1.37	1.00	3.49
l_{lr}	7.81	4.80	8.15	3.24
w_{ls}	7.41	3.53	3.32	3.48
l_{hc}	12.56	6.35	7.54	7.55
w_{ho}	N/A	8.15	8.05	8.83
w_{hi}	N/A	13.98	12.52	12.99
w_{po}	N/A	8.17	8.31	8.95

7.2. Verification of Optimal Model Using Three-Dimensional Finite Element Method

According to the previous research on the bearingless motors with a CPM structure [93], the analysis error between two-dimensional and three-dimensional analysis in the CPM bearingless motor has been much higher than in the SPM structure. This is caused by the reduction of the magnetic flux density of the iron poles. The part of the magnetic flux generated by the PMs does not pass through the iron poles due to leakage in the z -axis direction. Therefore, the two-dimensional analysis results must be validated by three-dimensional analysis, especially for bearingless motors with a consequent-pole structure.

Fig. 7.3 shows the three-dimensional FEM analysis results for the suspension characteristics of the optimal models selected for each topology. In Fig. 7.3, the suspension force generated towards the positive x -axis is demonstrated. The suspension current $i_{sus} = 10$ A is applied. In Fig. 7.3 (a) and (b), the radial forces F_x and F_y in the x - and y -axis directions are shown, respectively. Fig. 7.3 (c) shows the error angle θ_{err} , as defined in (3.31). Fig. 7.4 shows the unbalanced magnetic pull force F_{ux} , that is the x -axis radial force at the rotor radial displacement $x = 0.5$ mm in the high-speed rotor. In Fig. 7.4, the ripple of the SPM model is significantly higher compared to the other models. This is caused by the interaction occurring between the high-speed rotor PMs and the stator PMs depending on the rotational position of the high-speed rotor. The high ripple of the unbalanced magnetic pull force makes it difficult to control the high-speed rotor radial position. Therefore, the SPM structure is not very suitable due to the excessive unbalanced attractive force ripple, in addition to the requirement to detect the rotor angle for magnetic suspension control. Fig. 7.5 shows the low-speed rotor output torque. According to Fig. 7.5, the torque is different among the models, although the torque of the optimization results is almost the same. Thus, the SPM model has an advantage in the torque. Therefore, the most suitable model depends on the application.

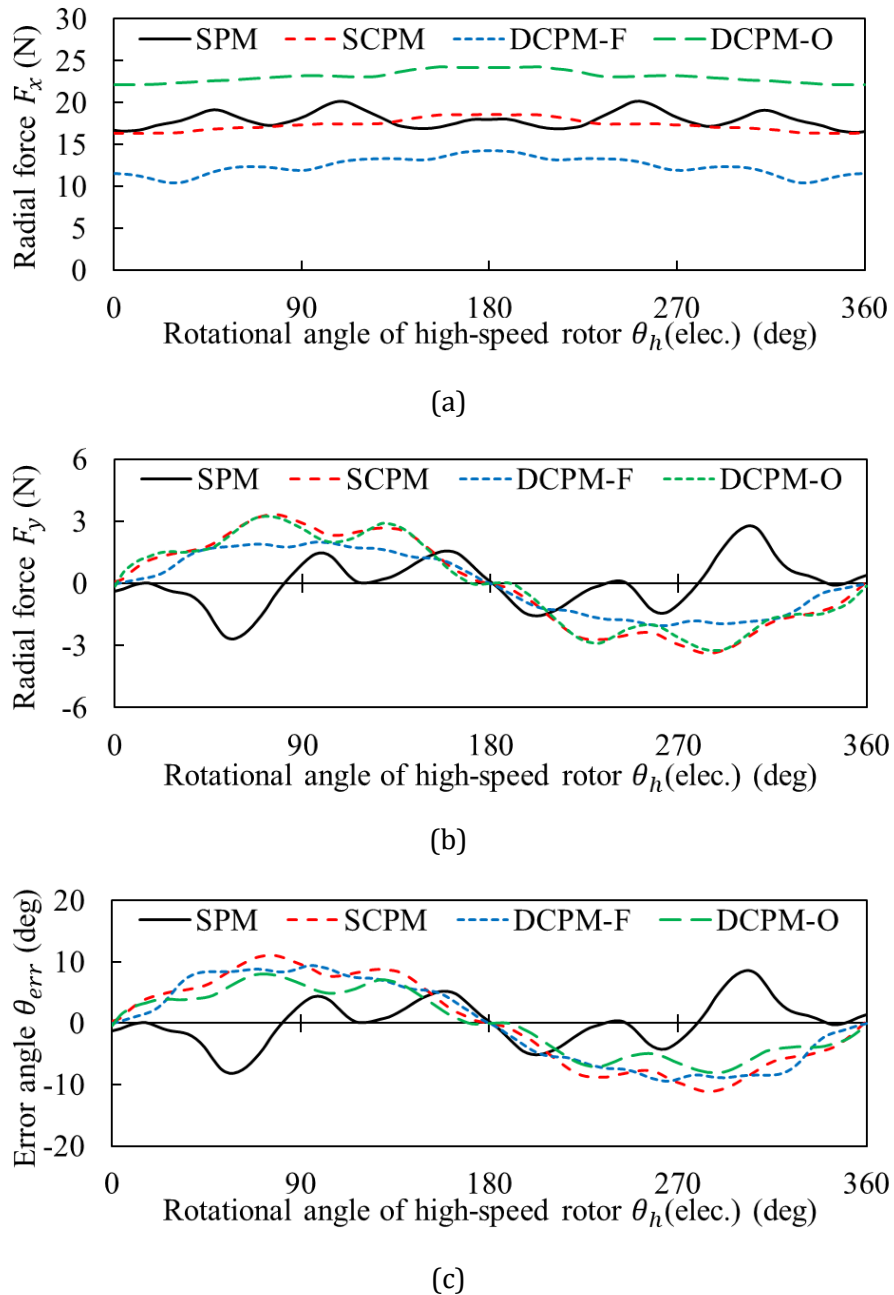


Fig. 7.3. Suspension characteristics waveform with respect to the high-speed rotor (HSR)
angular position θ_h .

- (a) Suspension force in x -axis direction F_x
- (b) Suspension force in y -axis direction F_y
- (c) Error angle θ_{err}

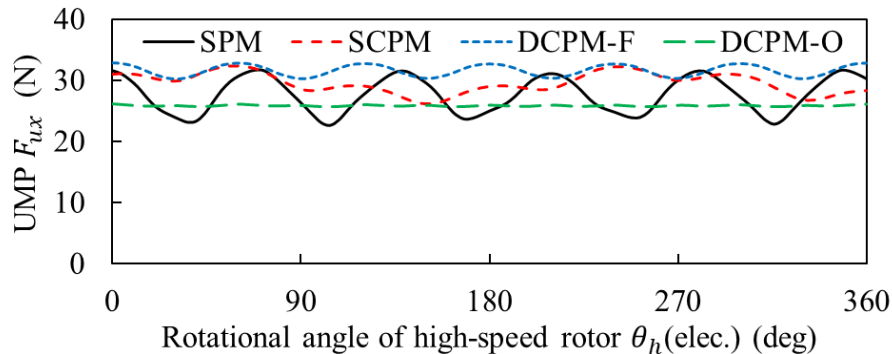


Fig. 7. 4. Unbalanced magnetic pull force F_{ux} waveforms with a high-speed rotor radially displaced by 0.5 mm in the x -axis direction without current.

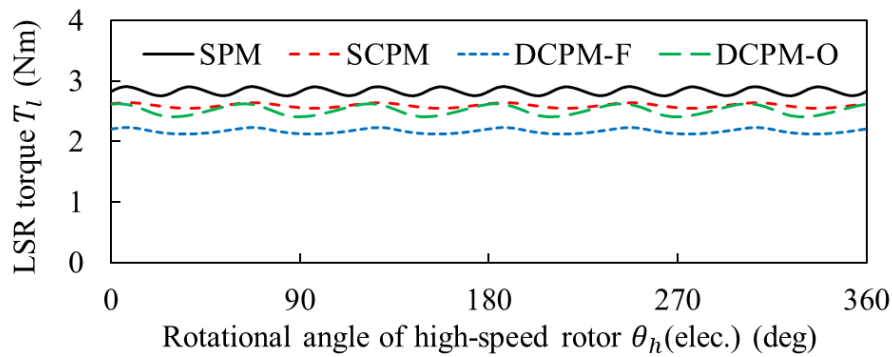


Fig. 7. 5. Low-speed rotor output torque waveforms T_l without current.

Fig. 7. 6 and Table 7. 5 show the comparison between two-dimensional and three-dimensional analysis results. According to these results, the values significantly deteriorated for all optimization objectives. The variation is approximately the same with the topology with the CPM structure. Thus, it is possible to predict the characteristics of the three-dimensional analysis from the results of the two-dimensional analysis. Additionally, the DCPM-O MGM model generates a larger radial force than the SPM-MGM even in the three-dimensional analysis. In addition, the DCPM-O MGM model performs equivalent to the SPM-MGM in terms of torque and error angle factor. Therefore, the DCPM-O MGM model can achieve the equivalent performance to the SPM MGM without the necessity to detecting the rotor angular position.

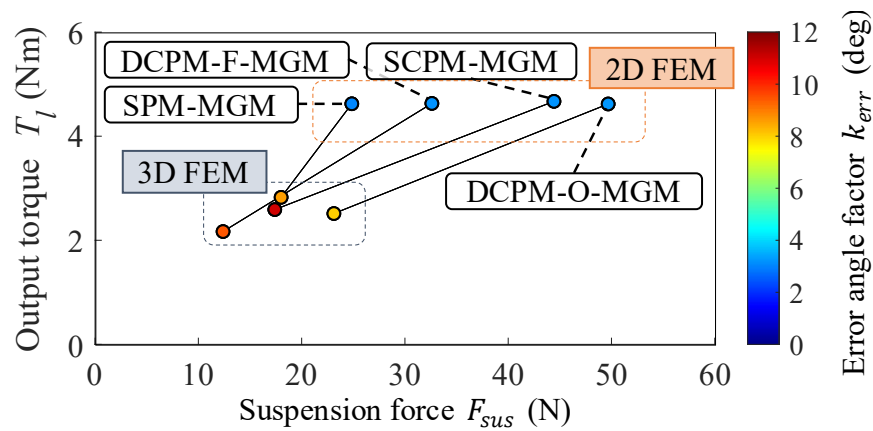


Fig. 7.6. Comparisons between two-dimensional and three-dimensional finite element method analysis results.

Table 7.5. Comparisons between two-dimensional and three-dimensional finite element method analysis results for the optimization objectives.

Average output torque T_l (Nm)				
	SPM	SCPM	DCPM-F	DCPM-O
2D	4.62	4.67	4.63	4.62
3D	2.83	2.59	2.17	2.51
Diff. (%)	-39%	-44%	-53%	-46%
Average suspension force F_{sus} (N)				
	SPM	SCPM	DCPM-F	DCPM-O
2D	24.9	44.4	32.6	49.7
3D	18.0	17.4	12.4	23.1
Diff. (%)	-28%	-61%	-62%	-53%
Maximum error angle factor k_{err} (°)				
	SPM	SCPM	DCPM-F	DCPM-O
2D	3.08	3.20	3.19	3.26
3D	8.59	11.05	9.44	8.04
Diff. (%)	+179%	+246%	+196%	+147%

Fig. 7.7 shows the flux density distribution when the suspension current is applied at 10 A towards the positive x -axis. In the SPM model, the flux density in the stator teeth and the stator back yoke is high compared to the other models. The magnetic flux saturation increases the fluctuation of the suspension characteristics, as shown in Section 4.2. In the SCPCM model, the flux density in the stator is small compared to the SPM model. Thus, the suspension characteristics fluctuation is reduced as shown in Fig. 7.3. In the DCPM-F MGM model, the magnetic flux density in the teeth opposing the PMs of the high-speed rotor is high. Whereas, in the DCPM-O MGM model, the magnetic flux density of the teeth facing the PMs of the high-speed rotor is low. Thus, the DCPM-O MGM model can generate a larger radial force due to the lower magnetic resistance of the magnetic circuit passing through the iron core poles of the high-speed rotor.

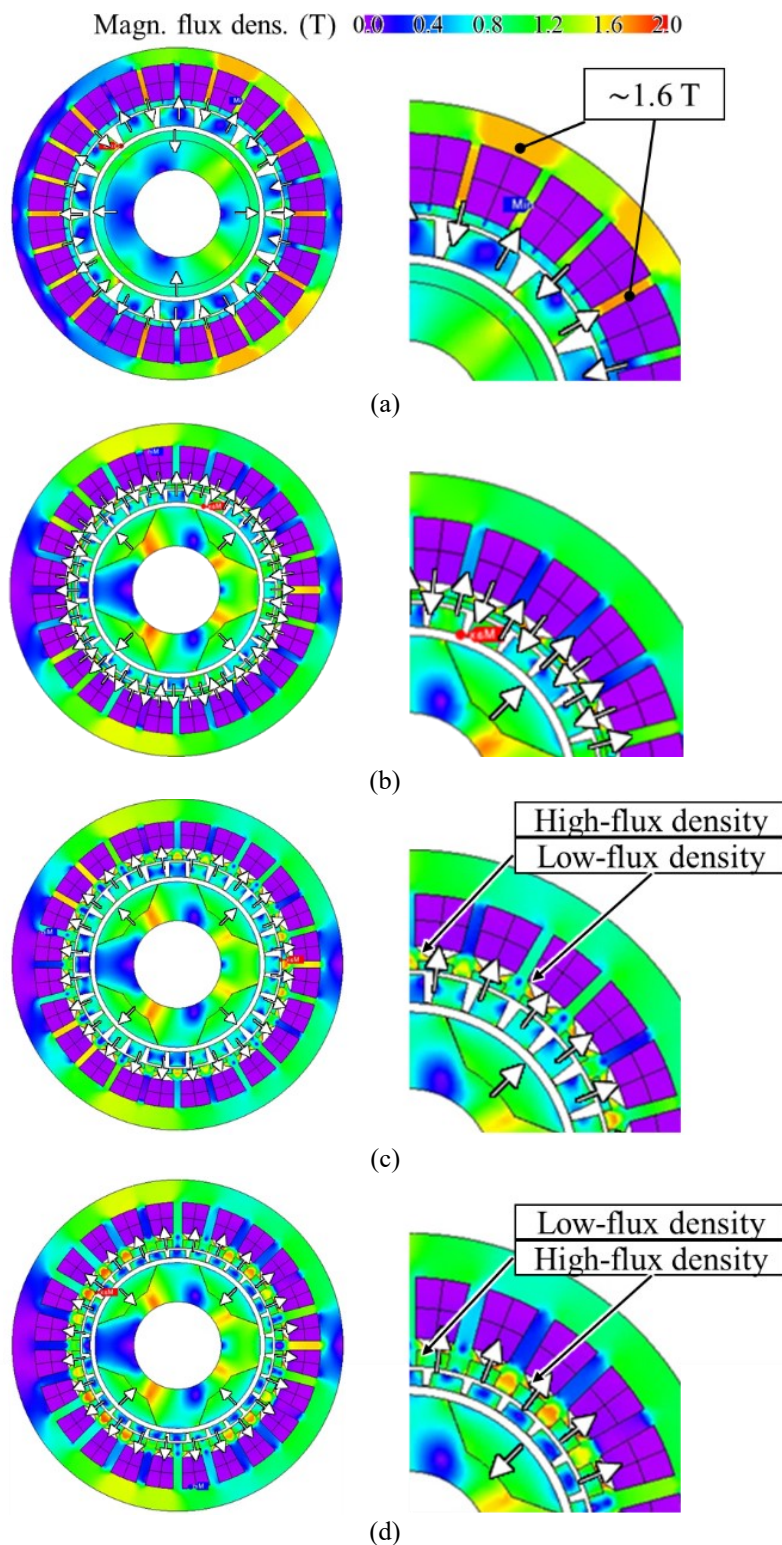
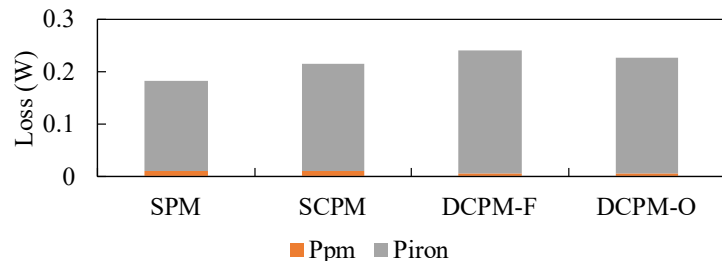


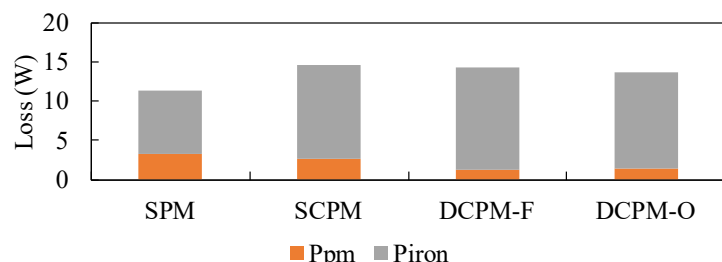
Fig. 7.7. Flux-density distribution of full model and enlarged view with x -axis direction suspension current $i_{sus} = 10$ A.

- (a) SPM-MGM model. (b) SCPM-MGM model.
- (c) DCPM-F-MGM model. (d) DCPM-O-MGM model.

Fig. 7.8 shows the iron loss in the optimal models for each topology. Ppm, Piron, indicate the magnetic eddy current loss and iron loss in laminated silicon steel, respectively. According to Fig. 7.8, at a low-speed rotor rotational speed of 1800 min^{-1} , the percentage of magnetic eddy current loss is higher than that at a low-speed rotor rotational speed of 100 min^{-1} . The efficiency considered only for iron loss in each topology is 99.5%, 99.1%, 96.8%, and 99.1% for SPM, SCPM, DCPM-F, and DCPM-O, respectively, at a low-speed rotor rotational speed of 100 min^{-1} . and 98.4%, 96.8%, 89.5%, and 97.0% at a low-speed rotor rotational speed of 1800 min^{-1} , respectively. Since the winding design has not been decided, copper loss due to winding current has not been taken into consideration.



(a)



(b)

Fig. 7.8. Iron loss in the optimal models for each topology.

(a) Low-speed rotor rotational speed of 100 min^{-1}

(b) Low-speed rotor rotational speed of 1800 min^{-1}

7.3. Summary of Chapter 7

In this chapter, the dimensions of the consequent-pole type magnetic-geared motor with a high-speed rotor in magnetic suspension proposed in Chapter 6 were optimized using a two-dimensional finite element method, and its performance was compared with that of an SPM-type magnetic-geared motor. In addition, the characteristics of the optimized model were analyzed using a three-dimensional finite element method.

In this chapter, the motor characteristics and radial magnetic suspension characteristics were analyzed. However, analysis of the tilt rigidity, functions related to magnetic suspension performance such as interference between the motor current and suspension current shown in Section 4.3, and analysis of the optimal stack length shown in Section 4.6 have not been performed, and the information necessary for manufacturing a prototype is not available. Since the rotor is not covered by permanent magnets, it is unclear how the magnetic flux path of the fringing magnetic flux at the iron core poles differs from that of SPM-type magnetic-geared motors. Therefore, the difference in tilt rigidity from SPM-type magnetic-geared motors needs to be investigated in the future. In addition, it has not been determined whether to detect the rotor position required to control the motor current or to eliminate the sensor and use open-loop control for the motor current, which is a future issue.

Furthermore, as shown in Section 7.2, analysis using the three-dimensional finite element method indicated that the performance of the SPM type was not significantly inferior. In particular, the difference between the two-dimensional and three-dimensional analysis results was smaller than that of the consequent-pole type, suggesting that further investigation of the SPM type is necessary. Specifically, regarding tilt stiffness, since the rotor gap surface is covered by permanent magnets, it is possible that the tilt stiffness is higher than that of the consequent-pole type. This means that it may be possible to achieve a higher stack length than the consequent-pole type, as shown in Section 4.6. For this reason, the torque density may be higher than that of the consequent-pole type. Based on the above, this research has proposed the advantages of the consequent-pole type because it does not require detection of the angular position of the magnetically suspended rotor. However, the SPM type may be superior in terms of torque density.

Chapter 8. Conclusion

8. 1. Summary

High-speed magnetic-gear motors and high-speed magnetic gear are generally challenging due to iron loss caused by magnetic modulation, compared to low-speed, high-torque magnetic-gear motors. Although high-speed magnetic-gear motors have been proposed, bearing loss has been shown to be significant, especially in small high-speed magnetic-gear motors. Therefore, this research proposes a structure for a magnetic-gear motor with a magnetically suspended high-speed rotor, and shows that this structure enables a reduction in bearing losses. In this motor, an additional three-phase winding actively generates a radial force on the high-speed rotor, enabling non-contact magnetic suspension without mechanical bearings on the high-speed rotor.

However, the functions of a bearingless motor and a magnetic-gear motor are contradictory. Particularly, it is unclear what pole combination is suitable for the proposed motor. In addition, unlike general bearingless motors, the proposed motor requires a large magnetic suspension magnetomotive force due to its two air gaps, large and thick permanent magnets, and low permeability resulting from the shape of the low-speed rotor and high magnetic flux density. Accordingly, this study conducted the following investigations and proposed solutions to these issues.

Chapter 1 "Introduction" presents the background and types of magnetic-gear motors and bearingless motors, and clarifies the purpose and significance of this research. It also provides an overview of this thesis.

Chapter 2 "Research Trends on High-Speed Magnetic-Gear Motors/Magnetic Gear and High-Torque Bearingless Motors" describes research trends and issues related to high-speed magnetic-gear motors and magnetic gears. In addition, research trends and issues related to bearingless motor topologies using magnetic modulation are described. The current issues with these motors are presented, and the objectives of this research and solutions to the research issues are described.

Chapter 3 "Structure and Principle of Magnetic-Gear Motor with Magnetic-Suspended High-Speed Rotor" shows the structure and principle of the magnetic-gear motor with a

high-speed rotor on magnetic suspension proposed in this research. In Chapter 3, the magnetic-gear motor topologies and bearingless motor topologies that can be adopted in the proposed method are presented, and possible combinations of topologies are shown. In addition, the principle of determining the pole slot combination, which was one of the research topics, is explained.

Chapter 4 “Proposal and Analysis of High-Speed Rotor Magnetic Suspension for Reluctance-Type Magnetic-Geared Motors” proposes the novel reluctance-type magnetic-gear motor integrated with high-speed bearingless motor. Analysis is used to derive the torque generation principle and magnetic suspension force of the proposed motor, and to clarify the structure that enables magnetic suspension. In this chapter, the method for determining pole slot combinations, which was one of the research topics, was verified by analysis. In addition to examining the basic magnetic suspension performance as a bearingless motor, the analysis of mutual interference between motor current and suspension current, which could be an issue in the manufacture of prototypes, and the examination of the installation method of Hall elements for angular position detection were presented.

Chapter 5 “Experimental Verification of High-Speed Rotor Magnetic Suspension for Reluctance-Type Magnetic-Geared Motors” verifies the magnetic suspension performance through experiments conducted using a prototype machine manufactured based on the model proposed in Chapter 4. Thus, the principle of the proposed reluctance-type magnetic-gear motor integrated with a high-speed bearingless motor has been confirmed by experiments. In this chapter, the results of the analysis in Chapter 4 are verified, and the maximum speed and power consumption during magnetic suspension, which were unclear in the analysis, are determined by experiments. The experiments conducted in this chapter demonstrated the efficiency advantages of magnetic suspension over mechanical bearings in the high-speed range.

Chapter 6 “Investigation of High-Speed Rotor Magnetic Suspension for Consequent-Pole Type Magnetic-Geared Motors” proposes a bearingless high-speed rotor for magnetic-gear motors using consequent poles to improve the torque density of the model proposed in Chapter 4. The characteristics of each motor topology are evaluated by analysis. In this chapter, consequent-type magnetic-gear motors were adopted to improve the low permeability, and motors that can improve torque density without reducing permeability were proposed. In addition, in response to concerns that the angle detection error caused by the

Hall element discovered in Chapter 5 could generate components that are not necessary for the magnetic suspension current, a structure that enables magnetic suspension without using angle detection values was proposed, thereby further simplifying control and reducing the magnetic suspension power.

Chapter 7: Optimization and Verification of High-Speed Rotor Magnetic Suspension for Consequent-Pole Type Magnetic-Geared Motors

Chapter 7 optimizes the dimensions of the motor proposed in Chapter 6, evaluates the torque and magnetic suspension force characteristics of each motor topology, and clarifies a structure capable of magnetic suspension while improving torque density. The motor proposed in Chapter 6 is a new type that has not been proposed before, and it has many design variables, making it difficult to derive the optimal design. Therefore, the optimal model was derived by using a genetic algorithm to optimize the magnetic suspension performance and transmission torque. By evaluating the advantages and disadvantages of each topology using this optimal model, it was shown that the model with the stator and high-speed rotor magnetization in opposite directions in the double-sided consistent type magnetic-geared motor exhibited good performance. All of the optimal models shown in this chapter exceed the performance of the model in Chapter 4, demonstrating improved torque density and magnetic suspension performance.

8. 2. Future Work

8. 2. 1 Change in Tilt Stiffness by *d*-Axis Current

As shown in Section 4. 5, it is difficult to improve the performance of magnetic-gear motors by applying *d*-axis current. However, changing the tilt stiffness by applying a *d*-axis current may change the resonance point in the tilt direction, which could further increase the speed of the prototype. If the speed can be increased, the efficiency of mechanical bearing suspension in the high-speed range may be improved. This requires further investigation, as it may achieve the reduction in bearing loss that is the objective of this research.

8. 2. 2 Investigation of the Optimal Stack Length for Reluctance-Type Magnetic-Geared Motors

As shown in Section 4. 6, the performance of bearingless motors and magnetic-gear motors varies greatly depending on the stack length. In the prototype motor fabricated in this paper, the stack length was set to 10 mm due to various constraints, but it is possible to improve the magnetic suspension performance and maximum transmission torque of the magnetic-gear motor by further increasing the stack length. However, since this research is the only case in which a prototype motor has been manufactured, it is unclear how increasing the stack length will affect performance. In addition, since the tilt stiffness of the prototype has not been measured, further investigation is necessary.

8. 2. 3 Reduction of Power Consumption During Magnetic Suspension

As shown in Section 5. 6, the efficiency of the prototype is not very high due to excessive magnetic suspension power. This may be because the current is unnecessary due to the rotation angle detection error shown in Section 5. 1. 4, which increases the magnetic suspension power. In addition, it may be possible to reduce the magnetic suspension power by improving control methods such as zero power control proposed in previous research. These magnetic suspension power reduction methods need to be investigated in prototype machines.

8. 2. 4 Detailed Measurement of Efficiency and Losses

As shown in Section 5. 6, although the losses and efficiency of the prototype were measured, they were only classified into load losses and no-load losses, and a detailed analysis was not performed. Since these losses differ significantly from analytical values, investigating the loss factors is expected to lead to improved efficiency. In particular, the current is assumed to be a sine wave in the analysis, and the supply voltage is also assumed to be a sine wave. However, in the experiment, the supply voltage is PWM, so the harmonic components of this voltage may contribute to increased losses. Additionally, the extent of mechanical losses is unknown, so further investigation is necessary in these aspects.

8. 2. 5 Evaluation for Prototype Manufacturing of a Consequent-Pole Type Magnetic-Geared Motor

The motor shown in Chapter 7 has significantly improved performance compared to the motor shown in Chapter 4. Meanwhile, there is insufficient evaluation for prototype manufacturing, such as whether the stack length and tilt stiffness considered in Chapter 4 can be completely eliminated, whether angle detection is necessary for motor control, and where to place the angle detection if it is necessary. In particular, further investigation is required for tilt stiffness, as considering this may result in a design that differs from the optimal design derived in Chapter 7.

8. 2. 6 Investigation of Torque Density Improvement by Changing the Magnetic Suspension Method

The motor examined in this paper is a two-axis actively controlled bearingless motor. However, this structure inevitably results in a flat motor, which reduces torque density. Therefore, various magnetic suspension methods can be considered, such as a four-axis actively controlled type with few constraints on torque density, or a single-axis actively controlled type using an axial gap type. It is necessary to examine magnetic suspension methods according to the application.

Annex A. Programs for the Experiment

The programs used in the experiment to conduct this research are listed below.

- a. sin_fitting

https://github.com/akira-kumashiro/sin_fitting

From the signals of each channel in multiple CSV files output by the oscilloscope (DLM2024, Yokogawa Test & Measurement Corp., Japan) used in 5. 1. 3, a sine wave approximation is performed using a genetic algorithm.

- b. OscilloscopeAverage-1

<https://github.com/akira-kumashiro/OscilloscopeAverage-1>

From the signals of each channel in multiple csv files output by the oscilloscope (DLM2024, Yokogawa Test & Measurement Corp., Japan) used in 5. 5, calculate the mean and variance and save them in a single csv file.

- c. OscilloscopeAverage-MW-WAVE

<https://github.com/akira-kumashiro/OscilloscopeAverage-MW-WAVE>

From the signals of each channel in multiple CSV files output by MWPE-WAVE2-USB and Wave Viewer used in 5. 5, calculate the average value and variance and save them in a single CSV file.

- d. BelM_current_control

https://github.com/akira-kumashiro/BelM_current_control

Program for controlling the prototype machine used in Chapter 5.

Annex B. Model Analyzed in Section 4. 1

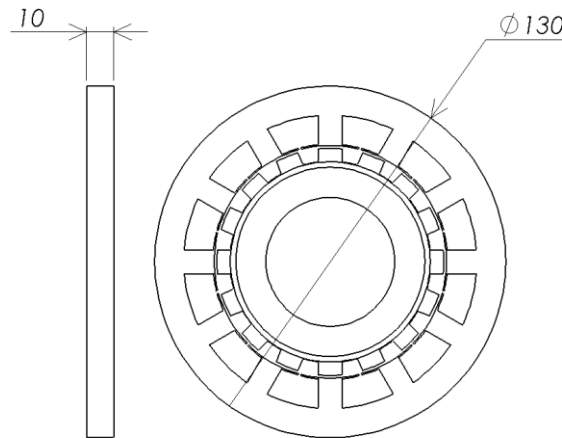


Fig. B. 1. Schematic diagram of all components of a reluctance-type magnetic-gear motor.

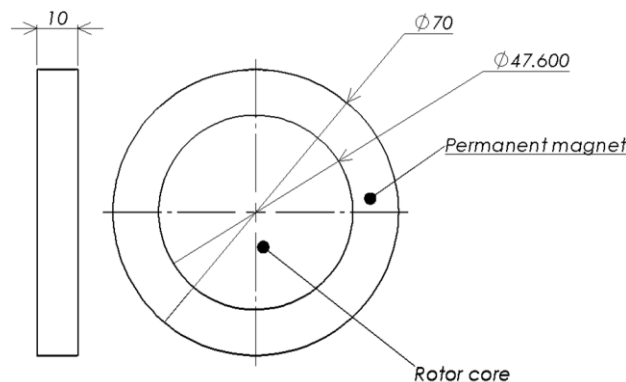


Fig. B. 2. Dimensional drawing of high-speed rotor (HSR).

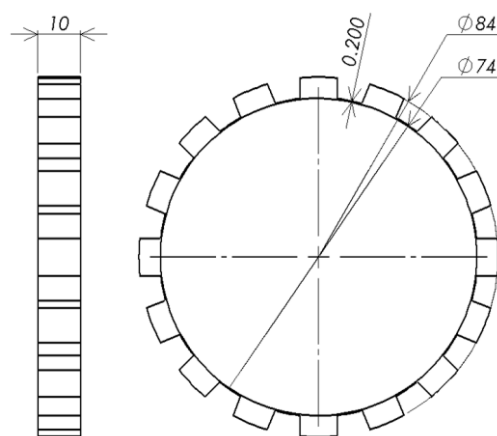


Fig. B. 3. Dimensional drawing of low-speed rotor (LSR).

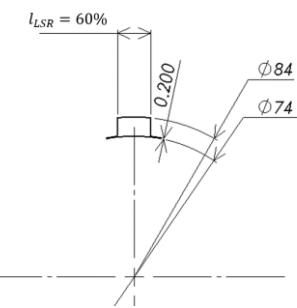


Fig. B. 4. Dimensional drawing of low-speed rotor (LSR) (partial enlargement).

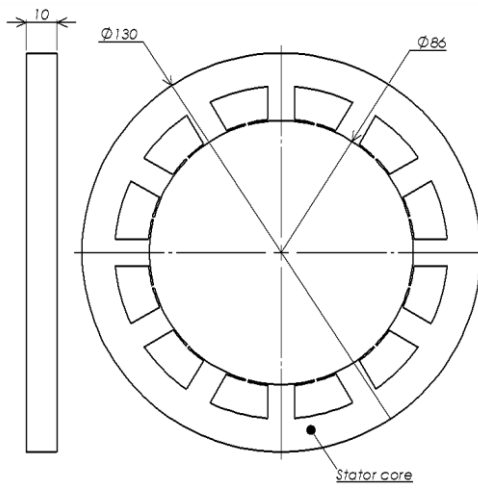


Fig. B. 5. Dimensional drawing of stator.

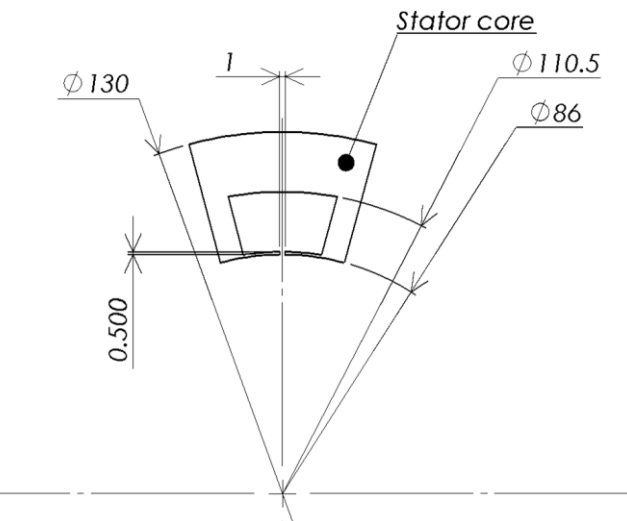


Fig. B. 6. Stator dimension diagram (partial enlargement).

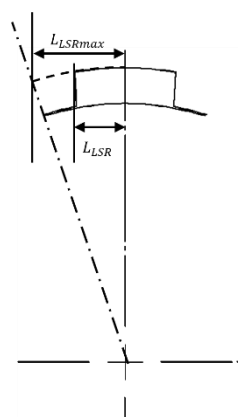


Fig. B. 7. Tooth width of the low-speed rotor (LSR).

Annex C. Reluctance-Type Magnetic-Geared Motor

Model After Section 4. 2

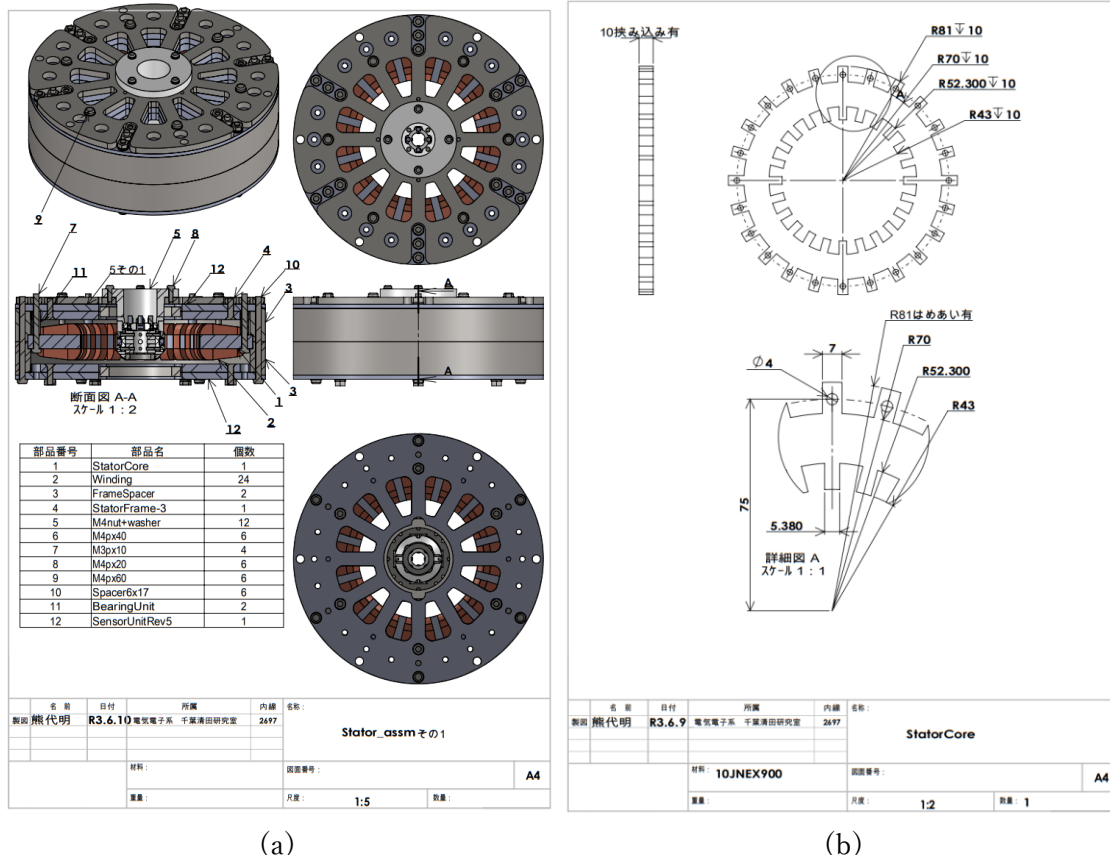


Fig. C. 1. Stator.

(a) Assembly drawing (b) Stator core drawing

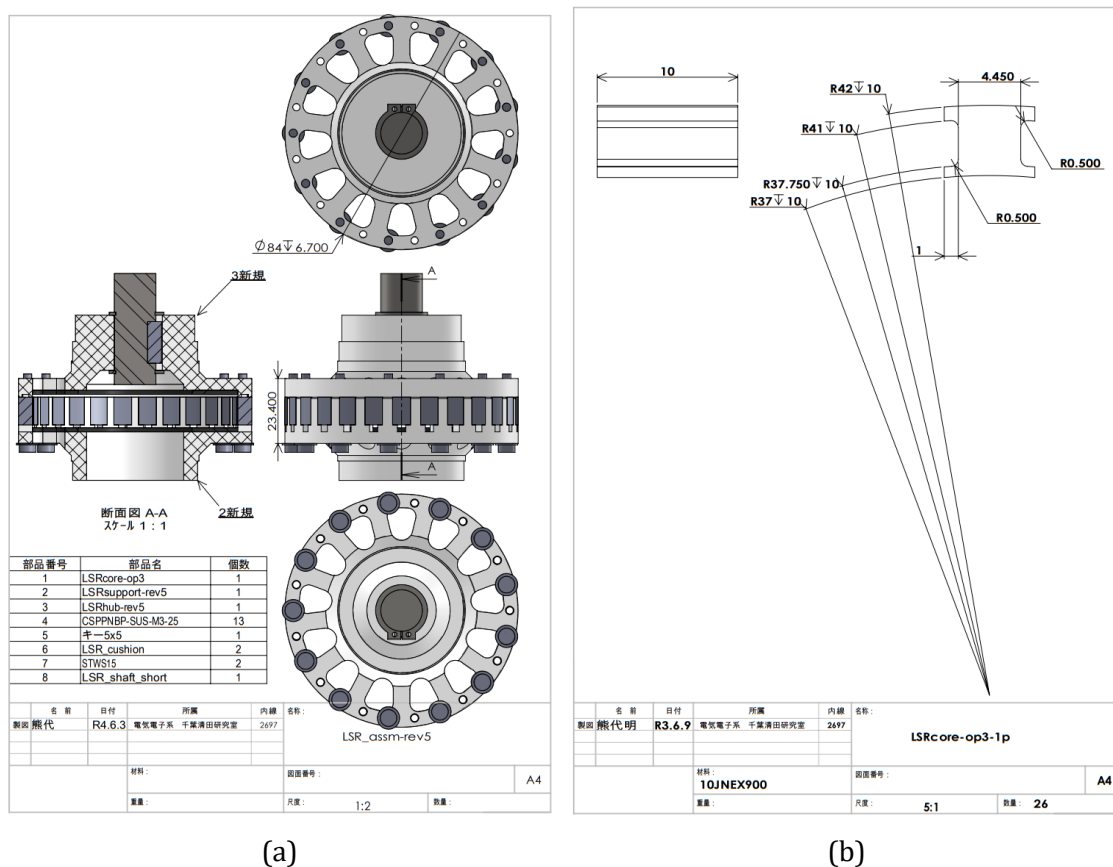


Fig. C. 2. Low-speed rotor.

(a) Assembly drawing (b) Low-speed rotor core drawing

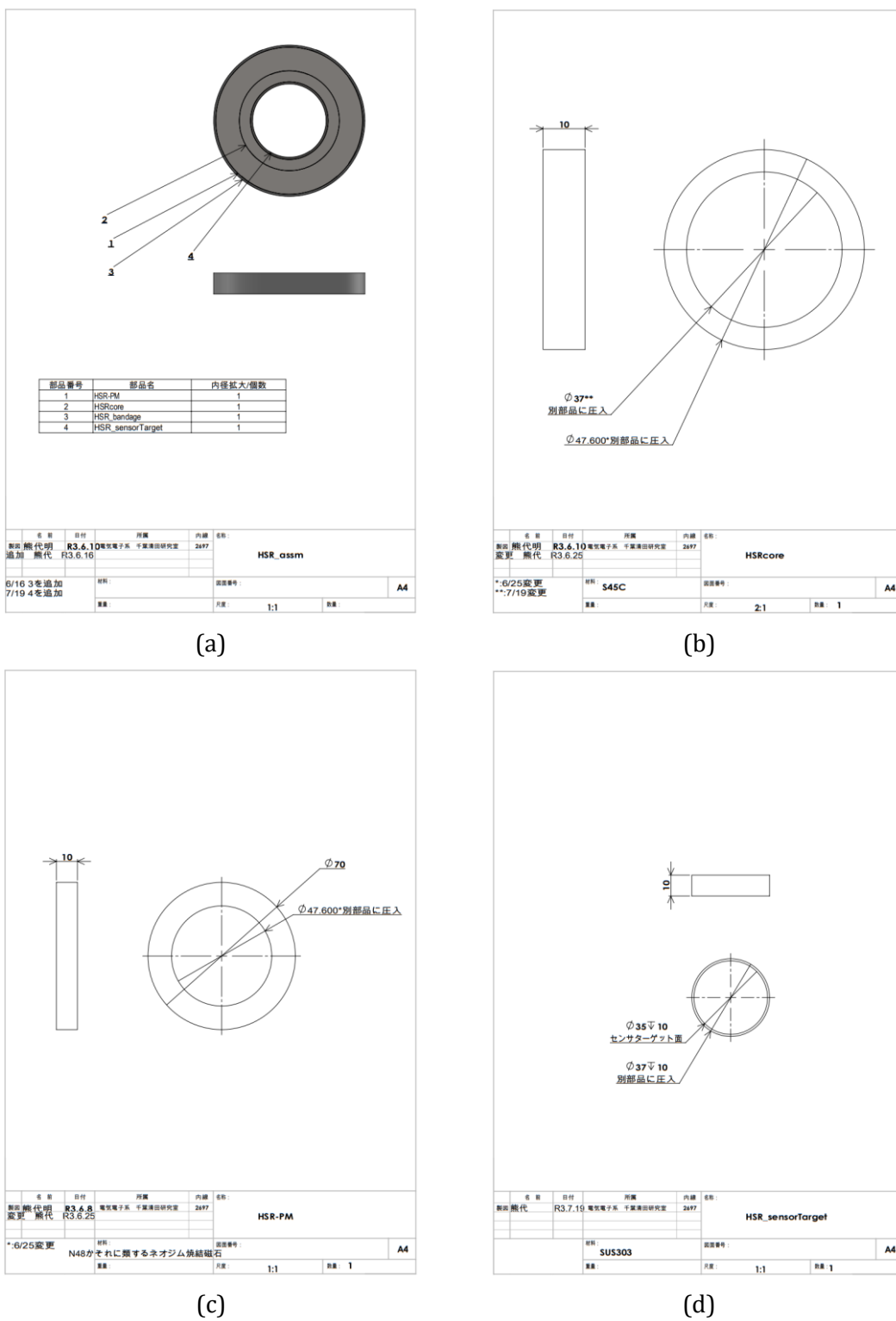


Fig. C. 3. High-speed rotor.

(a) Assembly drawing (b) High-speed rotor core drawing (c) High-speed rotor permanent magnet drawing (d) Sensor target drawing

Dedication

I would like to express my sincere gratitude to Professor Akira Chiba, who provided me with guidance throughout this research. Thanks to his careful guidance in writing seminar and conference papers, revising manuscripts, and preparing presentations, I was able to successfully complete my doctoral program. I am deeply grateful for his support. I would also like to express my sincere gratitude to Associate Professor Yusuke Fujii for his valuable advice on all aspects of my research. His precise guidance in reviewing my papers and determining the direction of my research enabled me to deepen the scope of this research. Thanks to the support of my advisors, I was able to make significant progress toward the actual development of the device. I am truly grateful for their support.

We would also like to express our gratitude to Professor Wolfgang Gruber, Professor Wolfgang Amrhein, Professor Gerald Jungmayr, and Professor Hubert Mitterhofer of Johannes Kepler University Linz for their assistance in editing the paper and providing various advice as co-researchers.

Professor Tadashi Fukami of the Department of Electrical and Electronic Engineering, College of Engineering, Kanazawa Institute of Technology reviewed my doctoral thesis. Thanks to his valuable comments, I was able to significantly improve my thesis. I would like to express my sincere gratitude to him.

I would like to express my sincere gratitude to Associate Professors Akitoshi Okino, Hiroshi Akatsuka, Makoto Hagiwara, and Kyohei Kiyota for conducting the internal review of my doctoral dissertation. In addition, I would like to thank Professor Hideaki Fujita for his valuable advice during each presentation.

I would like to express my gratitude to Mr. Morihiro Saito of Motion System Tech, Inc. for his assistance in manufacturing the prototype, and to Mr. Hiroshi Shimada of Applied Electronics Corporation for his assistance in manufacturing the displacement sensor. The perfect product was a great help to us.

I would like to express my deepest gratitude to Ms. Ei Tokioka, secretary, for her various support during my research. During my master's program, I often submitted documents late, causing her a lot of trouble. I would also like to express my deepest gratitude to Ms. Chikako Watanabe and Ms. Rumi Watanabe, also secretaries.

I would like to express my sincere gratitude to all the members who spent time with me in the laboratory. In particular, I would like to thank Fares S. El-Faouri^j and Yifei Cai^k, who worked diligently with me during my doctoral studies, Dr. Takahiro Noguchi, who kindly advised me as a senior colleague, and Dr. Lingyu Chen, who provided valuable guidance as a researcher in the field of low-speed high-torque motors.

I would like to express my sincere gratitude to Assistant Professor Seiji Ishikawa of the Department of Electrical and Electronic Engineering at the National Institute of Technology, Oita College, who introduced me to magnetic gears during my time at college.

I would like to express my gratitude to Takeru Sato, a graduate of the Takeuchi Laboratory. I was greatly supported by him for nine years from my time at the National Institute of Technology until my master's graduation, and even after that.

I would like to deeply thank my wife, Honoka, who has always strongly supported me. Thanks to her perfect support in all aspects of life, I was able to complete my doctoral program in three years.

Finally, I would like to express my deepest gratitude to my parents, Toru Kumashiro and Aya Kumashiro, my parents-in-law, Kenji Yama and Masayo Yama, and all my extended family members who have supported me throughout my life. In addition, I would like to express my heartfelt gratitude to my grandmother, Yumi Ikenaga, for her various words of advice. I hope you live a long and healthy life. And I would like to express my deepest gratitude to the late Futoshi Ikenaga for sparking my interest in science.

^j At the time of writing original version of this thesis, he was a doctoral student. He received his Doctor of Engineering degree in September 2024 and is currently an assistant professor at Princess Sumaya University for Technology.

^k At the time of writing original version of this thesis, he was a doctoral student. He received his Doctor of Engineering degree in September 2024.

Reference

- [1] A. Krings and C. Monissen, "Review and Trends in Electric Traction Motors for Battery Electric and Hybrid Vehicles," *Proceedings of the International Conference on Electrical Machines (ICEM)*, vol. 1, pp. 1807-1813, 2020.
- [2] J. C. Perry, J. Rosen and S. Burns, "Upper-limb powered exoskeleton design," *IEEE/ASME transactions on mechatronics*, vol. 12, no. 4, pp. 408-417, 2007.
- [3] B. McNiff, M. W. D. and R. Errichello, "Variations in Gear Fatigue Life for Different Wind Turbine Braking Strategies," in *Prepared for A WEA Wind Power '90* , Washington, D. C. , 1991.
- [4] Y. Wang, M. Filippini, N. Bianchi and P. Alotto, "A Review on Magnetic Gears: Topologies, Computational Models, and Design Aspects," *IEEE Transactions on Industry Applications*, vol. 55, no. 5, pp. 4557-4566, 2019.
- [5] T. B. Martin, "Magnetic transmission". US Patent 3 378 710, 1968.
- [6] N. Laing, "Magnetic transmission". US Patent 3 645 650, 1972.
- [7] N. Laing, "Centrifugal pump with magnetic drive". US Patent 3 762 839, 1973.
- [8] B. Ackermann and L. Honds, "Magnetic drive arrangement comprising a plurality of magnetically cooperating parts which are movable relative to one another". US Patent 5 633 555, 1997.
- [9] B. Ackermann, "Magnetic drive arrangement". US Patent 5 994 809, 1999.
- [10] C. G. Armstrong, "Power transmitting device". US Patent 687 292, 1901.
- [11] H. T. Faus, "Magnet gearing". US Patent 2 243 555, 1941.
- [12] S. Rand, "Magnetic transmission system". US Patent 3 523 204, 1970.
- [13] M. Hetzel, "Low friction miniature gear drive for transmitting small forces, and method of making same". US Patent 3 792 578, 1974.
- [14] K. Ikuta, S. Makita and S. Arimoto, "Non-contact magnetic gear for micro transmission mechanism," *Proceedings of IEEE Micro Electro Mechanical Systems*, pp. 125-130, 1991.

- [15] Y. D. Yao, D. R. Huang, C. C. Hsieh, D. Y. Chiang and S. J. Wang, "Magnetic coupling studies between radial magnetic gears," *IEEE Transactions on Magnetics*, vol. 33, no. 5, pp. 4236-4238, 1997.
- [16] Y. D. Yao, D. R. Huang, C. C. Hsieh, D. Y. Chiang and S. J. Wang, "Simulation study of the magnetic coupling between radial magnetic gears," *IEEE Transactions on Magnetics*, vol. 33, pp. 2203-2206, 1997.
- [17] E. Furlani, "A two-dimensional analysis for the coupling of magnetic gears," *IEEE Transactions on Magnetics*, vol. 33, no. 3, pp. 2317-2321, 1997.
- [18] K. Atallah and D. Howe, "A novel high-performance magnetic gear," *IEEE Transactions on Magnetics*, vol. 37, no. 4, pp. 2844-2846, 2001.
- [19] N. Niguchi and K. Hirata, "Torque Ripple Analysis of a Magnetic-Geared Motor," *Proceedings of the 2014 International Conference on Electrical Machines*, pp. 787-792, 2012.
- [20] K. T. Chau, "Magnetic-Geared Motor Drives," in *Electric Vehicle Machines and Drives: Design, Analysis and Application*, Wiley-IEEE Press, 2015, pp. 195-226.
- [21] S. Gerber and R.-J. Wang, "Analysis of the end-effects in magnetic gears and magnetically geared machines," *Proceedings of 2014 International Conference on Electrical Machines (ICEM)*, pp. 396-402, 2014.
- [22] P. M. Tlali, R.-J. Wang and S. Gerber, "Magnetic gear technologies: A review," *Proceedings of 2014 International Conference on Electrical Machines (ICEM)*, pp. 544-550, 2014.
- [23] M. Venturini and F. Leonardi, "High torque, low speed joint actuator based on PM brushless motor and magnetic gearing," *IEEE-IAS Annual Meeting*, vol. 1, pp. 37-42, 1993.
- [24] A. Razzell and J. Cullen, "Compact electrical machine". US Patent 6 794 781B2, 2004.
- [25] K. Chau, D. Zhang, Z. Jiang, C. Liu and Y. Zhang, "Design of a magnetic-geared outer-rotor permanent-magnet brushless motor for electric vehicles," *IEEE Transaction on Magnetics*, vol. 43, no. 6, pp. 2504-2506, 2007.
- [26] L. Jian, G. Xu, Y. Gong, J. Song, J. Liang and M. Chang, "Electromagnetic design and analysis of a novel magnetic gear integrated wind power generator using time-stepping

- FEM," *Progress in Electromagnetics Research-pier*, vol. 113, pp. 351-367, 2011.
- [27] K. Atallah, J. Rens, S. Mezani and D. Howe, "A Novel "Pseudo" Direct Drive Brushless Permanent Magnet Machine," *IEEE Transactions on Magnetics*, vol. 44, no. 11, pp. 4349-4352, 2008.
- [28] L. Jian, K. T. Chau and J. Z. Jiang, "A Magnetic-Geared Outer-Rotor Permanent-Magnet Brushless Machine for Wind Power Generation," *IEEE Transactions on Industry Applications*, vol. 45, no. 3, pp. 954-962, 2009.
- [29] B. Bidouche, T. Lubin and S. Mezani, "Design and Analysis of a Magnetically Geared Induction Machine," *Proceedings of 2018 XIII International Conference on Electrical Machines (ICEM)*, pp. 629-634, 2018.
- [30] K. Ito and K. Nakamura, "小型 EV 用インホイール磁気ギヤード SR モータの提案 / Proposal of In-wheel type Magnetic-Geared SR Motor for Compact EV," *Transaction on Magnetics Society Japan*, vol. 7, no. 1, pp. 55-60, 2023.
- [31] L. Jing, Y. Pan, T. Wang, R. Qu and P.-T. Cheng, "Transient analysis and verification of a magnetic gear integrated permanent magnet brushless machine with Halbach arrays," *IEEE Journal of Emerging and Selected Topics in Power Electronics*, vol. 10, no. 2, pp. 1881-1890, 2022.
- [32] P. O. Rasmussen, T. V. Frandsen, K. K. Jensen and K. Jessen, "Experimental evaluation of a motor-integrated permanent-magnet gear," *IEEE Transactions on Industrial Applications*, vol. 49, no. 2, pp. 850-859, 2013.
- [33] S. Du, Y. Zhang and J. Z. Jiang, "Research on a novel combined permanent magnet electrical machine," *Proceedings of 2008 International Conference on Electrical Machines and Systems*, pp. 3564-3567, 2008.
- [34] L. Jian, K. Chau and J. Jiang, "An integrated magnetic-geared permanent-magnet inwheel motor drive for electric vehicles," *Proceedings of 2008 IEEE Vehicle Power and Propulsion Conference*, pp. 1-6, 2008.
- [35] Z. Q. Zhu, H. Y. Li, R. Deodhar, A. Pride and T. Sasaki, "Recent developments and comparative study of magnetically geared machines," *CES Transactions on Electrical Machines and Systems*, vol. 2, no. 1, pp. 13-22, 2018.
- [36] R. O. Rasmussen, H. H. Mortensen, T. N. Matzen, T. M. Jahns and H. A. Toliat,

- "Motor integrated permanent magnet gear with a wide torque-speed range," *Proceedings of 2009 IEEE Energy Conversion Congress and Exposition*, pp. 1510-1518, 2009.
- [37] S. Gerber and R.-J. Wang, "Torque capability comparison of two magnetically geared PM machine topologies," *Proceedings of 2013 IEEE International Conference on Industrial Technology (ICIT)*, pp. 1915-1920, 2013.
- [38] K. Ito and K. Nakamura, "Investigation of Magnetic Interaction of IPM-Type Magnetic-Geared Motor," *IEEE Transactions on Magnetics*, vol. 57, no. 2, 2021.
- [39] N. Niguchi and K. Hirata, "磁気ギアードモータのコギングトルク特性 / Cogging Torque Characteristics of a Magnetic-Geared Motor," *IEEJ Transaction on Industry Applications*, vol. 132, no. 6, pp. 673-681, 2012.
- [40] S. Hasanpour, M. C. Gardner, M. Johnson and H. A. Toliyat, "Comparison of Reluctance and Surface Permanent Magnet Coaxial Magnetic Gears," *Proceedings of the IEEE Energy Conversion Congress and Exposition*, pp. 307-314, 2020.
- [41] N. Niguchi and K. Hirata, "新しい磁気ギアードモータ / A Novel Magnetic-Geared Motor," *Journal of the Japan Society of Applied Electromagnetics and Mechanics*, vol. 21, no. 2, pp. 110-115, 2013.
- [42] J. Chen, J. Zhu and E. L. Severson, "Review of Bearingless Motor Technology for Significant Power Applications," *IEEE Transactions on Industry Applications*, vol. 56, no. 2, pp. 1377-1388, 2020.
- [43] A. Chiba, T. Fukao, O. Ichikawa, M. Oshima, M. Takemoto and D. G. Dorrell, *Magnetic bearings and bearingless drives*, Elsevier, 2005.
- [44] M. T. Bartholet, T. Nussbaumer, S. Silber and J. W. Kolar, "Comparative Evaluation of Polyphase Bearingless Slice Motors for Fluid-Handling Applications," *IEEE Transactions on Industry Applications*, vol. 45, no. 5, pp. 1821-1830, 2009.
- [45] M. Neff, N. Barletta and R. Schoeb, "Bearingless centrifugal pump for highly pure chemicals," *Proceedings of 8th International Symposium on Magnetic Bearing*, pp. 283-288, 2002.
- [46] T. Masuzawa, T. Kita and Y. Okada, "An Ultradurable and Compact Rotary Blood Pump with a Magnetically Suspended Impeller in the Radial Direction," *Artificial*

- Organs*, vol. 25, no. 5, pp. 395-399, 2001.
- [47] H. Hoshi, T. Shinshi and S. Takatani, "Third-generation blood pumps with mechanical noncontact magnetic bearings," *Artificial organs*, vol. 30, no. 5, pp. 324-338, 2006.
 - [48] B. Warberger, R. Remo Kaelin, T. Nussbaumer and J. W. Kolar, "50-N·m/2500-W Bearingless Motor for High-Purity Pharmaceutical Mixing," *IEEE Transactions on Industrial Electronics*, vol. 59, no. 5, pp. 2236-2247, 2012.
 - [49] T. Reichert, T. Nussbaumer and J. W. Kolar, "Investigation of Exterior Rotor Bearingless Motor Topologies for High-Quality Mixing Applications," *IEEE Transactions on Industry Applications*, vol. 48, no. 6, pp. 2206-2216, 2012.
 - [50] T. Nussbaumer, P. Karutz, F. Zurcher and J. W. Kolar, "Magnetically Levitated Slice Motors—An Overview," *IEEE Transactions on Industry Applications*, vol. 47, no. 2, pp. 754-766, 2011.
 - [51] E. Severson, R. Nilssen, T. Undeland and N. Mohan, "Suspension force model for bearingless AC homopolar machines designed for flywheel energy storage," *Proceedings of 2013 7th IEEE GCC Conference and Exhibition (GCC)*, pp. 274-279, 2013.
 - [52] H. Mitterhofer, B. Mrak and W. Gruber, "Comparison of High-Speed Bearingless Drive Topologies With Combined Windings," *IEEE Transactions on Industry Applications*, vol. 51, no. 3, pp. 2116-2122, 2015.
 - [53] Z. Liu, A. Chiba, Y. Irino and Y. Nakazawa, "Optimum Pole Number Combination of a Buried Permanent Magnet Bearingless Motor and Test Results at an Output of 60 kW With a Speed of 37000 r/min," *IEEE Open Journal of Industry Applications*, vol. 1, pp. 33-41, 2020.
 - [54] H. Sugimoto, I. Shimura and A. Chiba, "Principle and Test Results of Energy-Saving Effect of a Single-Drive Bearingless Motor in Cooling Fan Applications," *IEEJ Journal of Industry Applications*, vol. 6, no. 6, pp. 456-462, 2017.
 - [55] G. Munteanu, A. Binder and S. Dewenter, "Five-axis magnetic suspension with two conical air gap bearingless PM synchronous half-motors," *Proceedings of International Symposium on Power Electronics Power Electronics, Electrical Drives, Automation and Motion*, pp. 1246-1251, 2012.

- [56] P. Kascak, R. Jansen, T. Dever, A. Nagorny and K. Loparo, "Levitation performance of two opposed permanent magnet pole-pair separated conical bearingless motors," *Proceedings of 2011 IEEE Energy Conversion Congress and Exposition*, pp. 1649-1656, 2011.
- [57] M. Ohsawa, "Study of the Induction type Bearingless Motor," *Proceedings of Seventh International Symp. on Magnetic Bearings (ISMB)*, pp. 389-394, 2000.
- [58] R. P. Jastrzebski, P. Jaatinen, A. Chiba and O. Pyrhnen, "Efficiency of buried permanent magnet type 5kW and 50kW high-speed bearingless motors with 4-pole motor windings and 2-pole suspension windings," *Proceedings of International Symposium on Magnetic Bearings*, pp. 1-8, 2016.
- [59] R. P. Jastrzebski, P. Jaatinen, H. Sugimoto, O. Pyrhoenen and A. Chiba, "Design of a bearingless 100 kW electric motor for high-speed applications," *Proceedings of 2015 18th International Conference on Electrical Machines and Systems (ICEMS)*, pp. 2008-2014, 2015.
- [60] R. P. Jastrzebski, P. Jaatinen, O. Pyrhoenen and A. Chiba, "Design of 6-slot inset PM bearingless motor for high-speed and higher than 100kW applications," *Proceedings of 2017 IEEE International Electric Machines and Drives Conference (IEMDC)*, pp. 1-8, 2017.
- [61] Y. Fu, M. Takemoto, S. Ogasawara and K. Orikawa, "Investigation of a high speed and high power density bearingless motor with neodymium bonded magnet," *Proceedings of 2017 IEEE International Electric Machines and Drives Conference (IEMDC)*, pp. 1-8, 2017.
- [62] O. Ichikawa, A. Chiba and T. Fukao, "Inherently decoupled magnetic suspension in homopolar-type bearingless motors," *IEEE Transactions on Industry Applications*, vol. 37, no. 6, pp. 1668-1674, 2001.
- [63] J. Asama, R. Natsume, H. Fukuura, T. Oiwa and A. Chiba, "Optimal Suspension Winding Configuration in a Homo-Polar Bearingless Motor," *IEEE Transactions on Magnetics*, vol. 48, no. 11, pp. 2973-2976, 2012.
- [64] E. Severson and N. Mohan, "Bearingless motor system design for industrial applications," *Proceedings of 2017 IEEE International Electric Machines and Drives*

- Conference (IEMDC)*, pp. 1-8, 2017.
- [65] M. Takemoto, "Basic characteristic of a two-unit outer rotor type bearingless motor with consequent pole permanent magnet structure," *Proceedings of 2014 International Power Electronics Conference*, pp. 1000-1005, 2014.
 - [66] J. Amemiya, A. Chiba, D. G. Dorrell and T. Fukao, "Basic characteristics of a consequent-pole-type bearingless motor," *IEEE Transactions on Magnetics*, vol. 41, no. 1, pp. 82-89, 2005.
 - [67] E. Severson, R. Nilssen, T. Undeland and N. Mohan, "Dual-Purpose No-Voltage Winding Design for the Bearingless AC Homopolar and Consequent Pole Motors," *IEEE Transactions on Industry Applications*, vol. 51, no. 4, pp. 2884-2895, 2015.
 - [68] S. Silber, W. Amrhein, P. Boesch, R. Schoeb and N. Barletta, "Design aspects of bearingless slice motors," *IEEE Transaction on Mechatronics*, vol. 10, no. 6, p. 611-617, 2005.
 - [69] Y. Okada, K. Dejima and O. T, "Analysis and comparison of PM synchronous motor and induction motor type magnetic bearings," *IEEE Transactions on Industry Applications*, vol. 31, no. 5, p. 1047-1053, 1995.
 - [70] Y. Okada, S. Miyamoto and T. Ohishi, "Levitation and torque control of internal permanent magnet type bearingless motor," *IEEE Transactions on Control Systems Technology*, vol. 4, no. 5, p. 565-571, 1996.
 - [71] W. Amrhein, S. Silber and K. Nenninger, "Levitation forces in bearingless permanent magnet motors," *IEEE Transactions on Magnetics*, vol. 35, no. 5, pp. 4052-4054, 1999.
 - [72] M. Ooshima, S. Miyazawa, T. Deido, A. Chiba, F. Nakamura and T. Fukao, "An Analysis and Characteristics of a Permanent Magnet Type Bearingless Motor," *IEEE Transactions on Industry Applications*, vol. 115, no. 9, pp. 1131-1139, 1995.
 - [73] M. Nakagawa, Y. Asano, A. Mizuguchi, A. Chiba, C. X. Xuan, M. Ooshima, M. Takemoto, T. Fukao, O. O. Ichikawa and D. G. Dorrell, "Optimization of stator design in a consequent-pole type bearingless motor considering magnetic suspension characteristics," *IEEE Transaction on Magnetics*, vol. 42, no. 10, p. 3422-3424, 2006.
 - [74] J. Asama, R. Kawata, T. Tamura, T. Oiwa and A. Chiba, "Reduction of force interference and performance improvement of a consequent-pole bearingless motor,"

- Precision Engineering*, vol. 36, no. 1, pp. 10-18, 2012.
- [75] T. Stallinger, W. Gruber and W. Amrhein, "Bearingless segment motor with a consequent pole rotor," *Proceedings of 2009 IEEE International Electric Machines and Drives Conference*, p. 1374–1380, 2009.
 - [76] P. N. Boesch and N. Barletta, "High Power Bearingless Slice Motor (3-4kW) for Bearingless Canned Pumps," *Proceedings of 9th International Symposium on Magnetic Bearings*, 2004.
 - [77] H. Mitterhofer, W. Gruber and W. Amrhein, "On the High Speed Capacity of Bearingless Drives," *IEEE Transactions on Industrial Electronics*, vol. 61, no. 6, pp. 3119-3126, 2014.
 - [78] E. Gobl, W. Amrhein and H. Mitterhofer, "Slotless bearingless high speed disk drive designed for speeds beyond 100krpm," *Proceedings of 2017 IEEE 12th International Conference on Power Electronics and Drive Systems (PEDS)*, pp. 1-17, 2017.
 - [79] T. Reichert, T. Nussbaumer and J. Kolar, "Bearingless 300-W PMSM for Bioreactor Mixing," *IEEE Transactions on Industrial Electronics*, vol. 59, no. 3, p. 1376–1388, 2012.
 - [80] J. Asama, Y. Hamasaki, T. Oiwa and A. Chiba, "Proposal and Analysis of a Novel Single-Drive Bearingless Motor," *IEEE Transactions on Industrial Electronics*, vol. 60, no. 1, pp. 129-138, 2013.
 - [81] H. Sugimoto and A. Chiba, "Dynamic Modeling and Experimental Validations of Passing Through Critical Speeds by High Acceleration in One-Axis Actively Positioned Bearingless Motors," *IEEE Transactions on Industrial Applications*, vol. 57, no. 6, p. 6956–6964, 2021.
 - [82] Q. D. Nguyen and U. Ueno, "Modeling and Control of Salient-Pole Permanent Magnet Axial-Gap Self-Bearing Motor," *IEEE/ASME Transactions on Mechatronics*, vol. 16, no. 3, pp. 518-526, 2011.
 - [83] J. V. Verdegem, M. Lefebvre, V. Kluyskens and B. Dehez, "Dynamical Modeling of Passively Levitated Electrodynamic Thrust Self-Bearing Machines," *IEEE Transactions on Industry Applications*, vol. 55, no. 2, pp. 1447-1460, 2019.
 - [84] V. Kluyskens, C. Dumont and B. Dehez, "Description of an Electrodynamic Self-

- Bearing Permanent Magnet Machine," *IEEE Transactions on Magnetics*, vol. 53, no. 1, 2017.
- [85] G. C. Rubio, V. C. H. F. Y. Komal and A. Chiba, "Experimental Verification of Passive Axial Electrodynamic Suspension in a Bearingless Motor," *IEEE Open Journal of Industry Applications*, vol. 4, pp. 49-59, 2023.
- [86] H. Sugimoto, T. Hashimoto, T. Arai, H. Suzuki and A. Chiba, "Novel Bearingless Motor Topology With Diamagnetic Salient-Pole Rotor," *IEEE Transactions on Industry Applications*, vol. 59, no. 2, pp. 1639-1647, 2023.
- [87] 一般社団法人電気学会磁気浮上技術調査専門委員会編, 磁気浮上技術の原理と応用, 科学情報出版株式会社, 2018.
- [88] D. J. J. M. J. M. G. T. Clark, "An Overview of Magnetic Bearing Technologyfor Gas Turbine Engines," 2004.
- [89] W. Gruber, T. Nussbaumer, H. Grabner and W. Amrhein, "Wide air gap and large-scale bearingless segment motor with six stator elements," *IEEE Transactions on Magnetics*, vol. 46, no. 6, pp. 2438-2441, 2010.
- [90] F. Zuercher, T. Nussbaumer, W. Gruber and J. W. Kolar, "Design and development of a 26-pole and 24-Slot bearingless motor," *IEEE Transactions on Magnetics*, vol. 45, no. 10, pp. 4594-4597, 2009.
- [91] O. Ichikawa, C. Michioka, A. Chiba and T. Fukao, "An analysis of radial forces and a rotor position control method of reluctance type bearingless motor," *IEE Transactions on Industry Applications*, vol. 117, no. 9, pp. 1123-1131, 1997.
- [92] H. Ding, H. Zhu and Y. Hua, "Optimization design of bearingless synchronous reluctance motor," *IEEE Transactions on Applied Superconductivity*, vol. 28, no. 3, pp. 1-5, 2018.
- [93] T. Noguchi, H. Sugimomto, Y. Fujii and A. Chiba, "ベアリングレスモータのギャップ磁束密度に基づく半径方向磁気支持力発生原理の理論 / Verifying the Calculation Approach for Radial Suspension Force based on the Airgap Flux Density for SPM, Consequent-Pole, and Bearingless AC Homopolar Motors," *IEEJ Transactions on Industry Applications*, vol. 142, no. 7, pp. 506-515, 2022.
- [94] E. Marth, G. Jungmayr, W. Amrhein and F. Jeske, "Magnetic-gearred motor in side-by-

- side arrangement-optimization," *Proceedings of the IEEE International Electric Machines & Drives Conference (IEMDC)*, pp. 839-846, 2019.
- [95] K. Aiso, K. Akatsu and Y. Aoyama, "A Novel Reluctance Magnetic Gear for High-Speed Motor," *IEEE Transactions on Industry Applications*, vol. 55, no. 3, pp. 2690-2699, 2019.
- [96] L. Chen, A. Thabuis, Y. Fujii, A. Chiba, M. Nagano and K. Nakamura, "Principle and Analysis of Radial-Force-Based Swirling Actuator for Low-Speed High-Torque Applications," *IEEE Transactions on Industry Applications*, vol. 58, no. 2, pp. 1963-1975, 2022.
- [97] M. Ooshima, "Analyses of rotational torque and suspension force in a permanent magnet synchronous bearingless motor with short-pitch winding," *Proceedings of the IEEE Power Engineering Society General Meeting*, pp. 1-7, 2007.
- [98] K. Radman, N. Bulić and W. Gruber, "Performance evaluation of a bearingless flux-switching slice motor," *Proceedings of 2014 IEEE Energy Conversion Congress and Exposition (ECCE)*, pp. 3811-3818, 2014.
- [99] N. Watanabe, H. Sugimoto, A. Chiba, T. Fukao and M. Takemoto, "Basic characteristic of the multi-consequent-pole bearingless motor," *Proceedings of the Power Conversion Conference*, pp. 1565-1570, 2007.
- [100] T. Noguchi, H. Sugimoto, Y. Fujii and A. Chiba, "A novel combined winding and test result of a 20-pole/24-slot consequent-pole bearingless motor with parallel motor winding," *IEEE Transactions of Industry Applications*, vol. 57, no. 6, pp. 6880-6891, 2021.
- [101] J. Asama, T. Fukao, A. Chiba, A. Rahman and T. Oiwa, "A design consideration of a novel bearingless disk motor for artificial hearts," *Proceedings of 2009 IEEE Energy Conversion Congress and Exposition*, pp. 1693-1699, 2009.
- [102] K. Minami, T. Sekine, K. Hijikata and Y. Tanaka, "A proposal of consequent-pole type bearingless vernier motor," *Proceedings of 2017 IEEE 12th International Conference on Power Electronics and Drive Systems (PEDS)*, pp. 373-379, 2017.
- [103] A. Abdel-Khalik, S. Ahmed and A. A. Massoud, "A bearingless coaxial magnetic gearbox," *Alexandria Engineering Journal*, vol. 53, no. 3, p. 573–582, 2014.

- [104] B. Praslicka, M. Johnson, M. C. Gardner, E. Dangtran and H. A. Toliyat, "Effects of Axial Flux Magnetic Gear Misalignment," *Proceedings of the IEEE Energy Conversion Conference and Expo*, pp. 293-300, 2020.
- [105] L. Xu, W. Zhao, G. Liu and C. Song, "Design Optimization of a Spoke-Type Permanent-Magnet Vernier Machine for Torque Density and Power Factor Improvement," *IEEE Transactions on Vehicular Technology*, vol. 68, no. 4, pp. 3446-3456, 2019.
- [106] G. Jungmayr, J. Loeffler, B. Winter, J. F and W. Amrhein, "Magnetic gear: Radial force cogging torque skewing and optimization," *Transactions on Industry Applications*, vol. 52, no. 5, pp. 3822-3830, 2016.
- [107] T. Takenaga, Y. Kubota, A. Chiba and T. Fukao, "A Principle and Winding Design of Consequent-Pole Bearingless Motors," *JSME International Journal Series C Mechanical Systems, Machine Elements and Manufacturing*, vol. 46, no. 2, pp. 363-369, 2003.
- [108] J. Asama, D. Kanehara, T. Oiwa and A. Chiba, "Development of a Compact Centrifugal Pump With a Two-Axis Actively Positioned Consequent-Pole Bearingless Motor," *IEEE Transaction on Industry Applications*, vol. 50, no. 1, pp. 288-295, 2014.
- [109] M. Miyoshi, H. Sugimoto and A. Chiba, "Axial vibration suppression by field flux regulation in two-axis actively positioned permanent magnet bearingless motors with axial position estimation," *IEEE Transactions on Industrial Applications*, vol. 54, no. 2, p. 1264–1272, 2018.
- [110] D. Steinert, T. Nussbaumer and J. W. Kolar, "Evaluation of One- and Two-Pole-Pair Slotless Bearingless Motors With Toroidal Windings," *IEEE Transactions on Industry Applications*, vol. 51, no. 1, pp. 172-180, 2016.
- [111] J. Asama, R. Nakamura, H. Sugimoto and A. Chiba, "Evaluation of Magnetic Suspension Performance in a Multi-Consequent-Pole Bearingless Motor," *IEEE Transactions on Magnetics*, vol. 47, no. 10, pp. 4262-4265, 2011.
- [112] H. Sugimoto, M. Miyoshi and A. Chiba, "Axial Vibration Suppression by Field Flux Regulation in Two-Axis Actively Positioned Permanent Magnet Bearingless Motors With Axial Position Estimation," *IEEE Transactions on Industry Applications*, vol. 54,

- no. 2, pp. 1264-1272, 2018.
- [113] H. Sugimoto, S. Tanaka, A. Chiba and J. Asama, "Principle of a Novel Single-Drive Bearingless Motor With Cylindrical Radial Gap," *IEEE Transactions on Industry Applications*, vol. 51, no. 5, pp. 3696-3706, 2015.
- [114] Y. Kamijo, H. Ito and Y. MARUYAMA, "ゼロパワー制御を用いた磁気軸受の構成と軸支持特性 / Structure and Characteristic of Magnetic Bearing with Zero Power Controlled Electromagnetic Suspension," *Transactions of the Japan Society of Mechanical Engineers. C*, vol. 79, no. 808, pp. 4963-4972, 2013.

List of publications

Peer-Reviewed Papers

- (1) A. Kumashiro, Y. Fujii, A. Chiba, W. Gruber, W. Amrhein, and G. Jungmayr, "Novel Reluctance-type Magnetic-geared Motor Integrated with High-speed Bearingless Motor," IEEE Transactions on Industry Applications, May/June 2024, DOI: 10.1109/TIA.2024.3357049
Corresponding to Chapter 3, Chapter 4, and Chapter 5.
- (2) A. Kumashiro, Y. Fujii, A. Chiba, W. Gruber, and G. Jungmayr, "コンシクエントポールを採用した磁気ギアードモータにおける高速ロータのベアリングレス化の検討 / Investigation of Integrated Bearingless Motor to High-Speed Rotor in Consequent-Pole Type Magnetic Geared Motor", Journal of the Japan Society of Applied Electromagnetics and Mechanics, Vol. 32, No. 1, March 2024
Corresponding to Chapter 3 and Chapter 6.
- (3) A. Kumashiro, Y. Fujii, A. Chiba, W. Gruber, and G. Jungmayr, "Design and Optimization of Different Integrated Bearingless Motor Topologies in Magnetic-Geared Motors," IEEJ Journal of Industry Applications, Vol. 13, No. 4
Corresponding to Chapter 3 and Chapter 7.

International Conferences

- (4) A. Kumashiro, A. Chiba, W. Gruber, W. Amrhein and G. Jungmayr, "Investigation of a Combined Electro Magnetic Structure of Bearingless Motor and Magnetic Gear", 2020 IEEE Energy Conversion Congress and Exposition (ECCE), pp. 278-284, October 2020.
- (5) A. Kumashiro, A. Chiba, H. Sugimoto, W. Gruber, W. Amrhein and G. Jungmayr, "Proposal of Magnetic Geared Motor with Bearingless High-Speed Rotor", 2020 23rd International Conference on Electrical Machines and Systems (ICEMS), pp. 1744-1747, December 2020.
- (6) A. Kumashiro, A. Chiba, W. Gruber, W. Amrhein and G. Jungmayr, "Novel Reluctance-type Magnetic Geared Motor with Integrated with High-speed Bearingless

- Motor", 2022 International Power Electronics Conference, pp. 1762-1768, May 2022.
- (7) A. Kumashiro, A. Chiba, W. Gruber, W. Amrhein and G. Jungmayr, "Optimization of Stack Length in Magnetic-Geared Motor with Magnetically Suspended High-Speed Rotor", 2022 IEEE Energy Conversion Congress and Exposition (ECCE), pp. 1-7, October 2022.

Domestic Conference

- (8) A. Kumashiro and A. Chiba," Proposal of a Novel Magnetic-Geared Motor with Integrated Bearingless Motor / 高速ロータが磁気浮上する磁気ギアとベアリングレスモータのハイブリッド回転機の提案,"2020 IEEJ National Convention, Tokyo, 5-009, March 2020.
- (9) A. Kumashiro, A. Chiba, Wolfgang Gruber, Wolfgang Amrhein, Gerald Jungmayr, "高速ロータが磁気浮上する表面磁石型磁気ギアードモータの提案 / Proposal of a Novel Surface Permanent Magnet Type Magnetic-Geared Motor with Integrated Bearingless Motor," Technical Meeting on "Motor Drive", "Rotating Machinery", and "Linear Drive", Web, MD-20-102, RM-20-095, LD-20-045, September 2020.
- (10) A. Kumashiro, NVIDIA GV100 GPU を使用した解析の高速化について / An investigation of accelerated analysis using the NVIDIA GV100 GPU, JMAG Users Conference 2020, November 2020.
- (11) A. Kumashiro, A. Chiba, Wolfgang Gruber, Wolfgang Amrhein, Gerald Jungmayr, "高速ロータが磁気浮上する磁気ギアードモータにおける支持力と構造の関係の調査 / Investigation of the Relationship between Suspension Force and Structure in Magnetic Geared Motor with Bearingless High-Speed Rotor," 2021 IEEJ National Convention, Osaka, 5-002, March 2021.
- (12) A. Kumashiro, A. Chiba, Wolfgang Gruber, Wolfgang Amrhein, Gerald Jungmayr, "高速ロータが磁気浮上する磁気ギアードモータにおける支持力と磁気吸引力の調査 / Investigation of Suspension and Magnetic Attractive Forces in Magnetically Geared Motors with Magnetically Levitated High-speed Rotors," 33rd Symposium on Electromagnetic and Dynamics, SEAD33-7, Gumma, May 2021.

- (13) A. Kumashiro, A. Chiba, Wolfgang Gruber, Wolfgang Amrhein, Gerald Jungmayr, "高速ロータが磁気浮上する磁気ギアードモータにおけるスロット構造と磁気支持力の調査 / Investigation of Slot Structure and Magnetic Suspension Force in Magnetically Geared Motor with Magnetically Levitated High-speed Rotor," 2021 IEEJ Industry Applications Society Conference, Y-67, Niigata, August 2021.
- (14) A. Kumashiro, A. Chiba, Wolfgang Gruber, Wolfgang Amrhein, Gerald Jungmayr, "高速ロータが磁気浮上する磁気ギアードモータにおける構造と特性の調査 / Investigation of Structure and Characteristics in Magnetic Geared Motor with Magnetically Levitated High-Speed Rotor," Technical Meeting on "Rotating Machinery," RM-21-111, Web, November 2021.
- (15) A. Kumashiro, NVIDIA GV100 GPU と JMAG-Designer v20 を使用した解析の高速化について / Investigation of accelerated analysis using NVIDIA GV100 GPU in JMAG-Designer v20, JMAG Users Conference 2021, Web, December 2021.
- (16) A. Kumashiro, A. Chiba, Wolfgang Gruber, Wolfgang Amrhein, Gerald Jungmayr, "高速ロータが磁気浮上する磁気ギアードモータにおける積厚と伝達トルクの調査 / Investigation of Stack Length and Transmission Torque in Magnetic Geared Motor with Bearingless High-Speed Rotor," 2022 IEEJ National Convention, Okayama, 5-022, March 2022.
- (17) A. Kumashiro, A. Chiba, Wolfgang Gruber, Wolfgang Amrhein, Gerald Jungmayr, "高速ロータが磁気浮上する磁気ギアードモータにおける諸特性の検証 / Evaluation of Characteristics in Magnetic Geared Motor with Magnetically Levitated High-Speed Rotor," Technical Meeting on "Rotating Machinery," pp29-34, October 2022.
- (18) A. Kumashiro, A. Chiba, Yusuke Fujii, Wolfgang Gruber, Wolfgang Amrhein, Gerald Jungmayr, "高速ロータが磁気浮上する磁気ギアードモータにおける回転角度位置検出の検証 / Evaluation of Rotational Angle Position Detection in Magnetic Geared Motor with Magnetically Levitated High-Speed Rotor," Technical Meeting on "Magnetics," "Motor Drive," and "Linear Drive," pp91-96, November 2022.
- (19) A. Kumashiro, "高速ロータを磁気浮上させた磁気ギアードモータの製作と試験," パワーアカデミー研究助成 2023 年成果報告会, Aichi, March 2023.

-
- (20) A. Kumashiro, Y. Fujii, A. Chiba, Wolfgang Gruber, Gerald Jungmayr, "コソシクエントポールを採用した磁気ギアードモータにおける高速ロータのベアリングレス化の検討 / Investigation of Integrated Bearingless Motor to High-Speed Rotor in Consequent-Pole Type Magnetic Geared Motor," 35th Symposium on Electromagnetic and Dynamics, OS3-3-1, Hiroshima, May 2023.
 - (21) A. Kumashiro, Y. Fujii, A. Chiba, Wolfgang Gruber, Wolfgang Amrhein, Gerald Jungmayr, "Design and Optimization of Integrated Bearingless Motor to Magnetic-Geared Motor with Different Motor Topologies," 2023 IEEJ Industry Applications Society Conference, R3-2 3-7, Aichi, August 2023.

List of Awards

- (22) A. Kumashiro, A. Chiba, Wolfgang Gruber, Wolfgang Amrhein, Gerald Jungmayr, "高速ロータが磁気浮上する磁気ギアードモータにおけるスロット構造と磁気支持力の調査 / Investigation of Slot Structure and Magnetic Suspension Force in Magnetically Geared Motor with Magnetically Levitated High-speed Rotor," 2021 IEEJ Industry Applications Society Conference, Y-67, Niigata, Au-gust 2021.
Received "YSP (若手エンジニア向けの研究発表) 優秀論文発表賞".
- (23) A. Kumashiro, "高速ロータを磁気浮上させた磁気ギアードモータの製作と試験," パワーアカデミー研究助成 2023 年成果報告会, Aichi, March 2023.
Received "2023 年 パワーアカデミー萌芽研究優秀賞".
- (24) A. Kumashiro, Y. Fujii, A. Chiba, Wolfgang Gruber, Wolfgang Amrhein, Gerald Jungmayr, "Design and Optimization of Integrated Bearingless Motor to Magnetic-Geared Motor with Different Motor Topologies," 2023 IEEJ Industry Applications Society Conference, R3-2 3-7, Aichi, August 2023.
Received "電気学会リニアドライブ技術委員会奨励賞".
- (25) A. Kumashiro, Y. Fujii, A. Chiba, W. Gruber, and G. Jungmayr, "コンシクエントポールを採用した磁気ギアードモータにおける高速ロータのペアリングレス化の検討 / Investigation of Integrated Bearingless Motor to High-Speed Rotor in Consequent-Pole Type Magnetic Geared Motor", Journal of the Japan Society of Applied Electromagnetics and Mechanics, Vol. 32, No. 1, March 2024
Received "令和 6 年 日本 AEM 学会奨励賞".

